

## Université de Lille, Sciences et Technologies

École doctorale :

Sciences de la Matière du Rayonnement et de l'Environnement

---

### **Advanced aerosol characterization using sun/sky photometer and multi-wavelength Mie-Raman lidar measurements**

---

Thèse préparée et soutenue publiquement par

**Qiaoyun Hu**

le 19/12/2018, pour obtenir le grade de Docteur en Physique

**Reviewer :**

Albert ANSMANN	Professor	Leibniz Institute for Tropospheric Research, Germany
Valery SHCHERBAKOV	Professor	Laboratoire de Météorologie Physique, France

**Examinator :**

Adolfo COMERON	Professor	Polytechnic University of Catalonia, Spain
Igor VESELOVSKII	Professor	General Physics institute, Russia
Iwona STACHLEWSKA	Professor	University of Warsaw, Poland
Lucas ALADOS ARBOLEDAS	Professor	University of Granada, Spain

**Director :**

Philippe GOLOUB	Professor	Université de Lille, France
Oleg DUBOVIK	Researcher	CNRS, France

### **Laboratoire d'optique atmosphérique**

Département Physique, Université de Lille, Sciences et Technologies

59655 Villeneuve d'Ascq, France



## Université de Lille, Sciences et Technologies

École doctorale :

Sciences de la Matière du Rayonnement et de l'Environnement

---

### Méthode avancée de caractérisation des aérosols par sondage lidar et photométrie solaire

---

Thèse préparée et soutenue publiquement par

**Qiaoyun Hu**

le 19/12/2018, pour obtenir le grade de Docteur en Physique

**Rapporteur :**

Albert ANSMANN

Professeur Leibniz Institute for Tropospheric Research, Germany

Valery SHCHERBAKOV

Professeur Laboratoire de Météorologie Physique, France

**Examineur :**

Adolfo COMERON

Professeur Polytechnic University of Catalonia, Spain

Igor VESELOVSKII

Professeur General Physics Institute, Russia

Iwona STACHLEWSKA

Professeur University of Warsaw, Poland

Lucas ALADOS ARBOLEDAS

Professeur University of Granada, Spain

**Directeur :**

Philippe GOLOUB

Professeur Université de Lille, France

Oleg DUBOVIK

Chercheur CNRS, France

### Laboratoire d'optique atmosphérique

Département Physique, Université de Lille, Sciences et Technologies

59655 Villeneuve d'Ascq, France



## Abstract

There are two objectives in this study : (i) aerosols characterization using multi-wavelength Mie-Raman lidar and (ii) the retrieval of aerosol properties through lidar and sun/sky photometer joint measurements. The measurements investigated were recorded in two observation sites : Lille (France) and M'bour, (Senegal). The measurements in M'bour were conducted in the SHADOW2 (Study of SaHaran Dust Over West Africa) campaign, in the framework of Labex CaPPA.

Aerosol characterization presented in this study concerns Saharan dust in M' Bour, long-range transported dust and Canadian smoke, as well as dust-smoke mixtures. Dust properties during the dry season and the transition period from dry to wet season, are characterized with lidar measurements in M' Bour. We found the contrast of dust properties during the two periods, explained by the intrusion of marine aerosols. Long-range transported Saharan dust in Lille showed distinct properties compared to the observations in M' Bour, indicating the impact of the transport process. Transported Canadian smoke plumes were detected at high altitude over Lille and exhibit surprisingly high depolarization ratios, which is possibly caused by the smoke ageing process. Additionally, dust-smoke mixtures measured in M' Bour and Lille point out the differences of aerosol origins.

In the second part of this study, lidar volume linear depolarization ratio has been included in the aerosol retrieval algorithm GARRLiC/GRASP. Sensitivity tests are performed to test the performance of GARRLiC/GRASP under different aerosol content, with different sphere fraction and with different error levels of molecular depolarization ratio and calibration coefficient. Then GARRLiC/GRASP is applied to real sun/sky photometer and lidar measurements and the retrievals are compared with results from independent methods for verification. The comparison shows that GARRLiC/GRASP retrievals are very consistent with the results from independent methods, but tend to produce lower dust particle depolarization ratio compared to the lidar measurements.

Over all, our results are relevant to the European scientific community since GARRLiC/GRASP is being implemented in the ACTRIS data and service center. This work will benefit to the evaluation of future European space missions.

**Key words :** Aerosol characterization ; remote sensing ; inversion algorithm



## Résumé

Les recherches que nous présentons ont principalement deux objectifs. D'une part la caractérisation des aérosols à l'aide du lidar Mie-Raman LILAS et d'autre part la restitution des propriétés aérosols par l'inversion simultanée des mesures Lidar et photométriques à l'aide l'algorithme GARRLIC/GRASP.

Les données analysées proviennent des super-sites d'observations de Lille (Hauts-de-France) et M'Bour (site côtier, Sénégal). Les mesures de M'Bour ont été acquises pendant SHADOW-2 (Study of SaHAran Dust Over West Africa), campagne réalisée dans le cadre du labex CaPPA. L'étude porte, tout d'abord, sur les poussières sahariennes caractérisées près des sources (Sénégal), puis les aérosols sahariens transportés à longue distance, les particules de fumée issues des feux de forêt canadiens, leur mélange caractérisés depuis le site de Lille. Pendant la saison sèche et la période de transition (i.e. de la saison sèche à la saison humide), les propriétés des poussières déduites du lidar LILAS opérant à M'Bour présentent des différences, en partie explicables par l'intrusion d'aérosols marins. Les poussières sahariennes transportées à longue distance et observées à Lille présentent des caractéristiques bien distinctes de celles de M'Bour, témoignant de l'impact du transport. A Lille, d'importants panaches de particules de fumée issus du Canada ont été détectés jusqu'à très haute altitude et présentent des rapports de dépolarisation étonnamment élevés, liés, en partie, au processus de vieillissement.

Dans la seconde partie de notre travail, nous nous sommes focalisés sur la validation, à l'aide de plusieurs cas d'étude, et d'une méthode indépendante, de l'algorithme GARRLIC/GRASP. En particulier, nous avons étudié l'apport de la dépolarisation lidar sur la restitution des propriétés caractéristiques des aérosols restituées. La comparaison montre une très bonne cohérence avec les résultats de méthodes indépendantes, sauf sur la dépolarisation (biais de l'ordre de 10%). Ces cas d'étude ont également permis de mesurer les profils d'absorption des aérosols, paramètre clef pour préciser leur impact radiatif. Nos résultats démontrent l'intérêt de l'algorithme GARRLIC/GRASP, en cours d'implémentation au Centre ICARE/AERIS, dans le cadre du projet et de l'infrastructure ACTRIS. Nos travaux aussi démontrent la pertinence des données du lidar et du photomètre sur les sites remarquables de Lille et M'Bour, et de leur interprétation à l'aide d'algorithmes tels que GARRLIC/GRASP pour la caractérisation fine des aérosols pour permettant leur impact radiatif et pour l'évaluation des futures missions de l'Agence Spatiale Européenne.

**Mots-clés :** Caractérisation des aérosols ; télédétection ; l'algorithme d'inversion



## Acknowledgement

I would like firstly to thank my supervisor Philippe Goloub for his guidance and support, without which this work cannot be fulfilled. Also I am grateful to Thierry Podvin, Igor Veselovskii, Oleg Dubovik and Anton Lopatin for their help in improving my technical skills and scientific knowledge. Three year ago I was almost a layman for lidar remote sensing and aerosol retrieval, it is with the help of them and also my own efforts that I can say today that I know something in the field. Although there is no end to learning, still I think this is a remarkable milestone in my journey and I do appreciate the unselfish help from the persons mentioned above.

Thanks are given to the European Space Agency who provided financial support for this thesis. And thanks to the ACTRIS-2 and EARLINET community who have offered many courses, trainings and meetings which provide students and young researchers a good opportunity to learn from more experienced experts in the community.

I am grateful to my colleagues Tatiana Lapyonok, Benjamin Torres, Ioana Popovici, Olivier Pujol, Fabrice Ducos, Cheng Chen, Lei Li, Yevgeny Derimian and Pavel Litvinov for their help in scientific or technical issues. Thanks to Vassilis Amiridis who was in my *comité de thèse* and gave me many encouragements. I sincerely thank my family, my parents and my brothers who always support me although they almost nothing about my work. Special thanks to my friend Mengyuan Hu, who understands me as she understands herself and to Shuo Li who cooked for me quite often during the period that I wrote my thesis.

I am also thankful to L<sup>A</sup>T<sub>E</sub>X community for their unselfish efforts in developing such a pleasant typesetting system.

# Contents

<b>Abstract</b>	<b>i</b>
<b>Résumé</b>	<b>iii</b>
<b>Acknowledgement</b>	<b>v</b>
<b>Contents</b>	<b>vi</b>
<b>List of Figures</b>	<b>ix</b>
<b>List of Tables</b>	<b>xiii</b>
<b>List of Abbreviations</b>	<b>xv</b>
<b>1 Introduction</b>	<b>1</b>
1.1 Context . . . . .	1
1.2 Aerosol sources . . . . .	2
1.3 Current state of aerosol studies . . . . .	6
1.4 Objectives of this study . . . . .	10
1.5 Layout of this study . . . . .	11
<b>2 Instrumentation and methodology</b>	<b>13</b>
2.1 Light scattering . . . . .	13
2.1.1 Molecular scattering . . . . .	13
2.1.2 Particle scattering . . . . .	17
2.2 Sun/sky photometer . . . . .	21
2.3 Lidar instrument . . . . .	24

---

2.3.1	General description of lidar . . . . .	24
2.3.2	LILAS system . . . . .	28
2.3.3	Lidar data quality assurance . . . . .	31
2.3.4	Lidar data processing . . . . .	44
2.4	Chapter summary . . . . .	47
<b>3</b>	<b>Aerosol observation and analysis</b>	<b>49</b>
3.1	Cirrus observation . . . . .	50
3.2	Saharan dust observation in M'Bour, Senegal . . . . .	55
3.2.1	Seasonal features of Saharan dust . . . . .	55
3.2.2	Case study . . . . .	66
3.2.3	Discussion . . . . .	75
3.3	Long-range transported aerosols . . . . .	78
3.3.1	Long-range transported dust observed in Lille . . . . .	78
3.3.2	Long-range transported Canadian smoke . . . . .	83
3.4	Dust and smoke mixture observed in Senegal and Lille . . . . .	90
3.5	Chapter summary . . . . .	100
<b>4</b>	<b>Lidar and photometer joint retrieval: GARRLiC/GRASP</b>	<b>103</b>
4.1	GARRLiC/GRASP algorithm . . . . .	104
4.1.1	Forward model . . . . .	105
4.1.2	Numerical inversion . . . . .	110
4.2	Sensitivity test . . . . .	112
4.2.1	Description of the sensitivity study . . . . .	112
4.2.2	Sensitivity to aerosol loading . . . . .	114
4.2.3	Sensitivity to the sphere fraction of coarse mode . . . . .	117
4.2.4	Sensitivity to the molecular depolarization ratio . . . . .	120
4.2.5	Sensitivity to the calibration coefficient . . . . .	122
4.3	Validation and application . . . . .	124
4.3.1	20 January 2016, M'Bour . . . . .	126
4.3.2	11 April 2015, M'Bour . . . . .	132
4.4	Chapter summary . . . . .	137

---

<b>5 Conclusion and perspectives</b>	<b>141</b>
5.1 Conclusions . . . . .	141
5.2 Perspectives . . . . .	143
<b>Bibliography</b>	<b>145</b>
<b>Appendix A: Supplementary materials</b>	<b>165</b>
<b>Appendix B: Article published on ACPD</b>	<b>169</b>

# List of Figures

1.1	Aerosol particles in scanning electron microscope . . . . .	3
1.2	Saharan dust observed from satellite and aircraft . . . . .	5
1.3	The map of global AERONET observation sites . . . . .	7
1.4	CALIPSO orbit and measured backscatter signal . . . . .	8
2.1	Elastic and Inelastic scattering . . . . .	15
2.2	Scattering components from laser illumination of a diatomic molecular gas [Miles et al., 2001] . . . . .	15
2.3	The scattering pattern calculated from Lorentz-Mie scattering . . . . .	18
2.4	The fitting of feldspar scattering matrix at $0.441 \mu\text{m}$ . . . . .	20
2.5	CIMEL sun/sky photometer . . . . .	21
2.6	CIMEL sky radiance measurements . . . . .	22
2.7	A schematic drawing of a photomultiplier tube . . . . .	25
2.8	The principle setup of a bi-axial lidar system . . . . .	26
2.9	LILAS lidar system operated by LOA . . . . .	29
2.10	The schematic drawing of LILAS system . . . . .	30
2.10	Rayleigh fit of LILAS system, 07 November 2017 . . . . .	34
2.11	The division of the telescope for telecover test . . . . .	35
2.12	Telecover test of 355 nm channel, 07 November 2017. . . . .	36
2.13	Telecover test of 532 nm channel, 07 November 2017 . . . . .	37
2.14	Telecover test of 1064 nm channel, cross (left) and parallel polarized (right), 07 November 2017 . . . . .	38
2.15	Telecover test of 387 nm and 530 nm channel, 07 November 2017 . . . . .	40
2.16	A scheme of polarization detection in lidar system . . . . .	41

2.17	Molecular depolarization ratio measured by LILAS system . . . . .	43
3.1	Cirrus observations on 24 August 2017, Lille . . . . .	50
3.2	Lidar observations on 16 December 2015, M'bour . . . . .	52
3.3	Ice clouds at 21:00–21:24 UTC, 16 December 2015, M'bour . . . . .	52
3.4	Mixed-phase cloud observations on 16 December 2015, M'bour . . . . .	53
3.5	The location of M'Bour, Senegal . . . . .	55
3.6	The meteorological condition near the ITCZ zone [Hastenrath and Lamb, 1977] . . . . .	57
3.7	The position of ITF in April 2015 . . . . .	58
3.8	Back trajectory in March 2015 at 500, 1000, 2000, 3000 m . . . . .	61
3.9	Back trajectory in April 2015 at 500, 1000, 2000, 3000 m . . . . .	62
3.10	Back trajectory in December 2015 at 500, 1000, 2000, 3000 m . . . . .	63
3.11	AERONET products for M'Bour site in 2014, 2015 and 2017 . . . . .	64
3.12	Dust lidar ratio, PLDR and color ratio in SHADOW2 campaign . . . . .	65
3.13	Lidar observations on 19–20 December 2015, M'Bour . . . . .	67
3.14	Averaged lidar observation 19:35–21:07 UTC, 19 December 2015 . . . . .	67
3.15	Five-day back trajectory from HYSPLIT model for 20:00 UTC, 19 De- cember 2015 . . . . .	68
3.16	The colormaps of Lidar observations on 10–11 April 2015 . . . . .	69
3.17	Averaged Lidar observation 23:00–01:57 UTC, 10–11 April 2015 . . . . .	70
3.18	Four-day back trajectory from HYSPLIT model for 01:00 UTC, 11 April 2015 . . . . .	70
3.19	The colormaps of Lidar observations on 20–21 April 2015 . . . . .	72
3.20	Averaged lidar observation 23:40–01:00 UTC, 21 April 2015 . . . . .	73
3.21	Five-day back trajectory from HYSPLIT model for 00:00 UTC, 21 April 2015 . . . . .	73
3.22	Modeled BAE, EAE and lidar ratio versus the imaginary part of the com- plex refractive index. . . . .	76
3.23	Modeled LR using aerosol components from MERRA2 . . . . .	77
3.24	Lidar observations on 10–11 March 2017 . . . . .	79

3.25	Four-day back trajectory for 23:00 UTC, 10 March 2017 and MODIS image . . . . .	80
3.26	Averaged observations at 21:00–23:00 UTC, 10 March 2017 . . . . .	81
3.27	Normalized size distributions in Lille, Dakar and Tamanrasset . . . . .	82
3.28	The surface reflectance from MODIS observation on 16 August 2017 . . . . .	83
3.29	The columnar CO concentration from AIRS product . . . . .	84
3.30	The profiles of backscatter and particle depolarization ratio from CALIPSO products . . . . .	85
3.31	The smoke layers observed in August 2017, Lille . . . . .	86
3.32	Lidar inversions at 20:00–22:00 UTC, 31 August 2017, Lille . . . . .	88
3.33	Lidar inversions at 20:00–02:00 UTC, 31 August–01 September 2017, Lille . . . . .	90
3.34	Lidar observations on 20 January 2016, M’Bour . . . . .	92
3.35	Averaged lidar observations between 01:20 and 05:00 UTC, 20 January 2016 . . . . .	92
3.36	168-hour back trajectory at 04:00 UTC, 20 January 2016 . . . . .	93
3.37	Observations on 15–18 October 2017 . . . . .	94
3.38	True color image overlaid with fire and thermal anomalies from MODIS on 15–16 October 2017 . . . . .	95
3.39	Columnar CO concentration from AIRS on 16–21 October 2017 . . . . .	96
3.40	Lidar observation on 16, 17 and 18 October 2017, Lille . . . . .	97
3.41	Averaged lidar observation at 21:00–24:00 UTC, 17 October 2017, Lille . . . . .	98
3.42	Retrieved $R_{eff}$ , volume concentration and complex refractive indices, 17 October 2017 . . . . .	98
4.1	The principle scheme of GARRLiC/GRASP algorithm [Lopatin, 2013]. . . . .	104
4.2	The concept of GARRLiC/GRASP forward model [Lopatin, 2013] . . . . .	107
4.3	The simulated aerosol size distribution and vertical concentration . . . . .	114
4.4	GARRLiC/GRASP retrieval under different aerosol loadings . . . . .	116
4.5	GARRLiC/GRASP retrievals with different sphere fraction of coarse mode . . . . .	119
4.6	GARRLiC/GRASP retrieval with different spectrum configuration and molecular depolarization ratio . . . . .	121

---

4.7	GARRLiC/GRASP retrievals with depolarization bias . . . . .	123
4.8	Lidar signal averaged between 09:00–09:44 UTC, 20 January 2016, M’Bour	126
4.9	GARRLiC/GRASP retrieval on 20 January 2016, 09:15 UTC . . . . .	129
4.10	Back trajectory at 09:00 UTC, 20 January 2016, M’Bour . . . . .	130
4.11	Validation of GARRLiC/GRASP retrieval on 20 January 2016 . . . . .	131
4.12	Lidar signal averaged between 08:00–08:40 UTC, 11 April 2015, M’Bour	132
4.13	GARRLiC/GRASP retrieval on 11 Apr 2015, 08:23 UTC . . . . .	134
4.14	Validation of GARRLiC/GRASP retrieval at 08:23 UTC, 11 Apr 2015 . .	135
4.15	Absorption profiles retrieved by GARRLiC . . . . .	137
A.1	Measurements and fittings of GARRLiC/GRASP on 20 January 2016 . .	167
A.2	Measurements and fittings of GARRLiC/GRASP on 11 April 2015 . . .	168

# List of Tables

1.1	Key aerosol types in the troposphere . . . . .	4
2.1	Relative Rayleigh and Raman scattering intensity [Kattawar et al., 1981] .	17
2.2	Optical elements in the scheme of LILAS system . . . . .	30
3.1	Optical depth, lidar ratio and particle depolarization ratio of smoke layers in the UTLS in Summer 2017 . . . . .	87
3.2	Optical depth, LR and PLDR of smoke layers in the UTLS in Summer 2017	90
4.1	The simulated observation of the GARRLiC/GRASP forward model. . .	105
4.2	Aerosol microphysical parameters in GARRLiC/GRASP . . . . .	106
4.3	The complex refractive indices of fine mode and coarse mode in the sen- sitivity tests . . . . .	113
4.4	Parameters of the size distribution used in the simulated scenarios . . . .	113



# List of Abbreviations

<b>Abbr</b>	<b>Full name</b>	<b>Symbol</b>	<b>Unit</b>
PLDR	Particle linear depolarization ratio	$\delta_p$	%
VLDR	Volume linear depolarization ratio	$\delta_v$	%
LR	Lidar ratio	$S$	sr
EAE	Extinction Angström exponent	–	unitless
BAE	Backscatter Angström exponent	–	unitless
AE	Angström exponent	–	unitless
SSA	Single scattering albedo	$\omega_0$	unitless
AOD	Aerosol optical depth	$\tau$	unitless
PMT	Photomultiplier tube	–	unitless



# Chapter 1

## Introduction

*“ I believe a leaf of grass is no less than the journey-work of the stars.”*

– Walt Whitman

### 1.1 Context

Aerosols are suspending solid or liquid particles in the atmosphere. Natural aerosol sources are widely spread on this planet, fires generated by solar radiation or lightning, desert, volcanic eruptions and vast oceans are emitting significant amount of aerosol particles into the atmosphere. The human has lived with various aerosols for millions of year since the beginning of our species. But it is after the industrial age that aerosols started to attract the attention of the research community. Concerns about air quality and human health arose due to the dramatic increase of anthropogenic aerosols, as well as toxic gases produced in industrial activities. There are several marked events in the history of aerosol research. Arnold et al. [1990] found that aerosols can act as the reaction site of heterogeneous chemistry thus promoting the destruction of stratospheric ozone in the polar region. The eruption of Mt Pinatubo in 1991 injected about 20 million tons of sulphur compounds into the atmosphere and the global mean temperature dropped about several tenths of a degree [Ansmann et al., 1997, Hansen et al., 1992, 1997] in 1992. After 2000, intense and frequent haze events in Asia especially in China and India have threatened the health of billions of citizens, flight safety and caused large economic losses [Menon et al.,

2002, Garland et al., 2008, Huang et al., 2014]. Through these events people started realizing the impacts of aerosols on human health and the climate. However, the quantitative estimation of aerosol impacts are still very uncertain, because the complexity of aerosol properties and processes. Aerosol particles can absorb and scatter the incident solar radiation, thus directly affecting the earth radiative budget. Aerosols can also perturb the vertical temperature profile and impact the cloud formation process, which is known as the semi-direct effect [Hansen et al., 1997]. The suspending aerosol particles may act as cloud condensation nuclei and ice nuclei, therefore, they impact the cloud formation process and cloud micro-physics, which is known as aerosol indirect impacts. The changes in the cloud microphysics lead to the change of cloud macro-physical properties, for example the cloud albedo, lifetime and precipitation release [Jones et al., 1994, Storelvmo, 2017]. The main challenges of estimating the aerosol impacts on the radiative budget and the climate are the characterization of aerosol particles, the understanding, parameterization and representation about aerosol processes and aerosol-climate interaction.

## 1.2 Aerosol sources

The origin of aerosols generally consists of two categories, natural source and anthropogenic source. No matter natural or anthropogenic aerosols, the particles are mainly formed in two ways: the emission of primary particulate matter and the generation of secondary particulate matter from gaseous precursors. The main aerosol types in the atmosphere are mineral dust, inorganic species including sulphate, nitrate, ammonium, sea salt and so on; organic aerosols (OA), black carbon and primary biological aerosols particles (PBAP) [Boucher et al., 2013]. Mineral dust, sea salt and PBAP are usually primary particles, while nitrate, ammonium and non-sea-salt sulphate are mainly generated through secondary formation process. Mineral dust particle, sea salt and PBAP are mainly from natural source, while black carbon, nitrate and ammonium are mostly with anthropogenic origins. The organic aerosols, including primary organic aerosols and secondary organic aerosols, have both natural and anthropogenic sources.

Figure 1.1 displays the images of four aerosol samples in scanning electron microscope. Aerosol particles are of different size, morphology and chemical compositions, depending

on the nature of the particles. Mineral dust is the most abundant aerosol particles in the atmosphere. Dust particles are produced mainly by wind erosion of soil particles [Gillette and Passi, 1988, Shao, 2001, Zender et al., 2004]. The emission rate of dust depends on the wind speed, characteristics of soils, such as soil moisture, vegetation and texture. The major natural dust sources on earth are the Saharan desert, the Arabian peninsula, and Asia (the Takla Makan and Gobi deserts) [Colarco et al., 2010]. Figure 1.2 shows the plumes of Saharan dust observed in flight. Additionally, dust particles can be generated by anthropogenic activities, such as road, constructions and land use. Recent studies suggest that the contribution of anthropogenic dust composes about 20–25% of the total dust emission [Ginoux et al., 2012a,b]. Dust particles are mainly composed of particles with radius larger than  $0.6 \mu\text{m}$  [Dubovik et al., 2002a] and the shape of dust particles is highly irregular as shown in Figure 1.1(b).

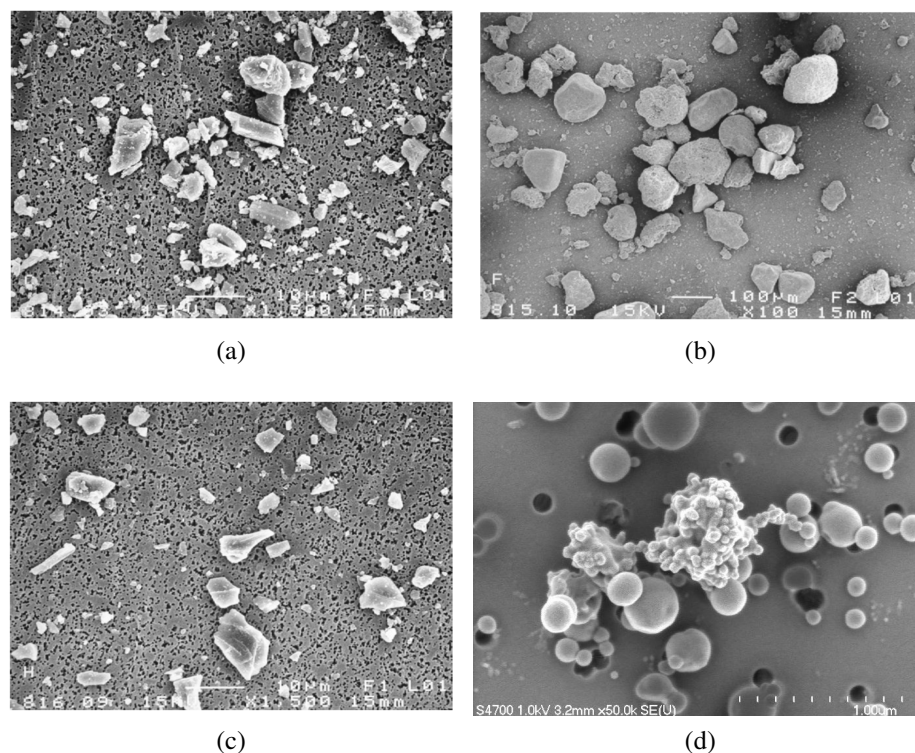


Figure 1.1. Aerosol particles in scanning electron microscope. (a) Feldspar particles, (b) Saharan dust particles, (c) smoke particle, (d) volcanic ash particles. (a), (b) and (c) are from Volten et al. [2001]. (d) is an image of an aggregation of soot particles from the Las Conchas fire ([link](#)).

Biomass burning aerosols originated from fire activities are another important aerosol

Table 1.1. Key aerosol types in the troposphere. Terrestrial primary biological aerosol particles (PBAPs), brown carbon and marine primary organic aerosols (POA) are particular types of organic aerosols (OA) but are treated here as separate components because of their specific properties. The table is adapted from Boucher et al. [2013].

Aerosol species	Main source	Key Climate relevant properties
Sulphate	Primary: marine and volcanic emissions Secondary: oxidation of SO <sub>2</sub> , and other S gases from natural and anthropogenic sources	Light scattering. Very hygroscopic. Enhances absorption when deposited as a coating on black carbon. CCN active
Nitrate	Oxidation of NO <sub>x</sub>	Light scattering Hygroscopic. CCN active
Black carbon	Combustion of fossil fuels, biofuels and biomass	Large mass absorption, efficiency in the shortwave. CCN active when coated, maybe IN active
Organic carbon	Combustion of fossil fuels, biofuels and biomass; continental and marine ecosystems, some anthropogenic and biogenic, non-combustion sources	Light scattering. Enhances absorption when deposited as a coating on black carbon. CCN active (depending on aging time and size)
... of which brown carbon	Combustion of fossil fuels, biofuels and biomass; natural humic-like substances from the biosphere	Medium mass absorption efficiency in the UV and visible. Light scattering
... of which terrestrial PBAP	Terrestrial ecosystems	Maybe IN active, may form giant CCN
Mineral dust	Wind erosion, soil resuspension. Some agricultural practices and industrial activities (cement)	IN active. Light scattering and absorption. Greenhouse effect
Sea spray	Breaking of air bubbles induced e.g. by wave breaking. Wind erosion	Light scattering. Very hygroscopic. CCN active, can include primary organic compounds in smaller size range
... of which marine POA	Emitted with sea spray in biologically active oceanic regions	CCN active

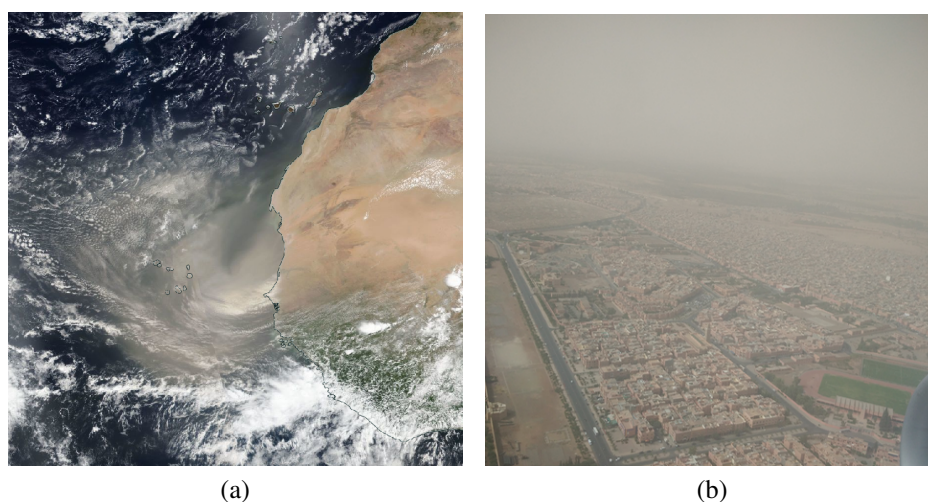


Figure 1.2. Saharan dust observed from satellite and aircraft. (a) Saharan dust outbreak on 16 September 2017 (b) Marrakech city enveloped by dust plumes, this photo is taken by the author in the flight from Paris to Marrakech on 16 August 2016.

type. The human evolution goes hand in hand with the use of fire. Smoke originated from biomass burning has both natural and anthropogenic origin. The yearly outbreak of boreal fires in summer in the northern hemisphere destroys a vast quantity of forest and emits copious smoke, as well as trace gases into the atmosphere. Smoke originated from fossil burning has gained the attention of the public since the last 2 centuries when the human history moved into the industrial age. Satellite observations have shown increased levels of carbon monoxide (CO), ozone (O<sub>3</sub>) and other trace gases possibly originated from biomass burning over South America, tropical Atlantic and Africa [Andreae and Merlet, 2001].

Black carbon is very effective in climate warming. Open burning of forests and savannas is claimed to be the largest global source of atmospheric black carbon. Diesel engines, industrial emission and solid fuels burning are also important sources of black carbon [Bond et al., 2013]. To date, black carbon has reached almost every corner on the continent, even the Amazonian rainforest, one of the few remaining pristine places [Morgan et al., 2014, Saturno et al., 2018].

Sea sprays are produced from the interaction of winds and waves. The bubbles generated by breaking waves introduce sea salt and marine primary organic aerosol into the atmosphere. The sea spray process is a highly variable process depending on the wind speed,

the state of the sea and the atmospheric conditions. The microphysics and chemical compositions of sea spray also have high uncertainties. Sea salt is usually big, spherical and low absorbing particles. While the maritime POAs are found to be particles smaller than  $0.2 \mu\text{m}$  [Leck and Keith Bigg, 2008, Russell et al., 2009]. Table 1.1 lists the source and climatic properties of the main aerosol types that are found in the troposphere.

### 1.3 Current state of aerosol studies

Observations and modeling are two important fields of aerosol research. Researchers usually study aerosol through in-situ and remote sensing. In-situ measurements provide rich and direct measurements about aerosol optical, microphysical and chemical characteristics. In-situ instruments are usually carefully calibrated and operated in a well-controlled environment. The platform of in-situ measurements is restricted to the ground or on an aircraft flying up to several kilometers over the ground level. In-situ measurements at very high altitude have been conducted using a laser ionization mass spectrometer mounted on-board a high altitude research airplane [Murphy, 1988]. But this kind of measurements are rarely realizable due to the cost and difficulties in operation. Unlike satellite data, in-situ data are not advantageous in producing data in large quantity or scale. Additionally, the data standardization, the sampling technique and experiment condition are, to some extent, questionable issues that gap the in-situ data and remote sensing data.

Passive and active remote sensing are two main branches in the remote sensing technique. Passive instruments do not emit radiation but detect the radiation transmitted or scattered by the targets, which could be aerosols, clouds and gases in the context of this study. There are various passive remote sensing instruments aiming at different atmospheric constituents. For example, the CIMEL sun/sky photometer was designed for measuring the optical depth and sky radiances. The Pandora spectrometer was designed specifically to measure ozone, nitrogen dioxide and formaldehyde in the atmosphere. Active remote sensing instruments are usually radar<sup>1</sup> or lidar<sup>2</sup>, which detect the reflected or scattered radiation. Lidar and radar provide distance-resolved information, which is helpful in studying the aerosol or cloud distributions and dynamics. Lidar is a widely used tool

in aerosol and cloud characterization. The development of lidar technique enhances the information abundance of lidar measurements. Multi-wavelength Mie-Raman lidar with polarization channels can derive multiple parameters at a single acquisition. To overcome the sparse distribution of the ground-based observational site, networks are built to provide regional or global monitoring. The Aerosol Robotic Network (AERONET, Holben et al. [1998]) is a global network based on CIMEL sun/sky photometers. AERONET provides long-term aerosol observations and retrievals over the world. Pandora is a global remote sensing network based on the instrument Pandora-2S. Lidar networks such as the European Aerosol Research Lidar network (EARLiNET, Papayannis et al. [2005], Wandinger et al. [2016]) and the Micro-pulse lidar network in the framework of NASA (MPLNET) are regional networks for lidar observations.

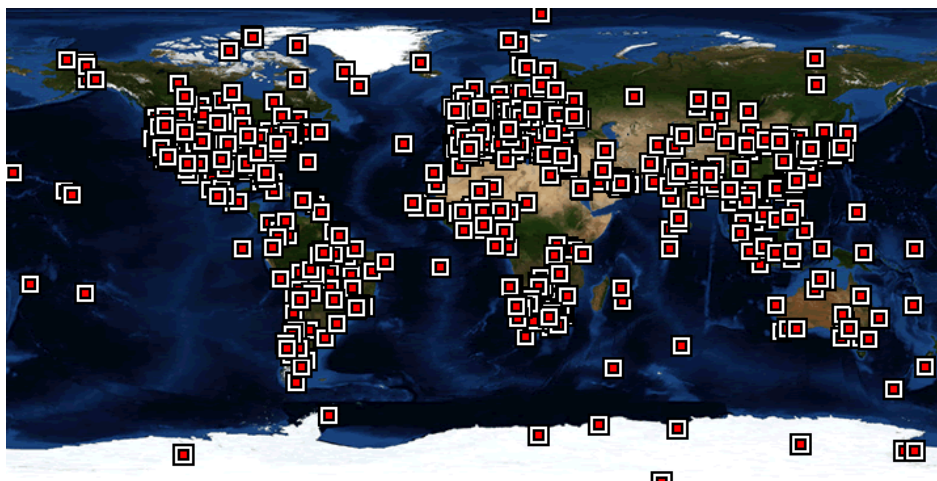


Figure 1.3. The map of global AERONET observation sites

Satellite remote sensing has a unique advantage in the spatial coverage compared to the other remote sensing techniques. Depending on its orbit, satellite sensor can provide observations with global coverage. A variety of sensors, including both passive and active instruments, can be deployed on satellites. Instruments designed for aerosol research, such as the Moderate Resolution Imaging Spectrometer (MODIS, Remer et al. [2005]), Polarization and Directionality of the Earth's Reflectances (POLDER, Tanré et al. [2011]) and so on, provide long-term and globally covered aerosol observations. The *Multi-viewing, multi-channel, multi-polarization Imager* (3MI, Manolis et al. [2013],

1. Radar: RAdio Detection and Ranging
2. Lidar: LIght Detection and Ranging

Marbach et al. [2013]) onboard EUMETSAT's Metop-SG A satellite, which is scheduled to be launched in 2021, is dedicated to aerosol characterization, climate monitoring and numerical weather prediction. The Cloud-Aerosol Lidar and Infrared Pathfinder Satellite Observations (CALIPSO, Winker et al. [2009, 2003]) is a successful space-borne lidar, following the first space lidar mission LITE (Lidar In-Space Technology Experiment). CALIPSO measures vertically resolved backscattered signal and depolarization ratio, which provide important information for the profiling and classification of aerosols and clouds in a global scale. The success of CALIPSO motivates the development and applications of new active space borne sensors. The Cloud-Aerosol Transport System (CATS) is lidar system installed on the International Space Station for short-term use. One lidar and one radar will be onboard the *Earth Clouds, Aerosols and Radiation Explore* (EarthCare, Illingworth et al. [2015]) mission. The data will contribute to the studies of aerosols, clouds, precipitation and other studies.

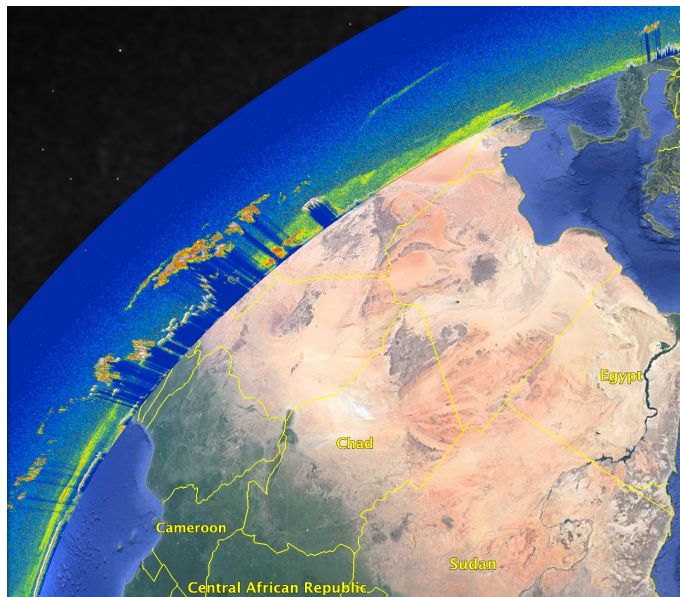


Figure 1.4. CALIPSO orbit and measured backscatter signal. The data is taken from CALIPSO track at 01:30 UTC, 23 August 2017.

All the techniques mentioned above, including in-situ, ground-based and space borne remote sensing technique have both advantages and limitations. Bridging the gaps between the datasets from different sources will definitely improve our knowledge about aerosols and their climate influences. This intense interest has stimulated many field campaigns devoted to different aspects of aerosol research. The Saharan Mineral Dust Experiment

project (SAMUM) is focused on the properties and transport of Saharan dust, as well as the interaction of dust with solar and terrestrial radiation. This campaign involved in-situ, lidar, aircraft and satellite measurements. Fresh dust, aged dust and dust mixed with marine aerosols were recorded and characterized in SAMUM campaign. Moreover, the measurements served as input and constraints for the modeling the radiative forcing effect of dust and for validating the output of dust model [Ansmann et al., 2009, Esselborn et al., 2009, Ansmann et al., 2011]. Following the success of the SHADE (Saharan Dust Experiment, Tanré et al. [2003]) field campaign in 2003, the SHADOW2 (Study of aerosol in Saharan dust over West Africa) took place in March, April, December 2015 and January 2016 in M'Bour, Senegal. SHADOW2 involved a comprehensive instrument sets, including in-situ, remote sensing and airborne measurements. The objective of SHADOW2 is the characterization of dust particles near the source. About 42-day measurements were accumulated and the measurements involved not only dust observation, but also dust mixed with marine aerosol and smoke. Several episodes are selected and presented in this study.

Observational data are valuable and fundamental for studying the aerosol properties and climatic effects. As mentioned above, there have been numerous contributions from different communities, in-situ and remote sensing, ground-based and space borne, laboratory measurements and field campaigns. These data are diverse in data quality, data type, spatial and temporal resolution and coverage. As a result, it is a great challenge to integrate these various measurements. Many efforts have been made to better represent and interpret aerosol properties based on modeling and data assimilation. In the past decades, several models coupling the main aerosol species or dust only, have been developed for short, medium range or global scale. The NMMB-MONARCH model (NMMB: Non-hydrostatic Multi-scale Model on the B grid; MONARCH: Multiscale Online Non-hydrostatic Atmosphere Chemistry, Pérez et al. [2011], Di Tomaso et al. [2017]) is a chemical weather forecast system operating in both regional and global scale. NMMB-MONARCH is initially focused on mineral dust and sea salt. The implementation of other aerosol species is under development [Spada et al., 2013, Badia et al., 2017]. The NMMB-MONARCH model considers observational dataset of MODIS, OMI (Ozone Monitor-

ing instrument, Levelt et al. [2006]) and AERONET measurements. NASA's GOCART model (Georgia Tech/Goddard Chemistry, Aerosol, Radiation and Transport, [Chin et al., 2000, Ginoux et al., 2001]) is an online aerosol transport modeling system that incorporates atmospheric components of dust, sea salt, black carbon and organic carbon, and sulphate aerosols. GOCART is driven by the GEOS-5 (Goddard Earth Observing System, version 5) atmospheric circulation model and provides global distributions of aerosol concentrations, vertical profiles, and optical thickness of individual as well as total aerosols [Chin et al., 2002, Colarco et al., 2010]. The MERRA-2 (Modern-Era Retrospective Analysis for Research and Applications, version 2 [Gelaro et al., 2017, Buchard et al., 2017]), is NASA's latest reanalysis for the satellite era. MERRA-2 uses the GEOS-5 model and the aerosol module in GOCART. MERRA-2 assimilates observational datasets from AERONET, MODIS, AVHRR, MISR. The products of MERRA-2 includes aerosol optical properties, vertical concentrations and mixing ratio of each aerosol component, as well as surface PM<sub>2.5</sub>. MERRA-2 is a helpful tool for the observation community, as it provides additional information for better understanding and interpreting the observations. At the same time, observations are very useful dataset for the verification and constraint of models. Veselovskii et al. [2018b] compared the Raman lidar observations collected in SHADOW2 with the vertical profiles from MERRA-2 in a smoke episode. Evaluation and comparison of MERRA-2 product with real measurements are studied by researchers [Buchard et al., 2017, Song et al., 2018] and more contributions are needed.

## 1.4 Objectives of this study

The main objective of this study is to characterize aerosol properties using multiple wavelength lidar observations and to improve lidar and sun photometer synergy retrieval with lidar measured depolarization ratio. To achieve this goal, the lidar system has been well tested and upgraded to assure and improve the quality of the measurements. During the SHADOW2 campaign and regular operation in Lille, abundant observational data were accumulated and provide a rich observational dataset for aerosol and cloud study. In this study we analyzed a series of aerosol observations, including Saharan dust, long-transported dust, smoke, as well as dust-smoke mixtures, which are among the main

aerosol components in the atmosphere. Lidar observations provide an excellent dataset for characterizing their optical and microphysical properties. Information from some extra data sources such as models and satellite sensors are used to better interpret the observations and related processes.

The lidar measured depolarization ratio is for the first time included in GARRLiC/GRASP (GARRLiC: Generalized Aerosol Retrieval from Radiometer and Lidar Combined data, GRASP: Generalized Retrieval of Aerosol and Surface Properties ) algorithm to improve the retrieval of aerosol columnar and vertically resolved optical and microphysical properties. Sensitivity tests are designed to investigate the performance of GARRLiC/GRASP when including depolarization ratio and to answer the questions related to the concerns of GARRLiC/GRASP users. Then GARRLiC/GRASP algorithm is applied on real lidar and sun/sky photometer observations. The results are verified by independent methods to demonstrate the strengths and limitations of GARRLiC/GRASP retrieval.

## **1.5 Layout of this study**

This thesis is divided into five chapters. The first chapter presents briefly the overview and background of aerosol research and is then followed by the objectives of this study. The second chapter presents firstly basic theories about molecular and particulate scattering. Then, the two main instruments, sun/sky photometer and multi-wavelength lidar are introduced. The lidar related data processing methods are presented in the end of the second chapter. The third chapter contains mainly lidar observations recorded in M'Bour and Lille site. Dust seasonal features were detected by lidar and sun/sky photometer observations and retrievals. Additionally, long-range transported dust, smoke, and dust-smoke mixture episodes are observed and analyzed. The fourth chapter presents the implementation of sun/sky photometer and lidar joint retrieval, GARRLiC/GRASP , using linear depolarization ratio derived from lidar measurements. The strategy of GARRLiC/GRASP algorithm is introduced based on the work of Lopatin et al. [2013]. Four groups of sensitivity tests are designed and performed to investigate the performance of GARRLiC/GRASP . Then GARRLiC/GRASP is applied to real measurements collected

in SHADOW2 campaign. The optical properties obtained from GARRLiC/GRASP are compared with independent AERONET retrieval and Raman inversion. The fifth chapter contains the conclusions and perspectives of this work. The supplementary materials and published paper are added in Appendix A and B.

# Chapter 2

## Instrumentation and methodology

*“Real knowledge is to know the extent of one’s ignorance.”*

– Confucius

In this chapter, the basis of molecular and particulate scattering are firstly introduced for better understanding the content of this thesis. Then the two main instruments: the sun/sky photometer and multi-wavelength Mie-Raman lidar are briefly presented. We take the CIMEL sun/sky photometer, CE318-N, as a model of all the serials of sun/sky photometers. Lidar is a unique instrument that is able to measure distance-resolved aerosol properties. LILAS (*Lille Lidar Atmospheric Study*) operated in LOA (*Laboratoire d’optique atmosphérique, Lille, France*) is a multi-wavelength Mie-Raman lidar affiliated to EAR-LiNET network. The system of LILAS, the calibration and the data-quality check procedure and the lidar data processing are written without giving too many technical details, in order to provide a concise introduction for lidar operation and lidar data treatment.

### 2.1 Light scattering

#### 2.1.1 Molecular scattering

When a monochromatic radiation of frequency  $\nu_0$  is incident on a molecular system, some of the radiation is transmitted with frequency preserved and some is scattered to other directions. The scattered light mostly preserves the frequency of the incident light, while a frequency shift in a fraction of the scattered light is detected. The scattering without

frequency change is called elastic scattering and the scattering with a shift of frequency is named as Raman scattering. The elastic molecular scattering is sometimes mistaken as Rayleigh scattering, named after the British physicist Lord Rayleigh. While the real meaning of Rayleigh scattering is the sum of the Cabannes lines and rotational Raman lines. In the time of Lord Rayleigh, Raman scattering has not been discovered and the spectral resolution of optical filters is not sufficient to separate the Cabannes line and rotational Raman lines which locate closely on both sides of the Cabannes lines [Young, 1982]. Raman scattering was firstly predicted by Smekal [1923] and then discovered by Raman [1928]. Due to the variation of temperature, pressure and collective motion of molecules, the spectrum of the elastically scattered light will be broadened. The exact elastically scattered radiation is located within the Cabannes lines. Figure 2.1 illustrates the principle of elastic and inelastic scattering.

The total Rayleigh scattering cross-section, including the Cabannes lines and rotational Raman lines, per molecule is expressed as follows:

$$\sigma_R(\lambda) = \frac{24\pi^3(n_s^2 - 1)^2}{\lambda^4 N_s^2(n_s^2 + 2)^2} \frac{6 + 3\rho_n}{6 - 7\rho_n}, \quad (2.1)$$

where  $\lambda$  is the wavelength of the incident light,  $N_s$  is the molecular density for standard air, and  $\rho_n$  is the depolarization factor of molecules, the term  $\frac{6+3\rho_n}{6-7\rho_n}$  is often called the ‘*King correction factor*’ [Bucholtz, 1995];  $n_s$  is the refractive indices of standard air. This formula is widely used in the calculation of molecular extinction and backscatter coefficients without distinguishing elastic scattering and rotational Raman scattering. Since elastic scattering is several orders stronger than the rotational Raman scattering in the atmosphere, it will not cause big differences. But, for lidar depolarization measurements, the Cabannes lines should be well separated from the rotational Raman lines because the latter is strongly depolarizing (about 75%) and insufficient suppression of rotational Raman lines will contaminated the depolarization measurements.

The phase function of Rayleigh scattering for unpolarized incident light is given below:

$$P_R(\Theta) = \frac{3}{4}(1 + \cos^2 \Theta), \quad (2.2)$$

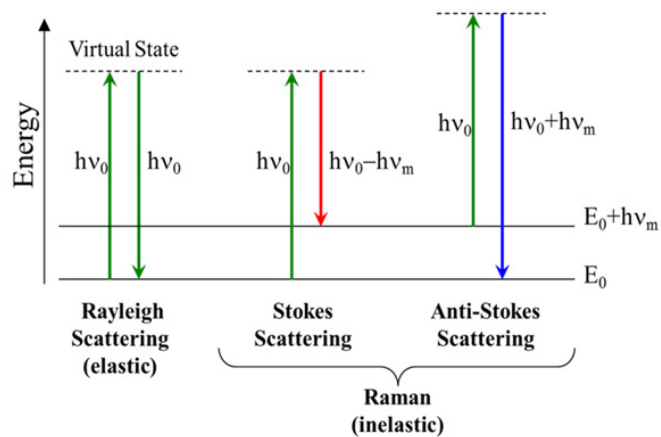


Figure 2.1. Elastic and inelastic scattering. The incident frequency is  $\nu_0$ . The scattered light with negative frequency shift  $-\nu_m$  is called Stokes scattering and positive frequency shift  $\nu_m$  is called anti-Stokes scattering.

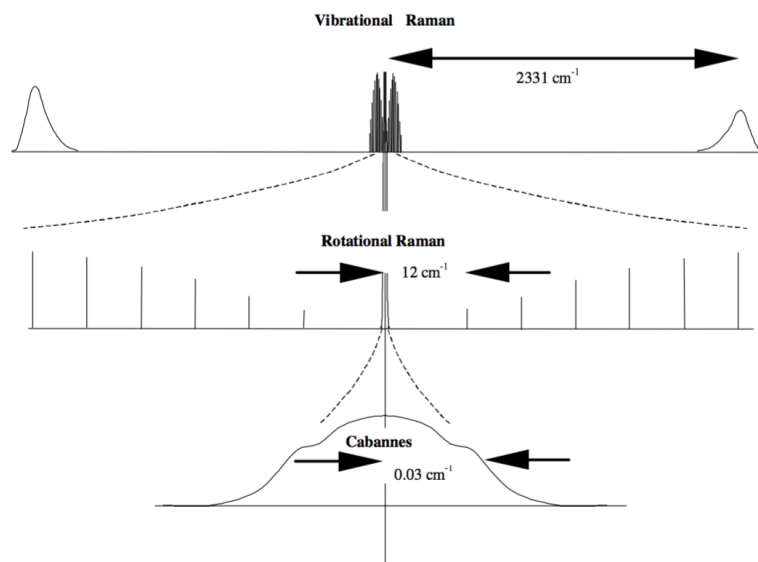


Figure 2.2. Scattering components from laser illumination of a diatomic molecular gas (e.g. nitrogen), at sequentially higher resolution [Miles et al., 2001].

where  $\Theta$  is the scattering angle, defined by the angle of the incident direction and scattering direction in the incident plane.

When the diatomic molecules, e.g.  $N_2$  and  $O_2$ , interact with linearly polarized light, the polarization state of elastically or inelastically scattered light can be described by the average molecule polarizability  $\bar{a}$  and the anisotropy of the polarizability  $\gamma$ . For example, the incident light is linearly polarized and the direction of the electric component is vertical to the scattering plane, if elastically scattering light is mostly polarized in the same direction while the anisotropy of molecules can cause a fraction of horizontally polarized light. The ratio between the two orthogonal polarized light is called the linear depolarization ratio. The depolarization of Raman scattering is more significant than the elastic scattering and their expressions are:

$$\delta_v^C = \frac{3\epsilon}{180 + 4\epsilon} \quad , \quad (2.3)$$

$$\delta_v^R = \frac{3}{4} \quad ,$$

Where the superscript ‘C’ and ‘R’ denote the Cabannes line and rotational Raman lines, and  $\epsilon = (\gamma/\bar{a})^2$ . For air, the weighted average accounting for  $N_2$  and  $O_2$  gives about  $\epsilon = 0.222$ , with very weak wavelength dependence. The subscript ‘v’ represents that the polarization direction of the incident light is vertical with respect to the scattering plane. If we take into account the Cabannes line and rotational Raman lines, the total depolarization ratio will be:

$$\delta_v^T = \frac{3\epsilon}{45 + 4\epsilon} \quad . \quad (2.4)$$

Table 2.1 presents the relative intensity of Rayleigh and Raman scattered light. The table summarizes unpolarized light, linearly polarized light with electric component in the vertical or horizontal plane, and for any scattering angle  $\Theta$ . The letters, ‘C’, ‘W’ and ‘T’ represent the Cabannes line, entire rotational Raman wings and the sum of the two. The superscripts on the left represent the polarization direction of the incident light and subscript on the right present the polarization direction of the scattered light. ‘V’ and ‘H’ represent respectively the linearly polarized light with electric vector vertical and parallel to the scattering plane. ‘0’ denote the unpolarized incident light or scattered light.

Table 2.1. Relative Rayleigh and Raman scattering intensity [Kattawar et al., 1981]

V polarization in	H polarization in	Sum (natural light in)
<b>Cabannes line</b>		
${}^V C_V = 180 + 4\epsilon$	${}^H C_V = 3\epsilon$	${}^0 C_V = 180 + 7\epsilon$
${}^V C_H = 3\epsilon$	${}^H C_H = 3\epsilon + (180 + \epsilon) \cos^2 \Theta$	${}^0 C_H = 6\epsilon + (180 + \epsilon) \cos^2 \Theta$
${}^V C_0 = 180 + 7\epsilon$	${}^H C_0 = 6\epsilon + (180 + \epsilon) \cos^2 \Theta$	${}^0 C_0 = 12\epsilon + (180 + \epsilon)(1 + \cos^2 \Theta)$
<b>Raman lines</b>		
${}^V W_V = 12\epsilon$	${}^H W_V = 9\epsilon$	${}^0 W_V = 21\epsilon$
${}^V W_H = 9\epsilon$	${}^H W_H = 9\epsilon + 3\epsilon \cos^2 \Theta$	${}^0 W_H = 18\epsilon + 3\epsilon \cos^2 \Theta$
${}^V W_0 = 21\epsilon$	${}^H W_0 = 12\epsilon + 3\epsilon \cos^2 \Theta$	${}^0 W_0 = 36\epsilon + 3\epsilon(1 + \cos^2 \Theta)$
<b>Total</b>		
${}^V T_V = 180 + 16\epsilon$	${}^H T_V = 12\epsilon$	${}^0 T_V = 180 + 28\epsilon$
${}^V T_H = 12\epsilon$	${}^H T_H = 12\epsilon + (180 + 4\epsilon) \cos^2 \Theta$	${}^0 T_H = 24\epsilon + (180 + 4\epsilon) \cos^2 \Theta$
${}^V T_0 = 180 + 28\epsilon$	${}^H T_0 = 24\epsilon + (180 + 4\epsilon) \cos^2 \Theta$	${}^0 T_0 = 48\epsilon + (180 + 4\epsilon)(1 + \cos^2 \Theta)$

### 2.1.2 Particle scattering

The interaction between electromagnetic wave and particles strongly depends on the ratio of the particle size to the wavelength of the incident light, which is also called size parameter,  $x = 2\pi r/\lambda$ . The size parameter is defined as a reference to separate the scheme of scattering. For particles or molecules with  $x \ll 1$ , Rayleigh scattering is considered; while for  $x \geq 1$ , the scattering is called *Lorentz-Mie scattering*. Lorentz and Mie independently derived the exact solution for the interaction between electromagnetic wave and homogeneous or radical stratification spheres [Lorentz, 1890, Mie, 1908]. The mathematical theory about Lorentz-Mie scattering can be found in Born and Wolf [2013]. Figure 2.3 shows the angular pattern of Lorentz-Mie scattering for particles with different size. The exact solution for the interaction between the electro-magnetic field and particles can be derived only for a few geometrical shapes [Mishchenko et al., 2002]. However, the morphology of real particles is highly diverse and difficult to be mathematically represented. Hence, the modeling of optical properties of non-spherical particles is still a challenge. Many efforts have been made in modeling the optical properties of non-spherical particles. Draine and Flatau [1994] presented that the discrete dipole approximation permits calculations of scattering and absorption with accuracy to within a few percent. Yang

et al. [2000] used the finite-difference-time domain technique for calculating the scattering. In principle, the two methods have no obvious limitations, but they require excessive computing time, which limits the usage of these methods. Mishchenko et al. [1997] presented that the randomly oriented spheroids with varying sizes and aspect ratios can reproduce the phase function of desert dust with adequate accuracy. The spheroid model has been applied on aerosol retrieval using remote sensing dataset [Dubovik et al., 2002b, 2006, Veselovskii et al., 2010, Lopatin, 2013]. The spheroid model is also used in the sun/sky photometer and lidar joint inversion method in Chapter 4.

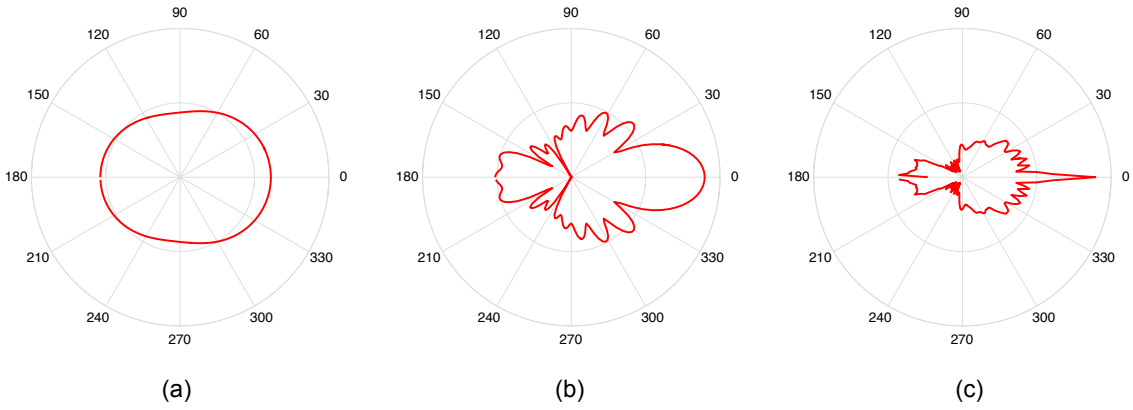


Figure 2.3. The scattering pattern calculated from Lorentz-Mie scattering. The incident light wavelength is  $0.5 \mu\text{m}$  (in vacuum), and the particle diameter is (a)  $0.1 \mu\text{m}$ , (b)  $1.5 \mu\text{m}$ , (c)  $5.0 \mu\text{m}$ .

The *Stokes vector* [Chandrasekhar, 2013] is a set of values that describe the intensity and polarization of a radiation. The effect of an optical system or object on polarizing light can be represented by applying a scattering matrix (also called Müller matrix) on the Stokes vector of the incident light. More theoretical details about Stokes vector and scattering matrix can be found in the publications of van de Hulst [1981], Bass et al. [1995], Mishchenko et al. [2002] and Goldstein [2003]. The scattering process of aerosols is described by the scattering matrix  $\mathbf{P}_{ij}(\Theta)$ . Specifically, the transformation of the Stokes vector of incident light into the scattered light is written as below:

$$\begin{pmatrix} I_s \\ Q_s \\ U_s \\ V_s \end{pmatrix} \propto \begin{pmatrix} P_{11}(\Theta) & P_{12}(\Theta) & 0 & 0 \\ P_{12}(\Theta) & P_{22}(\Theta) & 0 & 0 \\ 0 & 0 & P_{33}(\Theta) & P_{34}(\Theta) \\ 0 & 0 & -P_{34}(\Theta) & P_{44}(\Theta) \end{pmatrix} \begin{pmatrix} I_i \\ Q_i \\ U_i \\ V_i \end{pmatrix}, \quad (2.5)$$

where  $P_{ij}$  is the matrix element,  $\Theta$  is the scattering angle,  $I, Q, U, V$  are the four elements of the Stokes vector and the subscript ' $s$ ' and ' $i$ ' represent the scattered light and incident light, respectively. Expression 2.5 is a characteristic representation of any ensemble of randomly oriented particles with equal number of particles and their mirror-symmetric counterparts [Dubovik et al., 2006]. Each element in the scattering matrix is determined by the incident wavelength, the complex refractive index, the scattering angle and the morphology of the scattering particles. The element  $P_{11}(\Theta)$  in the scattering matrix is called the phase function. The phase function follows the normalisation rule:

$$\frac{1}{2} \int_0^\pi \sin(\Theta) P_{11}(\Theta) d\Theta = 1. \quad (2.6)$$

For spherically symmetric particles, i.e. homogenous or radically inhomogeneous spherical particles [van de Hulst, 1981, Mishchenko et al., 2002], the scattering matrix can be further simplified by:

$$P_{11} = P_{22}, P_{33} = P_{44}$$

Figure 2.4 shows the fitting of the elements in the scattering matrix of a Feldspar samples (at  $0.441 \mu\text{m}$ ) using spheroid model. Volten et al. [2001] measured the scattering matrices of a Feldspar sample, which is composed mostly of irregular particles. The size distribution and axis ratio distribution retrieved using spheroid model fit well with the measurements. The figure is taken from Dubovik et al. [2006].

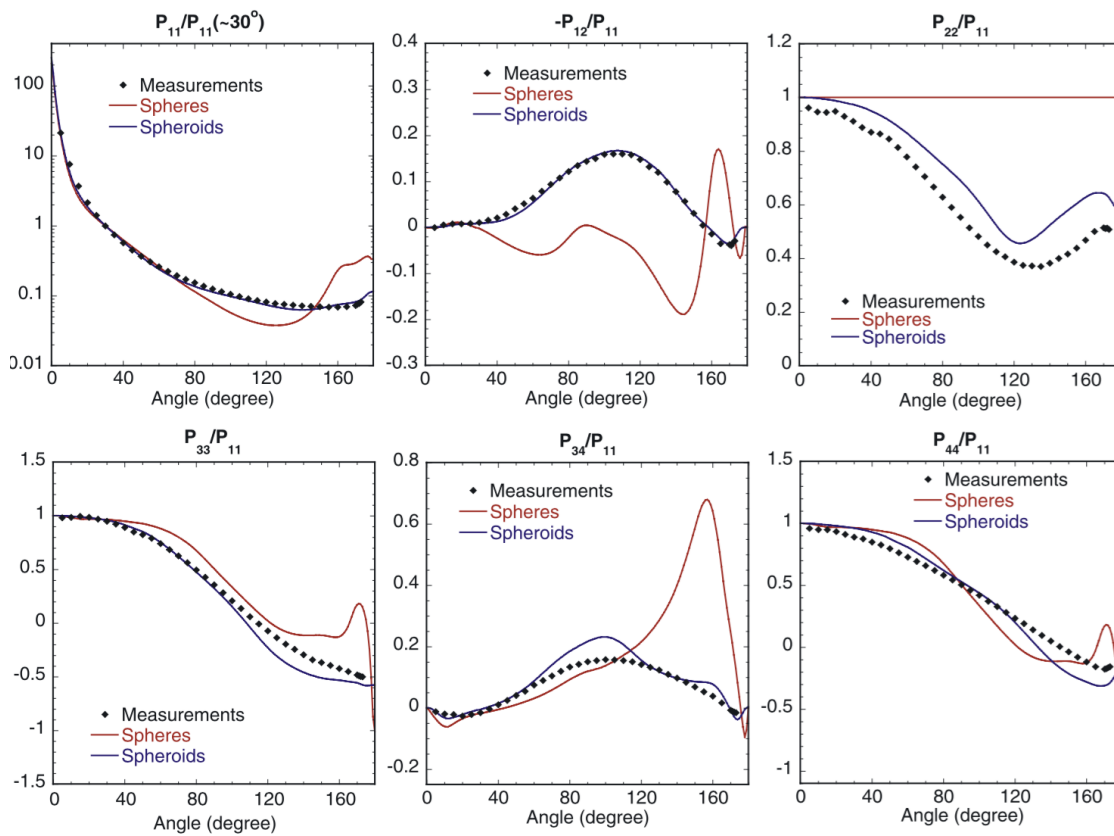


Figure 2.4. The fitting of feldspar scattering matrix at  $0.441 \mu\text{m}$ . The simulations for spheres and spheroids use the same size distribution and complex refractive index, which are retrieved using the spheroid model. The retrieval is based on the measurement of scattering matrices of irregular Feldspar particles [Volten et al., 2001].

## 2.2 Sun/sky photometer

The sun/sky photometers (in Figure 2.5, <https://www.ncas.ac.uk/en/cimel-sun-photometer>) deployed in the AERONET network are developed by the French company CIMEL Electronique. It is a multi-channel, automatic and solar-powered radiometer that measures both the solar irradiance and angular radiance on the surface of the Earth. The standard CE318-N sun/sky photometer uses 340, 380, 440, 500, 675, 870, 937, 1020 and 1640 nm filters. The measurements that will be introduced in this chapter are based on CE318-N model. In addition to the standard sensor head, four other sensor types: polarized, seaprisim, BRDF (Bidirectional Reflectance Distribution Function) and BRDF with 12 filters are also available on the presence of additional filters and mechanics.



Figure 2.5. A Cimel sun/sky photometer operated at M'bour, Senegal.

The sun/sky photometer measurements consist of two types: the direct sun measurements and sky radiance measurements. The direct sun measurements are performed on 9 different wavelengths: 340, 380, 440, 500, 675, 870, 937, 1020 and 1640 nm. The direct sun measurement determines the spectral attenuation of the atmosphere when the incident sunlight goes from the top of the atmosphere to the planet surface, reaching the detector of the photometer. The total attenuation of the atmosphere  $\tau(\lambda)$  consists in the contribution

of aerosols, molecules and absorbing gases. This can be expressed as follows:

$$I(\lambda) = I_0(\lambda)e^{-\frac{\tau(\lambda)}{\cos(\theta)}} \quad (2.7)$$

$$\tau(\lambda) = \tau_{aer}(\lambda) + \tau_{mol}(\lambda) + \tau_{gas}(\lambda),$$

where  $\tau$  is the total optical depth, and  $\tau_{aer}$ ,  $\tau_{mol}$  and  $\tau_{gas}$  represent the optical depth of aerosols, molecules and gases.  $I_0$  and  $I$  represent the incoming light flux at the top of the atmosphere and the light flux reaching the surface of the detector. The angle  $\theta$  represents the zenith angle of the detector. The direct sun measurements should be performed under a cloud-free condition to avoid the attenuation of clouds. The wavelengths of direct sun measurements are carefully selected at the band where low or no absorption of atmospheric gases is expected, except for the 937 nm channel where a water vapor absorption peak locates. The measurements at 937 nm are used to derive the total water vapor content. The number of the wavelengths depends on the model of the instruments, while the minimal dataset of the spectral direct sun measurements contains 440, 675, 870 and 1020 nm.

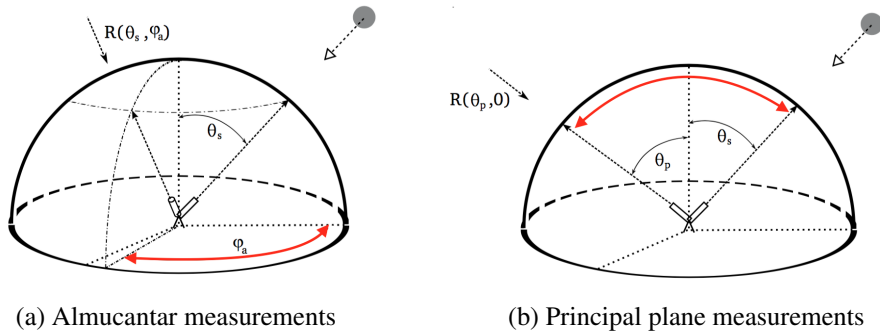


Figure 2.6. CIMEL sky radiance measurements: almicantar and principal plane measurements. The plots are adapted from Lopatin [2013]. The angle  $\theta_s$  represents the solar zenith angle,  $\varphi_a$  represents the azimuth angle.

The sky radiance measurements consist of two different protocols: the almicantar and principal plane measurements. The schematic of almicantar and principal plane measurements is plotted in Figure 2.6. The almicantar technique consists in measuring the sky radiance in aerosol channels, keeping a constant zenith angle equal to the zenith solar angle  $\theta_s$  with varying azimuthal angle  $\varphi_a$ . The principal plane technique keeps a constant azimuthal angle ( $180^\circ$  or  $0^\circ$ ) and varying zenith angles [CIMEL, 2015]. According

to the configuration of the standard CE318-N photometer, the almucantar and principal plane measurements are performed on the same wavelengths: 440, 500, 675, 870, 1020 and 1640 nm. In the almucantar measurements, the azimuthal angles vary from  $0.0^\circ$  to  $180.0^\circ$  for the right side and from  $0.0^\circ$  to  $-180.0^\circ$  for the left side. Assuming that the atmosphere is homogenous, almucantar measurements on the left and right side should be symmetrical. If this condition is met, the two measurement sets will be averaged at corresponding azimuthal angles (whose absolute values are the same). If not, the two values will be discarded. The reason causing the asymmetry is possibly due to clouds or non-homogeneity of the atmosphere. For the principal plane measurements, the zenith angle varies from  $-6^\circ$  to  $150.0^\circ$ . It is worthy to mention that the origin of the azimuthal angle is at the position where the photometer is pointing to the sun. More technical details can be found in the user's manual in CIMEL [2015]. The relationship between the scattering angle  $\Theta$  and the viewing angles  $(\theta_v, \varphi_v)$  and the solar zenith angle and azimuth angle  $(\theta_s, \varphi_s)$  is [Nakajima et al., 2007]:

$$\begin{aligned} \text{Almucantar: } \cos(\Theta) &= \cos^2(\theta_s) + \sin^2(\theta_s) \cos(\varphi_v - \varphi_s) \\ \text{Principal plane: } \cos(\Theta) &= \cos(\theta_v \mp \theta_s) \\ \theta_s, \theta_v &\in [0, \frac{\pi}{2}], \quad \varphi_v, \varphi_s \in [-\pi, \pi] \end{aligned} \quad (2.8)$$

In principle, the scattering angle reaches its maximum when

$$\theta_s = \frac{\pi}{2}, \text{ and } \varphi_v = \pm\pi,$$

however, this condition is not fulfilled in the real measurements because  $\theta_s$  is restricted to be smaller than  $\frac{\pi}{2}$ . So it is to say that the backward scattering cannot be measured, which is a great limitation for the almucantar measurements and a gap between the photometer measurements and lidar measurements. At current stage, the results retrieved from direct sun, almucantar and principal plane measurements are available in the AERONET database. A new scanning scenario, HYBRID, has been developed for new photometer models and the inversion products have recently been released on the AERONET database. The strategy of AERONET retrieval (using the direct AOD and almucantar measurements) will be introduced in Chapter 4.

## 2.3 Lidar instrument

### 2.3.1 General description of lidar

The first application of lidar dated back to 1963 [Goyer and Watson, 1963] when a conceptual possibility of laser application to the meteorology was described. Depending on the interaction processes that lidar emission interacts with the atmospheric constituents, lidar can be used to profile the temperature, pressure, wind, humidity, clouds, trace gases as well as aerosols [Wandinger, 2005]. The wavelengths used by a lidar system are selected according to the applications and the wavelength range varies from the ultraviolet to the mid-infrared. The Nd:YAG (Neodymium-doped Yttrium Aluminum Garnet;  $\text{Nd:Y}_3\text{Al}_5\text{O}_{12}$ ) lasers are widely used by the lidar community. The Nd:YAG crystal emits radiation typically at 1064 nm which can be converted into 532 nm and 355 nm by means of frequency doubling and tripling, respectively. 266 nm radiation can also be obtained by frequency quadrupling. Nd:YAG laser can operate in both continuous and pulsed mode. Other laser source such as ruby,  $\text{CO}_2$ , excimer are also widely used in different lidar applications.

A basic lidar setup consists of two parts: the emitting system and the receiving system. The emitting system is composed of laser source, beam expander as well as the emitting optics; the receiving system is composed of a telescope, receiving optics and the data acquisition. The laser beam emitted by the laser source is usually highly collimated and quasi-monochromatic. The beam expander is used to reduce the divergence and expand the diameter of the laser beam. The beam divergence after the beam expander can often reach few hundred micron radian. A telescope is used to collect the scattered photons. The Field-of-View (FOV) of the telescope has to be carefully selected. The FOV is determined by the size of a field stop that locates in the focal plane of the receiving optics. The increase of the FOV help to decrease the overlap range which is caused by the fact that in the near range the emitted beam is not completely covered by the FOV of the telescope. At the same time, the increase of the FOV of the telescope will increase the background light, thus decreasing the signal-to-noise ratio, and increase the possibility of detecting multiple scattered photons. Different lidars may have different ranges of interest, so the

FOV of the telescope is selected according to different usage. For example, lidars for cloud observation need very small FOV to avoid multiple scattering; stratospheric ozone lidar can use chopper to completely avoid the strong backscattered signal in the troposphere and only collect signal in the stratosphere; aerosol lidars need to find a balance for the choice of FOV to achieved a favorable performance of lidar system.

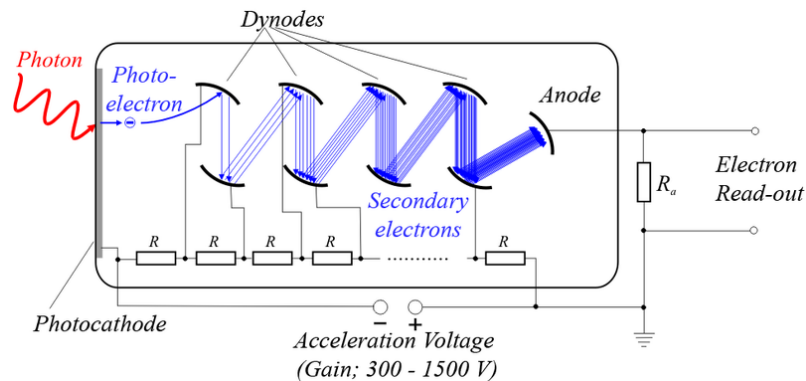


Figure 2.7. A schematic drawing of a photomultiplier tube, the figure is from Internet<sup>1</sup>. The photomultiplier consists of a photocathode, several dynode and a anode. Incident light reaching the surface of the photocathode will generate electrons as a consequence of photoelectric effect. The generated electrons are directed onto the dynodes and multiplied by the secondary emission.

The receiving optics consist mainly dichroic mirrors that split light by the wavelength, polarizing beam splitters that separate light by the polarization state, wave plates as well as density filters. The dichroic mirror reflects or transmits light depending on the wavelength. Interference filters are mainly used to transmit the backscatter light in the band of interest and suppress the light out of this band. The polarizing beam splitter splits the incident light into two beams with different polarization orientation. Half wave-plate is used to change the polarization orientation of the incident light. Density filters are used to regulate the amplitude of the backscattered signal in order to fit the dynamic range of the detector. The development of optical technique enables not only the detection of the intensity of the backscattered radiation but also the polarization state. Many atmospheric lidars can measure the particle linear depolarization ratio in order to characterize the shape of the aerosol particles or clouds phase. The measurement of the depolarization ratio does not require any additional optics in the emitting system as the laser beam used in a lidar system is usually linear polarized. Polarizing beamsplitters are used in the re-

1. To see the original webpage, please click [here](#).

ceiving system to split the backscattered light into parallel-polarized and cross-polarized channels. The two channels need to be calibrated to account for the optical and electronic gain between them. The calibration procedure will be introduced in the following section. The backscattered signal is detected by the photomultiplier tubes (PMTs) or photodiodes. The photon-counting technique enables the detection of an individual photon, hence, this technique is very sensitive to very weak signals. It is intrinsic for a detector to have limited sensitive range and the signal should be properly corrected especially when the incoming signal is strong. Due to this limitation of the photon-counting technique, the analog detection is preferable for strong backscattered signal. The analog detection measures the averaged current generated by the incident photons and converts it into digital signals. The data acquisition system usually records the time-averaged backscattered signal at corresponding range level. The number of averaged laser pulses varies from a few to a few hundreds, depending on the repetition rate of the laser.

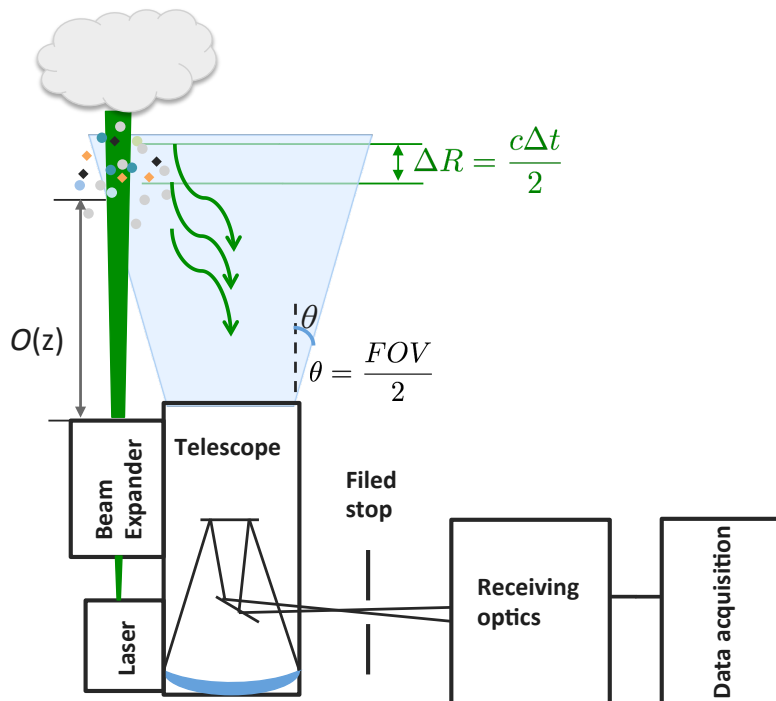


Figure 2.8. The principle setup of a bi-axial lidar system. The function  $O(z)$  is the overlap function of the lidar system.  $\theta$  is the half-angle of FOV.  $\Delta R$  is the range resolution of the lidar signal.  $\Delta R$  is determined by the light speed  $c$  and the frequency ( $= \frac{1}{\Delta t}$ ) of the data acquisition.

Figure 2.8 presents a typical lidar system. The general form of the lidar backscattered

signal can be expressed as:

$$\begin{aligned} R(r, \lambda) &= P(r, \lambda) r^2 \\ &= A O(r) \beta(r, \lambda) T(r, \lambda), \end{aligned} \quad (2.9)$$

where  $R(r)$  is the range-corrected lidar signal and  $P(r)$  is the recorded raw signal detected by the data acquisition system, without range correction. The factor  $A$  is determined by the characteristics of the lidar system. In reality, this factor is dependent on the laser source and the emitting optics. Also  $A$  should be wavelength-dependent, however, in a simplified form,  $A$  is assumed to be constant.  $\beta(r)$  is the backscatter coefficient of the scatters interact with the laser beam.  $T(r)$  is the round-way transmission as the photons propagate  $2r$  distance. The overlap function,  $O(r)$ , is related to the size, divergence and shape of the laser beam, the displacement between the laser beam and the center of the telescope, the FOV of the telescope, the optics before the detector as well as the homogeneity of sensitivities of the PMT surface.

In the atmosphere, the scatters that interact with the laser beam are usually gas molecules, aerosol particles and cloud particles. While aerosols and clouds make no difference in the expression of lidar equations when assuming no presence of multiple scattering. Considering elastic scattering, the lidar equation can be written as below:

$$\begin{aligned} R(r, \lambda) &= P(r, \lambda) r^2 \\ &= A O(r) [\beta_{mol}(r, \lambda) + \beta_{aer}(r, \lambda)] \exp\left\{-2 \int_0^r [\alpha_{mol}(r', \lambda) + \alpha_{aer}(r', \lambda)] dr'\right\}, \end{aligned} \quad (2.10)$$

where  $\alpha$  and  $\beta$  represent the extinction and backscatter coefficient, respectively. The subscripts '*mol*' and '*aer*' denote *molecule* and *aerosol*. When the polarization of the backscattered light is measured, the backscatter coefficient  $\beta_{mol/aer}(r)$  should be written as  $\beta_{mol/aer}^{\parallel}(r)$  or  $\beta_{mol/aer}^{\perp}(r)$ , depending on the polarization direction of the incoming backscattered light. In practice, the transmission term is regarded as polarization-independent although it might be possible that the transmission through certain anisotropic particles, e.g. uniformly oriented ice particles, is correlated with the polarization state [Weitkamp, 2006].

As to Raman scattering, usually the constant atmospheric constituents in the atmosphere,

i.e.  $N_2$  and  $O_2$ , are used as the reference molecules. Other molecules, such as water vapor  $H_2O$ , methane  $CH_4$  and  $CO_2$ ...etc, are also used as reference molecules of Raman scattering. The Raman lidar equation can be written as:

$$R(r, \lambda_R) = P(r, \lambda_R) r^2 = A O(r) \beta_R(r, \lambda_R) \exp\left\{-\int_0^r [\alpha_{mol}(r', \lambda) + \alpha_{aer}(r', \lambda) + \alpha_{mol}(r', \lambda_R) + \alpha_{aer}(r', \lambda_R)] dr'\right\}, \quad (2.11)$$

where  $\beta_R$  represents the backscatter coefficient of the Raman scattering and  $\lambda_R$  is the wavelength of the Raman radiation. The difference in the transmission term between Equation 2.10 and 2.11 is due to the fact that the laser emitted radiation keeps the wavelength before interacting with the Raman scatters and then the Raman radiation is emitted and returned to the receiving optics of the lidar system. Thus, the transmission term expands to four sub-terms.

### 2.3.2 LILAS system

The multi-wavelength Mie-Raman lidar – LILAS has three emitting wavelengths, 355, 532 and 1064 nm and three Raman wavelengths, including two nitrogen and dioxygen Raman channels at 387 and 530 nm, as well as one water vapor channel at 408 nm. The 530 nm is a rotational Raman channel [Veselovskii et al., 2015] and 387 and 408 nm are the vibrational-rotational channels. During the development of the instrument, the number of polarization channels varied from 1 to 3. At current stage, the system has 3 polarization channels at the three elastic wavelengths. Figure 2.9 displays LILAS system in LOA (left) and the laser beam of LILAS during the field campaign in 2015–2016 (right). LILAS uses a Nd:YAG laser produced by Spectra Physics. The pulse energy is 90/100/100 mJ at 355/532/1064 nm and the repetition ratio is 20 Hz. LILAS is biaxial system with a Newton telescope of 40 cm diameter. Figure 2.10 presents the scheme of the LILAS system. The laser source is installed on the back of the telescope. The laser beam emitted from the laser source is with a diameter of 3 mm and with divergence of 0.5 mrad. A beam expander is used to decrease the divergence of the laser beam with a factor of 5. The laser beam coming out of the beam expander is rotated by a beam rotator by



Figure 2.9. LILAS lidar system operated by LOA. (a) LILAS in Lille, (b) Laser beam of LILAS in M'bour during SHADOW2 campaign.

90° and redirected to the center of the telescope. As a result, one part in the north of the telescope is covered by the brace of the beam rotator. The backscattered light collected by the telescope is directed into the receiving optics and then split by the dichroic mirrors and polarizing beam splitters into different channels. PMT is used as the detector for all the channels except 1064 nm, which uses the avalanche photodiodes (APD). Water-cooling is used to suppress the thermal noise in 1064 nm channel. The polarization calibrator (PC) is applied in the polarization procedure and removed when making normal measurements. In 355, 387, 532 and 530 nm channel, both analog and photon-counting data are recorded by the data acquisition system. In 408 nm channel, only photon-counting is used and in 1064 nm only analog signal is recorded. The combination of analog and photon-counting signal enables the high-quality detection of the backscattered signal both in the near and far range, thus expanding the dynamic range of the lidar signal. A gluing method should be applied to attach the two analog signal and photon-counting signal.

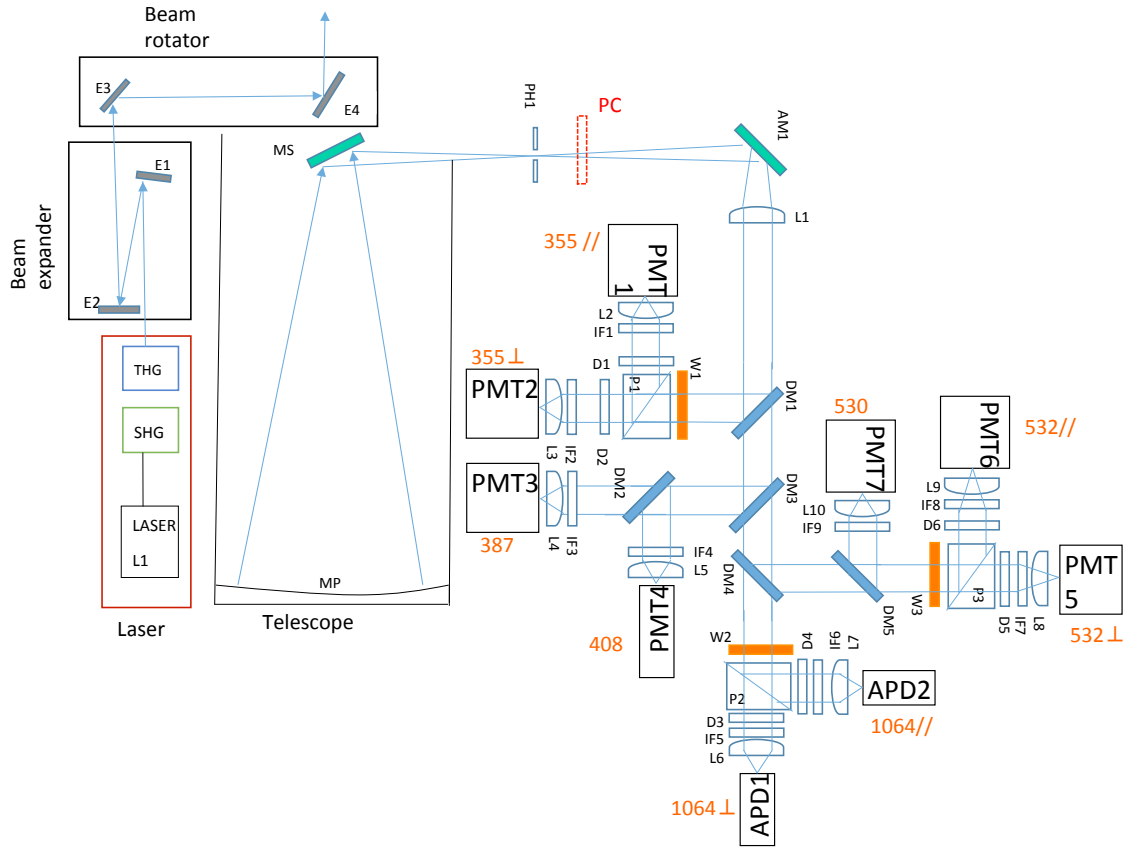


Figure 2.10. The schematic drawing of LILAS system.

E1–4	Dichroic mirrors in the beam expander and beam rotator
MP	Primary mirror
MS	Secondary mirror
AM	Aluminum Mirror
L1	Collimating lens, $f=69$ mm, $\Phi = 30$ mm
L2–10	Focusing lens, L2–4, $f=80$ mm; L5–9, $f=80$ mm; L10, $f=100$ mm
IF1–7	Interference filters
D1–6	Neutral density filters
W1–3	Half wave plates
P1–3	Polarizing beam splitters
PC	Polarization calibrator, only used in the calibration procedure
DM	Dichroic mirror

Table 2.2. Optical elements in the scheme of LILAS system

### 2.3.3 Lidar data quality assurance

As known, the lidar systems are diverse, differing from the wavelength, laser power, detecting objects as well as the optical and electronic setup. As a results, there is a need of lidar product standardization and the lidar data quality assurance. In EARLiNET, standard procedures are designed to evaluate the performance of the lidar systems This section presents the results of Rayleigh fit, telecover test and polarization calibration that are performed on LILAS system.

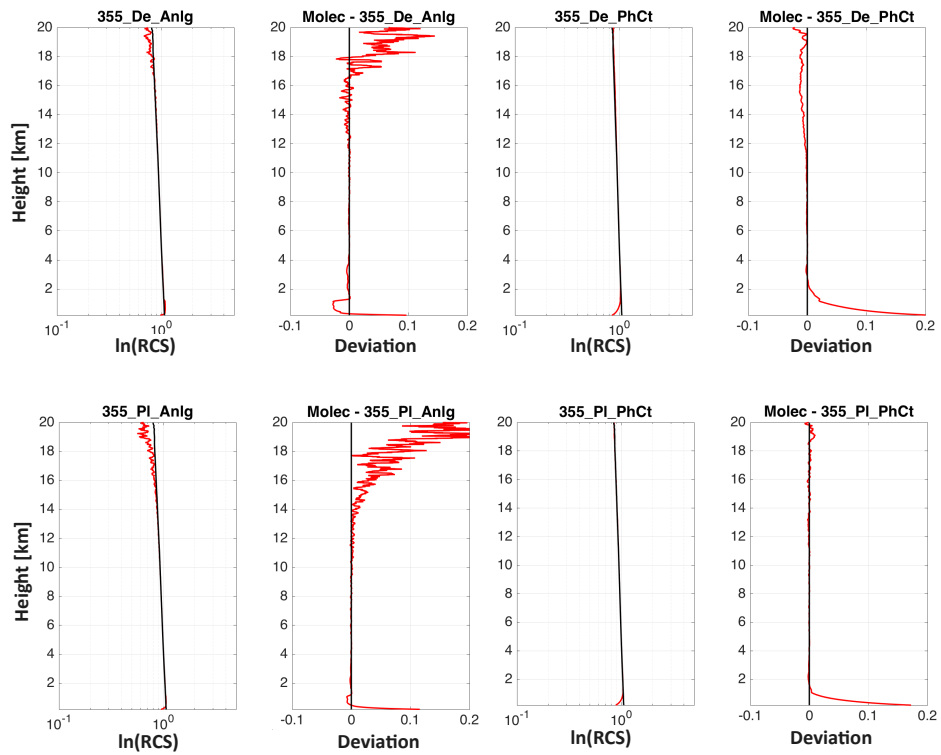
#### Rayleigh fit

The Rayleigh-fit check is comparing the lidar signal with the calculated molecular scattering signal in a clean atmosphere. The molecular extinction and backscatter coefficients can be obtained from the Rayleigh scattering model. The air density profile can be calculated from the temperature and pressure profile measured by radiosonde measurements or from standard atmospheric model. The Rayleigh fit is the only absolute calibration for the lidar signal [Freudenthaler et al., 2018].

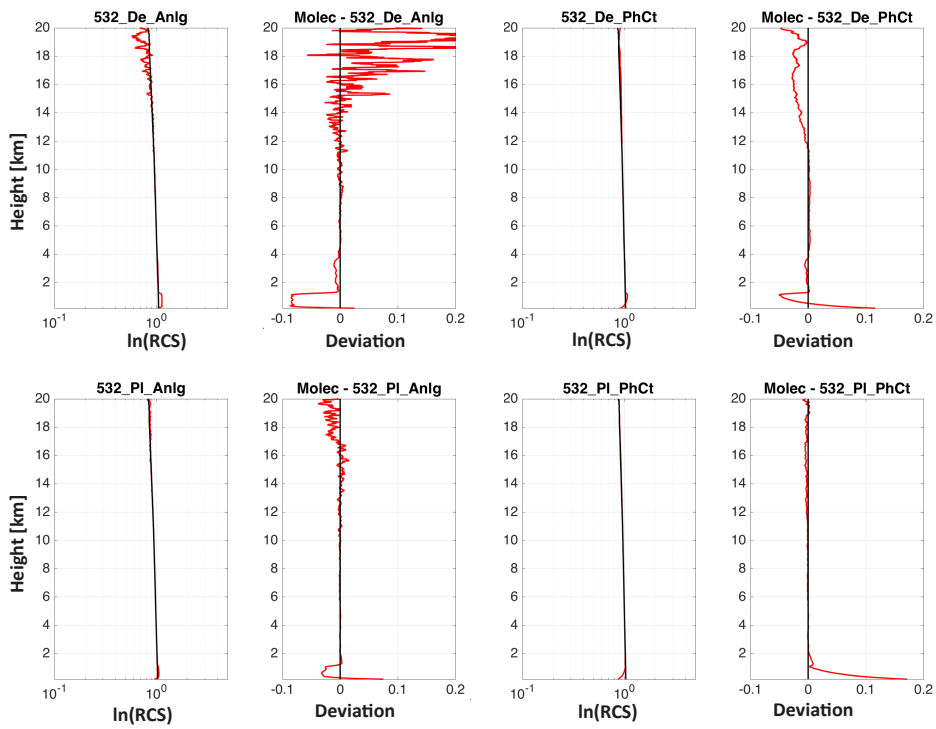
Figure 2.10 presents the Rayleigh fit of LILAS system. The lidar signal is accumulated at 00:00–00:30 UTC, 07 November 2017. Standard atmospheric temperature and pressure profiles are used for the calculation of the air density profile. The molecular extinction and backscatter coefficients are then calculated using the formulas presented in the study of Bucholtz [1995]. The normalized lidar signal and molecular profile, as well as the deviation are defined as follows:

$$\begin{aligned}
 \hat{R}_{lid}(r, \lambda) &= \frac{R_{lid}(r, \lambda)}{\bar{R}_{lid}} & \hat{R}_{mol}(r, \lambda) &= \frac{R_{mol}(r, \lambda)}{\bar{R}_{mol}} \\
 devi &= \frac{\hat{R}_{mol}(r, \lambda) - \hat{R}_{lid}(r, \lambda)}{\hat{R}_{mol}(r, \lambda)} \\
 \bar{R}_{lid}(\lambda) &= \sum_{r=r_1}^{r_n} \frac{R_{lid}(r, \lambda)}{n} \\
 \bar{R}_{mol}(\lambda) &= \sum_{r=r_1}^{r_n} \frac{R_{mol}(r, \lambda)}{n} & r_1, \dots, r_n & \text{are in the normalization range,}
 \end{aligned} \tag{2.12}$$

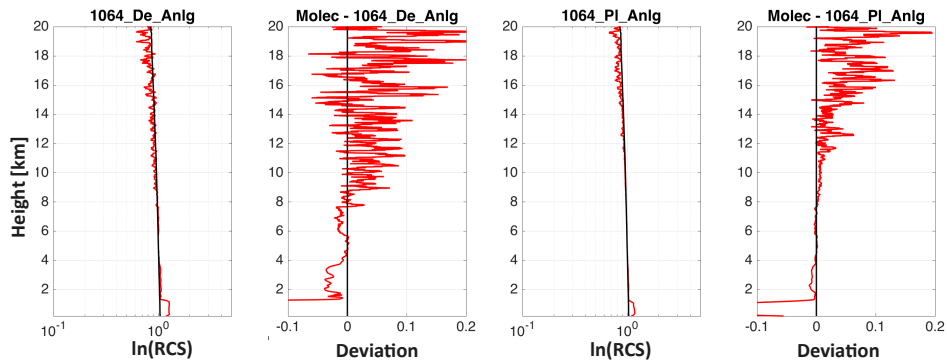
where  $\hat{R}_{lid}$  and  $\hat{R}_{mol}$  represent the normalized range corrected lidar signal and molecular signal, respectively.  $\bar{R}_{lid}$  and  $\bar{R}_{mol}$  are the mean signal of lidar and molecular scattering in the specified range  $[r_1, r_n]$ . The range is sometimes called calibration range and is always selected in a clean zone where no presence of aerosol is expected. The range-corrected lidar signal and molecular signal are normalized in the selected calibration zone where the deviation between the normalized lidar signal and molecular signal should be very small. A smoothing window of 20 points are used to vertically average the profiles, hence, the vertical resolution of the profile is 150 m (the original vertical resolution is 7.5 m). The lidar signal is normalized in the range of 5000–6000 m. For each channel, the comparison of normalized lidar signal and molecular profile is plotted with lognormal scale in the left panel; the deviation of the two profiles are plotted in the right panel. Most aerosols concentrate below 2000 m and there is still a fraction of aerosol between 2000 m and 4000 m. The negative values of the deviation in the boundary layer are due to the concentration of aerosols. These negatives values mostly appear to the analog channels because, the photon-counting channels are saturated in the boundary layer (except 532 cross-polarized channel) so that the corresponding deviations are positive. The positive deviations occurring to Raman analog channels in the boundary layer are due to the incomplete overlap range, which is approximately 1500 m for the two channels. All the analog channels show deviation less than 10% till at least 10000 m. The analog channel of 532 nm parallel-polarized and 530 nm go up to 20000 m with deviation less than 10%. The two cross-polarized channel at 1064 nm shows relatively worse performance, with approximately 10% deviation at 11000 m. All the photon-counting channels can go up to 20000 m with deviation smaller than 5% or even less.



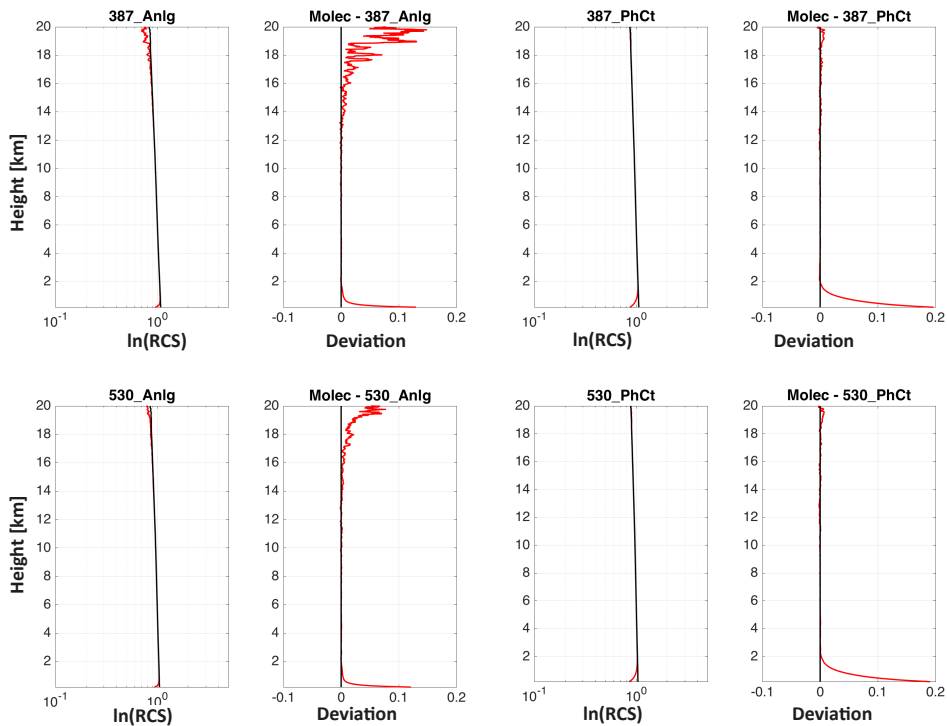
(a) Elastic channels: 355 nm



(b) Elastic channels: 532 nm



(c) Elastic channels: 1064 nm



(d) Raman channels: 387 nm and 530 nm

Figure 2.10. Rayleigh fit of LILAS system, 07 November 2017. The lognormal scale of the normalized lidar signal (red) and molecular signal (black) are plotted on the panel. The deviation is plotted on the right in red solid line. The black dash-dotted line represent zero.

### Telecover test

Due to the non-ideal optics or misalignments of the optical or mechanical elements, the signals collected by different parts of the telescope may differ, especially for the near range signal. Unlike the signal coming from the far range, the near range signal comes with relatively greater incident angle. The difference in the incident angle possibly leads to difference in the transmission of the dichroic mirrors, interference filters and beam splitters. Moreover, the light coming with different incident angles falls on different position on the surface detector whose spatial sensitivity is expected to be not ideally homogeneous. The laser tilt, telescope misalignments, displacement of the aperture stops, as well as the optical coating effects are all possible reasons causing the angle-dependent effects on the backscattered signal.

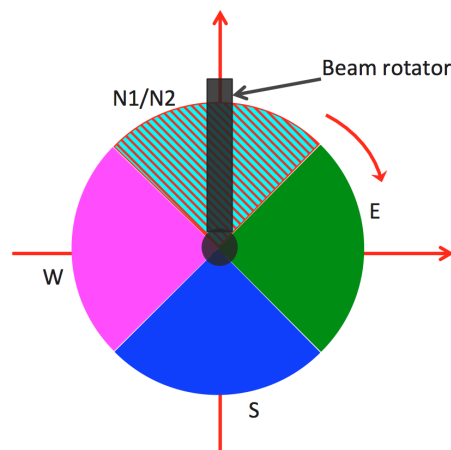
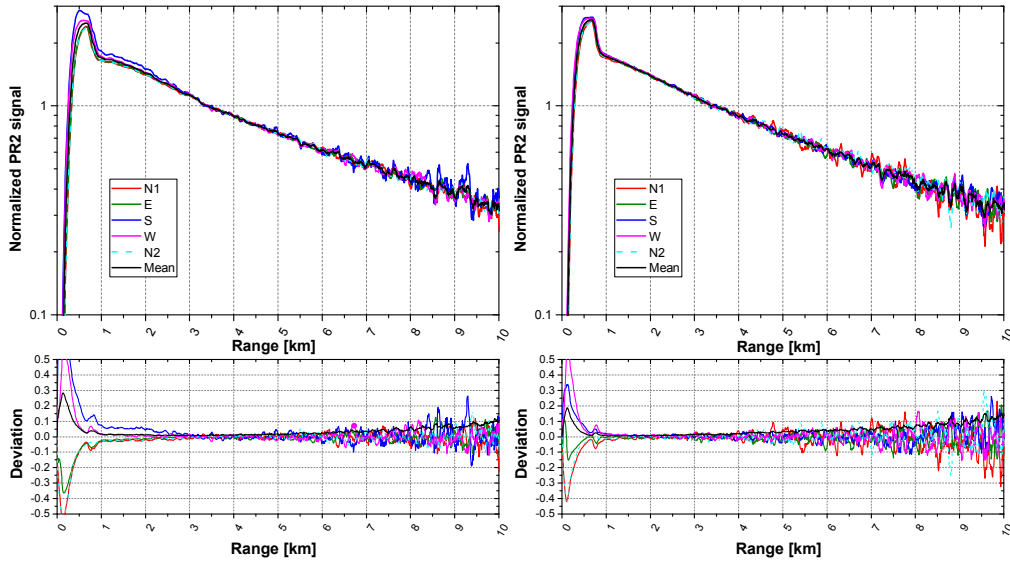


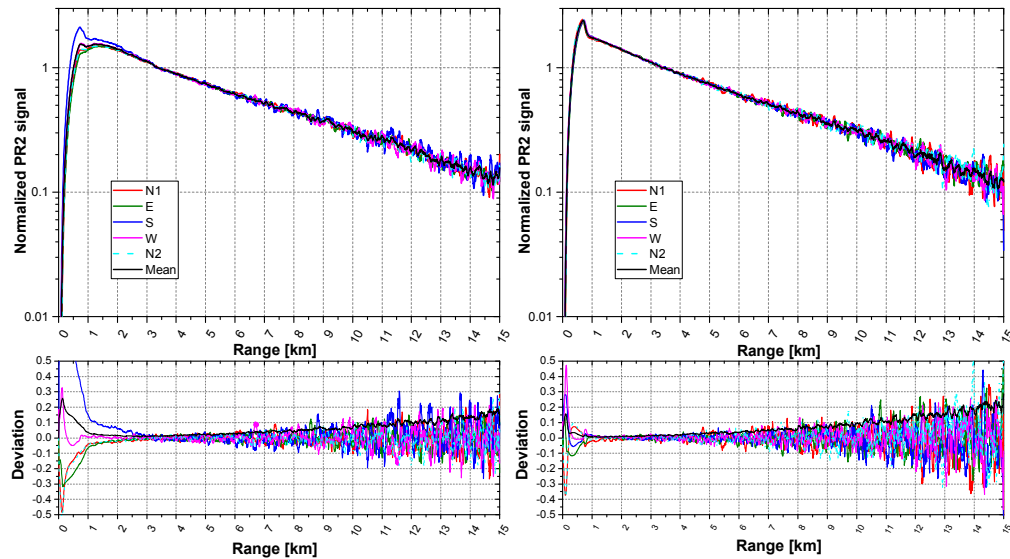
Figure 2.11. The division of the telescope for telecover test. The telescope is divided into four sectors, denoted as north (N), east (E), south (S) and west (W). A plate that covers three quarters of the telescope and passes light from the other one quarter is used.

In the telecover test, the telescope is divided into four symmetric sectors as displayed in Figure 2.11. It is worthy to be noted that one part of the northern sector is blocked by the brace of the beam rotator, indicated in Figure 2.11, so signal received by this sector should be less than the other two sectors. A plate blocking 3 quarters of telescope is specially designed to make the telecover test. The plate is rotated in order to pass light in different sector of the telescope. Fives acquisitions, following the order: north (N1), east (E), south (S), west (W) and north (N2), are made. The comparison of N1 and N2 is an

indication of the stability of the atmosphere. The results of telecover test are plotted in Figure 2.12–2.15. The range-corrected signals are normalized in 3000–4000 m range and plotted in the upper panels. The deviations of the normalized signals from the mean are plotted in the lower panels. All the profiles are vertical smoothed of 10 points, i.e. the range resolution is 75 m.



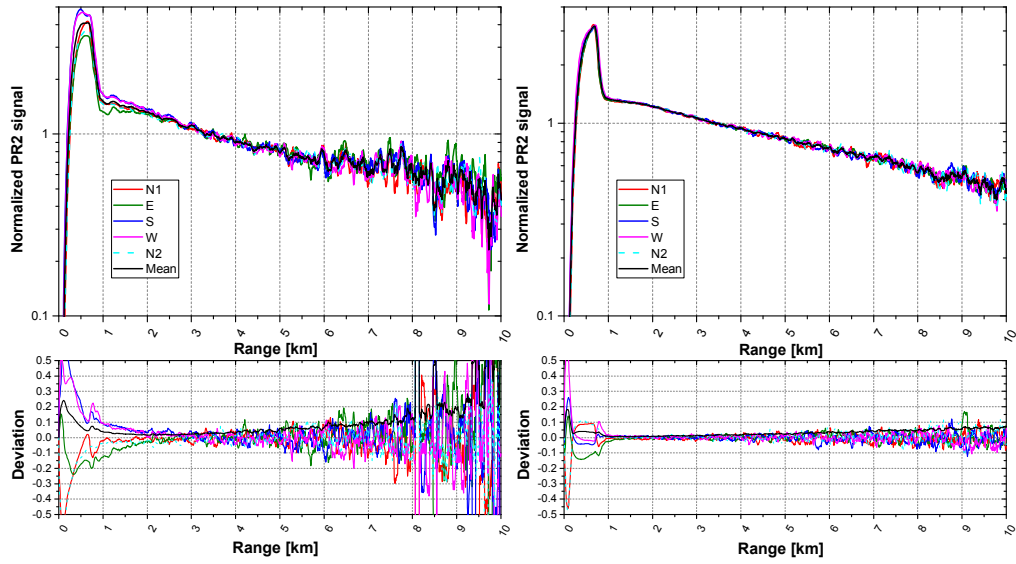
(a) 355 nm, analog channel, cross (left) and parallel polarized (right).



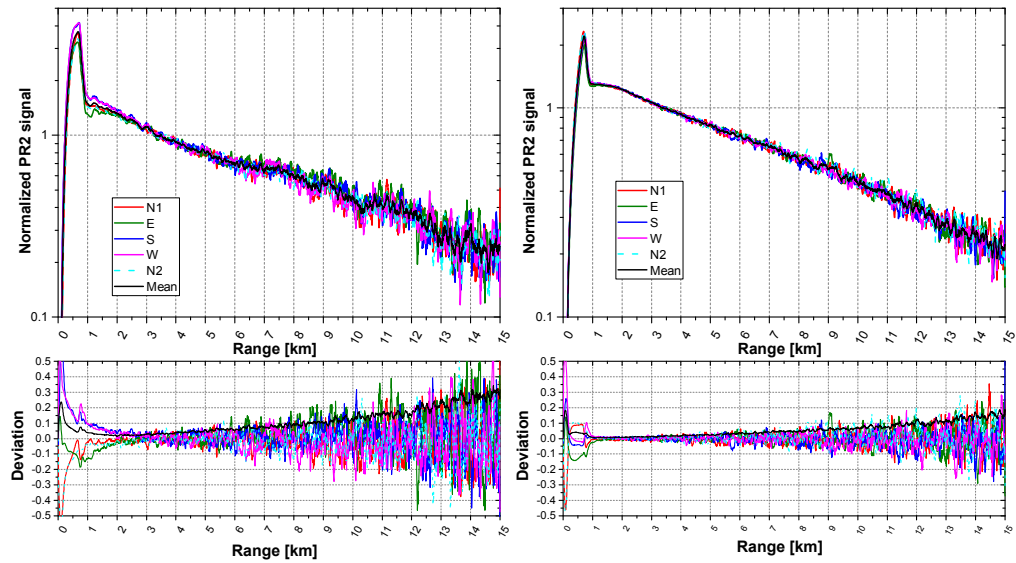
(b) 355 nm, photon-counting channel, cross (left) and parallel polarized (right).

Figure 2.12. Telecover test of 355 nm channel, 07 November 2017.

In the 355 nm cross-polarized channel, the south sector receives more signal than the



(a) 532 nm, analog channel, cross (left) and parallel polarized (right).



(b) 532 nm, photon-counting channel, cross (left) and parallel polarized (right).

Figure 2.13. Telecover test of 532 nm channel, 07 November 2017

other sectors. The deviation below 1000 m range is more than 10% and falls to under 10% between 1000 and 10000 m, approximately. In the 355 nm parallel-polarized channel, the deviation is less than 10% below 500 m and stays less than 10% in 500–8000 m range. For both the cross- and parallel-polarized, signals in the south and west sector are stronger than in the northern and east sector in the near range. In the 532 nm parallel-polarized channel, the deviation is less than 10% up to 10000 m. While in the 532 nm cross-polarized channel, the signals are noisy because the telescope is partially blocked and cross-polarized backscattered signal is much weaker than the parallel-polarized one. The deviation in 532 nm cross-polarized channel exceeds 10% when the range is further than 5000 m. The increase of deviation is due to the very weak signal in the far range. In the 1064 nm channel, a spike in the deviation is detected at about 800 m, it is possibly caused by the variation of the aerosols during the period of telecover test. The deviation is less than 10% between 1000 m and 5000–6000 m. The signal in 1064 nm cross-polarized channel is noisy above 6000 m. Two main causes should be responsible: the reduction of the telescope and the low cross-polarized signal in the far range.

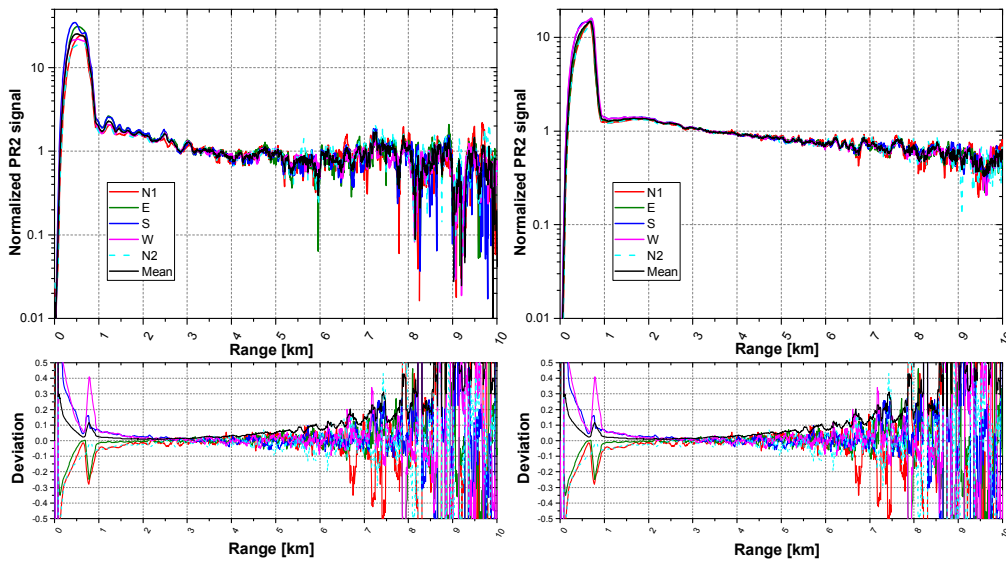
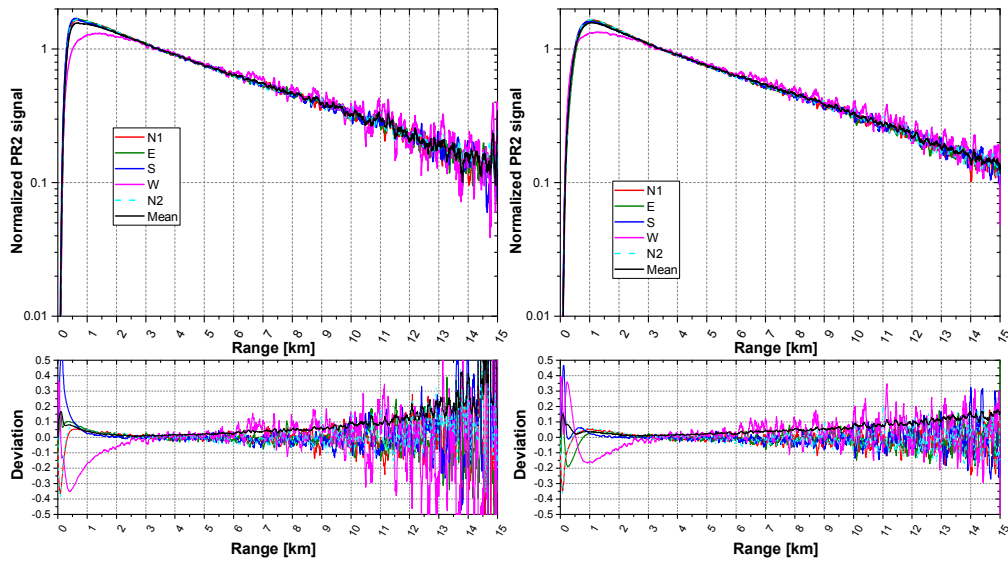


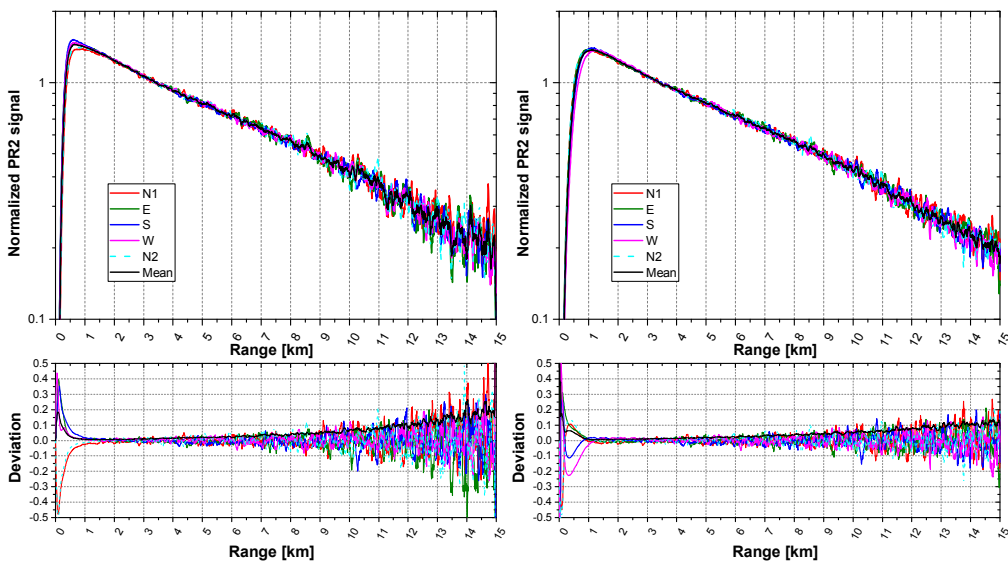
Figure 2.14. Telecover test of 1064 nm channel, cross (left) and parallel polarized (right), 07 November 2017

The 387 nm channel shows an anomaly in the west sector. Much less signal is received in this sector compared to the other three sectors. The deviation is about 10% at 1500 m in both analog and photon-counting channel. At 500 m, the deviation reaches 35% in

the analog channel and 15–20% in the photon-counting channel. The difference of the deviation in analog and photon-counting is possibly caused by the different sensitivity of the two detecting technique. This anomaly of 387 nm channel is improved in the after-ward optics adjustment by adjusting the reflecting mirror (DM3 in Figure 2.10) of 387 nm channel. The 530 nm channel shows excellent performance with the deviation less than 10% up to 9000–10000 m in the analog channel and 10000–12000 m in the photon-counting channel. In the near range, the 530 nm analog channel shows the deviation less than 10% in 400–1000 m range.



(a) 387 nm, analog channel (left) and photon-counting (right)



(b) 530 nm, analog channel (left) and photon-counting (right)

Figure 2.15. Telecover test of 387 nm and 530 nm channel, 07 November 2017

### Polarization calibration

The purpose of polarization lidar is to measure the parallel-polarized and cross-polarized backscattered light with respect to the polarization plane of the incident laser beam. To get the ratio between the two coupled channels, which is called as volume linear depolarization ratio (VLDR), a calibration coefficient is needed to account for the ratio of optical and electronic gain between the two channels.

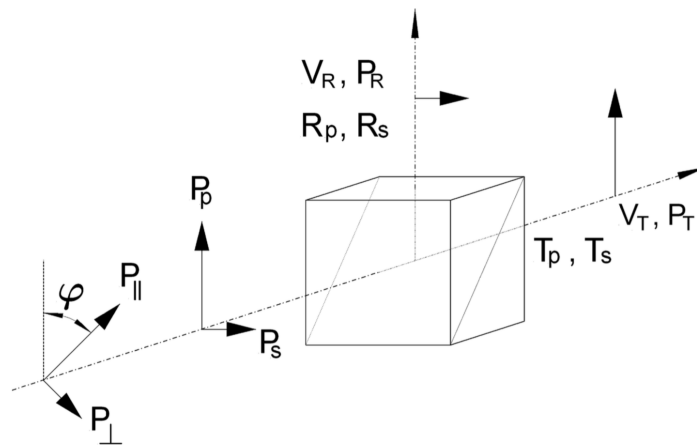


Figure 2.16. A scheme of polarization detection in lidar system. This figure is adapted from Freudenthaler et al. [2009]. .

Figure 2.16 draws the scheme of the lidar polarization channel.  $P_{\parallel}$  and  $P_{\perp}$  represent the signal scattering by aerosols or molecules in the parallel and crossed direction with respect to the polarization of the incident laser beam. The backscattered signal is directed to the polarizing beam splitter (PBS) and then separated into parallel and cross channels.  $P_p$  and  $P_s$  are the signal with respect to the incident plane of the PBS. The angle  $\varphi$  is the angle between the polarization plane of the emitted laser beam and the incident plane of the PBS. When adjusting the lidar polarization channel,  $\varphi$  needs to be adjusted to  $0^\circ$  or  $90^\circ$  to align the polarization plane of the emitting laser beam and the incident plane of the PBS and to separate the parallel and cross-polarized light. In LILAS system, a half wave plate is used to adjust this angle into  $0^\circ$  or  $90^\circ$ . The signal transmitted or reflected by the PBS is then directed to the detectors and recorded by the data acquisition system.  $P_R$  and  $P_T$  are the signals recorded by the data acquisition system in reflected and transmitted channels, respectively. Variables  $V_R$  and  $V_T$  represent the optical and electronic amplifi-

cation factor in the reflected and transmitted channels. The ratio of variables  $V_R$  to  $V_T$  is the calibration coefficient that needs to be determined.

The polarization calibration of LILAS system follows the  $\pm 45^\circ$  procedure proposed by Freudenthaler et al. [2009]. The calibration procedure requires two extra acquisitions before the normal measurements start. A sheet polarizer is inserted in the optical path after the pinhole, as shown in Figure 2.10, to rotate the polarization plane of the backscattered light by  $+45^\circ$  and  $-45^\circ$ . Then the calibration coefficient is calculated as below:

$$V^* = \frac{V_R}{V_T} = \frac{T_p + T_s}{R_p + R_s} \sqrt{\delta^*(+45^\circ) \times \delta^*(-45^\circ)} \quad (2.13)$$

where  $T_p$  and  $T_s$  represent the transmittance of the parallel and cross-polarized light of PBS;  $R_p$  and  $R_s$  represent of reflectance of the parallel and cross-polarized light. The relation of the values of transmittance and reflectance is:  $T_s + R_s = 1$ ,  $T_p + R_p = 1$ .  $\delta^*(\pm 45^\circ)$  represents the two acquisitions performed with the polarizer. Once the calibration coefficient is known, the volume linear depolarization ratio  $\delta_v$  can be determined:

$$\begin{aligned} \text{when } \varphi = 0^\circ \quad \delta_v &= \frac{P_\perp}{P_\parallel} = \frac{P_s}{P_p} \\ \text{when } \varphi = 90^\circ \quad \delta_v &= \frac{P_\perp}{P_\parallel} = \frac{P_p}{P_s} \end{aligned} \quad (2.14)$$

More detailed information and formula derivation about the polarization calibration can be found in Freudenthaler et al. [2009]. As long as the  $\delta_v$  is determined, the particle linear depolarization ratio (PLDR)  $\delta_p$  can be calculated as below:

$$\begin{aligned} \delta_p &= \frac{(1 + \delta_m)\delta_v R - (1 + \delta_v)\delta_m}{(1 + \delta_m)R - (1 + \delta_v)} \\ R &= \frac{\beta_m + \beta_a}{\beta_m} \end{aligned} \quad (2.15)$$

where  $\delta_m$  is the molecular depolarization ratio,  $R$  is the backscattering ratio.

A standard for estimating the performance of a polarization channel is the molecular depolarization ratio. The molecular depolarization ratio is a stationary property of molecular scattering and its theoretical value is calculated. Here the concept of scattering is limited to the Cabannes line. As  $N_2$  and  $O_2$  are the two main atmospheric constituents, compos-

ing 99% of the atmospheric gases. The calculation is based on the behavior of diatom molecules in the external radiation field. Details about the calculation can be found in Miles et al. [2001] and Freudenthaler et al. [2018]. The theoretical value of molecular depolarization ratio is about 0.4%, with negligible spectral dependency. However, due to the imperfection of the optics and misalignment of the polarization plane, the measured volume depolarization ratio in the aerosol-free zone is usually higher than the theoretical value. Another possible error source is the leakage of rotational Raman scattering which is strongly depolarizing. The displacement of the real measured molecular depolarization ratio to the theoretical values is an important parameter for estimating the performance of a polarization lidar.

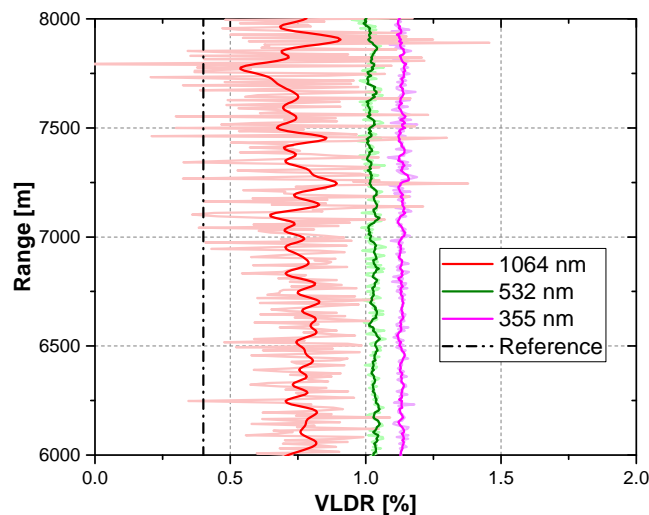


Figure 2.17. Molecular depolarization ratio measured by LILAS system. The dash-dotted line represent the theoretical value of the molecular depolarization ratio.

Figure 2.17 shows the measured volume depolarization ratio in a clean atmosphere on 07 November 2017. The light-colored lines are without smoothing and the deep-colored lines represent 10-point vertically averaged results. The molecular depolarization ratios measured by LILAS are about 0.75%, 1.0% and 1.2% at 1064, 532 and 355 nm, respectively. All these values are higher than the theoretical value. In the historical records, the minimum depolarization ratio LILAS has obtained is about 0.6% at 1064 nm, 0.8% at 532 nm and 1.2% at 355 nm. Apart from the optics and alignment, errors in the calibration coefficient are also an error source of the measured molecular depolarization ratio.

### 2.3.4 Lidar data processing

#### Data preparation

There are five steps, as listed below, to prepare the raw lidar data before the calculation of aerosol optical properties.

1. Trigger delay correction
2. Dead-time correction (only for photon-counting channel)
3. Electronic noise subtraction
4. Signal glueing
5. The combination of parallel and crossed signal

A trigger delay is the time between the actual laser emission to the assumed ‘zero’ range bin. This value can be measured in the laboratory. The dead-time is an intrinsic characteristic of photon-counting detection mode and the value of the dead-time provided by the manufacturer is 3.85 ns. The detector is regarded as a non-paralyzable system and the dead-time correction follows:

$$S = \frac{N}{1 - N\tau_d}, \quad (2.16)$$

where  $N$  and  $S$  are the measured and corrected count rate.  $\tau_d$  is the dead-time.

The electronic noise is measured by recording the signal with the telescope completely covered. This kind of acquisition is regularly performed. The analog in the near range is glued with the photon-counting signal in far range to obtain the glued signal that has large dynamic range. Linear regression is applied in the range of [2, 12] MHz in the photon-counting channel to find a glueing factor that re-scale the analog signal to ‘photon-counting’ signal. The combination of parallel and crossed signal gives the total backscattered signal:

$$P_{tot}(\lambda, h) = P_{\parallel}(\lambda, h) + C^*P_{\perp}(\lambda, h) \quad (2.17)$$

where  $C^*$  is the calibration coefficient,  $P_{tot}$ ,  $P_{\parallel}$  and  $P_{\perp}$  are the total signal, parallel and crossed polarized signal, respectively.

### Klett inversion

Raman inversion [Ansmann et al., 1992] and Klett inversion [Klett, 1985] are two widely used methods for the retrieval of extinction and backscatter coefficients. Klett inversion uses the elastic signal and retrieves extinction and backscatter coefficients. There are two unknowns to be resolved in the elastic lidar equation, thus a priori assumption of the aerosol lidar ratio  $S_{aer}$  is needed. The calculation is expressed in Equation 2.18.

$$\beta_{aer}(r, \lambda) = \frac{\exp\{R'(r, \lambda) - R'(r_m, \lambda)\}}{\beta^{-1}(r) + 2 \int_r^{r_m} \frac{\exp\{R'(r', \lambda) - R'(r_m, \lambda)\}}{S_{aer}(r')} dr'} \quad (2.18)$$

$$\alpha_{aer}(r, \lambda) = \beta_{aer}(r, \lambda) S_{aer}(r, \lambda)$$

and

$$\begin{aligned} R'(r, \lambda) - R'(r_m, \lambda) = & \ln[R(r, \lambda)] - \ln[R(r_m, \lambda)] \\ & + \frac{2}{S_{mol}} \int_r^{r_m} \beta_{mol}(r') dr' - 2 \int_r^{r_m} \frac{\beta_{aer}(r', \lambda)}{S_{aer}(r', \lambda)} dr' \end{aligned} \quad (2.19)$$

Aerosol lidar ratio is a parameter related to the aerosol type and could vary at different vertical levels. An accurate assumption of lidar ratio requires not only the information about aerosol type but also aerosol vertical distributions. Both conditions are very difficult to meet because aerosol types are diverse and vertical aerosol distribution is a dynamic process. The retrieved extinction and backscatter coefficients are strongly dependent on the assumption of lidar ratio, especially the extinction coefficient. Thus an improper lidar ratio can introduce significant errors into the Klett inversion.

### Raman lidar inversion

Raman inversion uses both the elastic signal and Raman signal to retrieve the extinction and backscatter coefficients, the extinction coefficient is calculated as follows:

$$\alpha_{aer}(r, \lambda) = \frac{\frac{d}{dr} \ln[N_R(r)/R(r, \lambda_R)] - \alpha_{mol}(r, \lambda) - \alpha_{mol}(r, \lambda_R)}{1 + (\lambda/\lambda_R)^k}, \quad (2.20)$$

where  $N_R$  is the air density of the reference gas(es), which can be computed using the pressure and temperature profile defined by a standard atmospheric model or from radiosonde measurements.  $k$  is the extinction Angström exponent, between the elastic wavelength  $\lambda$  and Raman wavelength  $\lambda_R$ . Since the Raman line, especially the rotational Raman line is close to the elastic wavelength, thus  $k$  is usually assumed to be 0. The backscatter coefficient of aerosols is expressed as:

$$\begin{aligned} \beta_{aer}(r, \lambda) + \beta_{mol}(r, \lambda) &= [\beta_{aer}(r_m, \lambda) + \beta_{mol}(r_m, \lambda)] \\ &\times \frac{P(r_m, \lambda_R)P(r, \lambda)N_R(r)}{P(r_m, \lambda)P(r, \lambda_R)N_R(r_m)} \\ &\times \frac{\exp\left\{-\int_{r_m}^r [\alpha_{aer}(r', \lambda_R) + \alpha_{mol}(r', \lambda_R)]dr'\right\}}{\exp\left\{-\int_{r_m}^r [\alpha_{aer}(r', \lambda) + \alpha_{mol}(r', \lambda)]dr'\right\}} \end{aligned} \quad (2.21)$$

The calculation of backscatter coefficient requires a reference zone,  $r_m$ , where no aerosols are present so the scattering in this zone is completely due to molecules, i.e.  $\beta_{aer}(r_m, \lambda)$  is approximately 0. The molecular extinction and backscatter coefficients can be calculated using Rayleigh scattering model [Bucholtz, 1995]. The Raman technique enables reliable calculation of the extinction profile and this technique has been widely applied to atmospheric lidar systems for aerosol and trace gases detections. After the calculation of backscatter coefficient and volume linear depolarization ratio, the particle linear depolarization ratio can be computed using Equation 2.15.

### Water vapor mixing ratio

Water vapor is an important gas in the atmosphere and strongly impact the convection process. The water vapor mixing ratio is defined as the ratio of the mass of water vapor to the dry air in a unit volume. The calculation of water vapor mixing ratio requires the signals of one Raman channel of permanent gas and the water vapor channel. The water

vapor mixing ratio can be calculated as follows [Ansmann et al., 1992]:

$$\begin{aligned}
 WVMR(r) = & K_w \frac{P(r, \lambda_{H_2O})}{P(r, \lambda_R)} \\
 & \times \frac{\exp\left\{-\int_0^r [\alpha_{aer}(r', \lambda_R) + \alpha_{mol}(r', \lambda_R)] dr'\right\}}{\exp\left\{-\int_0^r [\alpha_{aer}(r', \lambda_{H_2O}) + \alpha_{mol}(r', \lambda_{H_2O})] dr'\right\}} \quad (2.22)
 \end{aligned}$$

where  $K_w$  is the calibration coefficient of water vapor mixing ratio. The molecular extinction coefficient at  $\lambda_R$  and  $\lambda_{H_2O}$  can be calculated according to the Rayleigh scattering model. Additionally, the aerosol extinction coefficient at  $\lambda_R$  or  $\lambda_{H_2O}$ , as well as the Angström exponent are needed to calculate the exponential term. The aerosol extinction coefficient at  $\lambda_R$  can be calculated using the Raman signal. For the widely used lidar systems, as well as LILAS, the elastic wavelength is at 355 nm, the nitrogen and water vapor Raman wavelengths are at 387 nm and 408 nm. The wavelength shift between the water vapor channel and the elastic channel is approximately  $3650 \text{ cm}^{-1}$ , which is not very significant. The extinction Angström exponent can be chosen in the range of  $[0, 1]$ . Information about spectral extinction coefficient derived from Raman signals can be used to choose a better extinction Angström exponent, between  $\lambda_R$  or  $\lambda_{H_2O}$ . Generally, there are two ways to calibrate the water vapor channel, using water vapor mixing profile derived from collocated radiosonde measurements or model data; the other one is to use the columnar water vapor content measured by other instruments, spectrometer or photometer. The calibration of the water vapor channel is studied in Bovchaliuk [2016]. It is needed to be mentioned that the Raman scattering has certain temperature dependence. The correction of temperature dependence is studied in Whiteman [2003]. In our study, the temperature dependence is not considered.

## 2.4 Chapter summary

This chapter presents mainly the two main instruments: sun/sky photometer and lidar LILAS. Information about the sun/sky photometer is based in the CE-318N model. The main measurement types of this model are the direct sun measurements, almucantar and principal plane measurements. Standard inversion products are available in the AERONET

site. The quality check, calibration and signal processing are presented based in LILAS system following the procedure proposed in EARLiNET. The data-quality check demonstrates that LILAS system is well maintained regarding the Rayleigh fit, telecover test and polarization capability. The Rayleigh fit indicates that LILAS signal can reach about 20000 m with the deviation to molecular scattering under 10%. The telecover test shows that, above 1000 m, LILAS system is of good symmetry except for the 387 nm channel. It is due to the misalignment of the mirror for 387 nm. After adjusting, this anomaly has been diminished to some extent. The polarization calibration procedure is explained in detail and the molecular depolarization ratio of LILAS system is satisfactory. At last, we present the lidar signal correction, the calculation of aerosol parameters and water vapor mixing ratio.

# Chapter 3

## Aerosol observation and analysis

*“ Problems are not stop signs, they are guidelines. ”*

– Robert H. Schuller

This chapter presents lidar observations of cirrus clouds and aerosols, including Saharan dust, long-range transported dust and smoke, as well as dust and smoke mixtures. The cloud measurements provide characterizations for ice, mixed-phase clouds and super-cooled liquid water (SCLW) clouds. The obtained PLDRs at 2–3 wavelengths make these measurements particularly valuable because these parameters are rarely measured by lidar systems and are important parameters for improving the knowledge about clouds formation and optical properties. Also, the cloud observations are tests and verifications for the performance of the lidar system. Dust is the one of the main aerosol types presented in this chapter. Saharan dust observed near the source in M’Bour (14.95°N, 16.95°W) and long-range transported dust observed in Lille (50.61°N, 3.15°E), are studied in this chapter. The observations in M’Bour are taken from SHADOW2 campaign which took place in March, April, December 2015 and January 2016. Two events of dust-smoke mixture are presented in this chapter. In the first case, dust from Saharan desert mixing with smoke from west or middle Africa was observed in M’Bour on 19–20 January 2016. In the second case, long-range transported dust from Saharan mixing with smoke originated from Portugal was observed in Lille on 16–18 October 2017. Additionally, an unprecedented Canadian fire activity took place in the summer of 2017. Fire emissions were injected into the upper troposphere and lower stratosphere by the pyro-cumulonimbus clouds. LILAS detected aerosol layers both in the stratosphere and the troposphere in distributed days in

August and September 2017. The highlight of this event is the high depolarization ratios of smoke particles in the stratosphere in comparison with the low depolarization ratios of smoke in the troposphere. The causes of this curious optical properties of smoke particles have not been well resolved.

### 3.1 Cirrus observation

Cirrus clouds normally present in the upper troposphere and sometimes extend to the lower stratosphere. Cirrus plays an important role in the radiation budget in the earth-atmosphere system and the climate changes [Hansen et al., 1997]. However, the radiative effect of cirrus clouds is highly uncertain due to the poor representation of the cloud particle shape, cloud process, as well as the inadequate parameterization of the radiation-cloud interaction. Unlike the low-level clouds which mostly have a cooling effect on the surface, cirrus clouds can cool the surface by scattering the solar radiation and warm the surface by reflecting back the terrestrial radiation. The role of cirrus clouds depends on the thickness, altitude and physics of the cloud particles. Considerable observational and modeling efforts are required to improve the knowledge about cloud physics and many efforts have been done in the lidar community [Nazaryan et al., 2008, Sassen et al., 1985, Sassen, 1995, Veselovskii et al., 2017].

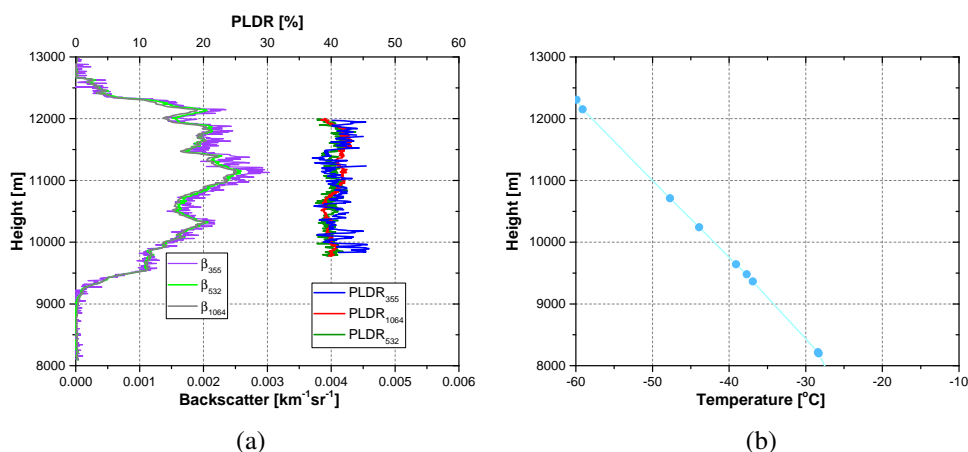


Figure 3.1. Cirrus observations at 22:00–24:00 UTC, 24 August 2017, Lille. (a) Backscatter coefficients and PLDRs at 355, 532 and 1064 nm. (b) Temperature profile from radiosonde measurements at 21:00 UTC, 24 August 2017 in Beauvechain, Belgium. The Lidar is with  $4^{\circ}$  inclination with respect to the zenith.

Figure 3.1 shows the backscatter coefficients and PLDRs at 355, 532 and 1064 nm retrieved from lidar observations. The observations are recorded at 22:00–24:00 UTC, 24 August 2017 in Lille. The cirrus layers spread from 9000 to 13000 m above the ground level. The backscatter coefficients and PLDRs at three wavelengths do not exhibit noticeable spectral dependence. The optical depth at 355 and 532 nm is about 0.17, calculated from the attenuation of molecular scattering from the cloud base to the cloud top. The backscatter coefficients at 355 and 532 nm are calculated by Raman inversion and at 1064 nm Klett inversion is used with lidar ratio assumed to be 20 sr. The mean lidar ratios at 355 and 532 nm are about  $20 \pm 4$  sr [Veselovskii et al., 2017]. The PLDRs are  $41 \pm 2\%$  without significant vertical variations. The observed lidar ratios and particle linear depolarization ratios are typical for cirrus clouds [Reichardt et al., 2002, Whiteman et al., 2004, Veselovskii et al., 2017]. Radiosonde measurements in Beauvechain ( $50.78^\circ\text{N}$ ,  $4.77^\circ\text{E}$ ), Belgium, which is about 120 km in the north-east of Lille provide the temperature profile at 21:00 UTC, 24 August 2017. The temperature within the cloud layer distributes between  $-35^\circ\text{C}$  and  $-60^\circ\text{C}$ . At such temperatures, cloud particles mostly are in ice phase.

West Africa is a favorable region for the study of mixed-phase cloud due to the fact that warm and moist air mass originated from the equatorial region can stimulate the formation of SCLW clouds [Ansmann et al., 2009]. SCLW clouds were detected over M'bour observation site on 16 December 2015 during SHADOW2 campaign. Figure 3.2 shows the lidar range-corrected signal and PLDR at 532 nm. The lidar quicklook depicts two cloud layers in the 7000–11000 m height range. The rising cloud layer during 21:00 and 22:00 UTC is characterized by PLDR of about 40%, which indicates the presence of ice particles. In contrast, PLDR less than 10% is observed within the horizontal cloud layer at 22:00–23:00 UTC, indicating the presence of liquid cloud droplets. Measurements in the period of 21:00–21:24 are averaged and plotted in Figure 3.3. The ice cloud observations reveal negligible spectral dependence of the backscatter coefficients and extinction coefficients. The lidar ratios at 355 at 532 nm are  $20 \pm 3$  sr and the PLDRs are about 40%, which is consistent with the observations in Lille on 24 August 2017. The PLDRs do not show significant spectral dependence or vertical distribution below 10500 m. The LRs do not show spectral dependence at 355 and 532 nm, while some vertical variations are

observed. The vertical variation of LRs maybe not a sign of the variation of ice particle properties but the effect of the smoothing applied on the extinction coefficient. The difference of smoothing between extinction and backscatter coefficient is able to cause ‘fake’ vertical variations to the LRs, especially for the profiles of complicated vertical structures.

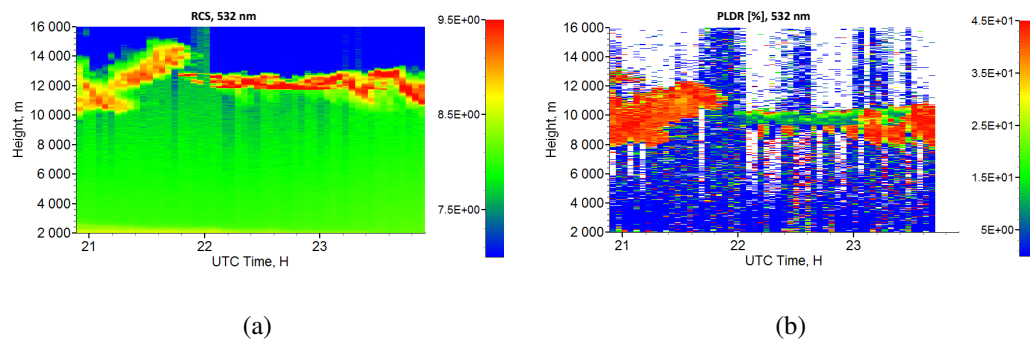


Figure 3.2. Lidar observations on 16 December 2015, M'bour

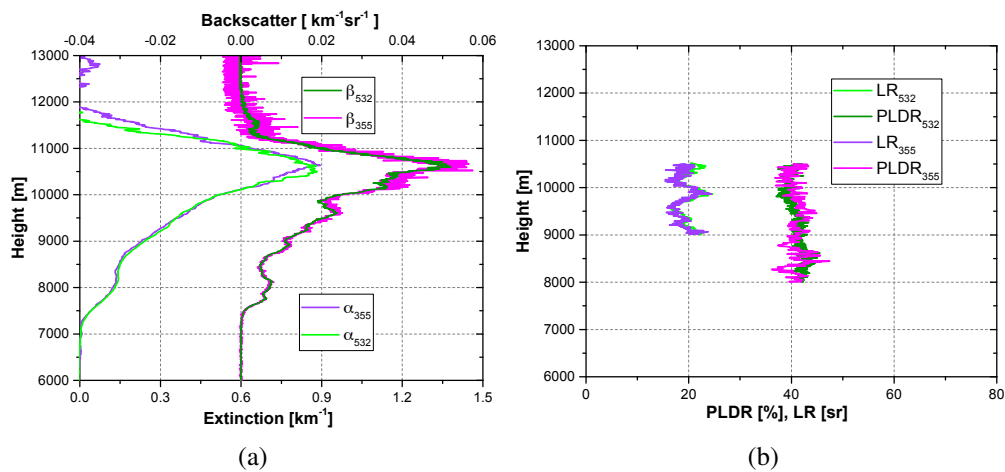


Figure 3.3. Ice clouds on 16 December 2015, M'bour. (a) Extinction and backscatter coefficients, (b) PLDR and LR at 355 and 532 nm. The Lidar is with  $47^\circ$  inclination with respect to the zenith..

Figure 3.4 presents a cloud layer characterized by strong backscattering but low PLDR. The 10% PLDR is much lower compared to ice clouds but still not negligible. For liquid clouds, 1–5% are more expectable values for the PLDRs as the droplet are mostly spherical. The increase of PLDR is possibly caused by multiple scattering or mixing with ice particles. It should be more rigorous to call it mixed-phase cloud. It is certain that SCLW

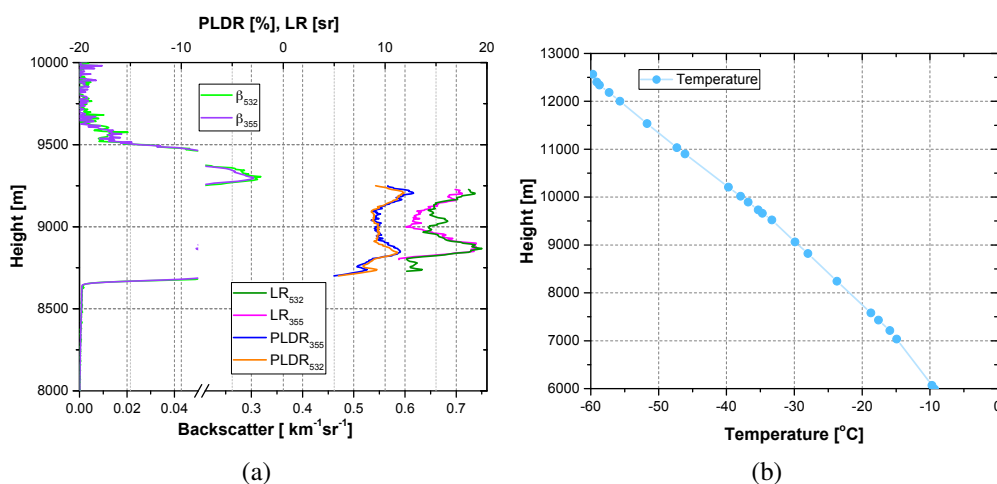


Figure 3.4. Mixed-phase cloud observations on 16 December 2015, M'bour. (a) Backscatter coefficient, PLDR and LR, (b) temperature profile on 00:00 UTC 17 December 2015, Dakar, Senegal. The lidar observations are averaged at 22:00–23:00 UTC, 16 December 2015.

survives under this cold condition and is an important composition of the observed clouds. The backscattering coefficient is 15 times higher than the ice cloud in Figure 3.3. The LR<sub>s</sub> at 355 and 532 nm are  $15 \pm 3$  sr, lower than ice particles. The PLDR<sub>s</sub> at 355 and 532 nm rise from approximately 5% at 8750 m to 12% at 9250 m. The vertical increase of PLDR can be caused by multiple scattering or the increase of the fraction of ice particles, or both. The SCLW cloud layer lasts for over 1 hour, from 22:00 to 23:30 UTC. The temperature profile is obtained from radiosonde measurements at 00:00 UTC from Dakar station. Within the SCLW cloud layer temperatures vary from  $-25^{\circ}\text{C}$  to  $-38^{\circ}\text{C}$ , which is generally higher than the limit temperature below which homogeneous ice nucleation starts. Below the SCLW cloud layer, the virga of clouds shows high depolarization ratios, indicating the formation and sedimentation of ice particles. In West Africa the Saharan desert is a permanent dust source and biomass burning aerosols are also frequently observed in the dry season between November and March. Aerosols can act as the ice condensation nuclei at temperatures higher than  $-38^{\circ}\text{C}$  before the homogeneous nucleation begins [Koop et al., 2000, Cziczo et al., 2013], which is consistent with our observations.

Many previous observations, although diverse in measuring geometry and geographical locations, are quite consistent with our results. Sassen and Benson [2001] found the depolarization ratio (at 694 nm) of cirrus cloud rises from 25% to 45% when the temperature

decreases from about  $-17.5^{\circ}\text{C}$  to  $-77^{\circ}\text{C}$  for cirrus in midlatitude. Reichardt et al. [2002] observed cirrus depolarization ratio ranging from 15% to 60% at  $67.9^{\circ}\text{N}$ , near the polar region. For depolarization ratio of about 40%, the corresponding LR (at 355 nm) is 20 sr, showing good agreements with our observations. However, the radiosonde and the lidar is not collocated, we are not sure if the temperature profile can well represent the real temperatures within the clouds. This is a big limitation that prevents us from obtaining more unambiguous conclusions.

## 3.2 Saharan dust observation in M'Bour, Senegal

### 3.2.1 Seasonal features of Saharan dust

Maritime aerosol, dust and smoke are three aerosol types that are commonly observed in M'Bour due to its specific location (Figure 3.5). In M'Bour, dust is a permanent aerosol component in the atmosphere. It could mix with maritime aerosols, smoke or other aerosol types. Both optical and microphysical properties will be modified if dust mixes with other aerosols. In this study, we do not distinguish dust by the exact chemical composition because remote sensing instruments, like lidar and sun/sky photometer do not measure the chemical compositions of aerosols. We define 'dust' by the extinction Angström exponent (EAE) lower than 0.1 and PLDR at 532 nm greater than 30%. These values are typical characteristics for dust according to field campaign measurements [Esselborn et al., 2009, Tesche et al., 2009, Ansmann et al., 2011, Veselovskii et al., 2016].

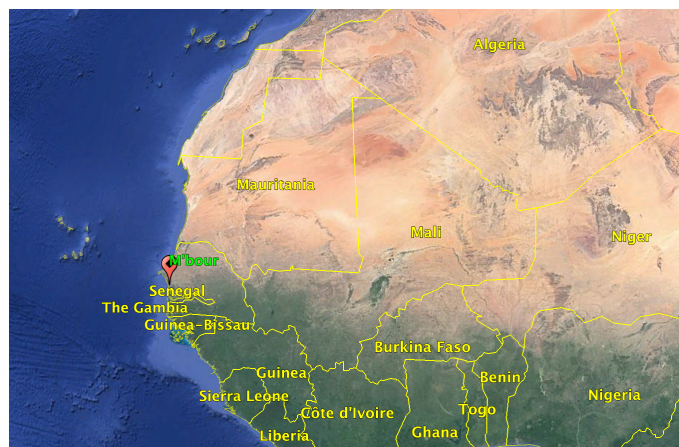


Figure 3.5. The location of M'Bour, Senegal

M'Bour is influenced by the Sahelian climate cycle that is composed of dry and wet season. The Sahelian climate cycle is controlled by the seasonal displacement of the Intertropical Convergence Zone (called ITCZ hereafter), which corresponds to the ascending part of the Hadley cell and where the water vapor concentration is maximum [Glickman, 2000]. The Hadley cell is an atmospheric circulation pattern between the tropics which produce easterly trades. The circulation is driven by solar energy and moved seasonally as the subsolar point moves. The advance and retreat of the ITCZ are related

to the changes of the pressure, surface wind convergence, cloudiness, sea surface temperature and precipitation [Grodsky et al., 2003, Sultan and Janicot, 2000, Janicot et al., 2008]. Different from the ITCZ, the Inter-tropical Front (ITF) is the wind discontinuity that separates the warm and moist southwesterly monsoon flow and the hot, dry and high dust-laden Harmattan flow coming from the Saharan region [Slingo et al., 2008, Issa Lélé and Lamb, 2010]. The ITF lies about 300 km in the north of the ITCZ and plays an important role in the establishment of the West African monsoon. Although, arguments exist for the precise concept of the ITCZ, our results and conclusions do not depend on the detailed definition of ITCZ and ITF.

The seasonal movement of ITCZ and ITF is coupled with the change of wind directions and convergence, thus impacting the motion of air mass. Figure 3.6 is taken from the study of Hastenrath and Lamb [1977]. Figure 3.6(a) shows the surface flow over the eastern equatorial Atlantic in July/August in 1911–1970. The south-eastern trades from the south Atlantic recurve to south-western direction after crossing the equator. When they meet the north-eastern Harmattan, a wind discontinuity is formed, which is the ITF, as denoted with the heavy dashed line in Figure 3.6(a). A band of convergent zone extends zonally from the ITF. Figure 3.6(b) shows the meridional-vertical transect for equatorial eastern Atlantic-West African sector, as indicated by the thin dotted vertical line in Figure 3.6(a). The hatched area represents the divergent zone and the arrows represent the direction of air motion. In the convergent zone, the air mass ascends from the surface to higher altitude, and in the divergent zone, the air mass descends from high altitude to the surface.

Slingo et al. [2008] studied the long-term annual movement of the ITF in West Africa and presented that the ITF reaches at 14°N in the first dekad of May. Although M’ Bour is not included in the investigated area in West Africa, the results provide indicative results about the seasonality of the meteorology in West Africa. Kaly et al. [2015] studied 5-year observations in M’ Bour and defined the dry season as the period from November to April, the wet season as the period from May to October and the transition as the period from April and May. The results are generally consistent with Slingo et al. [2008].

Figure 3.7 shows the mean positions of the ITF in the three dekads in April 2015. The maps are provided by USGS/EROS (United States Geological Survey’s Center for Earth

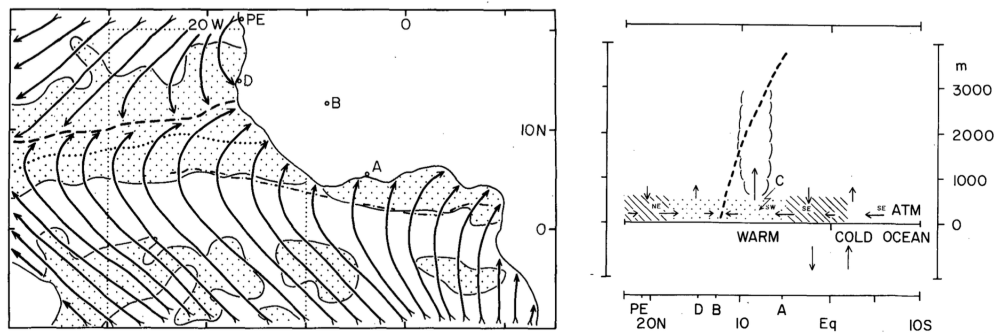


Figure 3.6. (a) Surface circulation, (b) transect of of the meridional in (a). The stippled areas represent the convergent zone. The solid lines represent the streamlines. The heavy dashed lines represent the discontinuity of the surface wind, which is the ITF. The dash-dotted line represents the speed maximum and the dotted line represent the convergence maximum, which is referred to the ITCZ. PE, D, B and A indicate radiosonde stations Port Etienne, Dakar, Bamako and Abidjan, respectively.

Resources Observation & Science). The ten-day mean position of the Africa ITF has been monitored since 1988 for the region from 15°W to 35°E. Daily analyses of the ITF position are based on the surface measurements and GDAS (Global Data Assimilation System) modeled surface wind streamlines. Dekadal ITF positions are calculated from the averages of daily positions. In the first two dekads, the western end of the mean ITF position is at about 10°N, and in the third dekad, it progresses to about 14°N, which is close to M'Bour. Given that the convergent zone expands zonally from where the ITF lies, we can speculate that M'Bour is entering into the convergent zone in April and till the third dekad of April, it has fully entered the convergent zone. It is worthy to mention that a certain range of vibrations of the convergent zone, as well as the ITF or ITCZ are normal, especially in the coastal region.

The NOAA HYSPLIT back trajectory analysis [Stein et al., 2015, Rolph et al., 2017] allows to determine the source and track the transport path of air mass at different vertical levels. GDAS dataset is used as the meteorological input of HYSPLIT model and the vertical velocity of air mass is modeled using vertical motion velocity calculation. Figure 3.8, 3.9 and 3.10 display the back trajectories in March, April and December 2015 at 500 m, 1000 m, 2000 m and 3000 m levels. The starting time of the back trajectories is 00:00 UTC for each day and the duration of each trajectory is 72 hours. The trajectory paths in

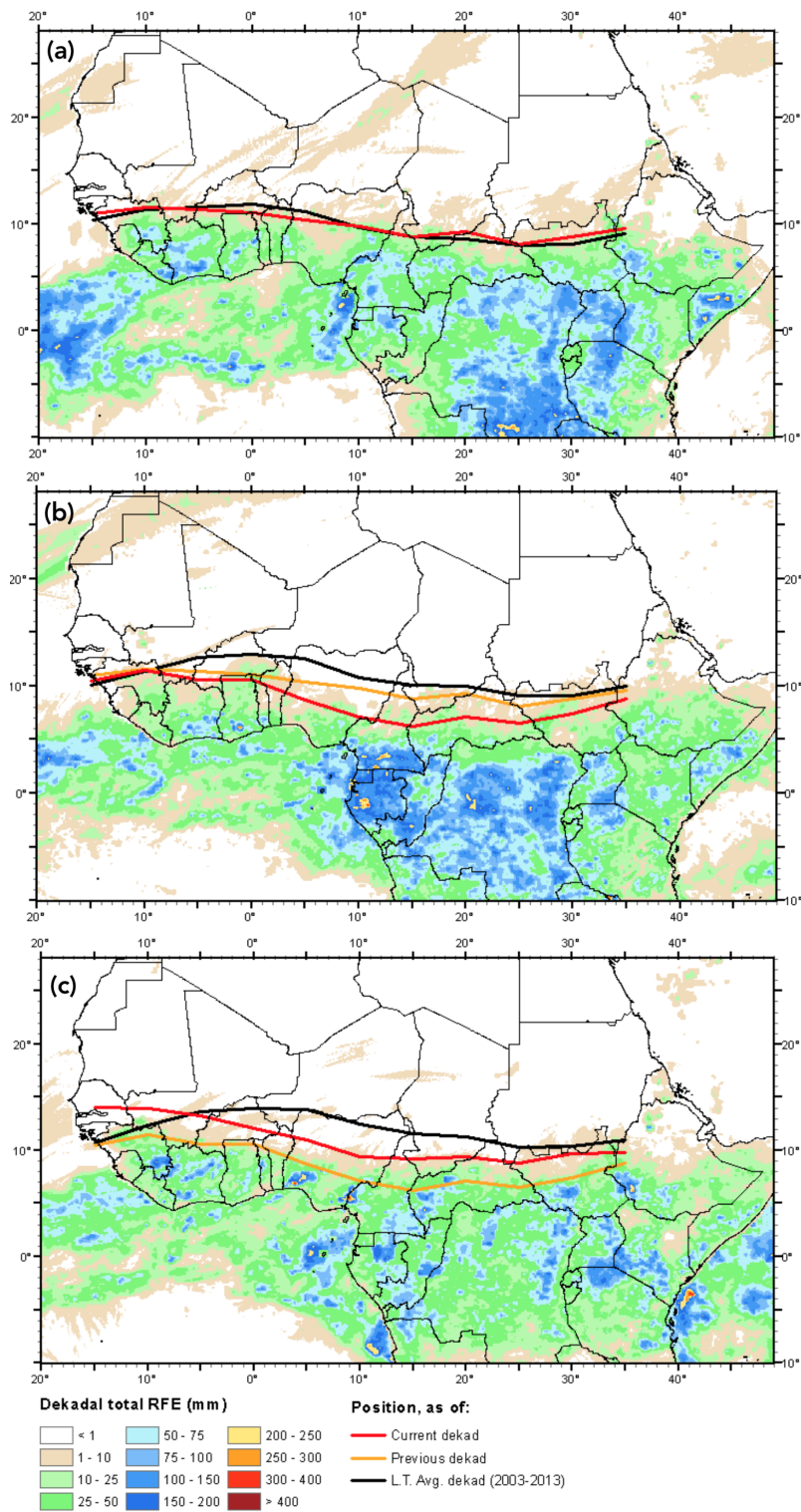


Figure 3.7. The position of ITF in April 2015. (a) 1–10 April, (b) 11–20 April, (c) 21–30 April. RFE represents ‘Rainfall estimates’.

red, blue and green represent the first, second and third dekad in the month, respectively. In the first dekad of March (red solid lines in Figure 3.8(a)), the air mass at 500 m, 1000 m and 2000 m are mostly from the desert region in the north-east. In the second and third dekad, air mass from North and East Atlantic, as well as the coast of Guinea and Côte d'Ivoire in the south-west are the main sources and could bring certain amount of maritime materials. The air mass at 3000 m comes mostly from the Atlantic and coastal region nearby. And the vertical motion of the air mass, in Figure 3.8(b) shows that downward convection is frequently observed in March, especially for 500 m and 1000 m in the first two dekads. This downward convection could bring air mass from high altitude, which is more likely to contain maritime materials, to the lower altitude. At 2000 m, both downward and upward convections are observed. At 3000 m, the occurrence of convection is not significant.

The back trajectories in April, shown in Figure 3.9, indicate that at 500 m, air mass northerly from North Atlantic and south-westerly from East Atlantic near Guinea-Bissau are of high occurrence. At 1000 m and 2000 m, air mass from the desert region and North Atlantic are both observed. While at 3000 m, the air mass comes mostly in the east where the Saharan desert lies. The most eye-catching feature of the wind map is the vertical convection. The ascending trend is obviously shown in Figure 3.9(b). At 1000 m, about 60% trajectories are traced back to altitude no greater than 500 m within the three-day . At 2000 m and 3000 m, about 87% and 50% trajectories are respectively originated from altitudes lower than 1000 m. The air mass at or below 500 m can be lofted to 1000 m, 2000 m or even 3000 m in half a day when approaching the coastal region. The enhancement of the upward convection is likely related to the advance of the ITCZ and ITF in April. The ascending air could bring the air mass near the surface which is most likely to contain maritime materials to higher altitude.

As to December 2015, the back trajectories at 500 m and 1000 m are all from the desert region in the east and north-east. At 2000 m and 3000 m, air mass is also mainly from the desert but a small fraction of trajectories originated from the Atlantic are found. Convections from the surface to high altitude are not significant in December. At 1000 and 2000 m, vertical convections are still seen, but both the intensity and occurrence are much reduced compare to April. Some downward convections are seen at all the four vertical

levels. All in all, 124 back trajectories are made for December and only 15 trajectories originate from or pass over the oceanic region. Hence, aerosols observed in December are not likely to mix with maritime aerosols.

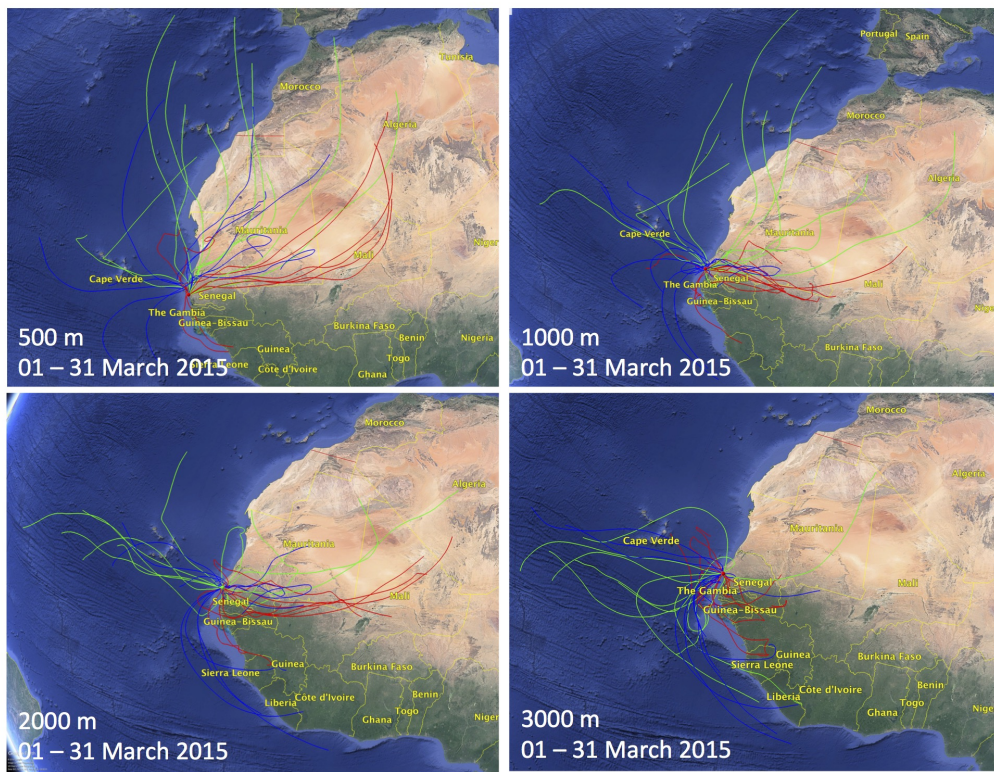
An AERONET photometer has been set up at M’ Bour site since 1996. From the historical AERONET products, we get a glimpse of the seasonal feature of aerosols. Figure 3.11(a) plots the AOD at 440 nm and the Angström exponent (AE) between 440 and 870 nm in 2014, 2015 and 2017 (Level 2.0 data, Version 3). Figure 3.11(b) displays the SSA at 440 and 675 nm. Due to the insufficient data quantity, the results in 2016 are not shown. The AE annual average in 2014, 2015 and 2017 are approximately 0.35, 0.31 and 0.34, respectively. During the wet season, the AE is of high possibility to be lower than the annual average. Especially in the period from April or May to August, the AE is about 0.15, 50% lower than the annual average and this low value is very stable during this period. The annual averages of SSA at 440 nm are about 0.900, 0.912 and 0.897 in 2014, 2015 and 2017, respectively. Correspondingly the annual mean SSA at 675 nm are 0.974, 0.979 and 0.972. During the period from mid-April or May to October, the SSA at 440 nm are higher than the annual average, indicating that the aerosols are less absorbing in the wet season than in the dry season. This increase of SSA at 440 nm starts mostly from mid-April or the beginning of May in the investigated three years, which coincides with the time of the transition from dry season to wet season. It is probably a stationary change coupled with the seasonal and meteorological changes. SSA at 675 nm also shows similar tendency but not as significant as 440 nm.

During SHADOW2 campaign, plenty of dust episodes have been recorded, the timeline covers March, April, December 2015 and January 2016. During the campaign, no precipitation occurred at the observation site and all the observations are made in the dry season and the transition season. The data are selected by the criteria:

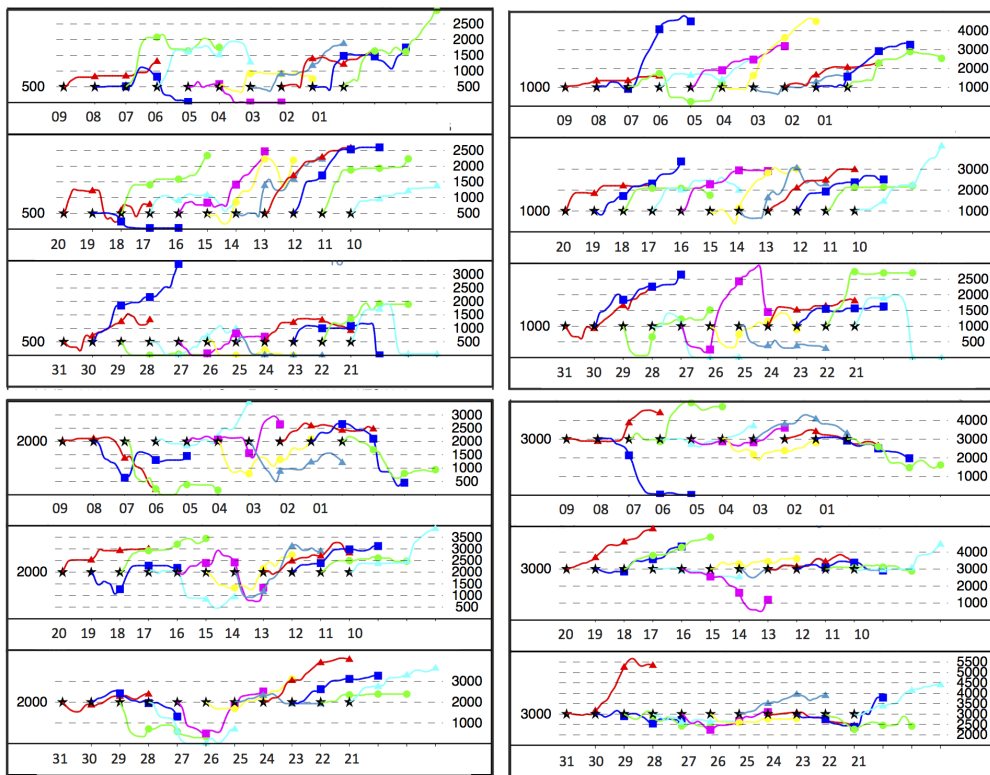
$$EAE \leq 0.1,$$

$$PLDR_{532} \geq 30\%.$$

Figure 3.12 displays the lidar ratios at 355 nm and 532 nm for dust observations during SHADOW2. The color ratio is defined as the ratio of lidar ratios at 355 nm and 532 nm. A marked characteristic is the bi-modal distribution of the color ratio, one at 1.0–1.1 and

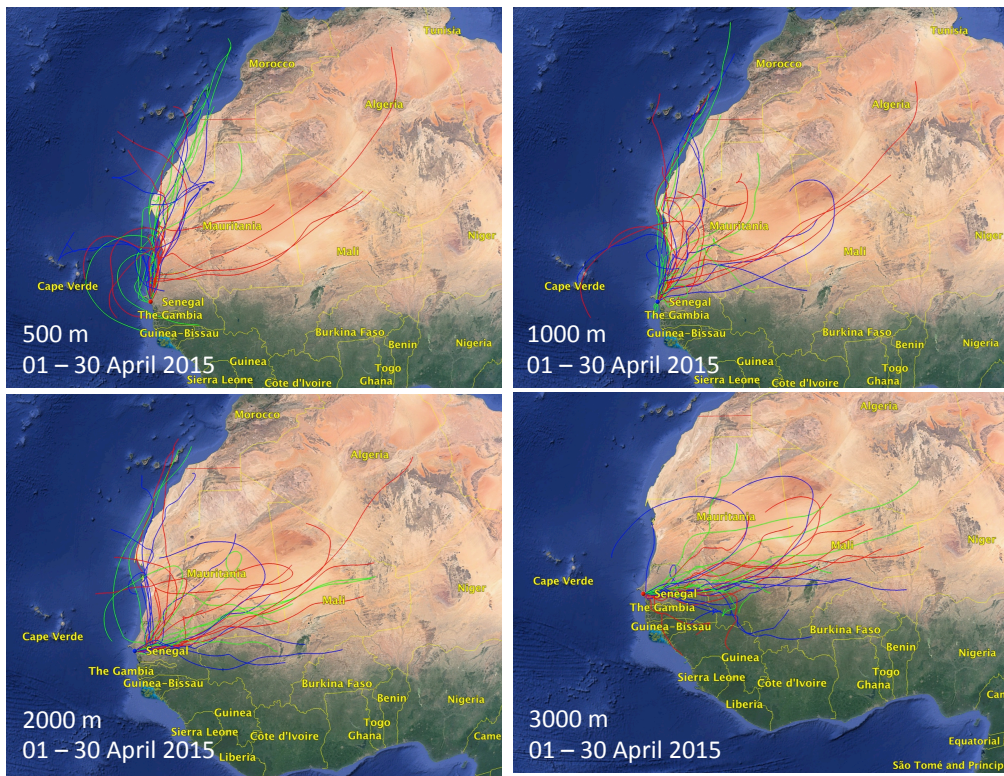


(a)

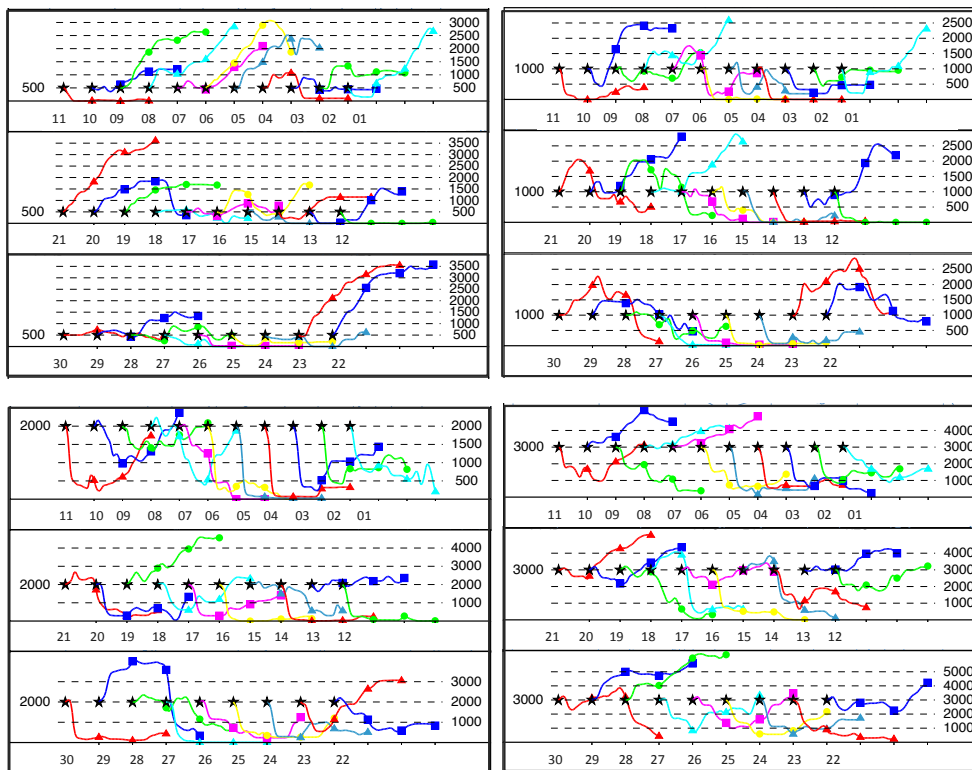


(b)

Figure 3.8. Back trajectory in March 2015 at 500, 1000, 2000, 3000 m. (a) Back trajectory direction, (b) vertical motion.

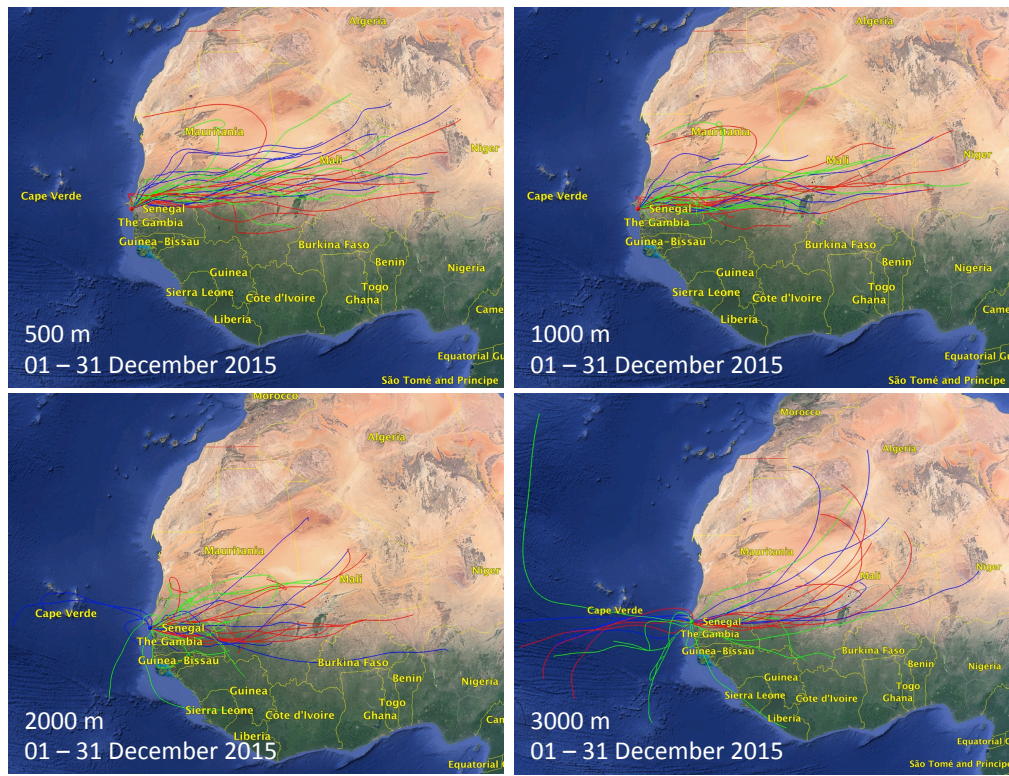


(a)

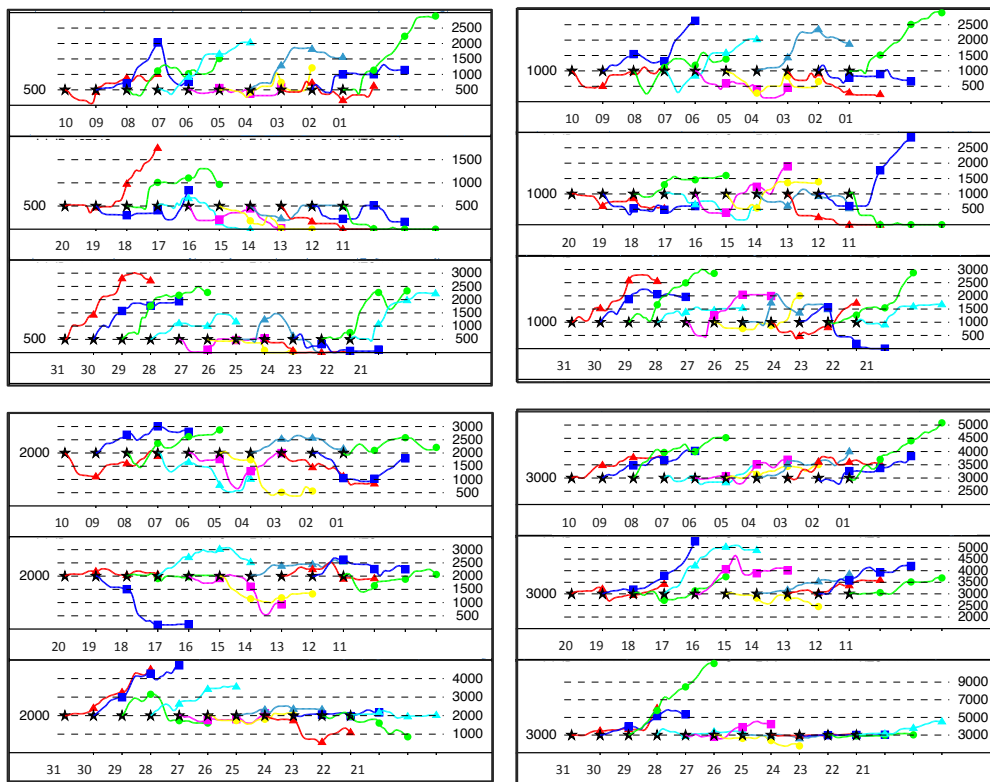


(b)

Figure 3.9. Back trajectory in April 2015 at 500, 1000, 2000, 3000 m. (a) Back trajectory direction, (b) vertical motion.

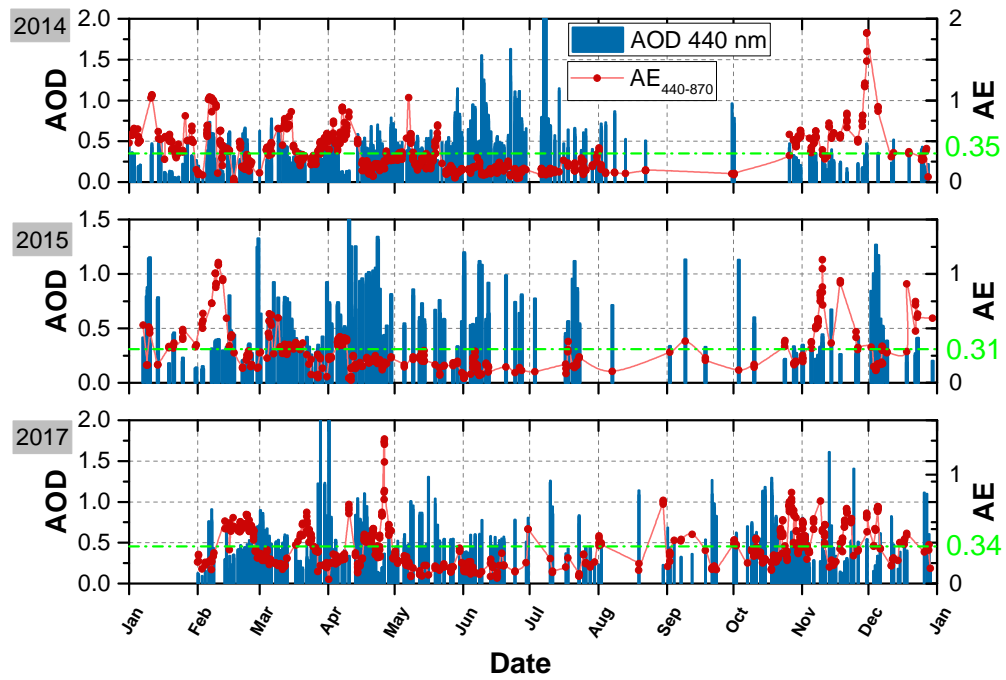


(a)

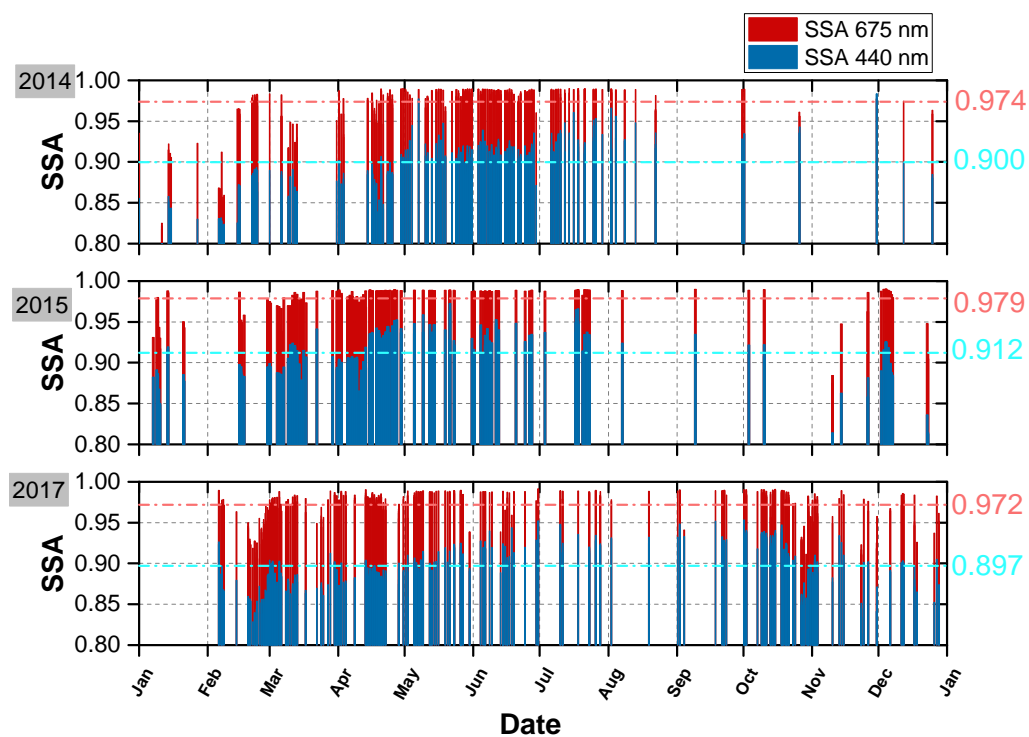


(b)

Figure 3.10. Back trajectory in December 2015 at 500, 1000, 2000, 3000 m. (a) Back trajectory direction, (b) vertical motion.



(a)



(b)

Figure 3.11. AERONET products for M'Bour site in 2014, 2015 and 2017. (a) AOD and AE, (b) SSA at 440 and 675 nm.

the other one at about 1.3. In dust episodes, 60–75 sr and 48–60 sr at 355 nm and 532 nm, respectively are observed in December 2015 and January 2016. Whereas, from mid-April to the end of April 2015, as well as some days in March 2015 the lidar ratios at 355 nm and 532 nm are approximately 50–60 sr, with very weak spectral dependence. Additionally, the decrease of the spectral dependence of lidar ratio in the last two dekads of April is accompanied by the increase of the backscatter Angström exponent (BAE) between 355 nm and 532 nm, as well as the increase of the water vapor mixing ratio in the investigated aerosol layers. The EAE and PLDR at 532 nm do not exhibit significant changes. March is usually classified as dry season in West Africa, but, some disturbances are detected. For example, the 22 March, the retrieved SSA in daytime is higher than the annual average and the lidar ratios detected in the early morning of 22 March are about 55 sr at 355 and 532 nm, show similar behaviors with the observation in the end of April. The signatures of lidar ratios and the time coincidence suggest that in April (also some days in March) the decrease of absorption in shortwave is correlated with the decrease of lidar ratio at 355 nm and these changes are possibly resulted from the transition of the meteorological environment from dry to wet season.

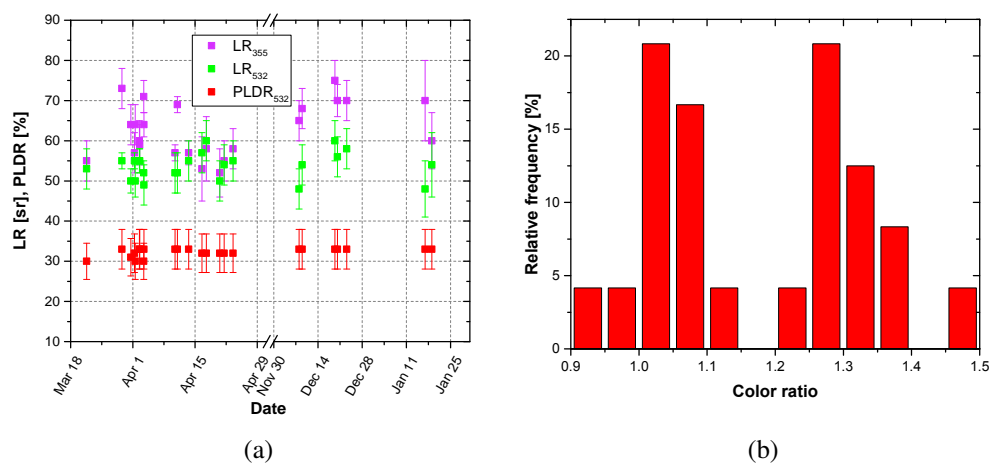


Figure 3.12. (a) LR and PLDR, (b) color ratio between 355 and 532 nm.

### 3.2.2 Case study

Three cases are selected from the observations in SHADOW2 campaign to show the seasonal feature of dust. On 19 December 2015, the lidar LILAS had two polarization channels at 355 and 532 nm. On 11 and 21 April 2015, only one polarization channel at 532 nm was available.

#### 19 December 2015, M'Bour

The observations on 19 December 2015 are a representative case of dust in the dry season. Figure 3.13 displays lidar observations from 19:37 UTC, 19 December to 06:40 UTC, 20 December 2015. The boundary layer height is about 2000–2500 m. The water vapor mixing ratio shows that the boundary layer is well mixed. The PLDR at 532 nm increases gently as the altitude decreases. A layer rises from below 500 m to 1000 m from in the period of 22:00–07:00 UTC. This layer is optically thick and shows no difference with the air mass at other altitudes in the particle linear depolarization ratio and the water vapor mixing ratio.

Lidar observations averaged between 19:35 and 21:07 UTC are processed and plotted in Figure 3.14. The water vapor mixing ratio is about 2.5 g/kg within the boundary layer then rapidly decreases to 0.5 g/kg at the top of the boundary layer. The relative humidity within the boundary layer is less than 20%. The extinction coefficient is about  $0.15 \text{ km}^{-1}$  at 1000 m and decreases to  $0.10 \text{ km}^{-1}$  at 2200 m. The EAE is about 0.0 and shows no noticeable vertical variations. The BAE reaches its minimum, -0.5, at 1500 m and then increases gently as the altitude decreases. The PLDR is about 25% at 355 nm and 30–34% at 532 nm. The lidar ratio is approximately  $55 \pm 5$  sr at 532 nm and  $65 \pm 5$  sr at 355 nm. The measured lidar ratio and PLDR at 532 nm are rather consistent with the results from SAMUM-1 and SAMUM-2 campaign [Müller et al., 2010a, 2007, Tesche et al., 2009]. The measured PLDR at 355 nm agrees well with the reported value, about 24%, from SAMUM campaign [Müller et al., 2010a,b]. But the measured lidar ratio at 355 nm is obviously higher than the value,  $55 \pm 6$  sr, reported in SAMUM campaign. Veselovskii et al. [2016] also presented lidar ratio at 355 nm as high as 70 sr, accompanied with negative BAE in the observation on 29 March 2015 during SHADOW2 campaign.

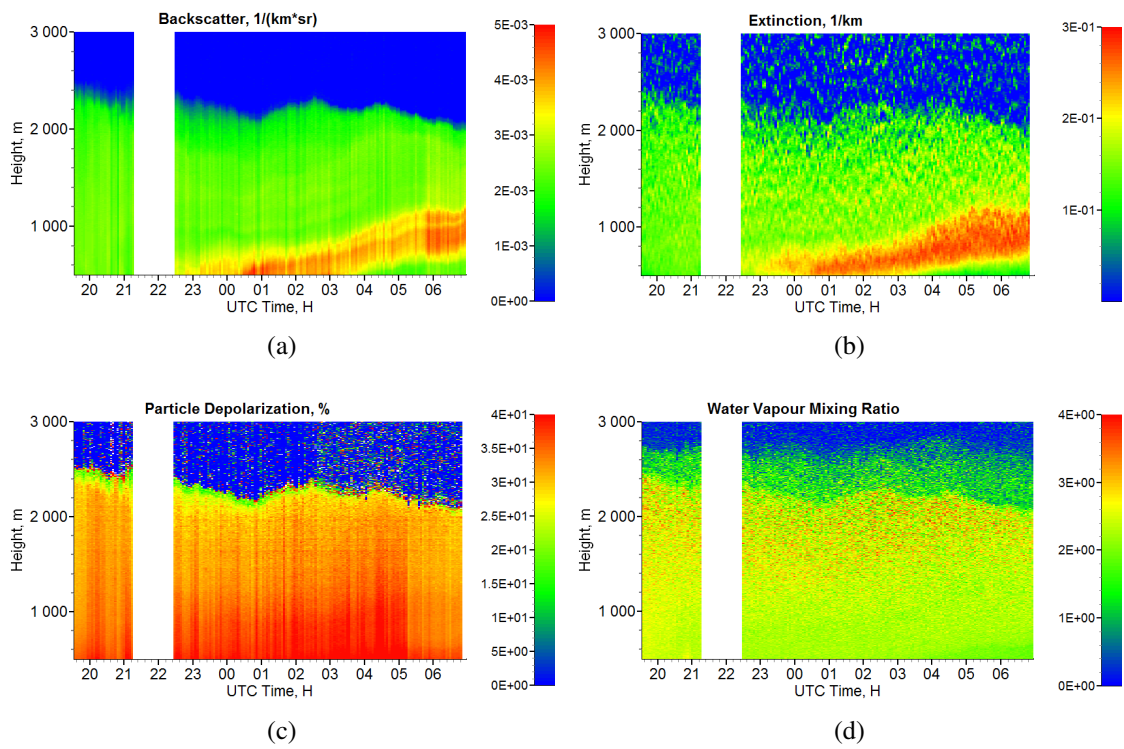


Figure 3.13. Lidar observations on 19–20 December 2015, M' Bour. (a) Backscatter coefficient ( $km^{-1}sr^{-1}$ ), 532 nm, (b) extinction coefficient ( $km^{-1}$ ), 532 nm, (c) PLDR (%) at 532 nm, (d) WVMR (g/kg).

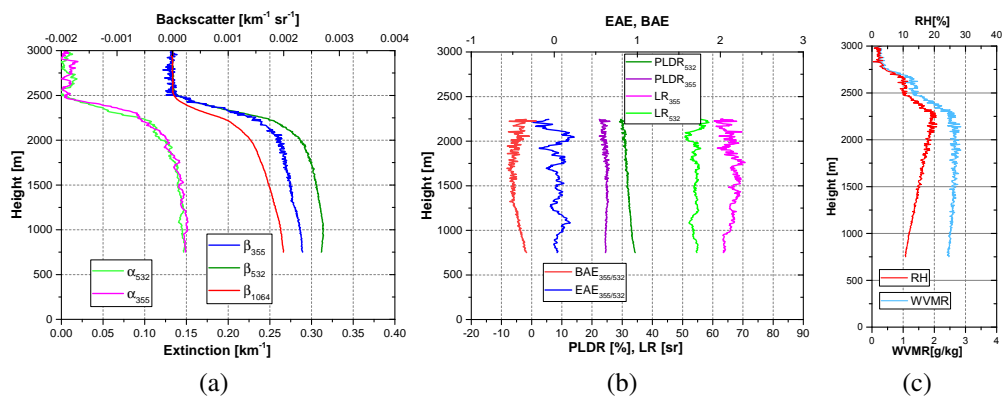


Figure 3.14. Averaged lidar observation at 19:35–21:07 UTC, 19 December 2015. (a) Extinction and backscatter coefficient, (b) PLDR, LR, EAE and BAE, (c) WVMR (g/kg).

Veselovskii et al. [2016] explained that the decrease of BAE is related to the increase of absorption of dust particles.

Figure 3.15 presents the five-day back trajectory for vertical levels at 1000 m, 1500 m and 2000 m. The air mass at 1500 and 2000 m originate from the desert region in Mali and the air mass has been lofted to 2000–2500 m on 15 December. The air mass at 1000 m is originated from near the surface in the northwest of Nigeria and during the transport, the air mass travels below 1200 m. In the dry season, fire activities are frequent, even lidar observation does not show any smoke signatures, the possibility of smoke contamination of dust cannot be strictly precluded.

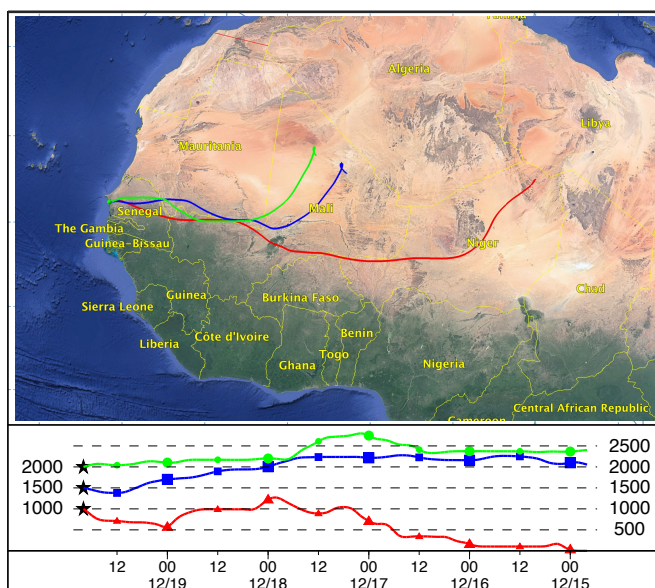


Figure 3.15. Five-day back trajectory from HYSPLIT model for 20:00 UTC, 19 December 2015. The fire and thermal anomalies are from MODIS observations. Fire maps from 13 to 19 December are overlaid.

### 11 April 2015, M'Bour

Figure 3.16 shows the backscatter, extinction coefficient, particle linear depolarization ratio and water vapor mixing ratio observed on 10–11 April 2015. The boundary layer height is about 4000–4500 m. The extinction colormap indicates that the aerosol loading decreases from around 20:00 UTC, 10 April to 06:00 UTC, 11 April 2015. However, the PLDR at 532 nm is stable, vary in the 30–35% range. The WVMR shows that the layer

between 2500 m and 4000 m is well mixed, while below 2500 m, a layer characterized by increased water vapor mixing ratio is observed, meaning the intrusion of a humid air mass.

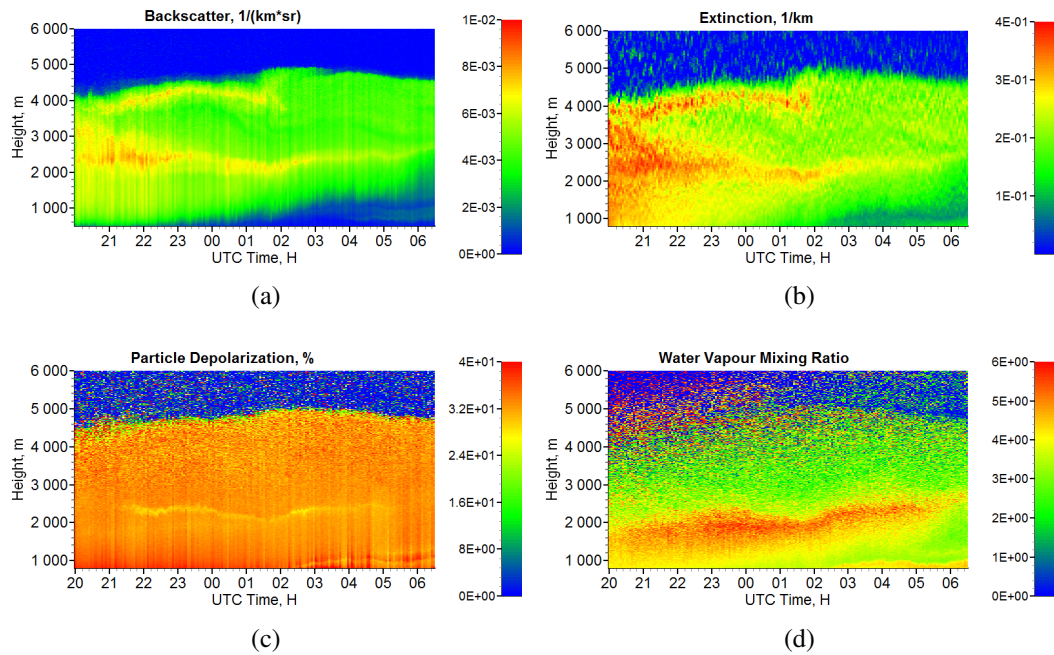


Figure 3.16. The colormaps of Lidar observations on 10–11 April 2015. (a) Backscatter coefficient ( $\text{km}^{-1}\text{sr}^{-1}$ ), 532 nm, (b) extinction coefficient ( $\text{km}^{-1}$ ), 532 nm, (c) PLDR (%) at 532 nm, (d) WVMR (g/kg).

Figure 3.17 presents the optical properties retrieved from the averaged Lidar observations in the night of 10–11 April 2015. In the 2500–4000 m range, aerosols are well mixed, as the PLDR, lidar ratios and water vapor mixing ratio are almost vertically constant. The PLDR at 532 nm is about 33%, indicating that dust is the dominant component. The lidar ratio is about  $53 \pm 3$  sr at 532 nm and  $68 \pm 4$  sr at 355 nm. The BAE varies between -0.5 and -0.7. Compared with the observation on 19 December 2015, the PLDR, lidar ratios and Angström exponent in 2500–4000 m range are very consistent. Given that the relative humidity increases from about 20% to about 60%, while the lidar ratios, PLDR, BAE and EAE do not change, we can conclude that dust is not hygroscopic under this condition. Below 2500 m, increased water vapor mixing ratio is observed with its maximum at about 2000 m. The PLDR at 532 nm reaches its local minimum of 32% in the 2000–2500 m range. The BAE also shows a sharp enhancement at 2500 m, while the EAE does not

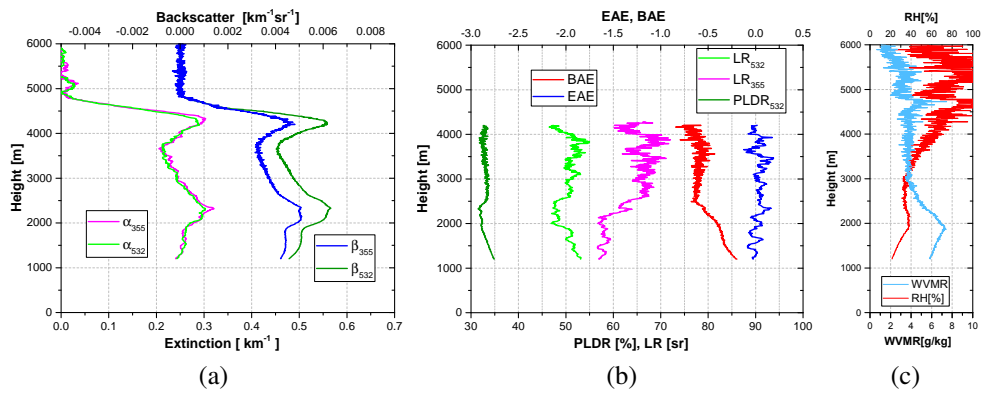


Figure 3.17. Averaged Lidar observation 23:00–01:57 UTC, 10–11 April 2015. (a) Extinction and backscatter coefficient, (b) PLDR, LR, EAE and BAE, (c) WVMR (g/kg).

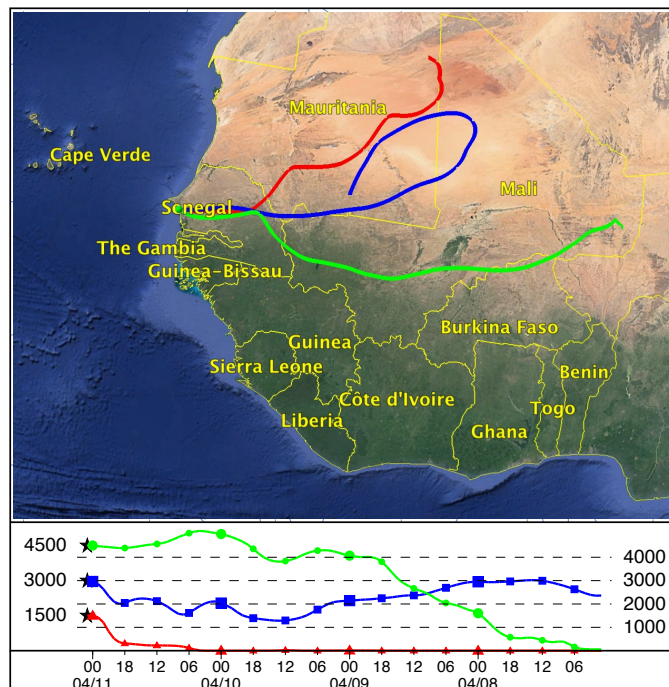


Figure 3.18. Five-day back trajectory from HYSPLIT model for 01:00 UTC, 11 April 2015.

show noticeable variations. As the altitude decreases from 2500 m to 1200 m, the lidar ratio at 532 nm increases from about 48 sr to 54 sr. And at the same time the lidar ratio at 355 nm decreases with a more noticeable speed, from about 67 sr to 57 sr. The derived lidar ratio, PLDR as well as the BAE are rather consistent with the observations reported in SAMUM campaign [Müller et al., 2010a, 2007, Tesche et al., 2009]. On the other hand, these features emphasize the diversity and complexity of dust properties.

The increase of water vapor in the 1500–2500 m range may lead to a question: are the comparisons of dust properties in 1500–2500 m and 2500–4000 m caused by the hygroscopic effect? Kaaden et al. [2009] studied the dust samples collected in SAMUM-1 campaign and concluded that mineral dust particles (with diameter larger than 720 nm) are completely hydrophobic. Kaaden et al. [2009] presented that mixing with anthropogenic material makes mineral dust more hygroscopic. Twohy et al. [2009] studied Saharan dust acting as cloud condensation nuclei and concluded that hygroscopic materials can also be present naturally in dust particles. However, in this case, even the water vapor increases below 2500 m, the relative humidity is still very low, less than 40%. Whereas, hygroscopic growth is expected at much higher relative humidity. The intrusion of air mass coming from a different source should be a more reasonable explanation for the distinct optical properties observed below 2500 m.

Four-day back trajectories of air mass at 1500, 3000 and 4500 m are plotted in Figure 3.18. The air mass at 1500 and 3000 m is originated from the desert region in Mauritania and Mali. The former is transported close to the surface and then lofted to 1500 m in less than 6 hours. While the latter is transported at higher altitudes, between 1000 and 3000 m. As introduced in previous section, air mass near the surface in M'Bour are mostly coming from the North and East Atlantic. When air mass is approaching the observation site with low altitudes, it is very possible to mix with maritime aerosols. And this air mass is then lofted to higher altitudes by strong upward convection.

### **21 April 2015, M'Bour**

Figure 3.19 displays the lidar observations in the night of 20–21 April 2015. The atmospheric boundary layer height is 4200–4500 m. Multiple layers with water vapor mixing

ratio greater than 3.0 g/kg are detected at 1000, 3000 and 4000 m. The particle linear depolarization ratio at 532 nm shown in Figure 3.19(c) is nearly homogeneous in the boundary layer and displays no temporal variation in the night. A slight decrease of particle depolarization ratio is detected at about 4000 m at 23:00–01:00 UTC.

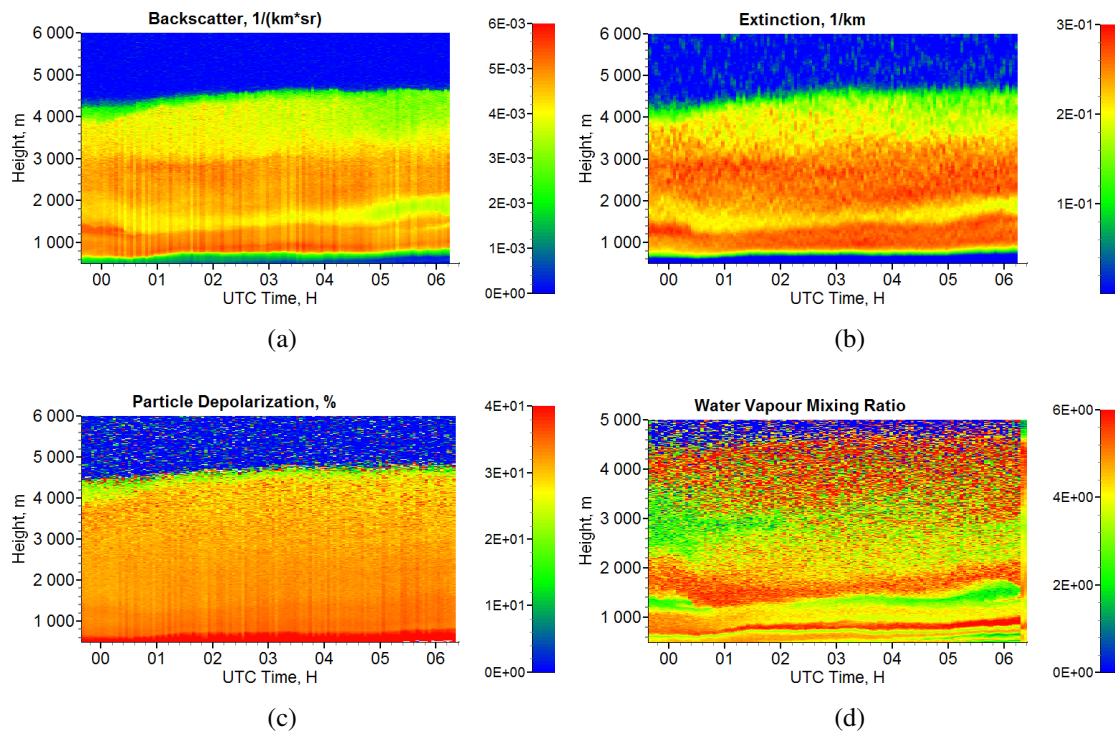


Figure 3.19. The colormaps of Lidar observations on 20–21 April 2015. (a) Backscatter coefficient ( $\text{km}^{-1}\text{sr}^{-1}$ ), 532 nm, (b) extinction coefficient ( $\text{km}^{-1}$ ), 532 nm, (c) PLDR (%) at 532 nm, (d) WVMR (g/kg).

Aerosol optical properties retrieved from averaged lidar observations at 23:40–01:00 UTC are plotted in Figure 3.20. The extinction coefficient at 1000–4000 m varies in 0.2–0.3  $\text{km}^{-1}$  range at both 355 and 532 nm. The BAE is about 0.0 and does not show noticeable vertical variations. The profile of WVMR enhances at 1000, 1500 and 4000 m. The PLDR at 532 nm is about 32% and is almost vertically constant in the range of 1500–3800 m. A slight increase, about 1–2% is observed below 1500 m. The lidar ratios at 355 and 532 nm are  $50 \pm 5$  sr and change in the same manner in 1000–3500 m range. As the altitude approaches 4000 m, the depolarization ratio decreases to about 28%, the lidar ratio decreases at 532 nm to about 48 sr, while the lidar ratio at 355 nm stays at  $55 \pm 5$  sr and the relative humidity increases to around 90%.

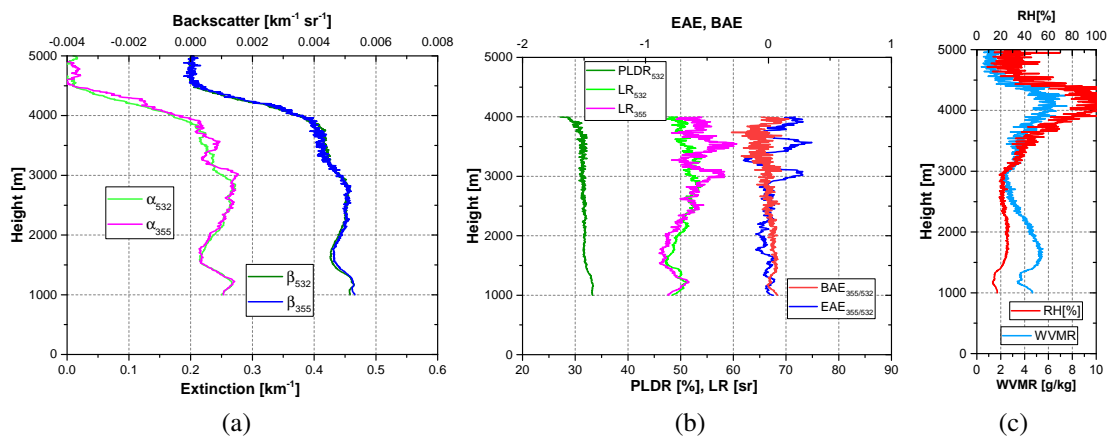


Figure 3.20. Averaged lidar observation 23:40–01:00 UTC, 21 April 2015. (a) Extinction and backscatter coefficient, (b) PLDR, LR, EAE and BAE, (c) WVMR (g/kg).

Five-day back trajectory in Figure 3.21 indicates that the air mass at 1000 m and 2000 m is originated from nearly the same region, the desert between Niger and Chad. The air mass is westwardly transported at altitude lower than 1000 m and then elevated to higher altitude when approaching the coastal region in West Africa. Whereas the air mass at 3000 m is originated from the area between Senegal and south-west of Mali. The air mass descends from above 5000 m to 3000 m.

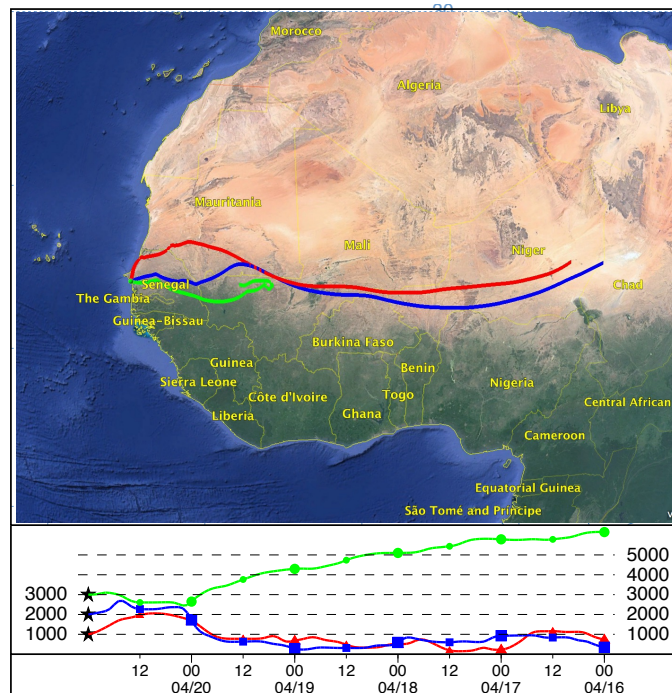


Figure 3.21. Five-day back trajectory from HYSPLIT model for 00:00 UTC, 21 April 2015



### 3.2.3 Discussion

The selected three cases show the comparisons of the two different dust types. The lidar measured WVMR can be used as a tracer for air mass coming from different origins. Lidar observation in the three cases point to that the dust layers with reduced lidar ratio at 355 nm are characterized with enhanced WVMR, meaning that they are possibly mixed with maritime aerosols which is an important moist aerosol source for M'Bour site. Rivellini et al. [2017] studied the chemical composition of non-refractory sub-micron particles during SHADOW2 campaign and found a significant contribution of air mass from sea breeze in March and April 2015. And the air mass brought by sea breeze is characterized by relatively high concentration of organic and sulphuric matter. Although the study is specific to the ground-level measurements and sub-micron particles, it supports and confirms, to some extent, our speculations that dust in March and April is likely to mix to maritime aerosols.

It is not surprising that maritime aerosol will dilute the absorption of dust because it contains usually low absorbing or non-absorbing materials such as sea salts and sulphates. Whereas, the spectral absorption of dust particles is highly variable and uncertain, and the mixing of dust and maritime aerosols is a complex subject. More efforts are needed in both observations and modeling. Here a simple modeling work is performed to illustrate the possible impacts of low absorbing maritime aerosols on dust properties. A size distribution dominated by coarse particles is simulated to represent the size distribution of dust. The particles are composed of 10% spheres and 90% spheroids. The real part of the complex refractive indices is assumed to be 1.50. The imaginary part varies from 0.0005 to 0.01. The EAE and BAE between 355 and 532 nm (in Figure 3.22(a)) are simulated with wavelength-independent refractive indices. The EAE does not show obvious sensitivity to the changes of the imaginary part of the refractive indices when the size distribution and real part is fixed. While BAE decreases from -0.3 to -0.55 as the imaginary part increases from 0.0005 to 0.01. Figure 3.22(b) plots the lidar ratios at 355 and 532 nm. Lidar ratio at 355 nm decreases from 120 sr to 50 sr as the imaginary part decreases from 0.01 to 0.0005, and lidar ratio at 532 decreases from 86 sr to 40 sr. Apparently lidar ratio at 355 nm decreases faster than 532 nm when the imaginary part decreases by the same value.

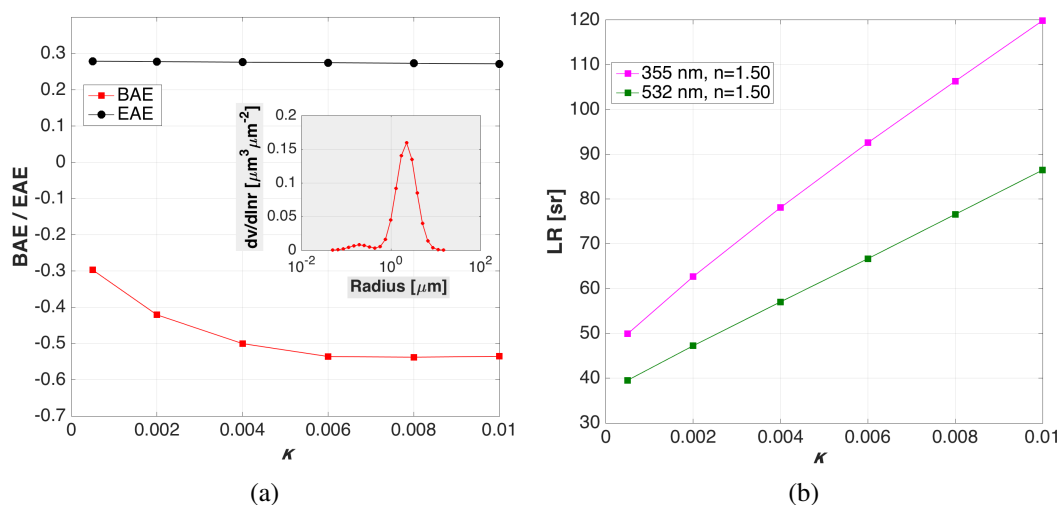


Figure 3.22. Modeled BAE, EAE and LR versus the imaginary part of the complex refractive index. The insert in (a) shows the particle size distribution that is used in the simulation. The real part of the refractive indices is fixed to 1.50 for both 355 and 532 nm. Varied imaginary parts are used in the range of 0.0005–0.01.

Figure 3.23 presents the lidar ratios of dust mixtures. The aerosol model is taken from MERRA-2 [Buchard et al., 2017, Gelaro et al., 2017, Randles et al., 2017]. MERRA-2 provides modeled aerosol properties based on five aerosol components: black carbon, dust, organic carbon, sea salts and sulphates. The released data provide 1980 onward data reanalysis with  $1^\circ \times 1^\circ$  spatial resolution and 3-hour time resolution. The aerosol model in MERRA-2 is borrowed from GOCART model [Colarco et al., 2010]. The lidar ratio for dust is about 66.8 sr at 355 nm and 40.7 sr at 532 nm. At 355 nm, the simulated lidar ratio is quite consistent with the lidar observation in the dry season. But at 532 nm, the simulated lidar ratio is about 10–15 sr lower than the lidar observation. One possible explanation is that MERRA-2 uses 0.0026 for the imaginary part of refractive indices at 532 nm, whereas this value is lower than the values obtained from field campaign studies [Ansmann et al., 2011]. We calculate the lidar ratios of dust externally mixed with sea salt, sulphates, and both sea salt and sulphate. The extinction ratio of the three mixtures are respectively 10:1, 10:1 and 10:1:2. The ratio of extinction coefficient for each aerosol component is used as weight when calculating the extinction and backscatter coefficients of the mixtures, from which the lidar ratios are calculated. When dust mixes with sea salt with extinction ratio of 10:1, the lidar ratio decreases to 53.2 sr at 355 nm and 35.3 sr

at 532 nm. When dust mixes with sulphate with extinction ratio of 10:1, the lidar ratio increases to 66.8 sr at 355 nm and 42.5 sr at 532 nm. When dust mixes with sea salt and sulphate with extinction ratio 10:1:2, the lidar ratio decreases to 55.5 sr at 355 sr and to 38.5 sr at 532 nm. The change of lidar ratio at 355 nm is consistent with the trend observed by lidar, but lidar ratio at 532 nm does not show significant change and is always lower than the observations. This is an illustration of the changes of lidar ratio when dust is mixed with sea salts and sulphates,

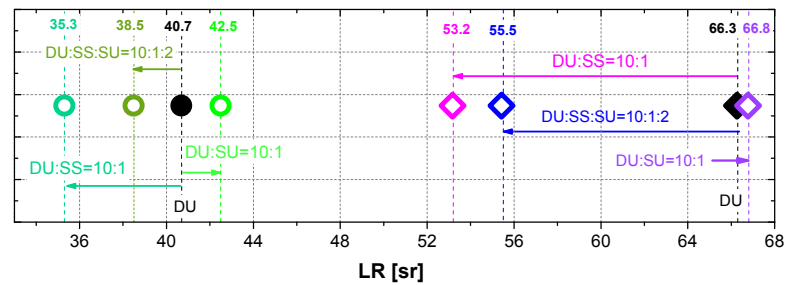


Figure 3.23. Modeled LR using aerosol components from MERRA2. DU: dust, SS: sea salt, SU: sulphate.

### 3.3 Long-range transported aerosols

#### 3.3.1 Long-range transported dust observed in Lille

As the largest dust source on the Earth, Saharan desert exports large quantities of dust into the atmosphere every year. The maximum of dust outbreak is usually in spring and the minimum is in winter [Papayannis et al., 2005, Nastos, 2012]. Transported Saharan dust has been reported in northern Europe [Ansmann et al., 2003], central Europe [Müller et al., 2003], and eastern Europe [Papayannis et al., 2008]. The study of Doherty et al. [2008] shows that, with the influence of displacements in the Azores and Hawaiian anti-cyclones, Saharan dust can cross the Atlantic ocean and reach the Caribbean area. The outbreak of Saharan dust is controlled by multiple meteorological factors, such as the precipitation, the absence of depression and thermal conditions. On 10 and 11 March 2017, large-scale transported Saharan dust was detected by LILAS system over Lille. Nighttime lidar observations show complicated dust stratifications distributing in the range of 2000–8000 m. A optically thick aerosol layers near the surface is observed between 22:00 and 05:00 UTC in the night of 10–11 March 2017.

The four-day back trajectory shown Figure 3.25(a) indicates that the dust layers are originated from East Atlantic near the north-west coast of Africa. An outbreak of Saharan dust is detected by MODIS imager on 08 March 2017. Figure 3.25(b) shows the true color image obtained from MODIS. The dust plume near the coast of West Africa can be clearly seen in the image. The back trajectory indicates that the air mass has travelled over the north-east Atlantic before arriving at the observation site. Lidar observations averaged between 21:00 UTC and 23:00 UTC are plotted in Figure 3.26. The maximum of extinction coefficient reaches approximately  $0.07 \text{ km}^{-1}$ . Both the extinction and backscatter coefficients have no noticeable spectral dependence between 355 nm and 532 nm. The lidar ratios are both about 50–60 sr at 355 and 532 nm, with negligible spectral dependence. The PLDR is approximately 25–28% at 532 nm and 17–21% at 1064 nm. Unlike the dust observed in M’Bour, the PLDR of transported dust at 532 nm decreases by 2-5%, while the PLDR at 355 nm remains the same with the observations in M’Bour. The changes may be linked with the processes that dust particles underwent during the transport.

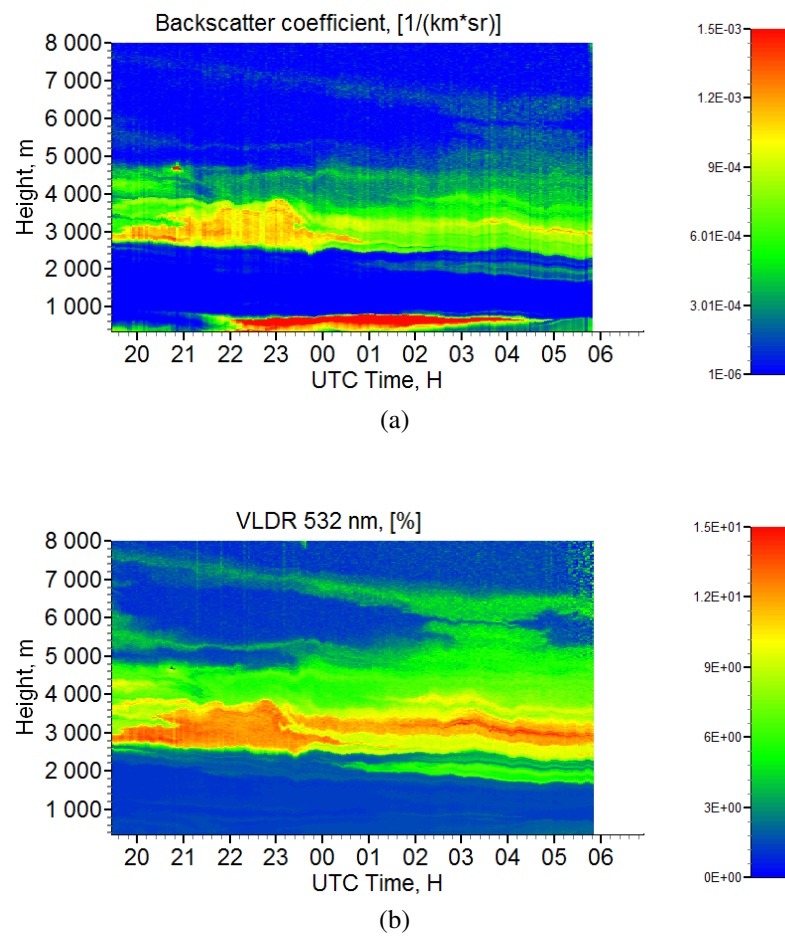


Figure 3.24. Lidar observations on 10–11 March 2017. (a) Backscatter coefficient at 532 nm, (b) VLDR at 532 nm.

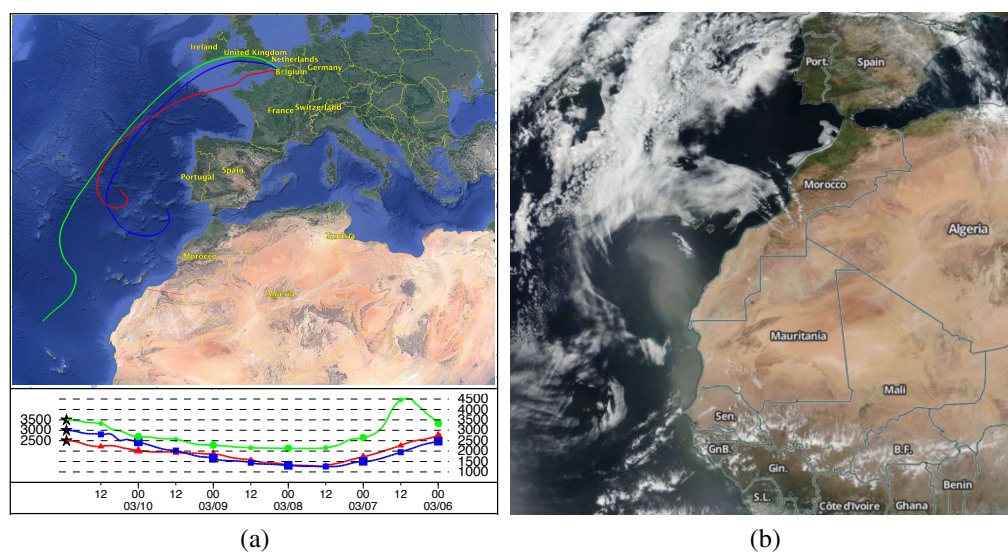


Figure 3.25. Four-day back trajectory for 23:00 UTC, 10 March 2017 and MODIS image. (a) Four-day back trajectory, (b) dust plumes observed on 08 March 2017.

As known, the dust deposition process, including wet and dry deposition, is size dependent. The dominant deposition factor differs depending on the size of dust particles. Gravitational sedimentation is significant for super-micrometer particles and Brownian diffusion is important for sub-micrometer particles [Osada et al., 2014]. Dust size distributions near the source and after long transport are expected to be different due to the deposition process. If we consider the dust observed in Lille is originated from the coast of West Africa, the transport distance is more than 5000 km. Given that these dust are possibly lofted and transported from the Saharan desert to the coast and then are transported to Lille crossing the Atlantic ocean, the transport distance could be even larger than 6000–7000 km. Figure 3.27 presents the monthly averaged size distributions in March 2017 for Dakar (14.39°N, 14.96°W) and Tamanrasset (22.79°N, 5.53°E), as well as the size distribution derived at 16:04 UTC, 10 March 2017. The size distributions are derived from the AERONET Version 3.0 data and normalized to 0–1.0 range. Tamanrasset site is located in the center of Saharan desert. Dakar is located in the westward transport pathway of Saharan dust. In Dakar, local dust could also be injected into the atmosphere from the exposed sand on the surface. The effective radii of the three AERONET size distributions in Tamanrasset, Dakar and Lille are  $0.79 \mu\text{m}$ ,  $0.74 \mu\text{m}$  and  $0.45 \mu\text{m}$ . The averaged  $2\alpha + 3\beta$  data are inverted using regularization algorithm [Müller et al., 1999, Veselovskii et al.,

2002] and the obtained size distribution is plotted in Figure 3.26 in green solid line. The effective radius of the lidar retrieved size distribution is about  $0.86 \mu\text{m}$ . The size distribution retrieved for the dust layer looks more ‘concentrated’ as it loses both some very small particles and bigger particles compared with the AERONET retrieved size distribution in Lille. The size distributions in Tamanrasset and Dakar show a pronounced coarse mode and a negligible fine mode with peaked radius at  $2.3 \mu\text{m}$ . While the size distribution in Lille has a peaking radius at  $1.3 \mu\text{m}$  and a non-negligible fine mode. Additionally, an altitude-dependent tendency of the particle depolarization ratio is observed in the dust layer. It could be a signature of hygroscopicity. As the dust plumes are transported over the ocean at low altitudes, it is very possible that they mix with hygroscopic maritime materials. At 3500 m, the relative humidity reaches about 70%, at which hygroscopic growth of sea salt is expected.

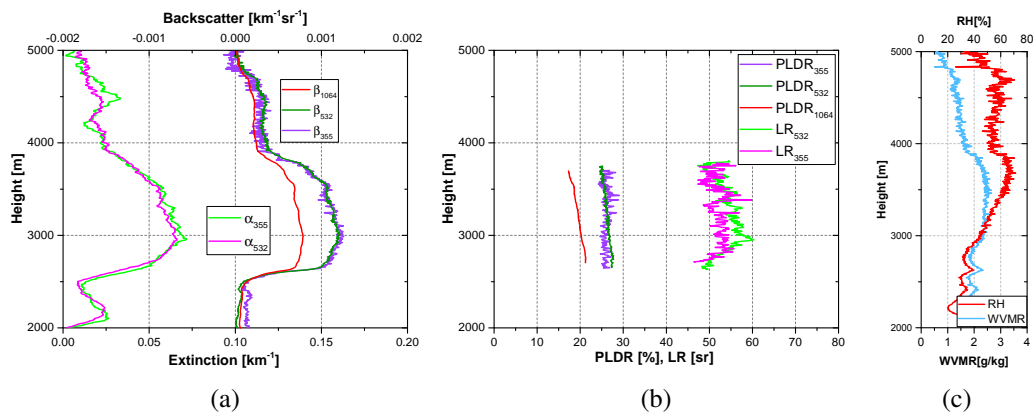


Figure 3.26. Averaged observations at 21:00–23:00 UTC, 10 March 2017. (a) Extinction and backscatter coefficient, (b) PLDR and LR, (c) WVMR and RH.

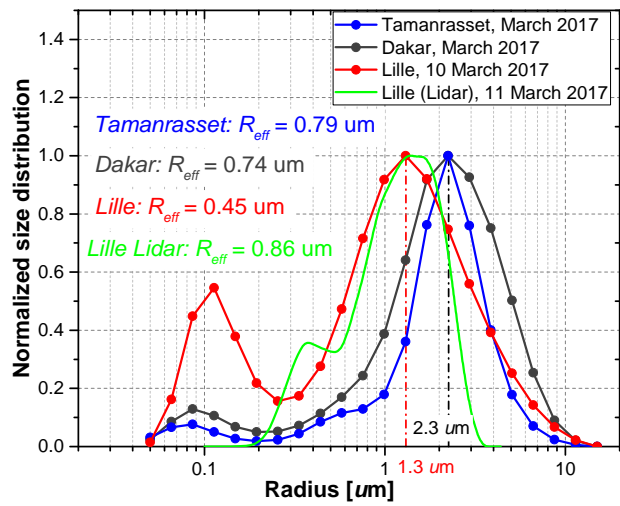


Figure 3.27. Normalized size distributions in Lille, Dakar and Tamanrasset.

### 3.3.2 Long-range transported Canadian smoke

In the summer of 2017, intense wildfires have been observed in the west and north Canada. MODIS recorded the strong pyro-cumulonimbus clouds generated by the severe wildfires (see [the link](#)). The pyro-cumulonimbus cloud has the potential to transport fire emissions to the Upper Troposphere/Lower Stratosphere (UTLS) [Luderer et al., 2006, Trentmann et al., 2006]. Previous researchers [Fromm et al., 2000, Fromm and Servranckx, 2003] have reported smoke aerosols lofted to the UTLS by strong convection. On 12 August 2017, the GOES-15 detected five pyro-cumulonimbus clouds over the British Columbia in the west of Canada. Figure 3.28 shows the true color image of MODIS on 16 August 2017. The green dashed line represents the area covered by smoke. CO is one product of the combustion process and can be taken as a tracer for smoke [Haskins and Kaplan, 1992]. Figure 3.29 displays the columnar CO concentration from the Atmospheric Infrared Sounder (AIRS, [Teixeira, 2013]) in the period of 11–29 August 2017. The evolution of the CO plumes indicates that they are originated from the British Columbia on 12 August and transported to Europe. We select six positions on the map, labeled as **a–f** in Figure 3.28. The six locations are intendedly selected following the transport pathway of the CO plumes. Figure 3.30 plots the profiles of backscatter coefficient and PLDR measured by CALIPSO over these six locations. CALIPSO detects aerosol layers in the UTLS over all the six locations. In Figure 3.30(d), a thin mixed phase clouds is detected at 5–10 km. LILAS detected the Canadian smoke layers in the UTLS during distributed

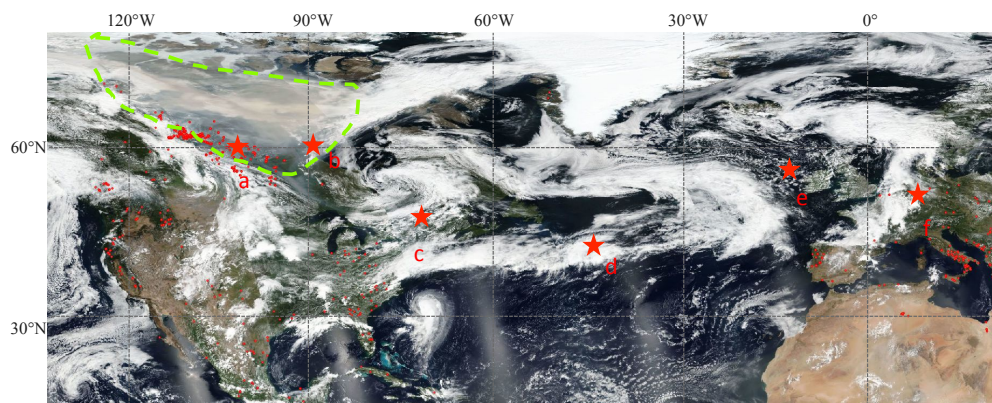


Figure 3.28. The surface reflectance from MODIS observation on 16 August 2017

days in August and September 2017. Figure 3.31 shows the observed aerosol layers on

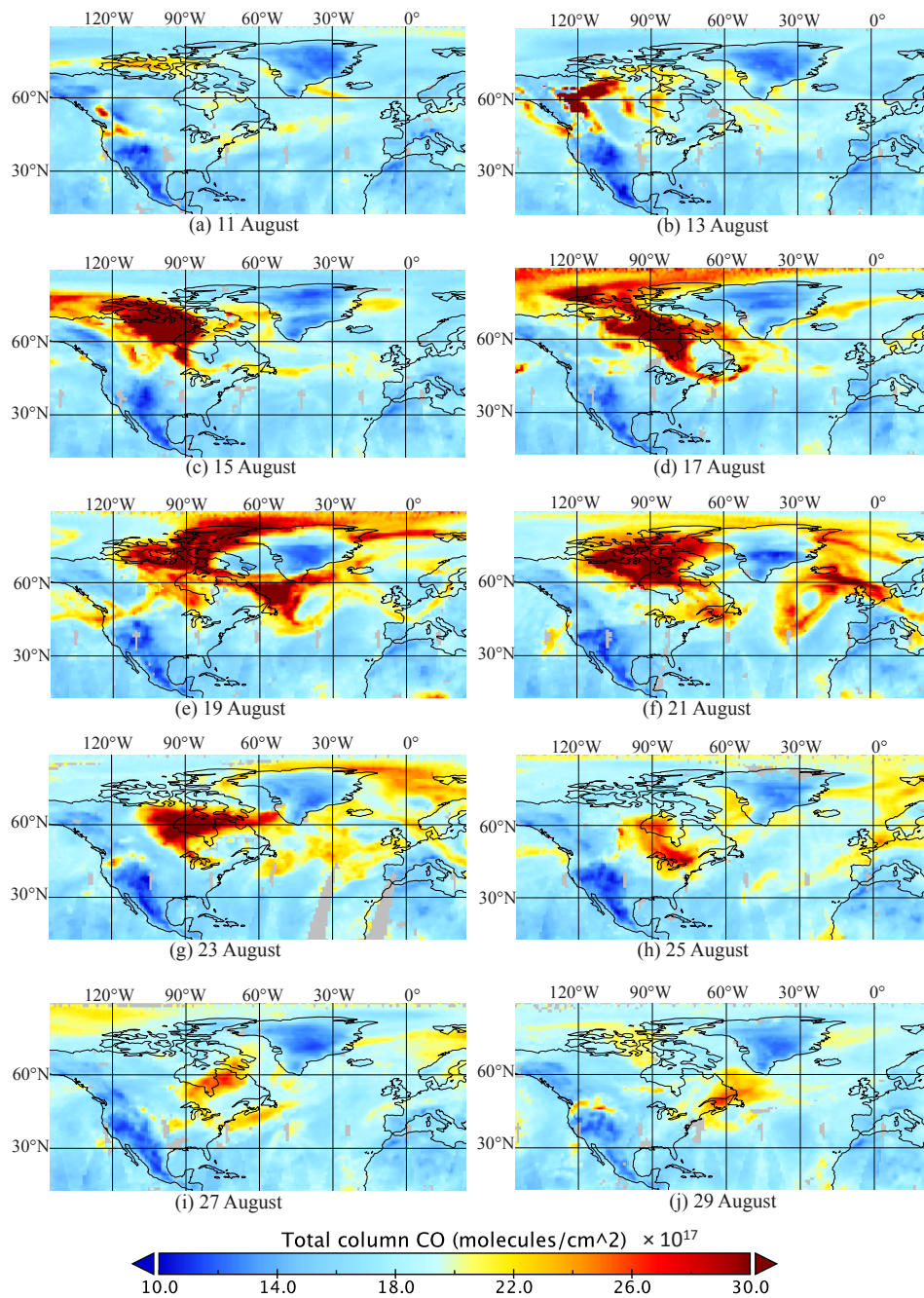


Figure 3.29. The columnar CO concentration from AIRS product

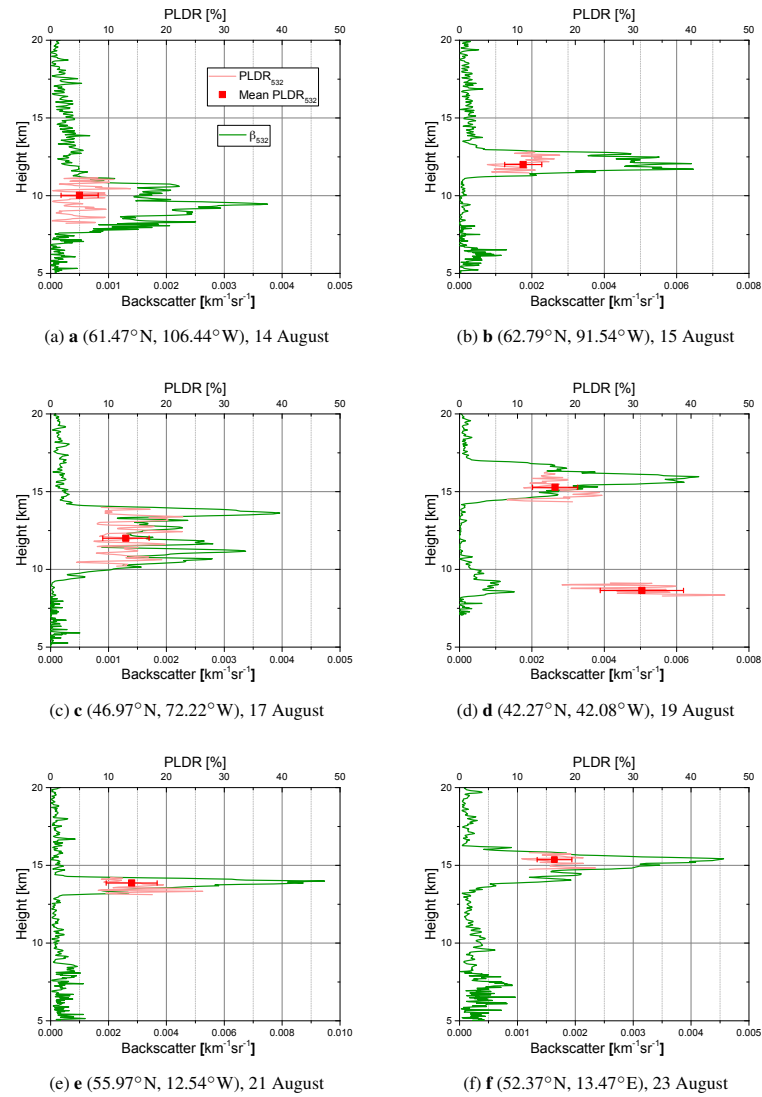


Figure 3.30. The profiles of backscatter and particle depolarization ratio from CALIPSO products

24–25, 29 August and 01 September 2017. The aerosol layers distributed at 16–20 km and on 29 August, the thickness of the aerosol layer reached 3–4 km. The aerosol layers are at very high altitude where the signal-to-noise ratio of the Raman signal is not sufficient to obtain high quality extinction coefficient. Klett method [Klett, 1985] is chosen to invert the lidar elastic signal. The optical depth of the smoke layer,  $\tau^{smoke}$ , is obtained by calculating the transmittance below and above the smoke layer and then used as an additional constraint of Klett inversion. We test a series of lidar ratios in the range of 10–120 sr, with a step of 0.5 sr and apply independent Klett inversions with each assumed lidar ratio. The integral of the extinction coefficient within the UTLS layer, expressed below, is compared with the pre-calculated optical depth  $\tau^{smoke}$ .

$$\tau^i(\lambda) = \int_{r_{base}}^{r_{top}} \alpha_a(\lambda, r) dr \quad (3.1)$$

where  $\tau^i$  is the integral of extinction coefficient  $\alpha_a$ , derived from Klett inversion,  $r$  is the distance, the subscripts 'top' and 'base' represent the top and base of the UTLS aerosol layer and  $\lambda$  is the elastic lidar wavelength. The lidar ratio resulting in the best fit optical depth are accepted. To exclude the impact of tropospheric aerosols, Klett inversion is only apply to the smoke layers in the UTLS.

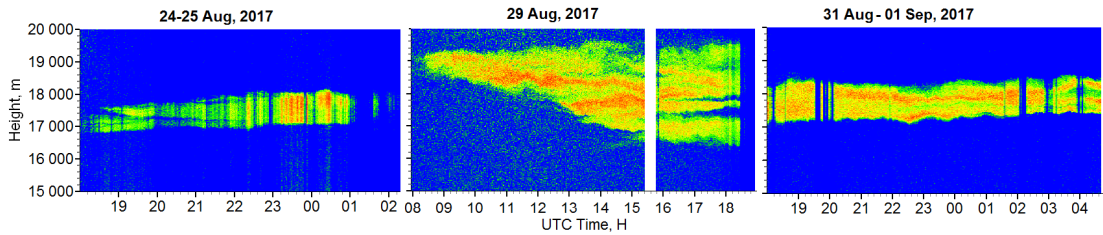


Figure 3.31. The smoke layers observed in August 2017, Lille

Table 3.1 summarizes the derived optical depth  $\tau^{smoke}$ , lidar ratios at two wavelengths and PLDRs at three wavelengths. Between 16:00 and 18:00 UTC, 29 August 2017, the aerosol optical depth reaches  $0.20 \pm 0.04$ . Lidar ratios vary between  $54 \pm 9$  sr and  $58 \pm 23$  sr at 532 nm and between  $31 \pm 15$  sr and  $45 \pm 9$  sr at 355 nm. In the night of 31 August, the error of lidar ratio is about 30 – 35%, relatively higher than the other days because of the low optical depth. Although the error varies, the mean values of derived lidar ra-

tio are relatively stable. At 1064 nm channel, the PLDR is very stable, varying in the  $4.0 \pm 0.6\%$  to  $5.0 \pm 0.8\%$  range. At 532 nm, the PLDR varies from  $18 \pm 3\%$  to  $20 \pm 3\%$ . The PLDR at 355 nm increased from  $23 \pm 3\%$  on 24 August, to  $28 \pm 8\%$  on 31 August. However, the increase is merely within the range of the uncertainties, thus making it difficult to conclude. The PLDR at 532 nm agrees well with CALIPSO observations in Figure 3.30(c)–(f). Haarig et al. [2018] and Ansmann et al. [2018] also observed the UTLS aerosol layers on 22 August 2017 and they measured 23.4%, 18.4% and 4.2% at 355 nm, 532 nm and 1064 nm. It is worthy to mention that this section is based on the study of Hu et al. [2019] (see the Appendix B). The error calculation is presented in detail in the paper and not repeated in this study.

Table 3.1. Optical depth, lidar ratio and particle depolarization ratio of smoke layers in the UTLS in Summer 2017. The values on the right of the symbol ‘ $\pm$ ’ represent the errors of the values on the left. The calculation of errors is presented in Hu et al. [2019].

Date	24 August	29 August		31 August	
Time (UTC)	2200 – 0030	1300 – 1600	1600 – 1800	2000 – 2300	2300 – 0200
$\tau_{355}^{smoke}$	$0.12 \pm 0.02$	$0.18 \pm 0.04$	$0.20 \pm 0.04$	$0.06 \pm 0.02$	$0.04 \pm 0.02$
$\tau_{532}^{smoke}$	$0.13 \pm 0.02$	$0.16 \pm 0.04$	$0.22 \pm 0.04$	$0.06 \pm 0.02$	$0.04 \pm 0.02$
LR <sub>355</sub> (sr)	$35 \pm 6$	$45 \pm 9$	$41 \pm 7$	$34 \pm 12$	$31 \pm 15$
LR <sub>532</sub> (sr)	$54 \pm 9$	$56 \pm 12$	$54 \pm 9$	$58 \pm 20$	$58 \pm 23$
PLDR <sub>355</sub> (%)	$23 \pm 3$	$24 \pm 4$	$24 \pm 4$	$28 \pm 8$	$28 \pm 8$
PLDR <sub>532</sub> (%)	$20 \pm 3$	$18 \pm 3$	$19 \pm 3$	$18 \pm 3$	$18 \pm 3$
PLDR <sub>1064</sub> (%)	$5.0 \pm 0.8$	$4.0 \pm 0.6$	$4.5 \pm 0.7$	$4.7 \pm 0.7$	$4.7 \pm 0.7$

Figure 3.32 shows the extinction and backscatter coefficients, PLDRs/VLDRs, the EAE and BAE obtained from averaged observations at 20:00–22:00 UTC, 31 August 2017. The extinction coefficients are calculated with the derived lidar ratios in Table 3.1. The backscatter coefficient from Klett and Raman inversion are both plotted and show very consistent results. The PLDR, EAE and BAE are vertically stable within the layer, i.e. 17–18.5 km, indicating that the aerosols are well mixed.

With the satellite measurements we are able to conclude that the smoke layers observed over northern France are transported from Canada through the UTLS. The smoke was elevated to the UTLS possibly by the pyro-cumulus clouds on 12 August 2017 over the British Columbia. The smoke plumes reported in this study have undergone more than

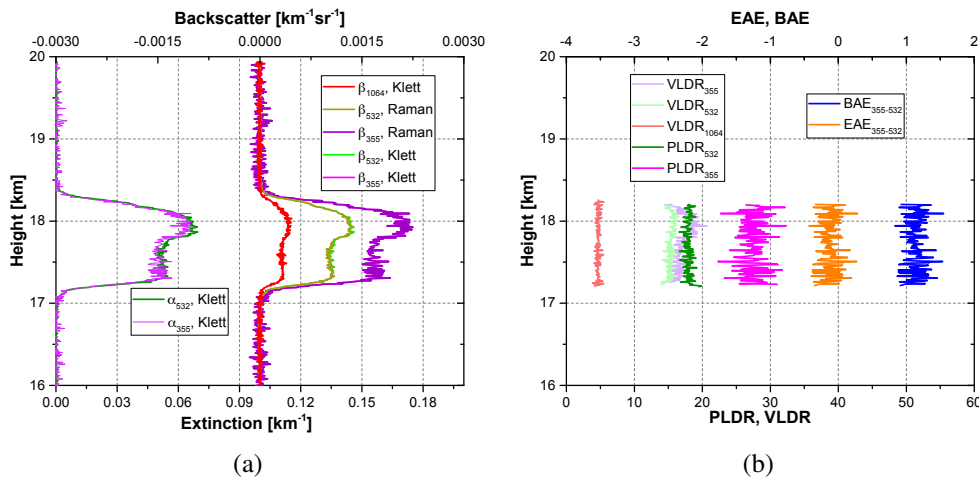


Figure 3.32. Lidar inversions at 20:00–22:00 UTC, 31 August 2017, Lille. (a) Extinction and backscatter coefficient, (b) PLDR, BAE and EAE.

10-day aging before being observed by LILAS, considering they were emitted on 12 August. During the transport, the plumes are not likely to mix with many other aerosol types due to the high altitude. The observed plumes are probably aged smoke particles because the high altitude prevented them from mixing with other aerosols during the transport, but mixing with other aerosols in the ascending and combustion process is also possible.

The measured high PLDRs are very rare compared with other smoke observations in the troposphere. Burton et al. [2015] presented similar spectral dependence of PLDRs for smoke aerosols: 20%, 9% and 2% at 355, 532 and 1064 nm, respectively. The causes of high PLDRs of smoke particles are not yet well understood. Previous studies suggest that soil particles mixing in smoke are an explanation, as strong convection has the potential to lift soil particles into smoke plumes [Fiebig et al., 2002, Murayama et al., 2004, Müller et al., 2007, Sugimoto et al., 2010, Burton et al., 2012, Haarig et al., 2018]. The particle coagulation also seems to be a reasonable explanation when there is no evident proof showing the presence of soil particles. Murayama et al. [2004] presented that no signature of mineral dust was found in the analysis of chemical compositions of the smoke samples. Mishchenko et al. [2016] tried to model the spectral depolarization ratios in Burton et al. [2015] and found that such behavior is resulted from complicated morphology of smoke particles. This study of Kahnert et al. [2012] achieved PLDRs of 12–20% at 304.0 nm, 8.0–18% at 533.1 nm and about 1.5% at 1010.1 nm, when modeling the optical properties

of light-absorbing carbon aggregates. Although the results are comparable, the discrepancy still cannot be neglected. At this stage, the inclusion of soil particle in the smoke plume still cannot be precluded.

Tropospheric smoke was observed simultaneously with the stratospheric smoke in the night between 31 August and 01 September. Unlike the stratospheric smoke, the PLDR is less than 10% at 355, 532 and 1064 nm. Figure 3.33 presents the retrieved optical properties averaged between 20:00 UTC, 31 August and 02:00 UTC, 01 September. The layer is optically thin, with maximal extinction coefficient of  $0.03 \text{ km}^{-1}$ . No noticeable spectral dependence is observed for the extinction coefficient, but the spectral dependence of backscatter coefficient is significant. The spectral dependence of the particle depolarization ratio is the same as in the stratosphere, whereas, the amplitude is much reduced. The PLDRs at 355, 532 and 1064 nm are 8–10%, 4–6% and 1%, respectively. The lidar ratio of the smoke layer is about 25–35 sr at 355 nm and 80–100 sr at 532 nm. Regularization [Müller et al., 1999, Veselovskii et al., 2002] method is applied to retrieve the particle microphysical properties using the  $2\alpha+3\beta$  dataset shown in Figure 3.32 and Figure 3.33. The retrieved properties are summarized in Table 3.2. The effective radius  $R_{eff}$  in the stratospheric layer is gently larger than in the tropospheric layer. The real part of the refractive indices is consistent in the tropospheric and stratospheric smoke layer. The imaginary part in the stratospheric layer is higher than in the troposphere but due to the uncertainty of the retrieval, they still overlap. The uncertainty of regularization algorithm has been discussed in Pérez-Ramírez et al. [2013] and is not introduced in this study. Here we take  $\pm 30\%$  relative uncertainty for the effective radius and volume concentration,  $\pm 50\%$  for the imaginary part of the refractive indices,  $\pm 0.05$  (absolute) for the real part of the refractive indices.

The distinct optical and microphysical properties of the tropospheric and stratospheric smoke layers are not yet fully understood. The two smoke layers are possibly from very similar source but underwent different aging process. The relative humidity in the tropospheric smoke layer is about 60% while in the stratospheric smoke layer, the relative humidity is less than 10%, according to the radiosonde measurements in Beauvechain (120 km to Lille) at 00:00 UTC, 01 September 2017. Moreover, the tropospheric smoke is more possible to mix with other aerosols during the transport. The transport time, as

well as transport environment, is also a potential factor that impacts the smoke particles during the aging process. To reveal the aging process of smoke particles is a complex study and requires not only remote sensing measurements but also in-situ and laboratory measurement.

Table 3.2. Optical depth, LR and PLDR of smoke layers in the UTLS in Summer 2017

Date	Stratospheric layer	Tropospheric layer
$R_{eff}$	$0.33 \pm 0.10$	$0.27 \pm 0.10$
$V_c [\mu m^{-3} cm^3]$	$6.4 \pm 2.1$	$2.6 \pm 0.8$
$m_R$	$1.52 \pm 0.05$	$1.50 \pm 0.05$
$m_I$	$0.020 \pm 0.010$	$0.010 \pm 0.005$

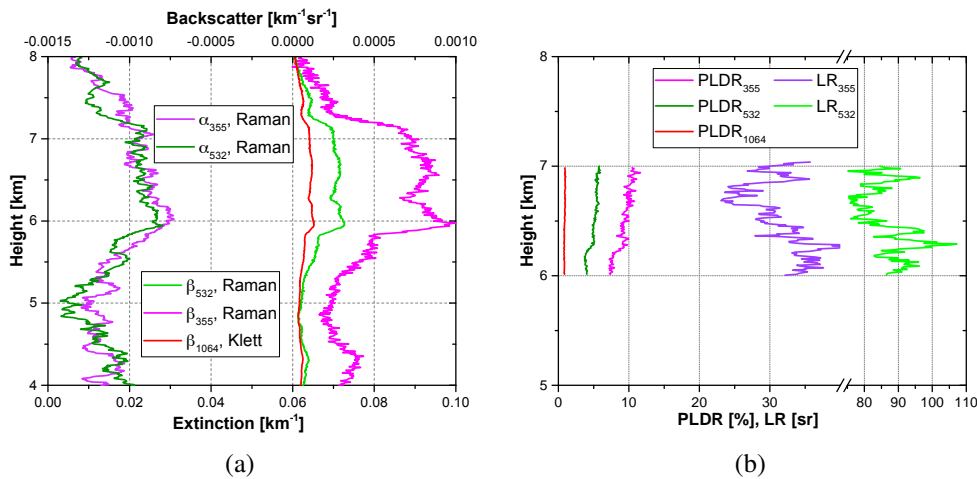


Figure 3.33. Lidar inversions at 20:00–02:00 UTC, 31 August–01 September 2017, Lille. (a) Extinction and backscatter coefficient, (b) PLDR and LR.

## 3.4 Dust and smoke mixture observed in Senegal and Lille

### 20 January 2016, M'bour

Biomass burning aerosols are widely emitted in the dry season of West Africa. During the SHADOW2 campaign, several smoke episodes have been observed and recorded. On 19–20 January 2016, LILAS observed a transported layer over the planet boundary layer.

Figure 3.34 shows the backscatter and extinction coefficients, PLDR at 532 nm and the WVMR. The colormaps show the transported layer is situated at 3500–5500 m, where the WVMR increases. The boundary layer is 2500–3000 m high and well mixed, as the WVMR profile is homogeneous inside the boundary layer. The PLDR in the boundary layer and the transported layer show distinct values: 30–35% in the boundary layer and 15% at 532nm in the transported layer. However, in the transported layer the PLDRs are slightly higher than biomass burning aerosols usually observed in the troposphere, for example in Section 3.3. One possible explanation is the presence of dust which is a persistent component in the atmosphere at M’Bour.

Observations averaged at 01:20–05:00 UTC are processed and the results are plotted in Figure 3.35. In the transported layer, the WVMR is about 2.5–3.5 g/kg and the relative humidity is 50–80%. The lidar ratio varies in 60–75 sr range at 532 nm and in 75–90 sr at 355 nm. The PLDR varies in 15–18% range and shows no spectral dependence between 355 and 532 nm. The EAE is about 0.8–1.2 and the BAE varies in the range of 0.3–0.6. In the boundary layer the WVMR is about 2.0 g/kg and the relative humidity is less than 50%. The PLDR is 28–30% at 355 nm and 30–35% at 532 nm. The lidar ratio is 60–75 sr at 355 nm and 55–65 sr at 532 nm. The EAE in the boundary layer is about -0.1 and the BAE is -0.4–0.0. The vertical gradient of the lidar ratio, BAE, and PLDR indicates the vertical changes of the fractions of dust and smoke aerosols.

Figure 3.36 shows the 168-hour back trajectory for the air mass at 1000 m, 2000 m and 3500 m. The true color image is taken from MODIS product and it is overlaid with the fire and thermal anomalies detected by MODIS on 18–19 January 2016. Widely spread fire activities are detected from West Africa to Central Africa. The observed smoke at 3500 m is possibly from the neighbor countries such as: Guinea, Guinea-Bissau, south-west of Mali and the northwest of Côte d’Ivoire. The air mass was transported at relatively lower altitude, 1000–2000 m, which makes it more likely to mix with smoke. The air mass at 1000 m also passed over the area with intense fire activities whereas, it was transported at much higher altitude, 2000–5000 m, which might reduce the possibility of mixing with smoke.

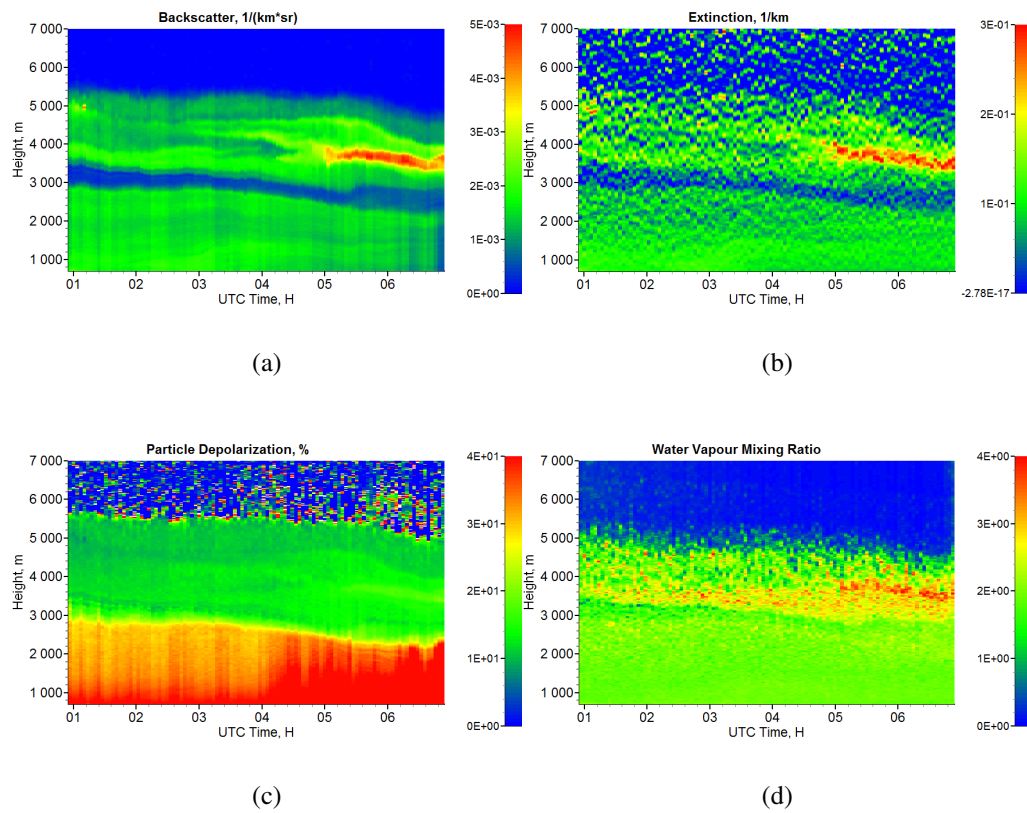


Figure 3.34. Lidar observations on 20 January 2016, M'bour. (a) Backscatter coefficient at 532 nm, (b) extinction coefficient and 532 nm, (c) PLDR at 532 nm and (d) WVMR (g/kg).

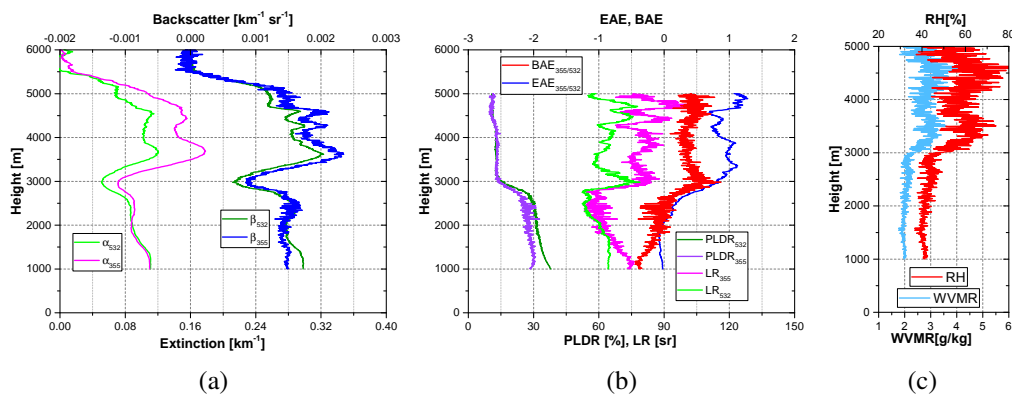


Figure 3.35. Averaged lidar observations between 01:20 and 05:00 UTC, 20 January 2016. (a) Extinction and backscatter coefficient, (b) PLDR, LR, BAE and EAE, (c) WVMR and RH.

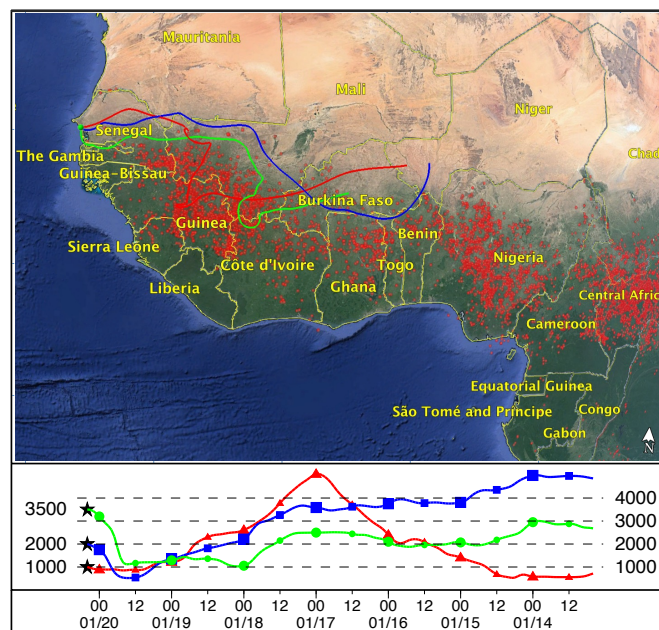


Figure 3.36. 168-hour back trajectory at 04:00 UTC, 20 January 2016. Fire and thermal anomaly maps on 18–19 January are overlaid.

### 16–18 October 2017, Lille

On 16–17 October 2017, unprecedented smoke aerosol layers were detected over Lille and AOD measured at 440 nm exceeded 3.0. Figure 3.37(a) shows a photo taken at 09:00 UTC in the morning of 17 October 2017. In the photo, the sky and the sun present a yellowish color. The AOD at 440 nm and AE between 440 and 870 nm are plotted in Figure 3.37(b). The AOD at 440 changes dramatically during 16 to 19 October with the minimum of 0.2 and maximum of 2.9. The AE varies from 0.3 to 1.3 during the same period. The maximal AOD was reached in the morning of 17 October, with AE about 1.2. The smoke aerosols are originated from the intense fire activities occurred in the west of Spain and Portugal on 15 and 16 October 2017. Figure 3.38 shows the true color image overlaid with fire and thermal anomalies detected on 15 and 16 October. The emitted smoke aerosols were carried by the cyclone to the north and east. Figure 3.39 presents

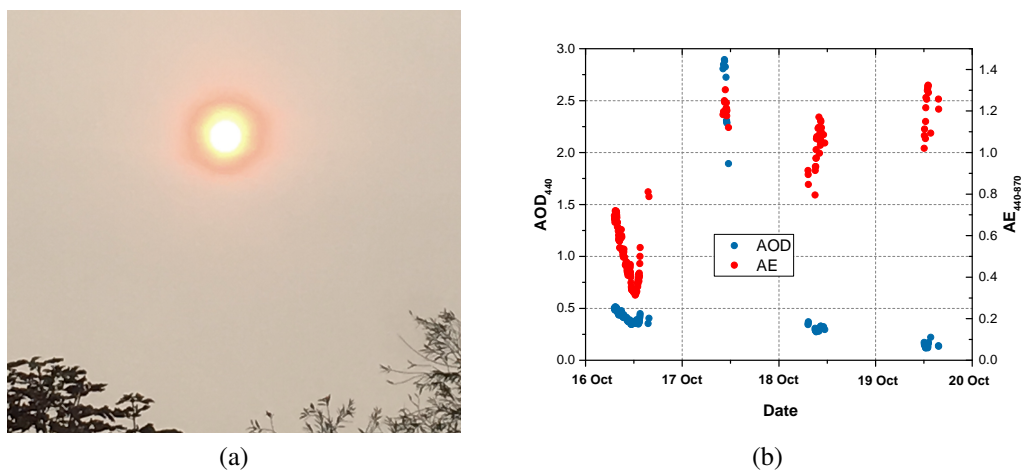


Figure 3.37. Observations on 15–18 October 2017. (a) A photo of the sun and sky observed at about 09:00 UTC, 17 October, (b) AOD and Angström exponent on 15–18 October 2017.

the CO plumes during 16–22 October. The CO plumes first appeared on 16 October in the west of Spain. The intensity of the CO plume is high but the spatial distribution is very limited. On 17 October, the CO plume has developed and spread to France, Netherland, Germany, northern and eastern Europe. On 18 and 19 October, the CO plume moved eastwardly and reached the region close to the Black Sea and Caspian Sea. On 20 and 21 October, the intensity and the coverage of the CO plumes decreased, but smaller areas with strong CO concentration can be seen in the surrounding area of the Black Sea and

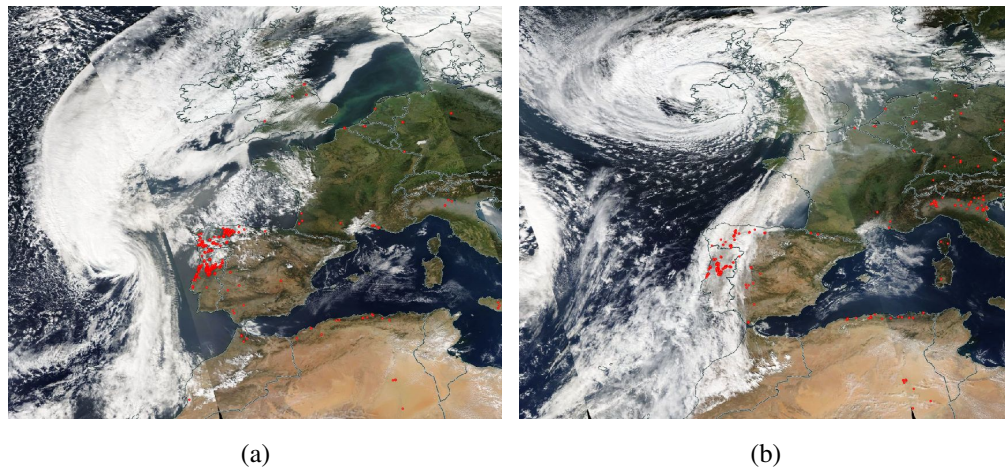


Figure 3.38. True color image overlaid with fire and thermal anomalies from MODIS on 15, 16 October 2017. (a) 15 October 2017, (b) 16 October 2017.

the Caspian Sea.

Transported Saharan dust has been observed over Lille by LILAS system since 14 October 2017. The smoke aerosols transported from Spain and Portugal arrived in the evening of 16 October, before the dust episode ended. The arrival of smoke caused the AOD at 440 nm to increase from about 0.4 in the afternoon of 16 October to about 2.9 in the morning of 17 October. The two aerosol components, dust and smoke, mixed in the atmosphere and formed very complex stratification during the night of 16–17 October. The range corrected lidar signal and volume linear depolarization ratio at 1064 nm on 16–17 October are shown in Figure 3.40(a) and (b), respectively. The layer spreading from 2000 m up to 6000 m at 20:00–22:00 UTC is mostly composed of dust particles, as the PLDR is much higher than other air mass when the range corrected lidar signal is comparable. The layers that appear at 2000–4000 m and 6000–8000 m are smoke aerosols as VLDR is as low as a few percent. The aerosol concentration started to decrease from the afternoon of 17 October due to the transport of smoke plumes. In the night of 17–18 October, LILAS observed an atmospheric stratification with smoke in the lower boundary layer and dust in the upper boundary layer. Figure 3.40(c) and (d) display the range corrected lidar signal and volume depolarization ratio at 1064 nm, respectively.

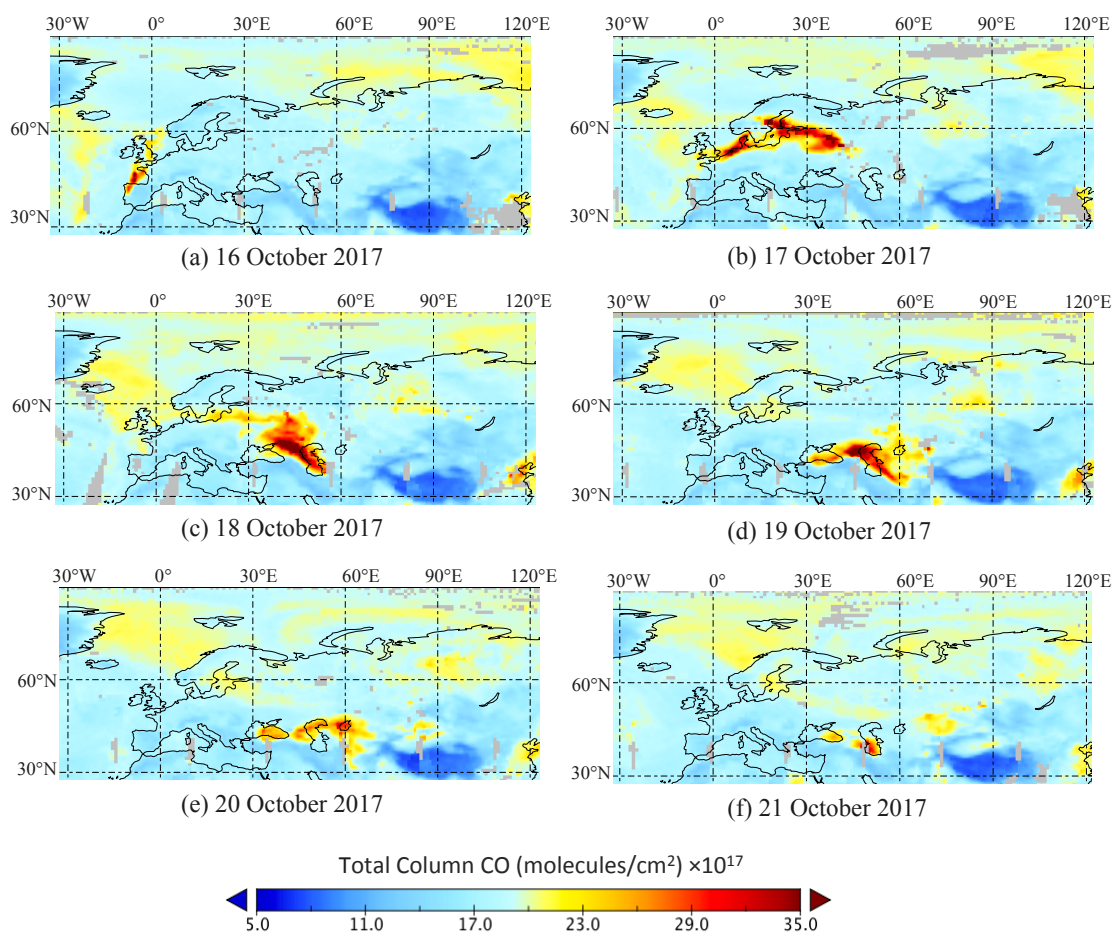


Figure 3.39. Columnar CO concentration from AIRS on 16–21 October 2017

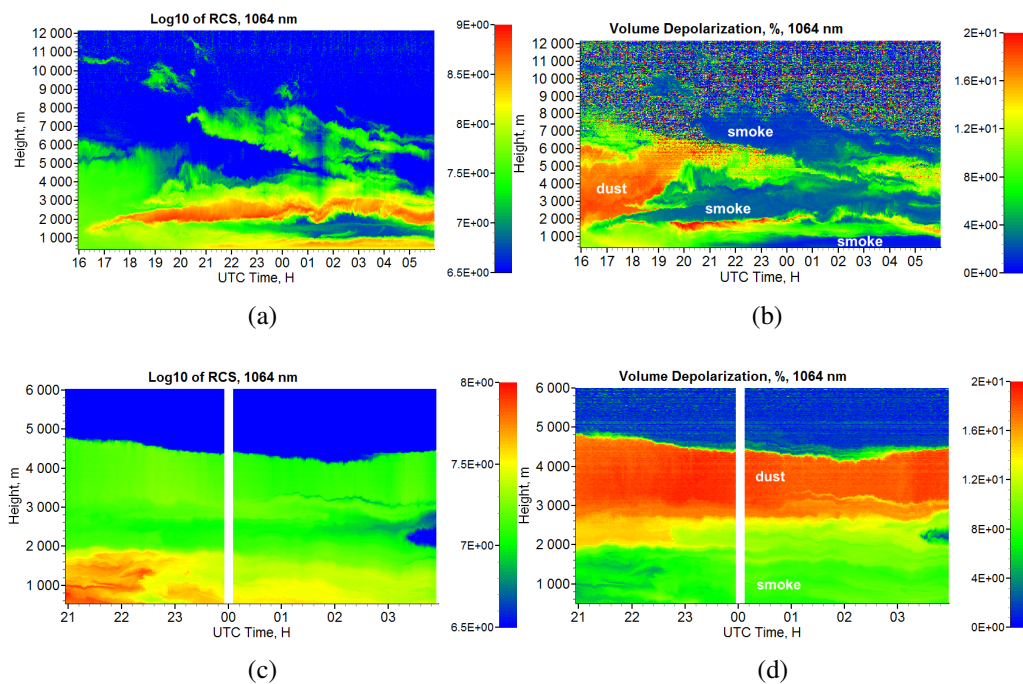


Figure 3.40. Lidar observation on 16, 17 and 18 October 2017, Lille. (a) Lidar signal at 1064 nm, 16–17 October, (b) VLDR at 1064 nm, 16–17 October, (c) Lidar signal at 1064 nm, 17–18 October, (d) VLDR at 1064 nm, 17–18 October.

Aerosol optical properties retrieved from averaged lidar observations at 21:00–24:00 UTC, 17 October are plotted in Figure 3.41. The layer between 1500 m and 3500 m is characterized by high PLDRs, greater than 20%, and relatively lower concentration. In 2400–3200 m range, the particle linear depolarization ratios are 26% at 355 and 532 nm and 22% at 1064 nm. This spectral dependence of PLDR has been observed in transported Saharan dust over Lille. It indicates that the aerosols within 2400–3200 m are transported dust. Very weak spectral dependence is observed in the extinction and backscatter coefficients at 355 nm and 532 nm. The lidar ratio is about  $50 \pm 5$  sr at 355 and 532 nm, which is also consistent with the dust observation on 10–11 March 2017.

From 2400 m to 1200 m, the values of PLDRs, as well as the spectral dependence decrease as altitude decreases. The EAE and BAE increases as altitude decreases. Lidar ratio is about  $45 \pm 5$  sr at 355 nm and  $56 \pm 5$  sr in this range. Below 1200 m, the depolarization ratios at three wavelengths are around 8%, with negligible spectral dependence. The EAE and BAE are over 1.0. It indicates that below 1200 m particles are mostly smaller and spherical.

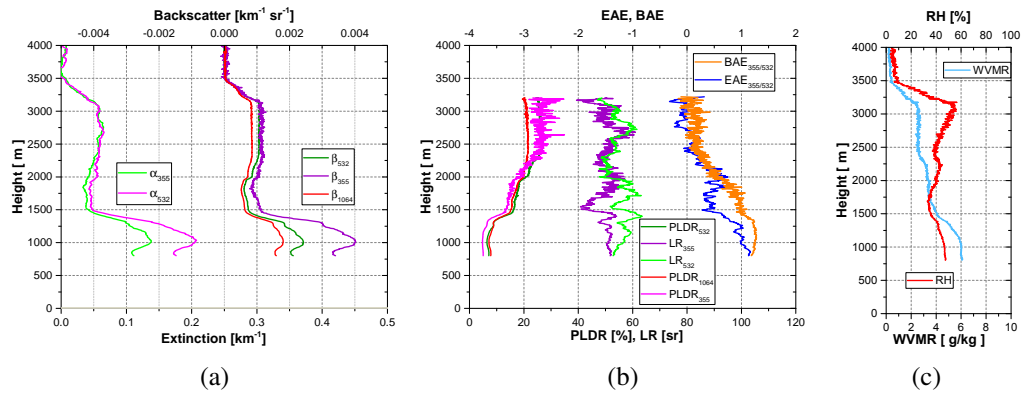


Figure 3.41. Averaged lidar observation at 21:00–24:00 UTC, 17 October 2017, Lille. (a) Extinction and backscatter coefficient, (b) PLDRs, LR, EAE and BAE, (c) WVMR and RH.

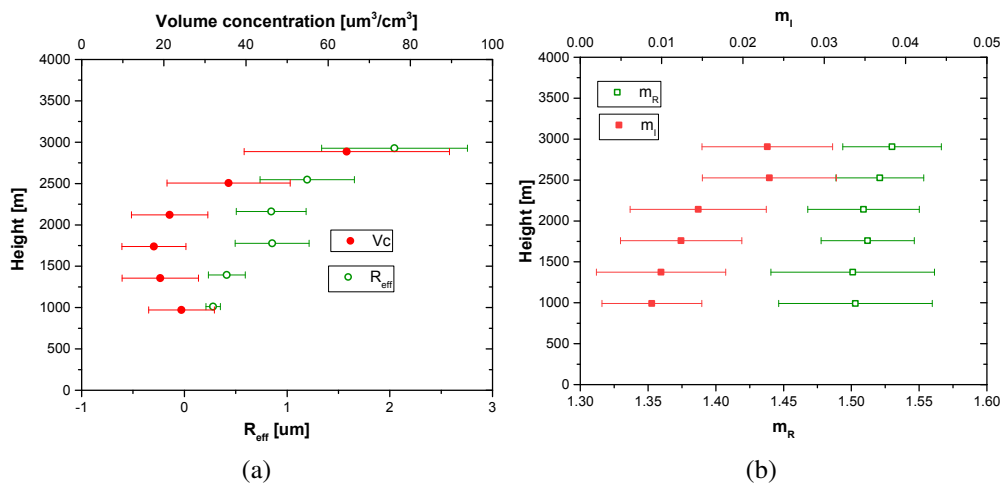


Figure 3.42. Retrieved  $R_{\text{eff}}$ , volume concentration and complex refractive indices, 17 October 2017. (a) Volume concentration and effective radius ( $R_{\text{eff}}$ ), (b) complex refractive indices. The error bars represent the standard deviation of all the solutions found by regularization.

Figure 3.42 presents the volume concentration, effective radius, and complex refractive indices retrieved using regularization algorithm. The effective radius decreases from about  $2 \mu\text{m}$  to  $0.25 \mu\text{m}$  as height decreases from 2800 m to 1000 m. The particle volume concentration peaks at about 2800 m. The real part of retrieved refractive indices is about 1.45–1.55, decreases gently with height. The imaginary part also decreases with height, with 0.022 at 1800 m and 0.01 at 1000 m. Considering that dust absorption is highly variable, such value for imaginary part still falls into the acceptable range. Also the observed dust is possibly polluted by smoke or has mixed with other aerosol types during the transport. One limitation of regularization retrieval is the assumption of wavelength-independent complex refractive indices, it could cause a certain level of errors.

Compared with the Canadian smoke observed in the troposphere, the retrieved complex refractive indices are rather comparable. But the spectral dependence of extinction and PLDR are very different. The Canadian smoke shows no spectral dependence in the extinction coefficient, while in this case, the EAE is about 1.0 in the lower layer. PLDR decreases as wavelength increases in the Canadian tropospheric smoke, while in this study the spectral dependency of PLDR is almost negligible in the lower layer. As both dust and smoke are present at the same time in this case, it is quite possible that the two components mix in the atmosphere but the mixing ratio varies at different altitude. The spectral dependency of depolarization in the lower layer agree well with the transported layer observed on 20 January, where aerosols are proved to be dust and smoke mixtures by airborne in-situ measurements. Whereas, the lidar ratios observed on 17 October is lower than that on 20 January 2016, M’ Bour. Although both cases are dust-smoke mixture, there are still these variables that need to be carefully considered:

- Dust properties: dust near the source shows distinct properties with long-transported dust
- Smoke properties: smoke aerosols from different origins and combustion process are possibly different in particle microphysics
- Smoke aging process: travel time and environmental conditions during the transport

### 3.5 Chapter summary

This chapter includes lidar observations and analysis about cirrus, dust and smoke, as well as dust-smoke mixtures. The objective of this chapter is to provide optical and micro-physical characterizations for the observed cloud and aerosol particles. The backscatter coefficient and particle linear depolarization ratio at three wavelength are presented for ice cloud particles. Wavelength-independent backscattering and particle depolarization ratio are found for cirrus. Super-cooled liquid water cloud is observed at temperatures of  $-25 - -38^{\circ}\text{C}$ . And a clear ice formation process is observed below this super-cooled liquid water cloud. This research could be continued for the study of aerosol-cloud interaction and more observations are required to broaden and deepen the current stage of study.

Saharan dust measurements collected in SHADOW2 campaign are presents. The observations reveal that Saharan dust has the following characteristics:

- Extinction Angström exponent, close to 0.0
- Low relative humidity, usually less than 40%
- Particle linear depolarization ratio of 30–35% at 532 nm and 24–28% at 355 nm.

The measurements show that the dust lidar ratio at 355 nm observed in 15–24 April tends to be steadily 15–25% lower than in December 2015 and January 2016. Correspondingly, the BAE is higher than in December 2015 and January 2016. Similar features are detected in some days of March 2015. Moreover, the AERONET retrieved SSAs reveal that aerosols during the period from mid-April or May to October is less absorbing at 440 nm than in the other months. The decrease of aerosol absorption after mid-April in the shortwave is likely responsible for the decrease of lidar ratio at 355 nm and the increase of BAE. This phenomenon is possibly related to the intrusion of maritime aerosols coming from eastern and North-eastern Atlantic. The day-by-day (at 00:00 UTC) trajectory shows that the meteorological conditions in March and April could promote the occurrence of maritime aerosols that 'diminish' the absorption of dust, whereas in December 2015 and January 2016, the dust has less chance to mix with air mass from the ocean. This conclusion is also supported by the atmospheric circulation changes brought by the northward advance of the ITCZ in West Africa.

Characteristics of long-range transported Saharan dust are presented. PLDRs at 3 wave-

lengths are: 25–28% at 355 and 532 nm and 17–21% at 1064 nm. The spectral dependence of extinction and backscatter coefficient, as well as lidar ratio is negligible. Dust deposition during the transport is expected to be one of the possible explanations for the observed spectral dependence of PLDRs. The inversion using  $2\alpha+3\beta$  dataset reveals the absence of very big particles compared with the distribution obtained for the dust in Africa. Long-range transported Canadian smoke was observed in August and September 2017. Using satellite measurements, the origin and transport pathway of the Canadian smoke are revealed. The highlight of the observation is the pronounced PLDR of stratospheric smoke in comparison with the low PLDR of the tropospheric smoke. The PLDRs at 355, 532 and 1064 nm are: 23–28%, 18–20%, 5% for the stratospheric smoke and 8–10%, 4–6% and 1% for the tropospheric smoke. The distinct optical and microphysical properties of the tropospheric and stratospheric smoke indicates the impact of smoke aging process on the particle morphology and microphysics.

Two event related to dust and smoke mixtures are presented. The observations show some common features of dust and smoke mixture: moderate and wavelength-independent depolarization ratios. Whereas, differences are observed in the lidar ratios. For example,  $65\pm 5$  sr at 532 nm and  $80\pm 10$  sr at 355 nm are obtained in the observation in M’ Bour, while in the observations in Lille,  $45\pm 5$  sr at 355 nm and  $56\pm 5$  at 532 nm are measured. The disagreements are expectable given that dust and smoke properties change during the transport, and smoke from different origins show different properties [Dubovik et al., 2002a].

This chapter provides very rich examples for aerosol characterization using multi-wavelength Mie-Raman lidar measurements. The results are also expected to contribute to aerosol profiling, classification as well as the aerosol radiative effect. In future work, some observations could be used to constrain models or verify model products.



## Chapter 4

# Lidar and photometer joint retrieval: GARRLiC/GRASP

*“Where there is no vision, there is no hope.”*

– George Washington

The chapter presents the **Generalized Aerosol Retrieval from Radiometer and Lidar Combined** data (GARRLiC). GARRLiC algorithm is a branch of the **Generalized Retrieval of Aerosol and Surface Properties** (GRASP), which is the first unified algorithm developed for characterizing atmospheric properties gathered from a variety of remote sensing observations [Dubovik et al., 2014]. Hence, GARRLiC is hereafter called as GARRLiC/GRASP in this study. GARRLiC/GRASP is based on the AERONET inversion algorithm. The objective of GARRLiC/GRASP is to retrieve both column-integrated aerosol parameters and vertically resolved parameters, by combining sun/sky photometer measurements and multi-wavelength lidar observations [Lopatin et al., 2013]. This chapter firstly introduces the methodology of GARRLiC/GRASP retrieval which is based on the previous studies [Dubovik and King, 2000, Dubovik et al., 2006, Lopatin et al., 2013, Dubovik et al., 2014].

The sensitivity tests and applications of GARRLiC/GRASP algorithm, with the use of sun/sky photometer measurements and multi-wavelength elastically backscattered lidar signals, have been well discussed by Lopatin et al. [2013]. The development of lidar technique enables the measurement of aerosol depolarization ratio at multiple wavelengths. The depolarization ratio is a useful parameter for characterizing the particle shape and

will bring new information into GARRLiC/GRASP retrieval. The volume linear depolarization ratio is included into GARRLiC/GRASP retrieval in this chapter. Four groups of sensitivity tests are performed to investigate the performance of GARRLiC/GRASP under different aerosol loadings, with varying fractions of spherical particles, with different error levels of molecular depolarization ratio and calibration coefficient. At last, real measurements are inverted using GARRLiC/GRASP to test the functionality of the algorithm. And the validation of GARRLiC retrieval is performed by comparing the GARRLiC/GRASP retrievals with simultaneous Raman lidar inversions, as well as AERONET inversions.

## 4.1 GARRLiC/GRASP algorithm

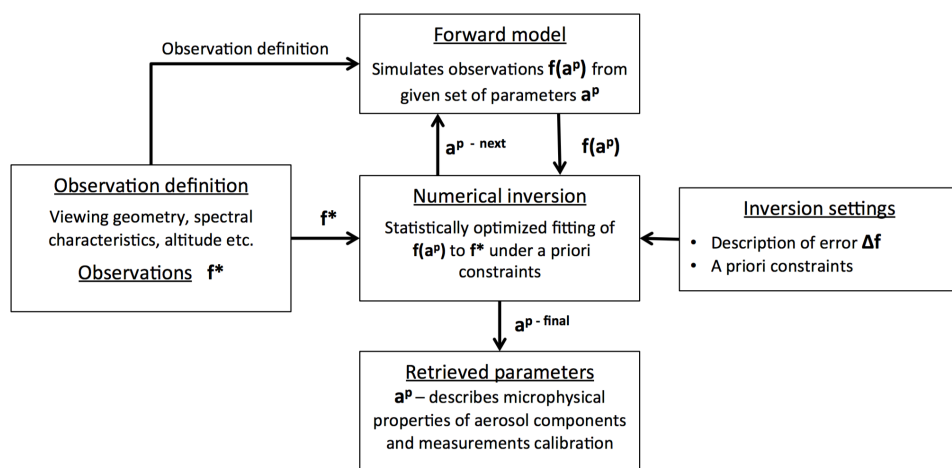


Figure 4.1. The principle scheme of GARRLiC/GRASP algorithm [Lopatin, 2013].

Figure 4.1 shows the principle scheme of GARRLiC/GRASP algorithm. The two modules: forward model and numerical inversion are the core of GARRLiC/GRASP algorithm. The forward model simulates the quantities of radiation and polarization measurements of a variety of remote sensing instruments based on the interaction of incident light with atmospheric gases, aerosols and the underlying surfaces [Dubovik et al., 2014]. The forward model is driven by the given properties of atmospheric aerosols, gases as well as underlying surfaces. The numerical inversion module retrieves the unknown parameters by fitting the (measured or simulated) observations following the multi-term least square

method strategy. GARRLiC/GRASP is a flexible algorithm and is applicable to different system configurations depending on the type and spectrum of the observations.

### 4.1.1 Forward model

Table 4.1 summarizes the sun/sky photometer and lidar observations that can be simulated by GARRLiC/GRASP. The typical sun/sky photometer observations inverted by GARRLiC/GRASP are the total/aerosol optical depth, angular sky radiances measurements at 440, 675, 870 and 1020 nm. The angular sky radiance measurements are performed in up to 35 directions [Holben et al., 1998]. More wavelengths could be included into GARRLiC/GRASP retrieval if the measurements are available at such wavelengths. For example, AOD measurements at 340, 380 and 1640 nm are measured according the protocol of the standard Cimel sun/sky photometer and could be added into GARRLiC/GRASP algorithm. Additionally, photometer polarization measurements can also be simulated by the forward model. At current stage, GARRLiC/GRASP retrieval using polarized sky radiance measurements are not yet performed but will be tested in future work. The attenu-

Table 4.1. The simulated observation of the GARRLiC/GRASP forward model.

<b>Sun/sky photometer measurements</b>	
$\tau(\lambda)$	The total/aerosol optical thickness at wavelength $\lambda$
$I(\Theta, \lambda)$	Sky radiances at scattering angle $\Theta$ and wavelength $\lambda$
<b>Lidar measurements</b>	
$L_{\parallel, \perp, tot}(h, \lambda)$	Lidar vertical profile of the backscattered elastic signal $h_m$ is the discrete altitude; $\parallel$ , $\perp$ and $tot$ represent the parallel-, cross-polarized signal and total signal
$\delta_v(h, \lambda)$	The vertical profile of the volume depolarization ratio $\delta_v = C^* \frac{L_{\perp}(h, \lambda)}{L_{\parallel}(h, \lambda)}$ , $C^*$ is the calibration coefficient

ated backscattered lidar signal, volume depolarization ratio measurements at elastic channels: 355, 532 and 1064 nm can be simulated. The number of the lidar wavelengths and the measurement types are optional and dependent on the system configuration. GARRLiC/GRASP is able to simulate the parallel-, cross-polarized lidar signal as well as the total signal. A calibration coefficient is required to account for the ratio of the optical-electro gain of the parallel- and cross-polarized lidar signal. The calibration procedure

is an extra procedure that needed to be performed each time when the electrical or optical gain of the coupled parallel- and cross-polarized channel is changed. The calibration procedure has been introduced in Chapter 2. In this study, we choose to simulate and invert the volume linear depolarization ratio instead of the two polarized lidar signals. The volume linear depolarization ratio is a function of the particle linear depolarization ratio, molecular depolarization ratio and the backscattering ratio. Compared with the particle linear depolarization ratio, the volume linear depolarization ratio suffers from less random noise which appears in low aerosol-laden region and is easy to compute because it is a ratio of the cross-polarized lidar signal to the parallel-polarized signal multiplied by the calibration coefficient.

Table 4.2 summarizes the aerosol microphysical parameters that drive the forward model.

Table 4.2. Aerosol microphysical parameters in GARRLiC/GRASP

$\frac{dV(r_j)}{dlnr_j}$	Volume size distribution, $r_j$ represents the $j$ -th size bin, $j = 1, \dots, N_r^k$ ; $k=1, 2$ , is the index of the aerosol components
$c^k(h_i)$	The concentration of the $k$ -th aerosol component at altitude $h_i, i = 1, \dots, N_h$ . The integral of $c_k(h_i)$ is normalized to 1
$C_{sph}^k$	The fraction of spheres in the $k$ -th aerosol component
$n^k(\lambda)$	The real part of the refractive indices for the $k$ -th aerosol component at the wavelength $\lambda$
$\kappa^k(\lambda)$	The imaginary part of the refractive indices for the $k$ -th aerosol component at the wavelength $\lambda$

The interaction between light and aerosol particles is based on the assumption of single scattering. As GARRLiC/GRASP inherits the scattering model from AERONET inversion, in which the aerosol single scattering properties in GARRLiC/GRASP are also modeled by a mixture of spheres and spheroids [Dubovik and King, 2000, Dubovik et al., 2002b, 2006]. Unlike the AERONET inversion which allows only one aerosol component, GARRLiC/GRASP assumes 1–2 aerosol components. When  $k = 2$ , the two components are characterized with two different size ranges, namely a fine mode and a coarse mode with two independent groups of complex refractive indices. Ground-based lidar usually cannot cover the whole column of the atmosphere because of the overlap in the near range and the insufficient signal-to-noise ratio in the far range where aerosol concentration is very low. The aerosol vertical concentration in the upper and lower limit of

lidar measurements, namely  $h_{min}$  and  $h_{max}$  respectively, are discretized into  $N_h$  levels. Aerosols above  $h_{max}$  are omitted and between  $h_{min}$  and the ground level, aerosol vertical concentration is assumed to be the vertically constant. The basic assumptions that link the columnar and vertical aerosol properties are:

- The aerosols throughout the atmosphere consist of  $k=1,2$  aerosol component(s) with independent microphysical properties characterized by  $C_{sph}^k$ ,  $\frac{dV(r_j)}{dlnr_j}$ ,  $n^k(\lambda)$  and  $\kappa^k(\lambda)$ .
- The concentration of the aerosol component(s),  $c^k(h_i)$ , can vary as a function of altitude but their properties do not change.

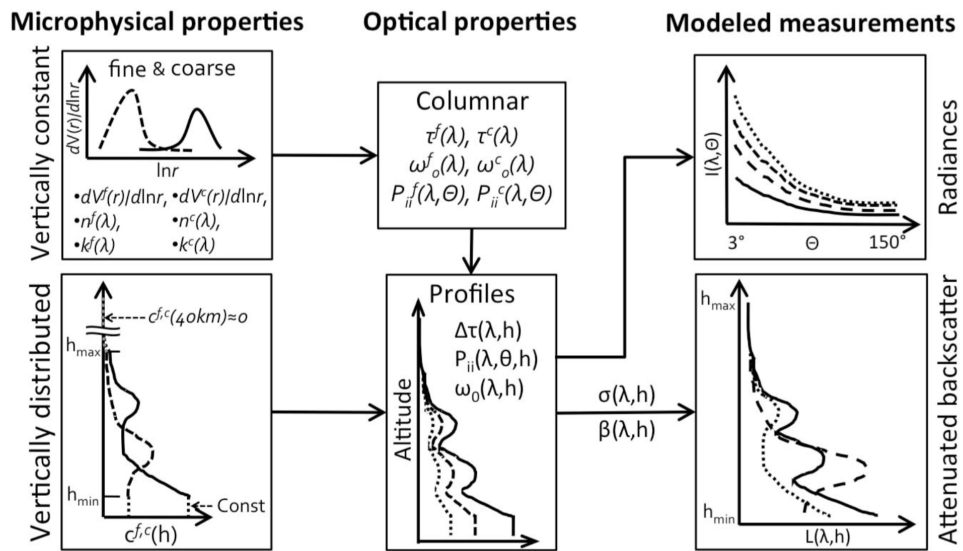


Figure 4.2. The concept of GARRLiC/GRASP forward model [Lopatin, 2013]

Figure 4.2 depicts the concept of GARRLiC/GRASP forward model. The columnar optical properties are reproduced by the particle scattering model using the particle distribution and complex refractive. Here we introduce briefly the formulas of the key optical quantities derived from the scattering model, more detailed information can be found in the publications [Dubovik and King, 2000, Dubovik et al., 2002b, 2006, Lopatin, 2013, Lopatin et al., 2013]. The relationship of sun/sky radiance measurements and each aerosol

component is expressed as follows:

$$\begin{aligned} \tau_{sca}^k(\lambda) P_{mn}^k(\lambda, \Theta) = \\ \sum_{j=1, \dots, N_r^k} \frac{dV(r_j)}{d \ln r_j} \{ C_{sph}^{jk} K_{mn}^{sph}(\lambda, \Theta, \kappa, n, r_j) + (1 - C_{sph}^{jk}) K_{mn}^{ns}(\lambda, \Theta, \kappa, n, r_j) \} \end{aligned} \quad (4.1)$$

and

$$\begin{aligned} \tau_{ext/sca}^k(\lambda) = \\ \sum_{j=1, \dots, N_r^k} \frac{dV(r_j)}{d \ln r_j} \{ C_{sph}^{jk} K_{ext/sca}^{sph}(\lambda, \kappa, n, r_j) + (1 - C_{sph}^{jk}) K_{ext/sca}^{ns}(\lambda, \kappa, n, r_j) \} \end{aligned} \quad (4.2)$$

where  $\tau_{ext}$  and  $\tau_{sca}$  represent the columnar extinction and scattering optical depth,  $k$  is the index of the aerosol component,  $P_{mn}(\lambda, \Theta)$  is the element of the scattering matrix,  $N_r$  is the number of size bins. The kernel matrices  $K_{mn}^{sph/ns}(\lambda, \Theta, \kappa, n, r_j)$ ,  $K_{ext}^{sph/ns}(\lambda, \kappa, n, r_j)$  and  $K_{sca}^{sph/ns}(\lambda, \kappa, n, r_j)$  are precomputed at corresponding particle size, shape and complex refractive indices. The simulation of sun/sky radiances is performed by the full radiative transfer equations in the plane parallel approximation using vertically dependent optical characteristics of the atmosphere [Lopatin et al., 2013]. The characteristics of each atmospheric layer are expressed as follows:

$$\Delta \tau_i^{aer,k}(\lambda) = \tau^{aer,k}(\lambda) \int_{h_i}^{h_{i+1}} c^k(h) dh \quad (4.3)$$

$$\Delta \tau_i^{tot}(\lambda) = \Delta \tau_i^{gas}(\lambda) + \Delta \tau_i^{mol}(\lambda) + \sum_{k=1,2} \Delta \tau_i^{aer,k}(\lambda) \quad (4.4)$$

$$\omega_0^i(\lambda) = \frac{\Delta \tau_i^{mol}(\lambda) + \sum_{k=1,2} \Delta \tau_i^{aer,k}(\lambda) \omega_0^k(\lambda)}{\Delta \tau_i^{gas}(\lambda) + \Delta \tau_i^{mol}(\lambda) + \sum_{k=1,2} \Delta \tau_i^{aer,k}(\lambda)} \quad (4.5)$$

$$P_{mn}^i(\Theta, \lambda) = \frac{\Delta \tau_i^{mol}(\lambda) P_{mn}^{mol}(\Theta, \lambda) + \sum_{k=1,2} \Delta \tau_i^{aer,k}(\lambda) \omega_0^k(\lambda) P_{mn}^{aer,k}(\Theta, \lambda)}{\Delta \tau_i^{mol}(\lambda) + \sum_{k=1,2} \Delta \tau_i^{aer,k}(\lambda) \omega_0^k(\lambda)} \quad (4.6)$$

where  $\Delta\tau_i$ ,  $\omega_0^i(\lambda)$  and  $P_{mn}^i(\Theta, \lambda)$  represent the extinction optical depth, single scattering albedo and the element of scattering matrix of the  $i$ -th homogeneous atmospheric layer. The variability of aerosol vertical distribution,  $c^k(h)$ , is a normalized aerosol vertical concentration.

$$\int_{h_{BOA}}^{h_{TOA}} c^k(h) dh = 1, \quad (4.7)$$

where  $h_{BOA}$  and  $h_{TOA}$  represent the altitude of the bottom and the top of the atmosphere. In the AERONET retrieval, the atmosphere is assumed to be vertically homogeneous or with a bi-layer structure, due to the low sensitivities of photometer measurements to aerosol vertical variability [Dubovik and King, 2000, Dubovik et al., 2000]. In GARLiC/GRASP, lidar profiles including the backscattered signal VLDR profile are very sensitive to aerosol vertical variability compared to passive remote sensing measurements [Lopatin, 2013], so that the vertical aerosol concentrations are designed to be retrieved parameters. If we ignore the anisotropism of extinction to the polarizing laser beam, the backscattered lidar signal is described as follows:

$$L_{\parallel, \perp, tot}(\lambda, h) = A_{\parallel, \perp, tot}(\lambda) [\beta_{\parallel, \perp, tot}^{mol}(\lambda, h) + \beta_{\parallel, \perp, tot}^{aer}(\lambda, h)] \exp\left(-2 \int_0^h \alpha(\lambda, h') dh'\right) \quad (4.8)$$

and

$$\begin{aligned} \beta_{tot}^{mol/aer}(\lambda, h) &= \frac{1}{4\pi} \alpha^{mol/aer}(\lambda, h) \omega_0^{mol/aer}(\lambda, h) P_{11}^{mol/aer}(\pi, \lambda, h), \\ \beta_{tot}^{mol/aer}(\lambda, h) &= \beta_{\perp}^{mol/aer}(\lambda, h) + \beta_{\parallel}^{mol/aer}(\lambda, h), \end{aligned} \quad (4.9)$$

where  $A_{\parallel, \perp, tot}$  is the instrumental coefficient depending on the transmission of the emitting optics and  $\beta^{mol/aer}$  is the backscatter coefficient of molecules/aerosols, and it is a function of single scattering albedo and phase function. It should be noted that the overlap function is not taken into account in the forward model of GARLiC/GRASP. The correction of overlap should be applied before running GARLiC/GRASP, otherwise, the lidar signal in the overlap ( $h < h_{min}$ ) range should be cut. The lidar profiles  $A_{\parallel, \perp, tot}$  entering into GARLiC/GRASP are normalized, which means:

$$\int_0^{h_{max}} L_{\parallel, \perp, tot}(\lambda, h) dh = 1. \quad (4.10)$$

From the measurement aspect, the VLDR is determined by the ratio of the cross-polarized and parallel-polarized channels, as well as the calibration coefficient. While from the modeling aspect, the VLDR is a function of the PLDR of aerosols, molecular depolarization ratio and the backscattering ratio:

$$\delta_v = \frac{\beta_{\perp}^{mol} + \beta_{\perp}^{aer}}{\beta_{\parallel}^{mol} + \beta_{\parallel}^{aer}} = \frac{R \delta_p (\delta_m + 1) + \delta_m - \delta_p}{R (\delta + 1) + \delta_p - \delta_m}$$

where

$$\delta_p = \frac{\beta_{\perp}^{aer}}{\beta_{\parallel}^{aer}} = \frac{P_{11}^{aer}(\pi, \lambda) - P_{22}^{aer}(\pi, \lambda)}{P_{11}^{aer}(\pi, \lambda) + P_{22}^{aer}(\pi, \lambda)} \quad (4.11)$$

$$\delta_m = \frac{\beta_{\perp}^{mol}}{\beta_{\parallel}^{mol}}$$

The calculation of volume depolarization  $\delta_v$  requires a predetermined molecular depolarization ratio. As discussed previously in Chapter 2, the theoretical value of molecular depolarization ratio is about 0.4% without considering the cross-talks of the optics and the ‘leakage’ of rotational Raman lines. Behrendt et al. [2002] presented a method to calculate the molecular depolarization ratio taking into account of the rotational Raman lines included into the elastic signal. The real measure VLDR in the aerosol-free zone is usually higher than the theoretical molecular depolarization due to the imperfection of optics and errors in the measurements and calibration procedure. The sensitivity of the molecular depolarization ratio and calibration procedure will be discussed in the following section.

### 4.1.2 Numerical inversion

The numerical inversion module tries to optimize the fitting of the observations following the multi-term least squares method strategy. The concept of numerical inversion is represented by the following equations:

$$\begin{cases} \mathbf{f}^* = \mathbf{f}(\mathbf{a}) + \Delta_{\mathbf{f}} \\ \mathbf{0}^* = \mathbf{S}\mathbf{a} + \Delta_{\mathbf{S}} \\ \mathbf{a}^* = \mathbf{a} + \Delta_{\mathbf{a}}, \end{cases} \quad (4.12)$$

The first equation represents the fitting of the observations. Vector  $\mathbf{a}$  is a vector of unknowns to be retrieved, which is also the output of the numerical inversion module as well as the dataset driving the forward model. Vector  $\mathbf{a}$  is composed of five components, as expressed below:

$$\mathbf{a} = \begin{pmatrix} \mathbf{a}_v \\ \mathbf{a}_{sph} \\ \mathbf{a}_n \\ \mathbf{a}_\kappa \\ \mathbf{a}_h \end{pmatrix} \quad (4.13)$$

where  $\mathbf{a}_v$ ,  $\mathbf{a}_{sph}$ ,  $\mathbf{a}_n$ ,  $\mathbf{a}_\kappa$ ,  $\mathbf{a}_h$  denote the unknowns corresponding respectively to the size distribution  $\frac{dV}{dlnr_j}$ , the sphere fraction  $C_{sph}^k$ , the real part  $n^k(\lambda)$  and imaginary part  $\kappa^k(\lambda)$  of the refractive indices, and the vertical distribution of the aerosol concentration  $c^k(h)$ .  $\mathbf{f}$  and  $\mathbf{f}^*$  represent the function of forward model and the vector of observations, respectively.  $\Delta_{\mathbf{f}}$  is the vector of measurement errors.

The second equation represents a priori smoothness constraints on the retrieved parameters. The matrix  $\mathbf{S}$  is used to smooth the size distribution  $\frac{dV}{dlnr_j}$  and the spectral dependencies of the real part  $n^k(\lambda)$ , as well as the imaginary part  $\kappa^k(\lambda)$  of the refractive indices. The assuming  $\mathbf{0}^*$  for the derivatives of the retrieved parameters allows the elimination of the strongly oscillating solutions with unrealistically high derivatives [Dubovik and King, 2000, Dubovik, 2004, Dubovik et al., 2006].

The third equation represents a priori estimates  $\mathbf{a}^*$  of the retrieved parameters  $\mathbf{a}$ .  $\Delta\mathbf{a}^*$  is a vector of the uncertainties of  $\mathbf{a}^*$ . In Equation 4.12 the uncertainties  $\Delta\mathbf{a}^*$ ,  $\Delta_{\mathbf{S}}$  and  $\Delta_{\mathbf{f}}$  are assumed to be normally distributed.

The solution of Equation 4.12 is performed by minimizing the following quadratic form:

$$\begin{aligned} \Psi(\mathbf{a}^p) &= \Psi_f(\mathbf{a}^p) + \Psi_{\Delta}(\mathbf{a}^p) + \Psi_a(\mathbf{a}^p) \\ &= \frac{1}{2} \{ (\Delta\mathbf{f}^p)^T \mathbf{W}_{\mathbf{f}}^{-1} \Delta\mathbf{f}^p + \gamma_S (\mathbf{a}^p)^T \mathbf{W}_{\mathbf{S}}^{-1} \mathbf{a}^p + \gamma_a (\Delta\mathbf{a}^p)^T \mathbf{W}_{\mathbf{a}}^{-1} \Delta\mathbf{a}^p \} \end{aligned} \quad (4.14)$$

and

$$\begin{aligned} \mathbf{W}_f &= \frac{1}{\epsilon_f^2} \mathbf{C}_f, & \mathbf{W}_S &= \frac{1}{\epsilon_S^2} \mathbf{C}_S, & \mathbf{W}_a &= \frac{1}{\epsilon_a^2} \mathbf{C}_a \\ \gamma_S &= \frac{\epsilon_f^2}{\epsilon_S^2}, & \gamma_a &= \frac{\epsilon_f^2}{\epsilon_a^2} \end{aligned} \quad (4.15)$$

where  $W_{\dots}$  represents the weighting matrix and  $\gamma_{\dots}$  represents the Lagrange multipliers.  $p$  is the index of the iteration.  $\epsilon_f^2$ ,  $\epsilon_S^2$  and  $\epsilon_a^2$  are the first diagonal elements of the corresponding covariance matrices  $\mathbf{C}_f$ ,  $\mathbf{C}_S$  and  $\mathbf{C}_a$ .

There are a variety of mathematical methods for minimizing quadratic forms, while the choice of methods is a critical question for the retrieved parameters. GARRLiC/GRASP uses a flexible generalized scheme of minimization to account for different datasets. The details about the iterative process for calculating the solutions of Equation 4.12 can be found in the publications Dubovik and King [2000], Dubovik [2004] and Lopatin [2013].

## 4.2 Sensitivity test

### 4.2.1 Description of the sensitivity study

The sensitivities of GARRLiC/GRASP to the random noise, aerosol type and aerosol loading have been performed and discussed by Lopatin [2013]. The results show that the combination of coincident sun/sky photometer and lidar measurements is beneficial for the retrieval of aerosol properties and aerosol profiling. Moreover, the accuracy of the retrieved parameters, including the size distribution, complex refractive indices, single scattering albedo as well as the vertical concentration profiles are dependent on the aerosol loading. Higher aerosol loading results in better retrieval accuracy. The accuracy of the retrieval for each mode, fine or coarse mode, is correlated with the proportion of the mode in the total aerosol mixture. Additionally, the presence of noise into the measurements affects the accuracy of the retrieved parameters and the separation of fine and coarse mode.

To study the impact of the VLDR measurements on the retrieval, several sensitivity tests are designed with pre-assumed atmospheric conditions. Two aerosol models, absorbing biomass burning aerosol and desert dust, are considered as the fine and coarse mode,

respectively. The properties of various aerosol components have been presented in the publication of Dubovik et al. [2002a]. Abundant urban-industrial, biomass burning, desert dust and oceanic aerosol observations from worldwide AERONET network are used to retrieve the optical properties using AERONET inversion code. The absorption of biomass burning aerosols varies significantly with the source and is potentially influenced by the aging process. The biomass burning properties used in this simulation are taken from the retrieval in Mongu site (Zambia) and for desert dust, the example is taken from Bahrain-Persian Gulf. The complex refractive indices of the two aerosol components are summarized in Table 4.3. The simulated vertical distribution of aerosol concentration is plotted

Table 4.3. The complex refractive indices of biomass burning (fine mode) and desert dust (coarse mode) in the simulation. The real and imaginary parts of the complex refractive indices (CRI) are labeled as rCRI and iCRI, respectively.

$\lambda$ (nm)		355	440	532	675	870	1020	1064
Fine	rCRI	1.50	1.50	1.50	1.50	1.50	1.50	1.50
	iCRI	0.02	0.02	0.02	0.02	0.02	0.02	0.02
Coarse	rCRI	1.55	1.55	1.55	1.55	1.55	1.55	1.55
	iCRI	0.004	0.0025	0.002	0.0015	0.001	0.001	0.001

in Figure 4.3. The fine and coarse mode are assumed to follow normal distribution and the characteristics are presented in Table 4.4. The volume concentration ratio of the fine to the coarse mode concentration is fixed to 1:6 in all the simulated scenarios. The coarse mode

Table 4.4. Parameters of the size distribution used in the simulated scenarios.  $r_{min}$  and  $r_{max}$  represent the minimum and maximum of the radius range for the size distribution.  $r_{mean}$  and  $\sigma$  are the mean radius and the standard deviation of the size distribution. We take 10 size bins for the fine mode and 15 size bins for the coarse mode.

Mode	$r_{min}$ ( $\mu m$ )	$r_{max}$ ( $\mu m$ )	$r_{mean}$ ( $\mu m$ )	$\sigma$
Fine	0.05	0.576	0.14	0.4
Coarse	0.335	15.0	2.0	0.6

here, i.e. the desert dust, is the dominant aerosol component and follows a normal distribution peaking at 2000 m. The fine mode, i.e. the biomass burning distributes uniformly from 0 m to 2800 m and then decreases linearly to negligible values. The minimum value of the vertical concentration in this study is set to be  $10^{-6}$  (unit less). This configuration simulates an atmospheric condition where local biomass burning aerosols mix with

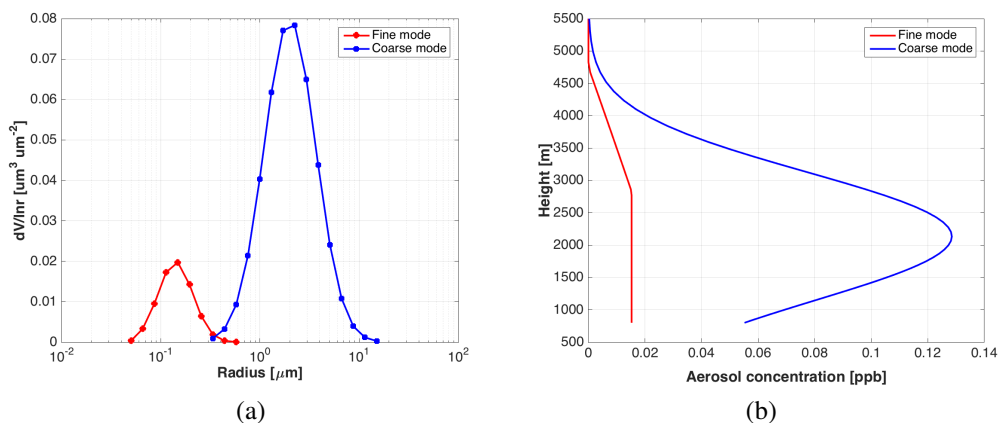


Figure 4.3. The simulated aerosol size distribution and vertical concentration. (a) Size distribution, (b) vertical concentration.

transported dust layer. The sensitivity tests are aimed at evaluating the performance of GARRLiC/GRASP retrieval with respect to the following issues:

- The comparison of GARRLiC/GRASP retrieval with/without VLDR measurements under different aerosol loading levels.
- The comparison of GARRLiC/GRASP retrieval with/without VLDR measurements with different sphere fractions of the coarse mode.
- The impacts of the molecular depolarization ratio on the retrieved parameters under different spectral configurations.
- The impacts of the calibration coefficient on the retrieved parameters under different spectral configurations.

#### 4.2.2 Sensitivity to aerosol loading

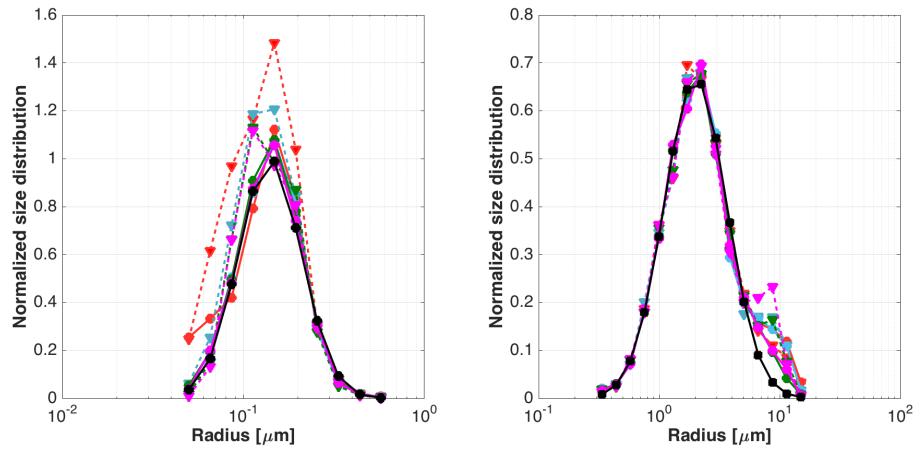
Observations at four different aerosol loading levels with  $\tau_{440}$  equal to 0.08, 0.15, 0.30 and 0.46, are simulated with the parameters above. The variation of the optical thickness is done by changing the aerosol concentrations, while the concentration ratio of the fine to the coarse mode, as well as other aerosol characteristics are kept. Two different observation types are generated from the forward model. The first type, regarded as the standard observation dataset of GARRLiC/GRASP algorithm, includes the sun/sky photometer measurements and lidar elastically backscattered signal at three elastic wavelengths: 355, 532 and 1064 nm. The second type includes the standard observation dataset as well as

the VLDR measurements at the three elastic wavelengths. The standard observation plus simulated VLDR measurements (at one or more wavelengths) is hereafter called extended observation dataset. The simulated observations are then retrieved by GARRLiC/GRASP. It is worthy to be mentioned that, in the forward model and the numerical inversion, the molecular depolarization ratio is assumed to be 0.4% at three wavelengths.

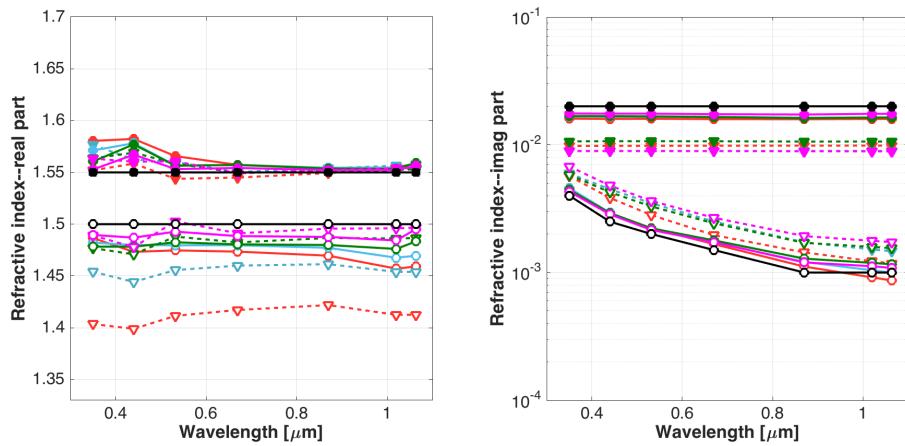
The retrieved size distribution, complex refractive indices and aerosol vertical concentration are plotted in Figure 4.4. The solid and dashed lines represent the retrievals with extended and standard observation dataset, respectively. The size distributions and vertical concentrations are normalized by the columnar volume concentration of each mode. Figure 4.4(a) shows the retrieved fine and coarse mode distributions. The retrievals with extended observation datasets show higher accuracy of the fine mode size distribution compared to the retrievals with standard observation datasets which tend to over-estimate the concentration of fine-mode particles. The error of the fine mode size distribution is correlated with the aerosol loading: the higher the aerosol loading the lower retrieval error. The retrieval accuracy of the coarse-mode size distribution is higher than the fine mode, which is consistent with the fact that coarse mode is the dominant aerosol component in the simulation. The retrievals with both standard and extended observation dataset tend to over-estimate the concentration of the particles with radius higher than  $5 \mu\text{m}$ . However, the retrievals with extended observation dataset show better performance compared to the retrievals with standard observation datasets.

Figure 4.4(b) shows the real and imaginary part of the complex refractive indices. The open and solid symbols represent the complex refractive indices of fine and coarse mode, respectively. The real parts of coarse mode do not show obvious differences no matter the VLDR measurements are included or not. While for the real part of fine mode, retrieval accuracy decreases as the aerosol optical thickness decreases and the retrievals with extended observation dataset show distinctive advantages compared to the retrievals with standard observation dataset. As to the imaginary part of the two aerosol modes, the inclusion of the VLDR brings significant improvements.

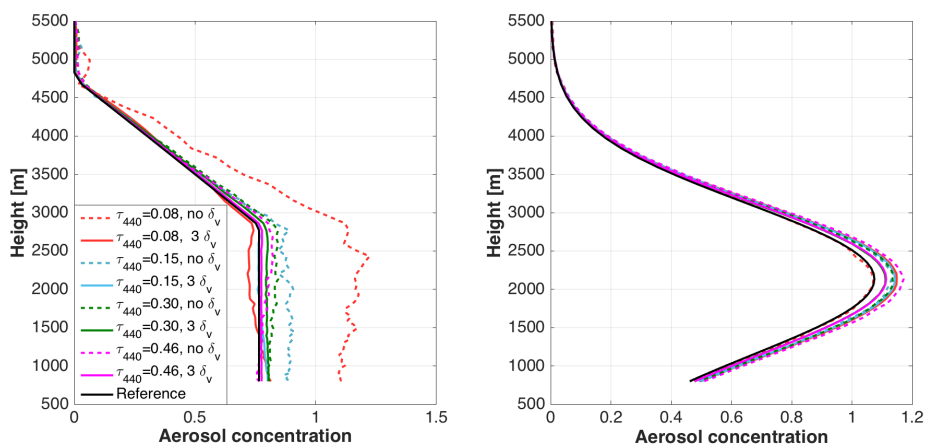
Figure 4.4(c) shows the aerosol vertical concentrations normalized by the columnar concentration of each mode. The inclusion of VLDR measurements into GARRLiC/GRASP obviously improves the profiling of fine mode. The improvements in the coarse mode are



(a) Size distributions of fine (left) and coarse (right) mode



(b) The real part (left) and imaginary part (right) complex refractive indices



(c) Aerosol vertical concentrations: fine (left) and coarse mode (right).

Figure 4.4. GARRLiC/GRASP retrieval under different aerosol loadings

not as evident as the fine mode, since the coarse mode is dominant in the aerosol mixture so the retrieval accuracy is high whether the VLDR measurements are included. It is worthy to be mentioned that all the retrievals in this group of tests are performed with the same constraints, however, due to different algorithm configurations, i.e. the aerosol loading and differences in the input datasets, one optimal constraint set for a specific configuration may not be optimal for another. In this situation, although more information is added, the retrieval may not be improved because the solution or some parameters in the solution may be misdirected by the improper constraints.

### 4.2.3 Sensitivity to the sphere fraction of coarse mode

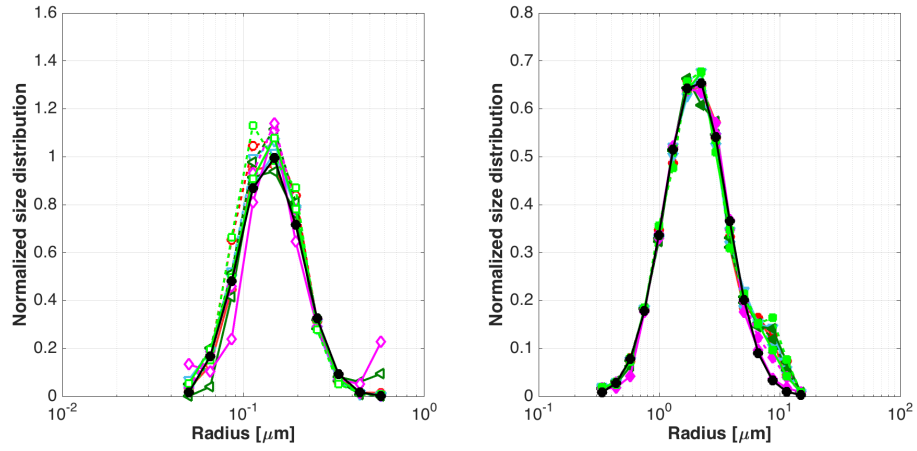
According to the scattering model, the PLDR of aerosol is determined by its size, shape as well as complex refractive indices. In reality, aerosol types and morphology are diverse: fresh smoke particles are mostly small and spherical particles; desert dust and volcanic ash are highly irregular particles. The amount of useful information about aerosol scattering contained in the VLDR measurements depends on the contribution of aerosol scattering in contrast to the total detected signals, which additionally include the cross-talks of optics and the errors of calibration procedure. In an extreme case where the aerosols particles are all spherical, the VLDR measurements contain no information from aerosol scattering, but only the optical cross-talks, molecular scattering and calibration errors. As a result, including the VLDR measurements into GARRLiC/GRASP will not be beneficial because it does not bring extra information about aerosol scattering.

To test the dependence of GARRLiC/GRASP retrieval on the sphere fraction of aerosol particles, 5 groups of simulation are made with coarse-mode sphere fraction equal to 1%, 20%, 40%, 60% and 80%, respectively. The sphere fraction of fine mode is set to 100% for all groups. The reason for fixing the sphere fraction of fine mode is due to that, according to the study of spheroid model, the scattering of fine mode particles is not sensitive to the sphere fraction. All the other aerosol micro-physical and optical parameters such as the size distribution, complex refractive indices, sphere fraction of fine mode and vertical distributions are kept the same in these five groups of simulation. The optical depth at 440 nm is set to 0.30 for all the five simulations. The forward model of GARRLiC/GRASP generates two different types of observation: standard dataset and extended observation

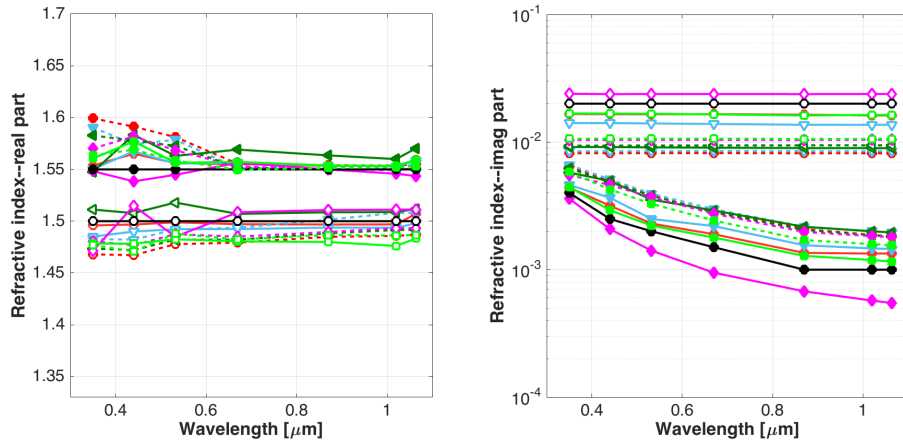
dataset and then the observations are inverted using the same constraints.

Figure 4.5 shows the retrieved size distributions, complex refractive indices and vertical concentrations. The solid and dashed lines represent the retrievals with extended and standard observation datasets, respectively. The open and solid symbols represent the fine and coarse modes. The size distribution of coarse mode are well retrieved, whether the VLDR measurements are included or not. An over-estimation of fine mode particles is observed in all the 5 groups of test and the retrievals with extended observation datasets generally show slight improvements compared to the retrievals with standard observation datasets. The retrievals with 60% and 80% sphere fraction of coarse-mode particles tend to over-estimate the concentration of fine mode at its two ‘wings’. As to the complex refractive indices, the inclusion of VLDR measurements generally brings improvements compared to the retrievals with standard datasets. The advantages of including VLDR measurements are more evident in the retrieval of the imaginary parts. However, when the sphere fraction of coarse-mode particles is up to 60% or 80%, the retrieval of some parameters do not show any improvements compared to not including depolarization. For example, when the sphere fraction of coarse mode is 60%, the retrieved imaginary part of the complex refractive indices show no improvements. And for sphere fraction of 80%, the retrieved imaginary part of coarse mode and real part of fine mode particles degrade. The vertical concentrations in Figure 4.5(c) show again highly spoiled profiles when the sphere fraction of coarse mode is up to 80%. The lowest point at 700 m of fine mode is dramatically pushed down to compensate the over-estimation of fine-mode concentration above 700 m.

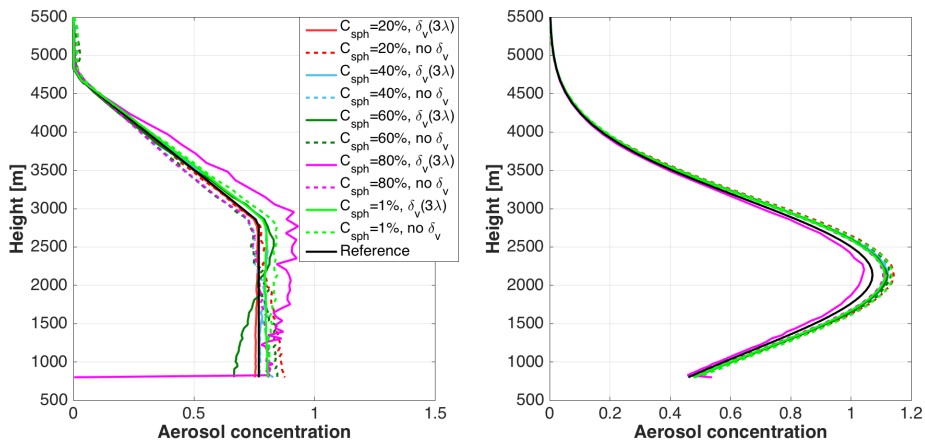
The degradation of the performance of GARRLiC/GRASP for high spherical particles is expectable. The increase of the sphere fraction of coarse mode leads to the decrease of the contribution of aerosol scattering in the VLDR and aggravates the information aliasing between the fine and coarse mode, which could lead to unrealistic changes in the retrieved parameters, for example the ‘flying-up’ of the fine mode distribution and the sharpe changes in the vertical concentration when the sphere fraction of coarse mode is 80%. The lowest point of the vertical profile is more vulnerable because of the lack of the information in the lidar overlap range, so it is in the position to balance the fitting of the



(a) Size distributions of fine (left) and coarse (right) mode



(b) Real (left) and Imaginary (right) part of the complex refractive indices



(c) Vertical concentrations of fine (left) and coarse (right) mode

Figure 4.5. GARRLiC/GRASP retrievals with different sphere fraction of coarse mode

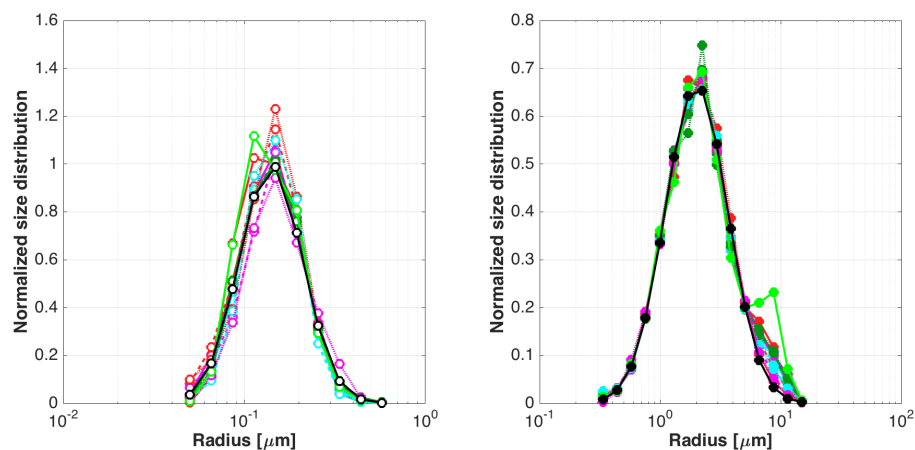
columnar AOD and vertical lidar measurements.

#### 4.2.4 Sensitivity to the molecular depolarization ratio

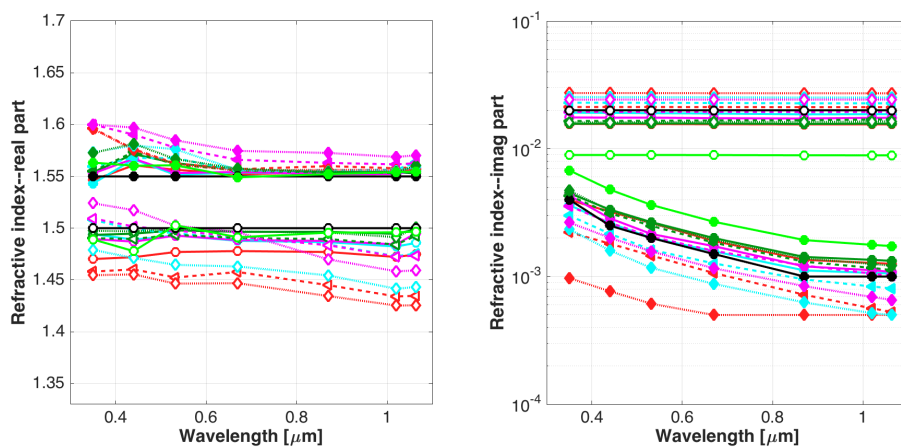
To extract the contribution of aerosols from the measured total depolarization ratio, i.e., the VLDR, we need assume a depolarization ratio to account for the depolarization of both molecular scattering and the optics. This requires a careful calculation of the molecular depolarization ratios, a precise characterization of optics, and an accurate calibration procedure is also needed. However, the cross-talks of the optics are complicated to be characterized and quantified. A characterization of the lidar channel as accurate as possible will be helpful for the calculation of PLDR or VLDR, and beneficial for GARRLiC/GRASP retrieval. This work is expected to be improved in future work. At current stage, the depolarizing effects of the optics are not taken into account in GARRLiC/GRASP forward modeling. Nevertheless, a sensitivity test to the assumption of molecular depolarization ratio can be helpful for understanding the influence of the mismatch between the measured and true depolarization ratio on the retrieved parameters.

We simulate three groups of extended observation dataset with molecular depolarization ratio of 0.4%, 0.8% and 1.2%. The optical thickness  $\tau_{440}$  is 0.3 and the sphere fractions of fine and coarse mode are 100% and 1%, respectively. In each group, the four different spectrum configurations are simulated: three single-wavelength configuration at 355, 532, and 1064 nm and one triple-wavelength configuration. In the numerical inversion, the molecular depolarization ratio is fixed to 0.4%. The retrievals are plotted in Figure 4.6. The results indicate that:

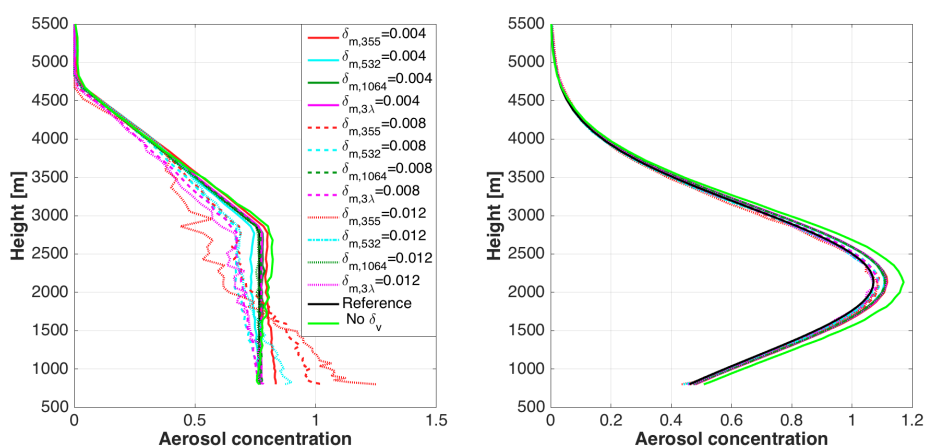
- The sensitivity of the retrievals is spectrally dependent, retrievals with depolarization measurements at 1064 nm (dark green lines), instead of triple-wavelength configuration, are the least sensitive to the assumption of molecular depolarization ratio, especially the complex refractive indices and the vertical concentration.
- Retrievals with VLDR at only 355 nm are the most sensitive to the assumption of molecular depolarization ratio. When  $\delta_m = 0.012(1.2\%)$  at 355 nm, the retrieved fine-mode vertical concentration suffers from distortions and the size distribution of fine mode is over-estimated.



(a) Size distributions of fine (left) and coarse mode (right)



(b) The real (left) and imaginary part (right) of the refractive indices



(c) Vertical distributions of fine (left) and coarse mode (right)

Figure 4.6. GARRLiC/GRASP retrieval with different spectrum configuration and molecular depolarization ratio

- The fine mode properties are more sensitive to the assumption of the depolarization ratio. As  $\delta_m$  increases, the errors in the fine mode refractive indices and vertical concentrations increase.

The users

#### 4.2.5 Sensitivity to the calibration coefficient

The VLDR is proportional to the calibration coefficient which is the ratio of the optical and electronic gain between the two polarization channels. Errors in the calibration coefficient may come from the optics of the calibration polarizer, misalignment and vibrations of the mechanics, or the variation of aerosols and the electronic signal. Errors in the calibration coefficient bring a relative bias into the VLDR measurements. In order to test the sensitivity of GARRLiC/GRASP algorithm to the errors in the calibration coefficient, we organize the tests as follows:

1. Four extended observation datasets are simulated, including three single-wavelength VLDR measurement at 355, 532 and 1064 nm, respectively and one triple-wavelength depolarization ratio at the three wavelengths.
2. For each of the four datasets, +10% and -10% bias are introduced by multiplying the simulated VLDR(s) by 110% and 90%, respectively. The simulated observations are then inverted with the same constraints.

To compare, the retrieval with standard observation dataset is also performed with the same input aerosol parameters. The optical depth in the tests is fixed to 0.3 at 440 nm. The retrievals are plotted in Figure 4.7. The solid and dashed lines represent the retrievals with VLDR(s) biased by -10% and +10%, respectively. The black solid line represents reference which is the aerosol properties used in the forward model. The green line represents the retrieval with the standard observation dataset. The results show that:

1. With  $\pm 10\%$  bias in the depolarization, the retrievals with extended observation dataset still show advantages in the size distribution, the imaginary part of the refractive indices and the vertical concentration of coarse mode, compared to the retrieval with standard observation datasets.
2. The over-estimation of coarse-mode size distribution at the right ‘wing’ still appears. And the positive bias tends to slightly decrease the concentration of fine

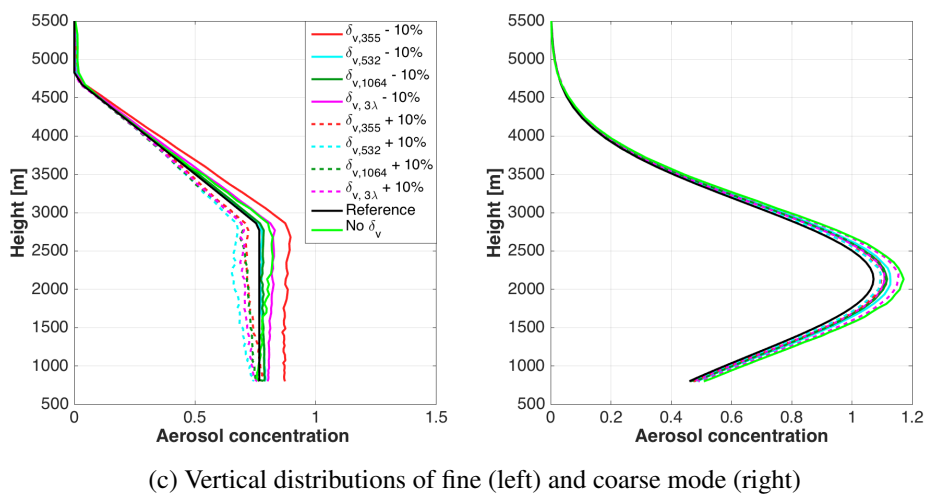
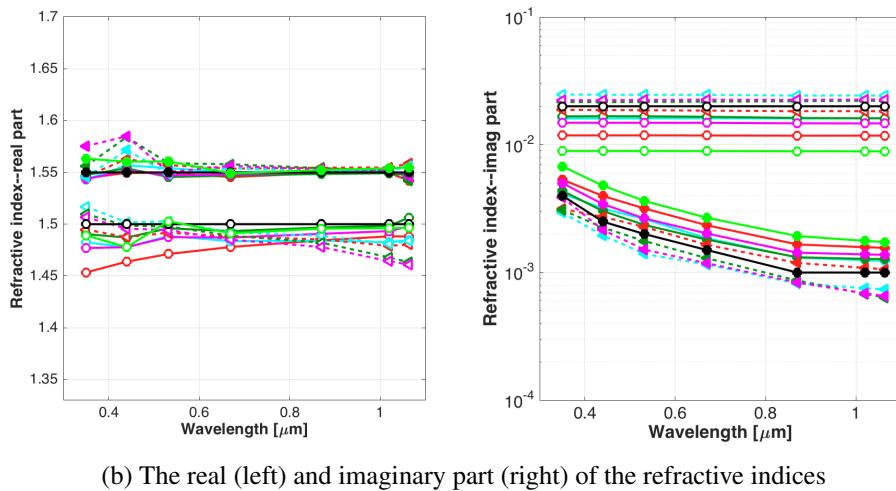
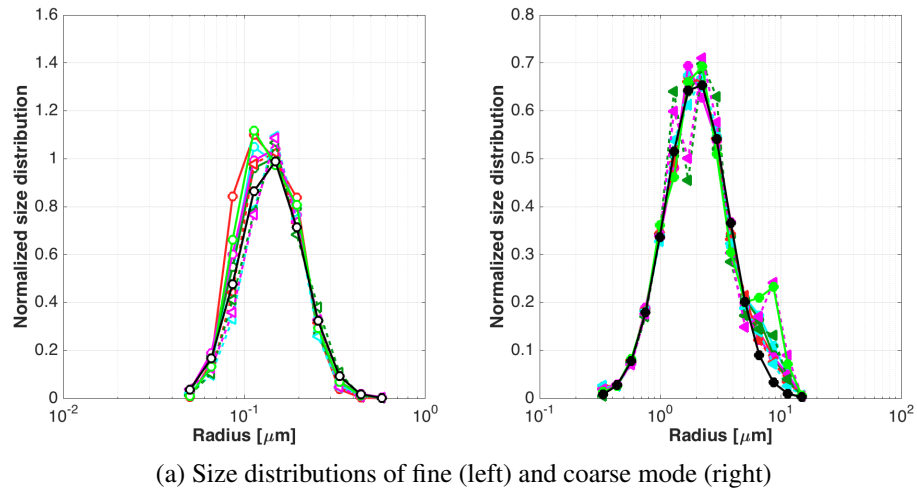


Figure 4.7. GARLLiC/GRASP retrievals with depolarization bias

mode, whereas negative bias in the depolarization ratio tends to increase the concentration of fine mode.

3. The retrievals with triple-wavelength depolarization do not show better accuracy compared to those with single-wavelength depolarization ratio at 532 or 1064 nm.

The sensitivity tests indicate that including VLDR into GARRLiC/GRASP retrieval generally brings improvements into the retrieved parameters, such as the size distribution, complex refractive indices and vertical concentrations. The advantages of the retrieval with extended observation datasets compared to the standard datasets are more significant under low aerosol loading condition. Moreover, improvements brought by the depolarization are dependent on the atmospheric condition and the errors of the depolarization measurements. When the aerosol particles are mostly spherical, the inclusion of VLDR measurements could introduce some artifacts into the size distribution and vertical concentration. The performance of GARRLiC/GRASP retrieval with extended observation datasets degrades with the errors in the VLDR measurements. Additionally, the performance of the retrieval depends on the wavelengths of the VLDR measurements. With the simulated scenarios in this study, the retrievals with depolarization ratio at 355 nm show relatively lower retrieval accuracy compared to the retrievals with VLDR at 532, 1064 nm. This wavelength dependence is related to the aerosol scattering which is wavelength-dependent, and errors in different polarization channels. In real lidar systems, the errors in the VLDR measurements are dependent on the optics, detectors as well as the electronics in different channels. Hence, the users of GARRLiC/GRASP are suggested to choose the configuration of the observation dataset according to the real atmospheric condition and the quality of the depolarization measurements.

### 4.3 Validation and application

To validate the GARRLiC/GRASP algorithm, real measurements are inverted and the retrievals are compared to the results obtained from other independent methods. Besides GARRLiC/GRASP retrieval, the lidar observations can be inverted using Klett method [Klett, 1985] and Raman lidar method [Ansmann et al., 1992] to get the extinction and backscattering coefficients. The Raman lidar inversion is independent of the particle scat-

tering model, the radiative transfer model, as well as the numerical inversion process which are the three important workhorses of GARRLiC/GRASP algorithm. And in this study the Raman signal is not used as input of GARRLiC/GRASP retrieval, so the extinction and backscatter coefficient from Raman inversion are used as verifications for GARRLiC/GRASP retrieval. The signal-to-noise ratio of Raman channels (especially the photon-counting channel) decreases as the sunlight and the aerosol loading increase, which limits the usage of the Raman signal in daytime. However, in some optimal conditions, i.e. when the sunlight and the aerosol loading allows sufficient signal-to-noise ratio in the Raman channel, the Raman signal in the analog channel can still be used for Raman lidar inversion. By assuming a prior and realistic lidar ratio, extinction and backscatter coefficient obtained from Klett method can also be regarded as the reference of GARRLiC/GRASP retrieval. While the lidar ratio is a vertical-dependent variable and varies with aerosol types, a realistic assumption for the lidar ratio profile requires a prior information about the aerosol type as well as the vertical distribution, which is not always available. AERONET products are also used as verifications of GARRLiC/GRASP. Although the particle scattering model, strategy of forward modeling and inversion of GARRLiC/GRASP are inherited from AERONET inversion, the two algorithms are different in the input dataset and retrieval constraints.

Abundant sun/sky and lidar observations are obtained during the SHADOW2 campaign [Bovchaliuk et al., 2016, Veselovskii et al., 2016, 2017] in M'Bour, Senegal. Two examples are selected for the validation of GARRLiC/GRASP algorithm. On 20 January 2016, transported smoke layers from middle Africa were detected over the observation site and in the boundary layer the aerosol was mostly composed of dust. On 11 April 2015, dust transported from the Saharan region dominated in the atmosphere. The two cases have been studied in Chapter 3. In this section, we apply GARRLiC/GRASP retrieval on the extended observation datasets collected in the morning of the two days. The retrieved column-integrated parameters are compared with AERONET retrievals and the vertical profiles of extinction and lidar ratio are verified with the results computed using independent Raman retrievals.

### 4.3.1 20 January 2016, M'Bour

Figure 4.8 shows the lidar data input into GARRLiC/GRASP retrieval. The lidar measurements are averaged between 09:00 and 09:44 UTC on 20 January 2016. The input lidar dataset includes the three elastic lidar backscattered profiles and two VLDR profiles at 355 and 532 nm. Due to the incomplete overlap of the lidar system, the lidar signal below 800 m is removed from the input dataset. The nearly simultaneous sun/sky photometer measurements are recorded at 09:15 UTC and the aerosol optical depth at 440 nm is about 0.82.

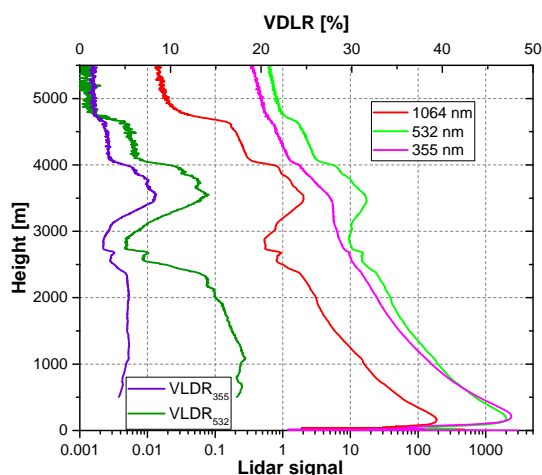


Figure 4.8. Lidar signal averaged between 09:00–09:44 UTC, 20 January 2016, M'Bour

The retrieved parameters are plotted in Figure 4.9. The size distribution retrieved from GARRLiC/GRASP shows a non-negligible fine mode and a dominant coarse mode, which is in agreement with the retrieved size distribution of AERONET inversion. The effective radius of the fine and coarse mode is about  $0.12 \mu\text{m}$  and  $1.5 \mu\text{m}$ , respectively. The single scattering albedo (SSA) of the fine mode, as plotted in Figure 4.9(b), decreases with the increase of the wavelength, which is a feature of biomass burning aerosols [Dubovik et al., 2002a]. The SSA of the coarse mode is consistent with desert dust, which is absorbing in the shortwave. The vertical concentration profiles indicate that fine mode aerosol is minor below 2000 m, compared to the coarse mode aerosols. A transported layer centered at 3500 m is composed of a fraction of fine particles and a pronounced fraction of coarse-mode particles. The real part of the fine and coarse mode is about 1.40 and 1.50, respectively. The imaginary part of the fine and coarse mode is about 0.014 and 0.006,

respectively. The retrieved properties of the fine mode agree well with biomass burning aerosols. The imaginary part of the coarse mode falls into the range of dust imaginary part of refractive indices. While compared to the imaginary part retrieved for dust in the study of Dubovik et al. [2002a], our retrieval is more absorbing. In the dry season of West Africa, fire activities in the surrounding areas occur frequently, therefore, dust particles are possibly contaminated by fire emissions. And it is also possible that dust in the Dubovik et al. [2002a] were different in the absorption due to different dust source or mixing with other low-absorbing aerosols.

Figure 4.10 presents the back trajectory (for 09:00 UTC) obtained from the HYSPLIT model [Stein et al., 2015, Rolph et al., 2017] and overlaid with the fire maps from MODIS [Schaaf et al., 2002]. The back trajectory shows that the air mass at 1500 m is from the desert region and passes over the areas where fire and thermal anomalies are detected. Air mass at 2500 m passes over the fire region and desert region. And before arriving the observation site, the air mass is transported near the surface so it possibly can mix with dust particles. The air mass at 3500 m is originated from the Atlantic ocean and is transported along the coastal region of West Africa, passing over the area with fire and thermal anomalies.

According the lidar measurements before the sunrise on 20 January 2016 (in Chapter 3), the relative humidity in the transported layer is much higher than in the boundary layer. Airborne measurements were performed in the afternoon and aerosol samples were analyzed using scanning electron microscope. The photos of the particle samples showed liquid water condensed around a fraction of dust particles and smoke particles [Unga et al., 2018]. The humidity effect impacts both the particle size and their properties, making the GARRLiC/GRASP's assumption that 'properties of fine and coarse mode particles do not change with altitude' fail. This could bring some errors into the retrieved properties.

The Figure 4.11 shows the extinction coefficients obtained from Raman lidar inversion at 355 and 532 nm. The Raman signal is averaged in the same time period and the calculation is performed by the Single Calculus Chain (SCC, <https://scc.imaa.cnr.it>). SCC is the standard data processing calculation developed by EARLINET community. The same measurement is also processed by our own algorithm and the results are quite consistent with SCC. To simply the plots, the extinction coefficient obtained from our own calcu-

lation is not shown, but the other parameters, such as backscatter coefficient, PLDR and lidar ratios are from our own calculation instead of SCC. The extinction profiles, as well as its spectral dependence from GARRLiC/GRASP and Raman inversion are very consistent in both the boundary and transported layers. The extinction coefficient at 800 m from GARRLiC/GRASP retrieval is lower than the extinction from Raman retrieval. Several reasons could explain this disagreement. Firstly, the mean extinction coefficient in the overlap range is lower than the value at 800 m, so GARRLiC/GRASP derived extinction coefficient is pulled down because it needs to compromise between the lidar observation and the direct AOD. The decrease of extinction coefficient in the overlap range has been confirmed by the profiles of a collocated CIMEL lidar whose overlap range is below 300 m after correction. Secondly, the optical path of the laser beam maybe not the same with the direct sun measurements. When the atmosphere is not homogeneous, the AOD corresponding to the optical path of the lidar beam may not be equal to the AOD measured by the sun/sky photometer. The homogeneity of the atmosphere is a fundamental assumption of GARRLiC/GRASP retrieval, however, in some special cases, the distribution of the aerosol is not spatially homogeneous. The failure of this assumption will impact, to a certain extent, all the retrieval parameters. Additionally, the different overlap functions in the elastic and Raman channels are also a possible reason for the disagreements of the extinction profile in the near range.

The lidar ratio profiles from GARRLiC/GRASP retrieval and Raman retrieval are generally in good agreement as well. However, some vertical structures detected in the Raman inversion are not re-produced by GARRLiC retrieval due to the limited vertical resolution. The comparison of backscatter coefficient from GARRLiC/GRASP and Raman inversion is very consistent, as shown in Figure 4.11(c). While the derived PLDRs from GARRLiC/GRASP are lower than the ones derived from lidar, especially in the boundary layer.

This case presents that, in the presence of dust-smoke mixtures, GARRLiC/GRASP retrieval is able to distinguish the two distinct aerosol modes and derive rather reasonable aerosol vertical distributions. The retrieved size distribution and single scattering albedo are compared and verified by corresponding AERONET inversion. The retrieved extinction and lidar ratio profiles are very consistent with the results obtained from independent Raman

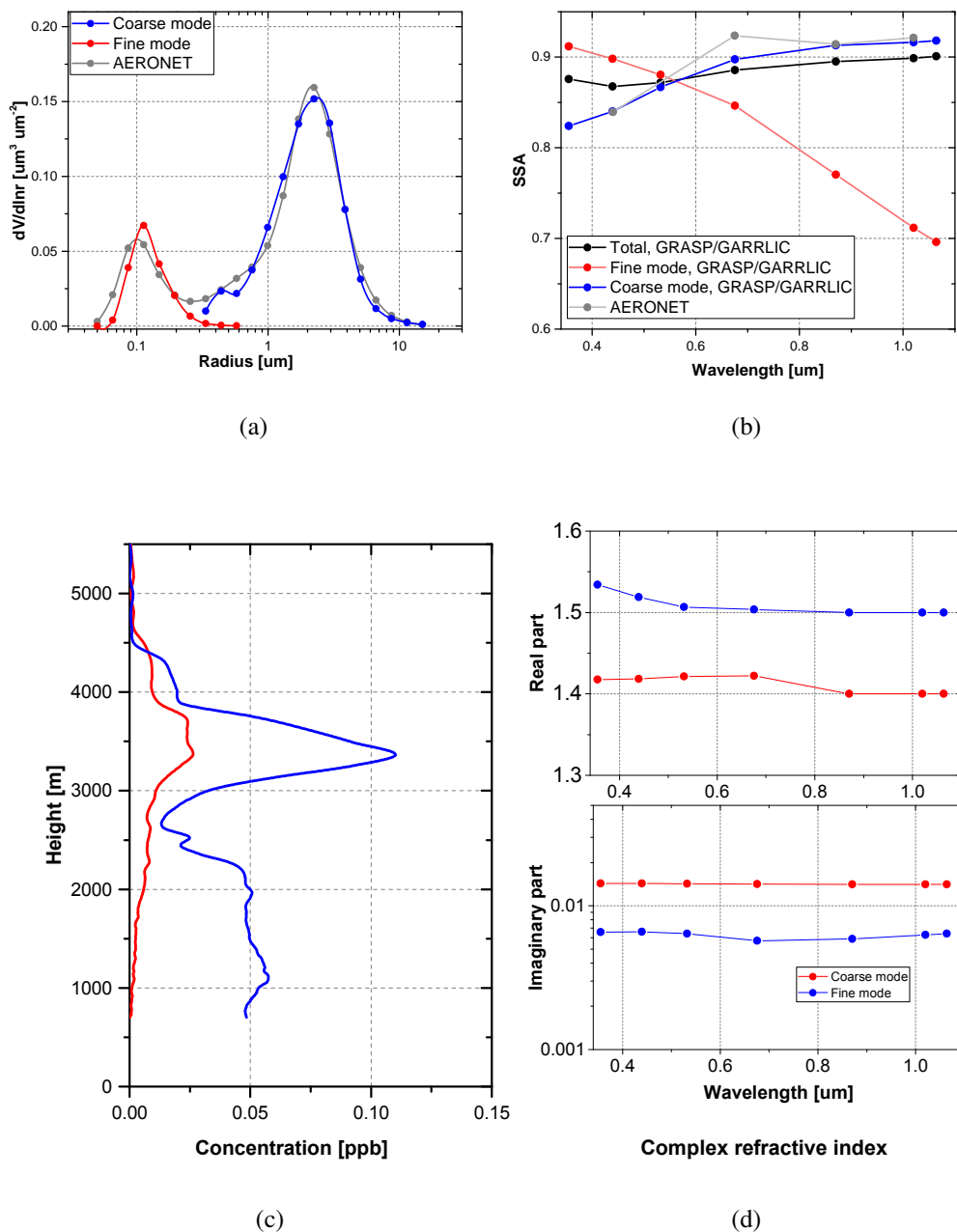


Figure 4.9. GARRLiC/GRASP retrieval on 20 January 2016, 09:15 UTC. (a) Size distribution, (b) single scattering albedo, (c) vertical distribution, (d) complex refractive indices.

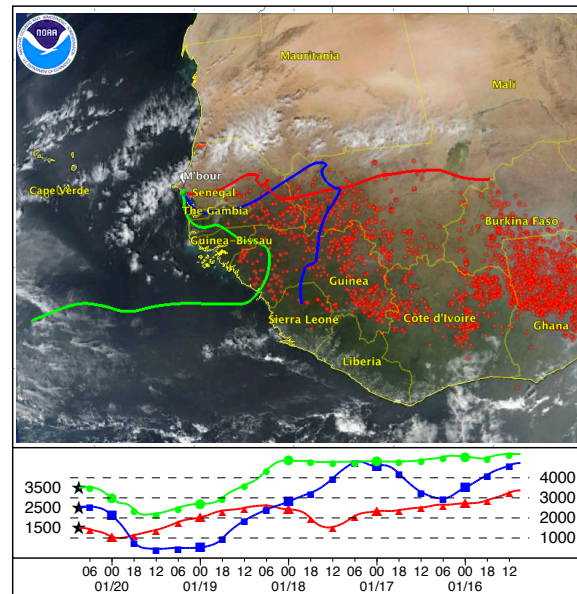


Figure 4.10. Back trajectory at 09:00 UTC, 20 January 2016, M'Bour

inversion. More fundamental comparisons are required for the verification of the column-integrated and the vertically resolved parameters, however, an in-depth comparison is very difficult to be achieved because of the limitations of in-situ techniques, such as particle loss, measuring condition control and so on. More efforts are needed for the verification of GARRLiC/GRASP retrievals in future work.

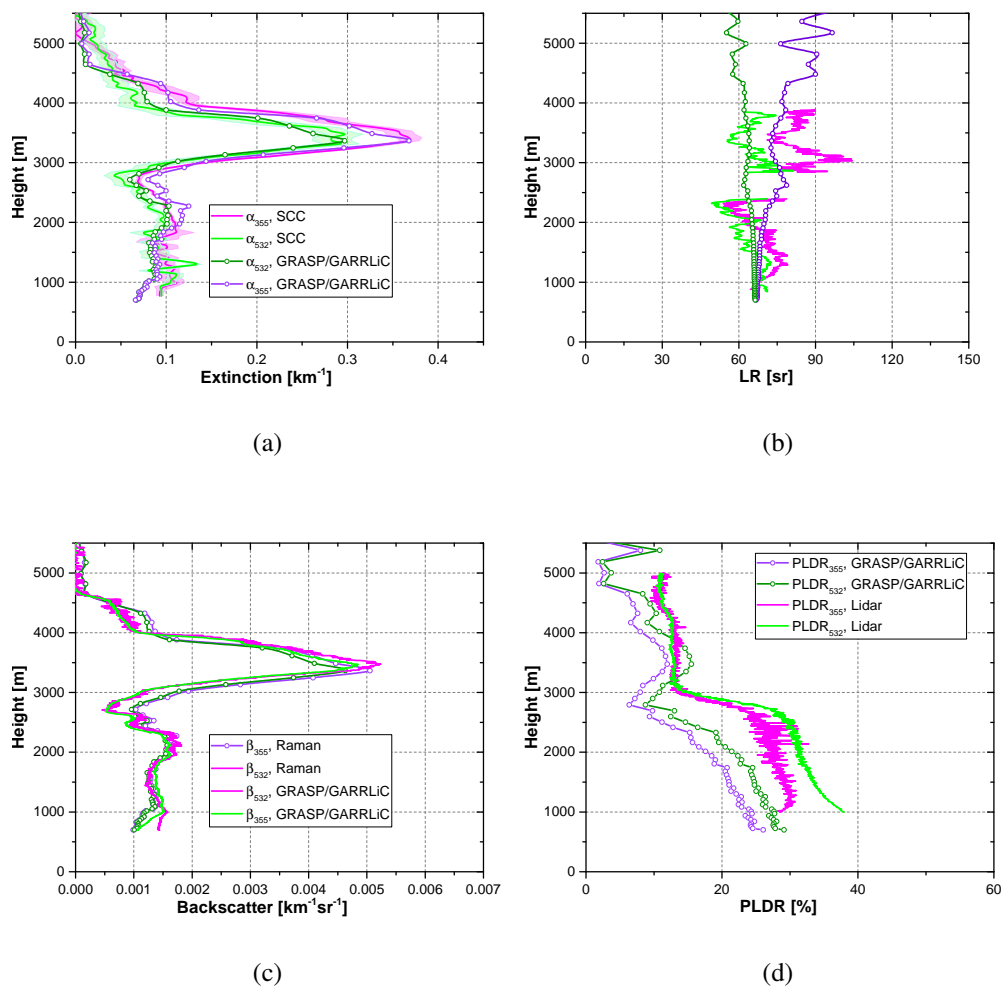


Figure 4.11. Validation of GARRLiC/GRASP retrieval on 20 January 2016, 09:15 UTC. (a) Extinction profile, (b) lidar ratio, (c) backscatter coefficient, (d) PLDR. The lidar derived extinction, backscatter coefficient and lidar ratio are calculated from the measurements averaged at 09:00–09:44 UTC, but the lidar derived PLDRs (green and magenta lines) in Figure (d) are calculated using measurements averaged at 01:30–05:00 UTC, 20 January 2016. Because the power of the laser on 20 January decreased so the signal-to-noise ratio in daytime was much lower compared to night measurements.

### 4.3.2 11 April 2015, M'Bour

Lidar observations on 10 and 11 April 2015 have been studied in Chapter 3 and the results suggest that desert dust is the dominant aerosol component and the contribution of fine particles is negligible. The nighttime observations on 10 and 11 April (in Chapter 3) indicate that dust layer stretches up 4500 m with PLDR at 532 nm varying between 30% and 32%. Three elastic lidar backscattered profiles and one VLDR profile at 532 nm, as well as sun/sky photometer measurement at 08:23 UTC are input into GARRLiC/GRASP algorithm. The lidar observations are averaged between 08:00 and 08:40 UTC. Figure 4.12 plots the input of lidar data into GARRLiC/GRASP algorithm. The retrievals are plotted in Figure 4.13.

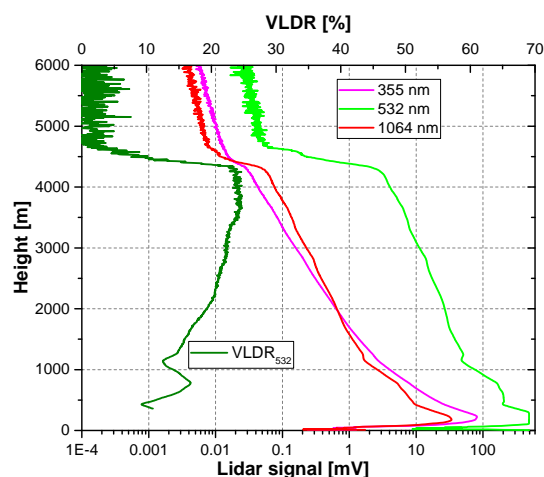


Figure 4.12. Lidar signal averaged between 08:00–08:40 UTC, 11 April 2015, M'Bour

The size distribution in Figure 4.13(a) shows a negligible fine mode and a pronounced coarse mode. The effective radius of the coarse mode is about  $2.1 \mu\text{m}$ . The size distribution retrieved from GARRLiC/GRASP is generally consistent with the one from AERONET, while GARRLiC/GRASP size distribution shows a right-shifted peak of coarse mode and a slightly increased concentration of particles of radius smaller than  $0.1 \mu\text{m}$ . This features are possibly coming from the lidar measurements, as adding lidar measurements extends the spectral coverage of the photometer measurements and also provides realistic vertical distribution of aerosol concentrations. The single scattering albedo of the coarse mode is consistent with desert dust, which is absorbing more in the

shortwave than in the longwave. The fine mode single scattering albedo is monotonically decreasing with wavelength, which is similar to urban/industrial pollution or weakly absorbing biomass burning. Although lidar measurements provide extra information, which is an advantage of GARRLiC/GRASP compared to AERONET retrieval, but more parameters need to be retrieved and the algorithm cannot assure that all the parameters are retrieved with equal accuracy. In this selected case the fine mode particles are very minor and the error of retrieved fine-mode properties is high. The vertical concentration indicates the fine mode is almost negligible compared with coarse mode and the coarse mode concentration peaks at about 3500 m. The refractive index for the coarse mode is about 1.42–1.47 in the real part and the imaginary part decreases from 0.0025 to 0.0015. Both the real and imaginary part of the refractive indices are lower than the values retrieved for the case on 20 January 2016.

Figure 4.14(a) plots the extinction coefficient derived from GARRLiC/GRASP and Raman inversion. The extinction coefficient at 532 nm retrieved from GARRLiC/GRASP coincides well with that derived from Raman inversion. The extinction coefficient at 355 nm is also very consistent above 2500 m. However, the difference of the extinction coefficient at 355 nm grows to  $0.02 \text{ km}^{-1}$  below 1500 m. The lidar ratios retrieved from GARRLiC/GRASP are about 80 sr and 55 sr at 355 and 532 nm, respectively. Simultaneous lidar observations derive very comparable lidar ratio at 532 nm. At 355 nm, lidar observations derive about 75 sr, slightly lower than the value retrieved from GARRLiC/GRASP. The two peaks occur in the lidar ratio profiles at about 1100 m are likely caused by the vertical smoothing applied to the ‘turning point’ at about 1100 m when calculating extinction profile from the Raman signal. The lidar ratio at 355 nm starts to decrease rapidly when the altitude decreases to lower than 1500 m, while such tendency is not shown in the lidar ratio at 532 nm. This phenomenon has been introduced in Chapter 3, where we explain that the intrusion of marine aerosols is possibly the reason. GARRLiC/GRASP is not able to reproduce this feature in the retrieval, while it is present in the lidar observations. The most possible explanations are either the lack of sensitivity or the limitation of assumptions in GARRLiC/GRASP algorithm. This vertical change of aerosol properties is only shown in 355 nm, while in this channel only the total backscat-

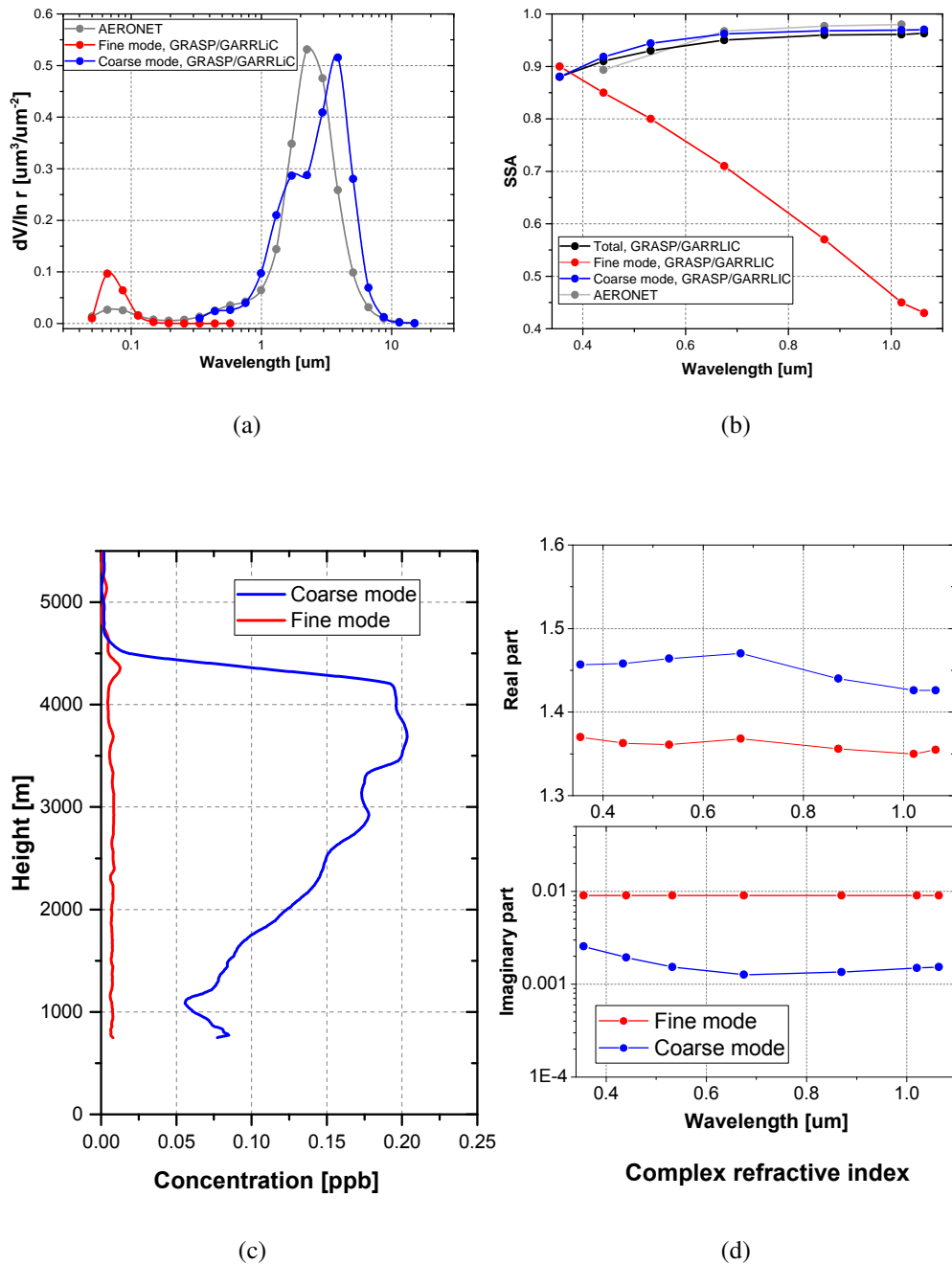


Figure 4.13. GARRLIC/GRASP retrieval on 11 Apr 2015, 08:23 UTC. (a) Size distribution, (b) single scattering albedo, (c) vertical distribution, (d) complex refractive indices.

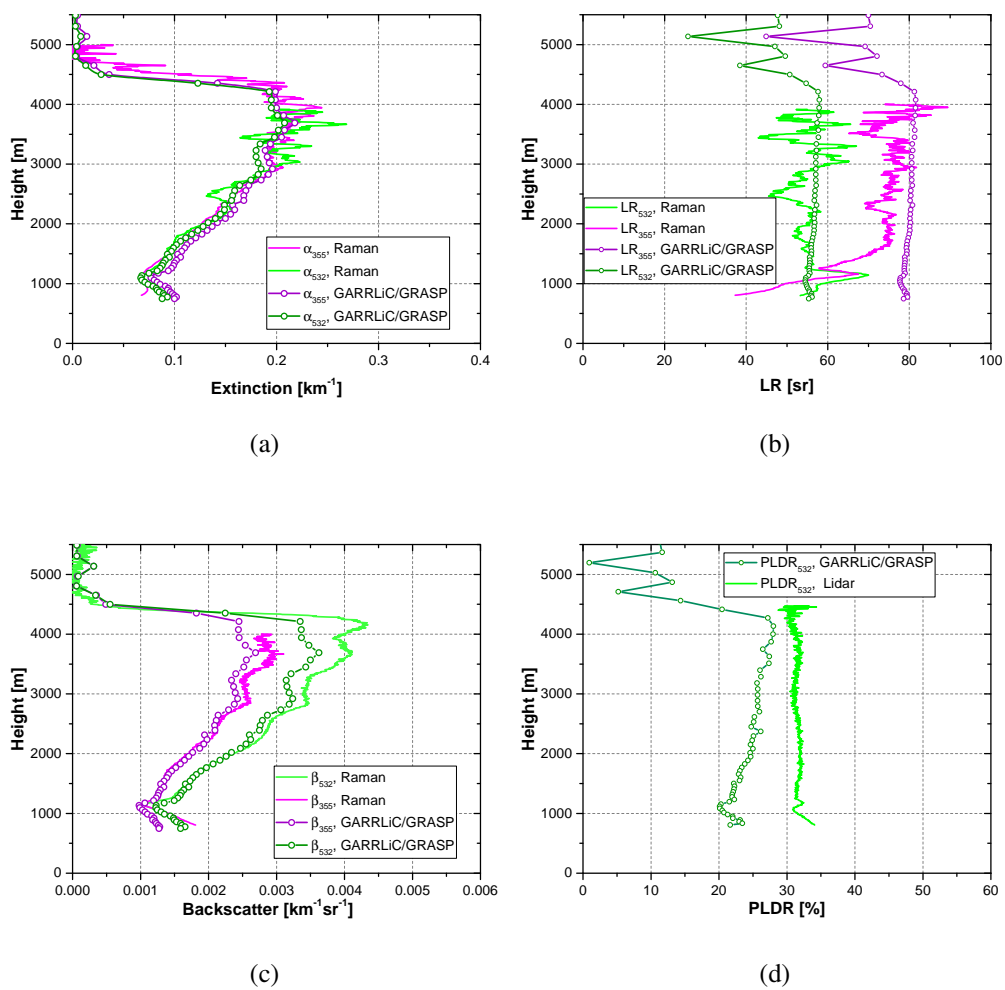


Figure 4.14. Validation of GARRLiC/GRASP retrieval at 08:23 UTC, 11 Apr 2015. (a) Extinction coefficient, (b) lidar ratio, (c) backscatter coefficient, (d) PLDR.

tered lidar signal is measured, so the information contained in 355 nm is very limited. As to GARRLiC/GRASP, one of the basic assumption is that the properties of the two assumed aerosol mode do not change with altitude, but the concentration of each mode can vary at different altitude. Marine aerosols are mostly big particles, so is dust. If marine aerosols present simultaneously with dust but not at the same altitude, GARRLiC/GRASP is not able to represent this vertical variations of any concentration-independent parameter, such as lidar ratio and PLDR. The reason why the lidar ratio at 355 nm channel is more sensitive to the mixing with marine aerosols than the 532 nm channel is not yet fully resolved. The simulation shown in Figure 3.2.23 indicates the same tendency: when dust mixes with sea salt, the increase of lidar ratio at 355 nm is more significant than 532 nm. It is related to the strong absorption of dust in the shortwave band. In addition, marine aerosol could also bring a fraction of small particles, for example, the primary biology aerosol particles, which are smaller than  $0.2 \mu\text{m}$  in diameter and are very scattering. Rivellini et al. [2017] found that sea breeze tend to bring significantly increased organic materials and sulphates in the PM1 mass concentration measured in M'Bour. The 355 nm is possibly more sensitive to the scattering particles in fine mode than the 532 nm channel. More solid explanations and proofs require in-situ measurements.

The comparison of backscatter coefficient is shown in Figure 4.14(c). The backscatter coefficients generally agree well between GARRLiC/GRASP retrieval and Raman lidar inversion. Figure 4.14(d) shows the comparison of PLDR at 532 nm. Like the results present for 20 January 2016, the retrieved PLDR from GARRLiC/GRASP is 3–10% (in absolute values) lower than the values derived from lidar observations. The fitting error of VLDR in this retrieval is about 3% (input minus fitting) in absolute values, indicating that GARRLiC/GRASP does not reproduce adequate depolarization effect. Such behavior is also seen in the retrieval for 20 January in the boundary layer where aerosols are mostly dust.

Aerosol absorption profiles can also be retrieved by GARRLiC/GRASP algorithm. Figure 4.15 shows the retrieved aerosol absorption coefficients for the two cases: 20 January 2016 and 11 April 2015. The first attempt of validating the absorption profiles has been introduced by Tsekeri et al. [2018] by comparing airborne measurements and GARRLiC/GRASP retrievals. The comparisons show several promising results where the in-situ measurements are quite consistent with GARRLiC/GRASP retrievals, but in some cases, disagreements are also observed. The difficulties of the work are the low aerosol loading in the investigated cases and the uncertainties in the in-situ sampling process. More data are required in the future work in order to validate the retrieval of aerosol vertical absorption coefficient.

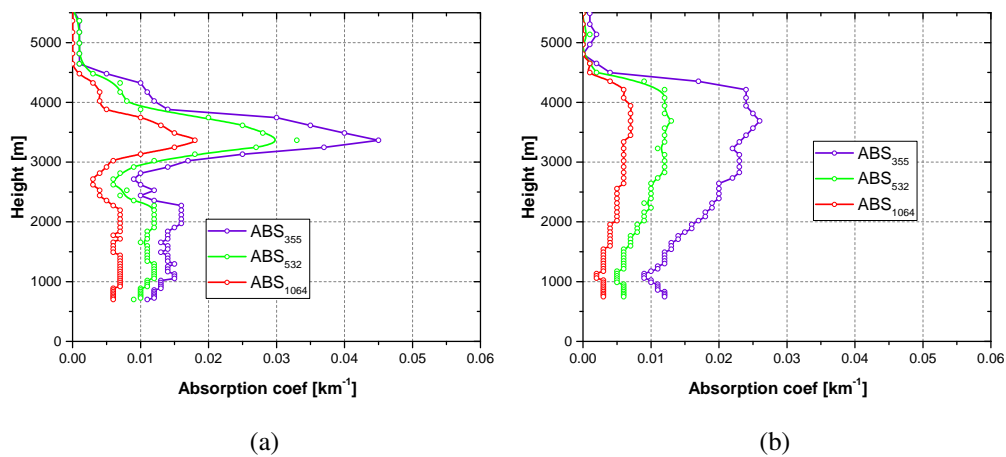


Figure 4.15. Absorption profiles retrieved by GARRLiC. (a) 09:15 UTC, 20 January 2016, (b) 08:23 UTC, 11 April 2015.

## 4.4 Chapter summary

In this chapter, the strategy of GARRLiC/GRASP retrieval, including the forward model and numerical inversion, is firstly presented. VLDR measurements are implemented into the algorithm. Four groups of sensitivity tests are designed and dedicated to answering the following three questions concerning the usage and configuration of GARRLiC/GRASP algorithm:

- Is the inclusion of VLDR measurements beneficial for GARRLiC/GRASP retrieval?
- Are the benefits brought by VLDR measurements dependent on the aerosol types or the error of the depolarization measurements?
- Is the performance of GARRLiC/GRASP retrieval with VLDR measurements dependent on the wavelength?

The answers to the three questions are all ‘Yes’, according to the sensitivity tests. The tests reveal that:

- The inclusion of VLDR(s) in GARRLiC/GRASP improves the accuracy of the retrieval, especially in the low aerosol loading conditions. Compared to the retrievals with standard observation dataset, the ones with extended observation dataset, i.e. that include VLDR measurements, show obvious improvements in all the retrieved parameters.
- With the configuration in the investigated cases, the improvements resulting from the VLDR measurements are dependent on the sphere fraction of the coarse mode. As the sphere fraction of coarse mode increases, the accuracy of the retrieval decreases. Because the information of aerosol scattering contained in the volume depolarization ratio decreases when the number of spherical particles increases. When the sphere fraction of the coarse mode grows to 80% or more, distortions appear in the size distribution and the vertical concentration of fine mode. The dependence on the sphere fraction of the fine mode is also expected, but it is fixed to 100% in this study.
- The assumption of the molecular depolarization ratio has an impact on the performance of GARRLiC/GRASP retrieval and this impact is wavelength dependent. In the tests, the coarse mode is dominant and contains only 1% spherical particles, so the depolarization ratio at larger wavelengths, i.e. 532 and 1064 nm, contains more information about the aerosols. When only the depolarization ratio at 355 nm is included into GARRLiC/GRASP, the error of the retrieval is higher compared to other configurations. A prior information about the aerosol size and shape will be useful when applying GARRLiC/GRASP retrieval with the depolarization measurements to set up an optimal configuration for the algorithm.
- The errors in the calibration procedure impose a bias on the derived VLDR, which

influences the retrieval especially the fine mode parameters. The influences depend on the spectral configuration of polarization channel of lidar systems. In our tests, the bias on the VLDR at 355 nm results in higher errors in the retrieved parameters. Additionally, including the VLDR measurements at 3 wavelengths may not be the best configuration when bias appears equally at all the wavelengths. The user should evaluate the quality of their lidar systems and choose a proper configuration when applying GARRLiC/GRASP retrieval.

GARRLiC/GRASP retrieval is applied to the observations collected in SHADOW2 campaign. The first case presents a mixture of desert dust and biomass burning aerosols observed on 20 January 2016. The sun/sky photometer measurements and lidar elastically backscattered signal, as well as VLDRs at 2 wavelengths are inverted by GARRLiC/GRASP algorithm. The results indicate that GARRLiC/GRASP is able to distinguish the two distinct aerosol components in the microphysical properties and vertical distributions. The retrieved size distribution and single scattering albedo agree well with AERONET retrievals. GARRLiC/GRASP is able to well reproduce the extinction and backscatter coefficient profiles derived from the independent Raman inversion. The lidar ratio profiles obtained from GARRLiC/GRASP also show good agreements with the results obtained from Raman method. The features of (polluted) dust and dust-smoke mixture are well represented by GARRLiC/GRASP regarding aerosol vertical distributions. However, the comparison of PLDRs show that GARRLiC/GRASP is able to reproduce the increasing trend of PLDRs when altitude decreases, but in the boundary layer the particle depolarization produced by GARRLiC/GRASP is approximately 10% lower than the lidar measured PLDR.

The second case involves an example of coarse mode dominated atmosphere with a negligible fine mode. The observation was recorded on 11 April 2015. The retrieval reveals that the properties of the coarse mode are generally consistent with the properties of dust, regarding the single scattering albedo and size distribution. While real part of refractive indices, ranging from 1.42 to about 1.47, is relatively low compared with dust, and the imaginary part is also slightly lower compared to the reported values for dust. The extinction, backscatter coefficients and lidar ratios show good agreements with the results derived from independent Raman inversion at 532 nm. At 355 nm, the agree-

ments of extinction, backscatter coefficient and lidar ratio are acceptable as well. But GARRLiC/GRASP does not reproduce the decrease of lidar ratio below 1500 m. The causes could be either the lack of sensitivity in 355 nm channel or the limitation of the assumptions of GARRLiC/GRASP algorithm. As to the comparison of PLDR, GARRLiC/GRASP reproduced PLDR is about 3–10% lower than the lidar observations. In both cases, VLDR from GARRLiC/GRASP is about 1–3% (in absolute values) lower than the measurements (See the appendix) in the dust layer. It is an indication that GARRLiC/GRASP has difficulties in reproducing the high depolarization ratio of dust particles. This deficiency of GARRLiC/GRASP is not surprising given that dust particles are highly irregular and have edges and corners, which may not be adequately modeled by the spheroid model. Figure 2.4 taken from Dubovik et al. [2006] presents that the  $P_{22}$  element in the scattering matrix of the feldspar sample is not fitted as well as  $P_{11}$  and  $P_{12}$  using spheroid model. Generally, the application of GARRLiC/GRASP on real measurements achieves good agreements with AERONET and Raman method, regarding the size distribution, single scattering albedo (compared to AERONET), extinction, backscatter coefficient and lidar ratios (compared to Raman lidar method), while GARRLiC/GRASP produced PLDR for dust tends to be lower than the lidar observations. Further investigations and improvements about the modeling capability of spheroid model in reproducing PLDR, especially in the backward direction, are needed in future work.

# Chapter 5

## Conclusion and perspectives

*“ Always to look life in the face and to know it for what it is. At last, to know it, to love it for what it is, and then... to put it away. ”*

– Virginia Woolf

### 5.1 Conclusions

The study is dedicated to the aerosol characterization using lidar observations and the implementation of aerosol retrieval algorithm GARRLiC/GRASP using VLDR measurements. The key instrument, a multi-wavelength Mie-Raman lidar LILAS, is maintained and operated in LOA. And during the SHADOW2 campaign, the system was transported to M'Bour. All the instrumental activities and measurements are performed in the two observation sites. Sun/sky photometers involved are within the framework of AERONET. Credits are given to the EARLINET in the framework of ACTRIS-2 and AERONET-Europe for their expertise in the instrumental operation and calibration.

The lidar quality check and calibration are performed following the procedure proposed by EARLINET. The Rayleigh fit, telecover test and molecular depolarization ratio are verified analyzed and compared in order to verify the performance of the lidar system. Results indicate that LILAS system has a satisfactory capability for profiling aerosols from the troposphere to lower stratosphere. While there are still imperfections (e.g. the molecular depolarization) caused by the optics and efforts are still needed in the upgrade

and characterization of the system.

Aerosol episodes, including Saharan dust near the source, long-range transported dust, smoke and dust-smoke mixtures are carefully analyzed and presented. The dust measurements in M'Bour, covering the dry season and the transition period from dry to wet season, reveal a season feature of dust: the spectral dependence of measured lidar ratio of 355 and 532 nm are distinct in the dry and transition season. By using the HYSPLIT dispersion model, we found that the changes of air motion from dry to wet season could potentially bring maritime aerosols which '*deluted*' the absorption of dust, especially in the shortwave.

The comparison of long-range transported Saharan dust observed in Lille and Saharan dust in M'Bour shows the modification of aerosol optical and microphysical properties possibly resulted from the transport. The observations about Canadian smoke in the stratosphere and troposphere point out the curious changes of smoke particles' morphology and optical properties during the aging process. Moreover, this event provides an direct proof of the aerosol semi-direct effect. Dust-smoke mixtures were detected in M'Bour and Lille. Although dust and smoke are the main atmospheric components in both cases, differences are observed in the lidar ratios and backscatter coefficient. The observed differences are probably related to the smoke origins and the transport process. The implementation of GARRLiC/GRASP algorithm is the other objective of this study. The lidar measured VLDR is firstly included into the scheme of GARRLiC/GRASP algorithm. Sensitivity tests using synthetic data indicate that the inclusion of VLDR brings improvements to the aerosol profiling and the retrieval of complex refractive indices especially the imaginary part. The inclusion of VLDR is particularly advantageous in low aerosol-laden condition. The benefits brought by the VLDR measurements in GARRLiC/GRASP are dependent on the quality of the measurements and the atmospheric condition. The users of GARRLiC/GRASP are suggested to evaluate the quality of their measurements and choose proper configurations for obtaining an optimal performance.

GARRLiC/GRASP is then applied to real measurements collected in SHADOW2 campaign. The retrievals are verified by independent AERONET retrieval and Raman lidar retrieval. The comparisons show that the size distribution and SSA are rather comparable

with AERONET products. GARRLiC/GRASP can also well reproduce the extinction and backscatter coefficient profiles, as well as the lidar ratio profiles compared to independent Raman retrievals. In a smoke-dust mixed atmosphere on 20 January 2016, GARRLiC/GRASP can well distinguish the two distinct aerosol modes in their optical and microphysical properties as well as vertical distribution. However, the comparison also shows that GARRLiC/GRASP has some deficiencies in representing the PLDRs of dust particles. The spheroid model used by GARRLiC/GRASP may not be able to reproduce the depolarizing effect of dust particles, which are highly irregular with corners and edges. Some vertical features caused by the intrusion of marine aerosols are missed in GARRLiC/GRASP retrievals. The reason could be explained by the failure of GARRLiC/GRASP assumption that the properties of fine and coarse mode are vertically constant.

## 5.2 Perspectives

Following the work presented in this thesis, there are several tasks to be fulfilled in future work. The first objective is the verification and application of GARRLiC/GRASP retrieval. Although GARRLiC/GRASP has achieved satisfactory results in retrieving dust or dust mixture aerosols, more applications on other types of aerosols are needed. A future campaign will be conducted in China in April and May 2019. This campaign is under the framework of the Chinese *Belt and Road* project and it incorporates researchers from China, France, Russia and Belarus. LILAS system will be transported to the Kashi (also called Kashgar), the west most part of China, and Beijing. The two-month campaign is expected to bring new observations, including Asian dust and city pollution, for aerosol characterization and GARRLiC/GRASP application.

In parallel, the validation of the current version of GARRLiC/GRASP routine processing (including volume linear depolarization ratio) must be continued in the framework of the ACTRIS implementation phase. This activity is particularly relevant to provide standard products and services to European users within ACTRIS through ICARE/AERIS Data and Service Center (a component of ACTRIS Data Center) and through CARS (Centre for Aerosol Remote Sensing) central facility. Moreover, our results have shown the limits

of the spheroid model in representing the depolarization ratio of dust particles, a thorough study is therefore needed to investigate the ability of the spheroid model and the impact of including volume depolarization ratio into the GARRLiC/GRASP on the retrieved parameters.

During the SHADOW-2 campaign, several dust and smoke episodes collected in SHADOW2 campaign will be assimilated into or used as constraints for the aerosol emission model [Chen et al., 2018] to test if the observations help in the retrieval of aerosol source in a regional scale. The interaction between cirrus and aerosols can be investigated using the observations in SHADOW2 campaign.

Our work also demonstrates that LOA atmospheric platform provides valuable data and expertise for validation of future satellite missions. Several future missions are aimed at atmospheric research, for example EarthCare mission, 3MI and the Sentinel series. Especially, LILAS measurements will be useful for the verification of the space borne aerosol lidar on EarthCare. It is worthy to be mentioned that the improvement of LILAS system will be continued in the meantime, in order to extend the capability of the system. A near range telescope will be added. In addition, measurement of  $\text{CH}_4$  vertically resolved concentration has been validated and published [Veselovskii et al., 2018a]. The  $\text{CH}_4$  measurements could be used for the verification of the  $\text{CH}_4$  products satellite missions, e.g. the TROPOMI (Tropospheric Monitoring Instrument, [Butz et al., 2012]) onboard Sentinel-5 and also for the study of tropospheric  $\text{CH}_4$  variation, which is still a shortcoming of current satellite  $\text{CH}_4$  sensors [Jacob et al., 2016].

# Bibliography

- M. O. Andreae and P. Merlet. Emission of trace gases and aerosols from biomass burning. *Global biogeochemical cycles*, 15(4):955–966, 2001.
- A. Ansmann, M. Riebesell, U. Wandinger, C. Weitkamp, E. Voss, W. Lahmann, and W. Michaelis. Combined raman elastic-backscatter lidar for vertical profiling of moisture, aerosol extinction, backscatter, and lidar ratio. *Applied Physics B: Lasers and Optics*, 55(1):18–28, 1992.
- A. Ansmann, I. Mattis, U. Wandinger, F. Wagner, J. Reichardt, and T. Deshler. Evolution of the pinatubo aerosol: Raman lidar observations of particle optical depth, effective radius, mass, and surface area over central europe at 53.4 n. *Journal of the atmospheric sciences*, 54(22):2630–2641, 1997.
- A. Ansmann, J. Bösenberg, A. Chaikovsky, A. Comerón, S. Eckhardt, R. Eixmann, V. Freudenthaler, P. Ginoux, L. Komguem, H. Linné, et al. Long-range transport of saharan dust to northern europe: The 11–16 october 2001 outbreak observed with earlinet. *Journal of Geophysical Research: Atmospheres*, 108(D24), 2003.
- A. Ansmann, M. Tesche, P. Seifert, D. Althausen, R. Engelmann, J. Fruntke, U. Wandinger, I. Mattis, and D. Müller. Evolution of the ice phase in tropical altocumulus: Samum lidar observations over cape verde. *Journal of Geophysical Research: Atmospheres*, 114(D17), 2009.
- A. Ansmann, A. Petzold, K. Kandler, I. Tegen, M. Wendisch, D. Mueller, B. Weinzierl, T. Mueller, and J. Heintzenberg. Saharan mineral dust experiments samum–1 and samum–2: what have we learned? *Tellus B: Chemical and Physical Meteorology*, 63(4):403–429, 2011.

- A. Ansmann, H. Baars, A. Chudnovsky, I. Mattis, I. Veselovskii, M. Haarig, P. Seifert, R. Engelmann, and U. Wandinger. Extreme levels of canadian wildfire smoke in the stratosphere over central europe on 21–22 august 2017. *Atmospheric Chemistry and Physics*, 18(16):11831–11845, 2018.
- F. Arnold, T. Bührke, and S. Qiu. Evidence for stratospheric ozone-depleting heterogeneous chemistry on volcanic aerosols from el chichon. *Nature*, 348(6296):49, 1990.
- A. Badia, O. Jorba, A. Voulgarakis, D. Dabdub, C. Pérez García-Pando, A. Hilboll, M. Gonçalves Ageitos, and J. Zavisa. Description and evaluation of the multiscale online nonhydrostatic atmosphere chemistry model (nmmb-monarch) version 1.0: gas-phase chemistry at global scale. *Geoscientific Model Development*, 10:609–638, 2017.
- M. Bass, E. W. Van Stryland, D. R. Williams, and W. L. Wolfe. *Handbook of optics*, volume 2. McGraw-Hill New York, 1995.
- A. Behrendt, T. Nakamura, M. Onishi, R. Baumgart, and T. Tsuda. Combined raman lidar for the measurement of atmospheric temperature, water vapor, particle extinction coefficient, and particle backscatter coefficient. *Applied optics*, 41(36):7657–7666, 2002.
- T. C. Bond, S. J. Doherty, D. Fahey, P. Forster, T. Berntsen, B. DeAngelo, M. Flanner, S. Ghan, B. Kärcher, D. Koch, et al. Bounding the role of black carbon in the climate system: A scientific assessment. *Journal of Geophysical Research: Atmospheres*, 118(11):5380–5552, 2013.
- M. Born and E. Wolf. *Principles of optics: electromagnetic theory of propagation, interference and diffraction of light*. Elsevier, 2013.
- O. Boucher, D. Randall, P. Artaxo, C. Bretherton, G. Feingold, P. Forster, V.-M. Kerminen, Y. Kondo, H. Liao, U. Lohmann, et al. Clouds and aerosols. In *Climate change 2013: the physical science basis. Contribution of Working Group I to the Fifth Assessment Report of the Intergovernmental Panel on Climate Change*, pages 571–657. Cambridge University Press, 2013.

- V. Bovchaliuk. *Aerosols properties as retrieved from the GARRLIC synergetic approach applied to multi wavelength Raman LiDAR observations performed over Lille and Dakar sites*. PhD thesis, Université de Lille 1, 2016.
- V. Bovchaliuk, P. Goloub, T. Podvin, I. Veselovskii, D. Tanre, A. Chaikovsky, O. Dubovik, A. Mortier, A. Lopatin, M. Korenskiy, et al. Comparison of aerosol properties retrieved using garrlic, lyric, and raman algorithms applied to multi-wavelength lidar and sun/sky-photometer data. *Atmospheric Measurement Techniques*, 9(7):3391–3405, 2016.
- V. Buchard, C. Randles, A. Da Silva, A. Darmenov, P. Colarco, R. Govindaraju, R. Ferrare, J. Hair, A. Beyersdorf, L. Ziemba, et al. The merra-2 aerosol reanalysis, 1980 onward. part ii: Evaluation and case studies. *Journal of Climate*, 30(17):6851–6872, 2017.
- A. Bucholtz. Rayleigh-scattering calculations for the terrestrial atmosphere. *Applied Optics*, 34(15):2765–2773, 1995.
- S. Burton, R. Ferrare, C. Hostetler, J. Hair, R. Rogers, M. Obland, C. Butler, A. Cook, D. Harper, and K. Froyd. Aerosol classification using airborne high spectral resolution lidar measurements-methodology and examples. *Atmospheric Measurement Techniques*, 5(1):73–98, 2012. doi: 10.5194/amt-5-73-2012.
- S. Burton, J. Hair, M. Kahnert, R. Ferrare, C. Hostetler, A. Cook, D. Harper, T. Berkoff, S. Seaman, J. Collins, et al. Observations of the spectral dependence of linear particle depolarization ratio of aerosols using nasa langley airborne high spectral resolution lidar. *Atmospheric Chemistry and Physics*, 15(23):13453–13473, 2015.
- A. Butz, A. Galli, O. Hasekamp, J. Landgraf, P. Tol, and I. Aben. Tropomi aboard sentinel-5 precursor: Prospective performance of ch4 retrievals for aerosol and cirrus loaded atmospheres. *Remote sensing of environment*, 120:267–276, 2012.
- S. Chandrasekhar. *Radiative transfer*. Courier Corporation, 2013.
- C. Chen, O. Dubovik, D. K. Henze, T. Lapyonak, M. Chin, F. Ducos, P. Litvinov, X. Huang, and L. Li. Retrieval of desert dust and carbonaceous aerosol emissions over

- africa from polder/parasol products generated by the grasp algorithm. *Atmospheric Chemistry & Physics*, 18(16), 2018.
- M. Chin, R. B. Rood, S.-J. Lin, J.-F. Müller, and A. M. Thompson. Atmospheric sulfur cycle simulated in the global model gocart: Model description and global properties. *Journal of Geophysical Research: Atmospheres*, 105(D20):24671–24687, 2000.
- M. Chin, P. Ginoux, S. Kinne, O. Torres, B. N. Holben, B. N. Duncan, R. V. Martin, J. A. Logan, A. Higurashi, and T. Nakajima. Tropospheric aerosol optical thickness from the gocart model and comparisons with satellite and sun photometer measurements. *Journal of the atmospheric sciences*, 59(3):461–483, 2002.
- CIMEL. Multiband photometer ce318-n, user’s manual, April 2015. URL <https://www.ncas.ac.uk/en/all-docman-documents/amf/manuals/1383-ce-318n-user-manual/file>.
- P. Colarco, A. da Silva, M. Chin, and T. Diehl. Online simulations of global aerosol distributions in the nasa geos-4 model and comparisons to satellite and ground-based aerosol optical depth. *Journal of Geophysical Research: Atmospheres*, 115(D14), 2010.
- D. J. Cziczo, K. D. Froyd, C. Hoose, E. J. Jensen, M. Diao, M. A. Zondlo, J. B. Smith, C. H. Twohy, and D. M. Murphy. Clarifying the dominant sources and mechanisms of cirrus cloud formation. *Science*, 340(6138):1320–1324, 2013.
- E. Di Tomaso, N. A. Schutgens, O. Jorba, and C. Pérez García-Pando. Assimilation of modis dark target and deep blue observations in the dust aerosol component of nmmb-monarch version 1.0. *Geoscientific Model Development*, 10:1107–1129, 2017.
- O. Doherty, N. Riemer, and S. Hameed. Saharan mineral dust transport into the caribbean: Observed atmospheric controls and trends. *Journal of Geophysical Research: Atmospheres*, 113(D7), 2008.
- B. T. Draine and P. J. Flatau. Discrete-dipole approximation for scattering calculations. *JOSA A*, 11(4):1491–1499, 1994.
- O. Dubovik. Optimization of numerical inversion in photopolarimetric remote sensing. In *Photopolarimetry in remote sensing*, pages 65–106. Springer, 2004.

- O. Dubovik and M. D. King. A flexible inversion algorithm for retrieval of aerosol optical properties from sun and sky radiance measurements. *Journal of Geophysical Research: Atmospheres*, 105(D16):20673–20696, 2000.
- O. Dubovik, A. Smirnov, B. Holben, M. King, Y. Kaufman, T. Eck, and I. Slutsker. Accuracy assessments of aerosol optical properties retrieved from aerosol robotic network (aeronet) sun and sky radiance measurements. *Journal of Geophysical Research: Atmospheres*, 105(D8):9791–9806, 2000.
- O. Dubovik, B. Holben, T. F. Eck, A. Smirnov, Y. J. Kaufman, M. D. King, D. Tanré, and I. Slutsker. Variability of absorption and optical properties of key aerosol types observed in worldwide locations. *Journal of the atmospheric sciences*, 59(3):590–608, 2002a.
- O. Dubovik, B. Holben, T. Lapyonok, A. Sinyuk, M. Mishchenko, P. Yang, and I. Slutsker. Non-spherical aerosol retrieval method employing light scattering by spheroids. *Geophysical Research Letters*, 29(10):54–1, 2002b.
- O. Dubovik, A. Sinyuk, T. Lapyonok, B. N. Holben, M. Mishchenko, P. Yang, T. F. Eck, H. Volten, O. Muñoz, B. Veihelmann, W. J. van der Zande, J.-F. Leon, M. Sorokin, and I. Slutsker. Application of spheroid models to account for aerosol particle nonsphericity in remote sensing of desert dust. *Journal of Geophysical Research*, 111(D11208), 2006. ISSN 0148-0227. doi: 10.1029/2005jd006619. URL <http://dx.doi.org/10.1029/2005JD006619>.
- O. Dubovik, T. Lapyonok, P. Litvinov, M. Herman, D. Fuertes, F. Ducos, A. Lopatin, A. Chaikovsky, B. Torres, Y. Derimian, X. Huang, M. Aspetsberger, and C. Federspiel. Grasp: a versatile algorithm for characterizing the atmosphere, 2014.
- M. Esselborn, M. Wirth, A. Fix, B. Weinzierl, K. Rasp, M. Tesche, and A. Petzold. Spatial distribution and optical properties of saharan dust observed by airborne high spectral resolution lidar during samum 2006. *Tellus B: Chemical and Physical Meteorology*, 61(1):131–143, 2009.

- M. Fiebig, A. Petzold, U. Wandinger, M. Wendisch, C. Kiemle, A. Stifter, M. Ebert, T. Rother, and U. Leiterer. Optical closure for an aerosol column: Method, accuracy, and inferable properties applied to a biomass-burning aerosol and its radiative forcing. *Journal of Geophysical Research: Atmospheres*, 107(D21):LAC 12–1–LAC 12–15, 2002. doi: 10.1029/2000JD000192.
- V. Freudenthaler, M. Esselborn, M. Wiegner, B. Heese, M. Tesche, A. Ansmann, D. Müller, D. Althausen, M. Wirth, A. Fix, G. Ehret, P. Knippertz, C. Toledano, J. Gasteiger, M. Garhammer, and M. Seefeldner. Depolarization ratio profiling at several wavelengths in pure saharan dust during samum 2006. *Tellus B*, 61(1):165–179, 2009.
- V. Freudenthaler, H. Linné, A. Chaikovski, D. Rabus, and S. Groß. Earlinet lidar quality assurance tools. *Atmospheric Measurement Techniques Discussions*, 2018:1–35, 2018. doi: 10.5194/amt-2017-395. URL <https://www.atmos-meas-tech-discuss.net/amt-2017-395/>. in review.
- M. Fromm, J. Alfred, K. Hoppel, J. Hornstein, R. Bevilacqua, E. Shettle, R. Servranckx, Z. Li, and B. Stocks. Observations of boreal forest fire smoke in the stratosphere by poam iii, sage ii, and lidar in 1998. *Geophysical Research Letters*, 27(9):1407–1410, 2000.
- M. D. Fromm and R. Servranckx. Transport of forest fire smoke above the tropopause by supercell convection. *Geophysical Research Letters*, 30(10), May 2003. ISSN 0094-8276. doi: 10.1029/2002gl016820.
- R. Garland, H. Yang, O. Schmid, D. Rose, A. Nowak, P. Achtert, A. Wiedensohler, N. Takegawa, K. Kita, Y. Miyazaki, et al. Aerosol optical properties in a rural environment near the mega-city guangzhou, china: implications for regional air pollution, radiative forcing and remote sensing. *Atmospheric Chemistry and Physics*, 8(17): 5161–5186, 2008.
- R. Gelaro, W. McCarty, M. J. Suárez, R. Todling, A. Molod, L. Takacs, C. A. Randles, A. Darmenov, M. G. Bosilovich, R. Reichle, et al. The modern-era retrospective anal-

- ysis for research and applications, version 2 (merra-2). *Journal of Climate*, 30(14): 5419–5454, 2017.
- D. A. Gillette and R. Passi. Modeling dust emission caused by wind erosion. *Journal of Geophysical Research: Atmospheres*, 93(D11):14233–14242, 1988.
- P. Ginoux, M. Chin, I. Tegen, J. M. Prospero, B. Holben, O. Dubovik, and S.-J. Lin. Sources and distributions of dust aerosols simulated with the gcart model. *Journal of Geophysical Research: Atmospheres*, 106(D17):20255–20273, 2001.
- P. Ginoux, L. Clarisse, C. Clerbaux, P.-F. Coheur, O. Dubovik, N. Hsu, and M. V. Damme. Mixing of dust and nh<sub>3</sub> observed globally over anthropogenic dust sources. *Atmospheric chemistry and physics*, 12(16):7351–7363, 2012a.
- P. Ginoux, J. M. Prospero, T. E. Gill, N. C. Hsu, and M. Zhao. Global-scale attribution of anthropogenic and natural dust sources and their emission rates based on modis deep blue aerosol products. *Reviews of Geophysics*, 50(3), 2012b.
- T. S. Glickman. Glossary of meteorology. american meteorological society. MA, USA, 2000.
- D. H. Goldstein. *Polarized Light, revised and expanded*. CRC press, 2003.
- G. G. Goyer and R. Watson. The laser and its application to meteorology. *Bulletin of the American Meteorological Society*, 44(9):564–570, 1963.
- S. A. Grodsky, J. A. Carton, and S. Nigam. Near surface westerly wind jet in the atlantic itcz. *Geophysical Research Letters*, 30(19), 2003.
- M. Haarig, A. Ansmann, H. Baars, C. Jimenez, I. Veselovskii, R. Engelmann, and D. Althausen. Depolarization and lidar ratios at 355, 532, and 1064 nm and microphysical properties of aged tropospheric and stratospheric canadian wildfire smoke. *Atmospheric Chemistry and Physics*, 18(16):11847–11861, 2018.
- J. Hansen, A. Lacis, R. Ruedy, and M. Sato. Potential climate impact of mount pinatubo eruption. *Geophysical Research Letters*, 19(2):215–218, 1992.

- J. Hansen, M. Sato, and R. Ruedy. Radiative forcing and climate response. *Journal of Geophysical Research: Atmospheres*, 102(D6):6831–6864, 1997.
- R. Haskins and L. Kaplan. Remote sensing of trace gases using the atmospheric infrared sounder. In *IRS*, volume 92, pages 278–281, 1992.
- S. Hastenrath and P. Lamb. Some aspects of circulation and climate over the eastern equatorial atlantic. *Monthly Weather Review*, 105(8):1019–1023, 1977.
- B. N. Holben, T. F. Eck, I. Slutsker, D. Tanre, J. Buis, A. Setzer, E. Vermote, J. Reagan, Y. Kaufman, T. Nakajima, et al. Aeronet—a federated instrument network and data archive for aerosol characterization. *Remote sensing of environment*, 66(1):1–16, 1998.
- Q. Hu, P. Goloub, I. Veselovskii, J. Bravo-Aranda, I. Popovici, T. Podvin, M. Haeffelin, A. Lopatin, C. Pietras, X. Huang, et al. Long-range-transported canadian smoke plumes in the lower stratosphere over northern france. *Atmospheric Chemistry and Physics*, 19(2):1173–1193, 2019. doi: 10.5194/acp-19-1173-2019.
- R.-J. Huang, Y. Zhang, C. Bozzetti, K.-F. Ho, J.-J. Cao, Y. Han, K. R. Daellenbach, J. G. Slowik, S. M. Platt, F. Canonaco, et al. High secondary aerosol contribution to particulate pollution during haze events in china. *Nature*, 514(7521):218, 2014.
- A. J. Illingworth, H. Barker, A. Beljaars, M. Ceccaldi, H. Chepfer, N. Clerbaux, J. Cole, J. Delanoë, C. Domenech, D. P. Donovan, et al. The earthcare satellite: The next step forward in global measurements of clouds, aerosols, precipitation, and radiation. *Bulletin of the American Meteorological Society*, 96(8):1311–1332, 2015.
- M. Issa Lélé and P. J. Lamb. Variability of the intertropical front (itf) and rainfall over the west african sudan–sahel zone. *Journal of Climate*, 23(14):3984–4004, 2010.
- D. J. Jacob, A. J. Turner, J. D. Maasakkers, J. Sheng, K. Sun, X. Liu, K. Chance, I. Aben, J. McKeever, and C. Frankenberg. Satellite observations of atmospheric methane and their value for quantifying methane emissions. *Atmospheric Chemistry and Physics*, 16(22):14371–14396, 2016.

- S. Janicot, C. D. Thorncroft, A. Ali, N. Asencio, G. J. Berry, O. Bock, B. Bourlès, G. Carniaux, F. Chauvin, A. Deme, et al. Large-scale overview of the summer monsoon over west africa during the amma field experiment in 2006. In *Annales Geophysicae*, volume 26, pages 2569–2595, 2008.
- A. Jones, D. Roberts, and A. Slingo. A climate model study of indirect radiative forcing by anthropogenic sulphate aerosols. *Nature*, 370(6489):450, 1994.
- N. Kaaden, A. Massling, A. Schladitz, T. Müller, K. Kandler, L. Schütz, B. Weinzierl, A. Petzold, M. Tesche, S. Leinert, et al. State of mixing, shape factor, number size distribution, and hygroscopic growth of the saharan anthropogenic and mineral dust aerosol at tinfou, morocco. *Tellus B: Chemical and Physical Meteorology*, 61(1):51–63, 2009.
- M. Kahnert, T. Nousiainen, H. Lindqvist, and M. Ebert. Optical properties of light absorbing carbon aggregates mixed with sulfate: assessment of different model geometries for climate forcing calculations. *Optics express*, 20(9):10042–10058, 2012.
- F. Kaly, B. Marticoréna, B. Chatenet, J.-L. Rajot, S. Janicot, A. Niang, H. Yahi, S. Thiria, A. Maman, A. Zakou, et al. Variability of mineral dust concentrations over west africa monitored by the sahelian dust transect. *Atmospheric Research*, 164:226–241, 2015.
- G. Kattawar, A. T. Young, and T. J. Humphreys. Inelastic scattering in planetary atmospheres. i-the ring effect, without aerosols. *The Astrophysical Journal*, 243:1049–1057, 1981.
- J. D. Klett. Lidar inversion with variable backscatter/extinction ratios. *Applied Optics*, 24(11):1638–1643, 1985.
- T. Koop, B. Luo, A. Tsias, and T. Peter. Water activity as the determinant for homogeneous ice nucleation in aqueous solutions. *Nature*, 406(6796):611, 2000.
- C. Leck and E. Keith Bigg. Comparison of sources and nature of the tropical aerosol with the summer high arctic aerosol. *Tellus B: Chemical and Physical Meteorology*, 60(1): 118–126, 2008.

- P. F. Levelt, G. H. van den Oord, M. R. Dobber, A. Malkki, H. Visser, J. de Vries, P. Stammes, J. O. Lundell, and H. Saari. The ozone monitoring instrument. *IEEE Transactions on geoscience and remote sensing*, 44(5):1093–1101, 2006.
- A. Lopatin. *Enhanced Remote Sensing of atmospheric aerosol by joint inversion of active and passive remote sensing observations*. PhD thesis, Lille 1, 2013.
- A. Lopatin, O. Dubovik, A. Chaikovsky, P. Goloub, T. Lapyonok, D. Tanré, and P. Litvinov. Enhancement of aerosol characterization using synergy of lidar and sun-photometer coincident observations: the GARRLiC algorithm. *Atmospheric Measurement Techniques*, 6(8):2065–2088, 2013. doi: 10.5194/amt-6-2065-2013.
- L. Lorentz. Lysbevaegelsen i og uden for en af plane lysbølger belyst kugle. *Vidensk. Selk. Skr.*, 6:1–62, 1890.
- G. Luderer, J. Trentmann, T. Winterrath, C. Textor, M. Herzog, H. Graf, and M. Andreae. Modeling of biomass smoke injection into the lower stratosphere by a large forest fire (part ii): sensitivity studies. *Atmospheric Chemistry and Physics*, 6(12):5261–5277, 2006.
- I. Manolis, S. Grabarnik, J. Caron, J.-L. Bézy, M. Loiselet, M. Betto, H. Barré, G. Mason, and R. Meynard. The metop second generation 3mi instrument. In *Sensors, Systems, and Next-Generation Satellites XVII*, volume 8889, page 88890J. International Society for Optics and Photonics, 2013.
- T. Marbach, P. Phillips, A. Lacan, and P. Schlüssel. The multi-viewing,-channel,-polarisation imager (3mi) of the eumetsat polar system-second generation (eps-sg) dedicated to aerosol characterisation. In *Sensors, Systems, and Next-Generation Satellites XVII*, volume 8889, page 88890I. International Society for Optics and Photonics, 2013.
- S. Menon, J. Hansen, L. Nazarenko, and Y. Luo. Climate effects of black carbon aerosols in china and india. *Science*, 297(5590):2250–2253, 2002.
- G. Mie. Beiträge zur optik trüber medien, speziell kolloidaler metallösungen. *Annalen der physik*, 330(3):377–445, 1908.

- R. B. Miles, W. R. Lempert, and J. N. Forkey. Laser rayleigh scattering. *Measurement Science and Technology*, 12(5):R33–R51, 2001.
- M. I. Mishchenko, L. D. Travis, R. A. Kahn, and R. A. West. Modeling phase functions for dustlike tropospheric aerosols using a shape mixture of randomly oriented polydisperse spheroids. *Journal of Geophysical Research: Atmospheres*, 102(D14):16831–16847, 1997.
- M. I. Mishchenko, L. D. Travis, and A. A. Lacis. *Scattering, absorption, and emission of light by small particles*. Cambridge university press, 2002.
- M. I. Mishchenko, J. M. Dlugach, and L. Liu. Linear depolarization of lidar returns by aged smoke particles. *Applied optics*, 55(35):9968–9973, 2016.
- W. Morgan, J. Allan, M. Flynn, E. Darbyshire, D. Liu, K. Szpek, J. Langridge, B. Johnson, J. Haywood, K. Longo, et al. Black carbon over the amazon during sambba: it gets everywhere. In *AGU Fall Meeting Abstracts*, 2014.
- D. Müller, U. Wandinger, and A. Ansmann. Microphysical particle parameters from extinction and backscatter lidar data by inversion with regularization: theory. *Applied Optics*, 38(12):2346–2357, 1999.
- D. Müller, I. Mattis, U. Wandinger, A. Ansmann, D. Althausen, O. Dubovik, S. Eckhardt, and A. Stohl. Saharan dust over a central european earlinet-aeronet site: Combined observations with raman lidar and sun photometer. *Journal of Geophysical Research: Atmospheres*, 108(D12), 2003.
- D. Müller, A. Ansmann, I. Mattis, M. Tesche, U. Wandinger, D. Althausen, and G. Pisani. Aerosol-type-dependent lidar ratios observed with raman lidar. *Journal of Geophysical Research: Atmospheres*, 112(D16202), 2007. doi: 10.1029/2006JD008292.
- D. Müller, A. Ansmann, V. Freudenthaler, K. Kandler, C. Toledano, A. Hiebsch, J. Gasteiger, M. Esselborn, M. Tesche, B. Heese, et al. Mineral dust observed with aeronet sun photometer, raman lidar, and in situ instruments during samum 2006: Shape-dependent particle properties. *Journal of Geophysical Research: Atmospheres*, 115(D11), 2010a.

- D. Müller, B. Weinzierl, A. Petzold, K. Kandler, A. Ansmann, T. Müller, M. Tesche, V. Freudenthaler, M. Esselborn, B. Heese, et al. Mineral dust observed with aeronet sun photometer, raman lidar, and in situ instruments during samum 2006: Shape-independent particle properties. *Journal of Geophysical Research: Atmospheres*, 115 (D7), 2010b.
- T. Murayama, D. Müller, K. Wada, A. Shimizu, M. Sekiguchi, and T. Tsukamoto. Characterization of asian dust and siberian smoke with multi-wavelength raman lidar over tokyo, japan in spring 2003. *Geophysical Research Letters*, 31(L23103), 2004. doi: 10.1029/2004GL021105.
- W. Murphy. Studies of gaseous molecules by raman spectroscopy. *TrAC Trends in Analytical Chemistry*, 7(2):64–67, 1988.
- T. Nakajima, S.-C. Yoon, V. Ramanathan, G.-Y. Shi, T. Takemura, A. Higurashi, T. Takamura, K. Aoki, B.-J. Sohn, S.-W. Kim, et al. Overview of the atmospheric brown cloud east asian regional experiment 2005 and a study of the aerosol direct radiative forcing in east asia. *Journal of Geophysical Research: Atmospheres*, 112(D24), 2007.
- P. Nastos. Meteorological patterns associated with intense saharan dust outbreaks over greece in winter. *Advances in Meteorology*, 2012, 2012.
- H. Nazaryan, M. P. McCormick, and W. P. Menzel. Global characterization of cirrus clouds using calipso data. *Journal of Geophysical Research: Atmospheres*, 113(D16), 2008.
- K. Osada, S. Ura, M. Kagawa, M. Mikami, T. Tanaka, S. Matoba, K. Aoki, M. Shinoda, Y. Kurosaki, M. Hayashi, et al. Wet and dry deposition of mineral dust particles in japan: factors related to temporal variation and spatial distribution. *Atmospheric Chemistry and Physics*, 14(2):1107–1121, 2014.
- A. Papayannis, D. Balis, V. Amiridis, G. Chourdakis, G. Tsaknakis, C. Zerefos, A. Castanho, S. Nickovic, S. Kazadzis, and J. Grabowski. Measurements of saharan dust aerosols over the eastern mediterranean using elastic backscatter-raman lidar, spec-

- trophotometric and satellite observations in the frame of the earlinet project. *Atmospheric Chemistry and Physics Discussions*, 5(2):2075–2110, 2005.
- A. Papayannis, V. Amiridis, L. Mona, G. Tsaknakis, D. Balis, J. Bösenberg, A. Chaikovski, F. De Tomasi, I. Grigorov, I. Mattis, V. Mitev, D. Mueller, S. Nickovic, C. Perez, A. Pietruczuk, G. Pisani, F. Ravetta, V. Rizi, M. Sicard, T. Trickl, M. Wiegner, M. Gerding, and R. Mamouri. Systematic lidar observations of saharan dust over europe in the frame of earlinet (2000–2002). *Journal of Geophysical Research: Atmospheres*, 113(D10204), 2008. doi: 10.1029/2007JD009028.
- C. Pérez, K. Haustein, Z. Janjic, O. Jorba, N. Huneus, J. Baldasano, T. Black, S. Basart, S. Nickovic, R. Miller, et al. Atmospheric dust modeling from meso to global scales with the online nmmb/bsc-dust model—part 1: Model description, annual simulations and evaluation. *Atmospheric Chemistry and Physics*, 11(24):13001–13027, 2011.
- D. Pérez-Ramírez, D. Whiteman, I. Veselovskii, A. Kolgotin, M. Korenskiy, and L. Alados-Arboledas. Effects of systematic and random errors on the retrieval of particle microphysical properties from multiwavelength lidar measurements using inversion with regularization. *Atmospheric Measurement Techniques*, 6(11):3039–3054, 2013.
- C. V. Raman. A new radiation. 1928.
- C. Randles, A. Da Silva, V. Buchard, P. Colarco, A. Darmenov, R. Govindaraju, A. Smirnov, B. Holben, R. Ferrare, J. Hair, et al. The merra-2 aerosol reanalysis, 1980 onward. part i: System description and data assimilation evaluation. *Journal of Climate*, 30(17):6823–6850, 2017.
- J. Reichardt, S. Reichardt, M. Hess, and T. McGee. Correlations among the optical properties of cirrus-cloud particles: Microphysical interpretation. *Journal of Geophysical Research: Atmospheres*, 107(D21):AAC–8, 2002.
- L. A. Remer, Y. Kaufman, D. Tanré, S. Mattoo, D. Chu, J. V. Martins, R.-R. Li, C. Ichoku, R. Levy, R. Kleidman, et al. The modis aerosol algorithm, products, and validation. *Journal of the atmospheric sciences*, 62(4):947–973, 2005.

- L.-H. Rivellini, I. Chiapello, E. Tison, M. Fourmentin, A. Féron, A. Diallo, T. N'Diaye, P. Goloub, F. Canonaco, A. S. H. Prévôt, et al. Chemical characterization and source apportionment of submicron aerosols measured in senegal during the 2015 shadow campaign. *Atmospheric Chemistry & Physics*, 17(17), 2017.
- G. Rolph, A. Stein, and B. Stunder. Real-time environmental applications and display system: Ready. *Environmental Modelling & Software*, 95:210–228, 2017.
- L. M. Russell, L. N. Hawkins, A. A. Frossard, P. K. Quinn, and T. S. Bates. Carbohydrate-like composition of submicron atmospheric particles and their production from ocean bubble bursting. *Proceedings of the National Academy of Sciences*, 2009.
- K. Sassen. Lidar cloud research. *The Review of Laser Engineering*, 23(2):148–153, 1995.
- K. Sassen and S. Benson. A midlatitude cirrus cloud climatology from the facility for atmospheric remote sensing. part ii: Microphysical properties derived from lidar depolarization. *Journal of the Atmospheric Sciences*, 58(15):2103–2112, 2001.
- K. Sassen, K. N. Liou, S. Kinne, and M. Griffin. Highly supercooled cirrus cloud water: Confirmation and climatic implications. *Science*, 227(4685):411–413, 1985.
- J. Saturno, B. A. Holanda, C. Pöhlker, F. Ditas, Q. Wang, D. Moran-Zuloaga, J. Brito, S. Carbone, Y. Cheng, X. Chi, et al. Black and brown carbon over central amazonia: Long-term aerosol measurements at the atto site. *Atmospheric Chemistry and Physics*, 18(17):12817–12843, 2018.
- C. B. Schaaf, F. Gao, A. H. Strahler, W. Lucht, X. Li, T. Tsang, N. C. Strugnell, X. Zhang, Y. Jin, J.-P. Muller, et al. First operational brdf, albedo nadir reflectance products from modis. *Remote sensing of Environment*, 83(1-2):135–148, 2002.
- Y. Shao. A model for mineral dust emission. *Journal of Geophysical Research: Atmospheres*, 106(D17):20239–20254, 2001.
- A. Slingo, N. Bharmal, G. Robinson, J. Settle, R. Allan, H. White, P. J. Lamb, M. I. Lélé, D. D. Turner, S. McFarlane, et al. Overview of observations from the radagast experiment in niamey, niger: Meteorology and thermodynamic variables. *Journal of Geophysical Research: Atmospheres*, 113(D13), 2008.

- A. Smekal. Zur quantentheorie der dispersion. *Naturwissenschaften*, 11(43):873–875, 1923.
- Z. Song, D. Fu, X. Zhang, Y. Wu, X. Xia, J. He, X. Han, R. Zhang, and H. Che. Diurnal and seasonal variability of pm<sub>2.5</sub> and aod in north china plain: Comparison of merra-2 products and ground measurements. *Atmospheric Environment*, 191:70–78, 2018.
- M. Spada, O. Jorba, C. Pérez García-Pando, Z. Janjic, and J. Baldasano. Modeling and evaluation of the global sea-salt aerosol distribution: sensitivity to size-resolved and sea-surface temperature dependent emission schemes. *Atmospheric Chemistry and Physics*, 13(23):11735–11755, 2013.
- A. Stein, R. R. Draxler, G. D. Rolph, B. J. Stunder, M. Cohen, and F. Ngan. Noaa’s hysplit atmospheric transport and dispersion modeling system. *Bulletin of the American Meteorological Society*, 96(12):2059–2077, 2015.
- T. Storelvmo. Aerosol effects on climate via mixed-phase and ice clouds. *Annual Review of Earth and Planetary Sciences*, 45:199–222, 2017.
- N. Sugimoto, B. Tatarov, A. Shimizu, I. Matsui, and T. Nishizawa. Optical characteristics of forest-fire smoke observed with two-wavelength mie-scattering lidars and a high-spectral-resolution lidar over japan. *SOLA*, 6:93–96, 2010.
- B. Sultan and S. Janicot. Abrupt shift of the itcz over west africa and intra-seasonal variability. *Geophysical Research Letters*, 27(20):3353–3356, 2000.
- D. Tanré, J. Haywood, J. Pelon, J. Léon, B. Chatenet, P. Formenti, P. Francis, P. Goloub, E. Highwood, and G. Myhre. Measurement and modeling of the saharan dust radiative impact: Overview of the saharan dust experiment (shade). *Journal of Geophysical Research: Atmospheres*, 108(D18), 2003.
- D. Tanré, F. Bréon, J. Deuzé, O. Dubovik, F. Ducos, P. François, P. Goloub, M. Herman, A. Lifermann, and F. Waquet. Remote sensing of aerosols by using polarized, directional and spectral measurements within the a-train: the parasol mission. *Atmospheric Measurement Techniques*, 4(7):1383–1395, 2011.

- M. Tesche, A. Ansmann, D. Mueller, D. Althausen, I. Mattis, B. Heese, V. Freudenthaler, M. Wiegner, M. Esselborn, G. Pisani, et al. Vertical profiling of saharan dust with raman lidars and airborne hsrl in southern morocco during samum. *Tellus B: Chemical and Physical Meteorology*, 61(1):144–164, 2009.
- A. S. T. Texeira. AIRS/Aqua L3 Daily Standard Physical Retrieval (AIRS-only) 1 degree x 1 degree V006, Greenbelt, MD, USA, Goddard Earth Sciences Data and Information Services Center (GES DISC), 2013. Accessed: 2018-04-28.
- J. Trentmann, G. Luderer, T. Winterrath, M. Fromm, R. Servranckx, C. Textor, M. Herzog, H.-F. Graf, and M. Andreae. Modeling of biomass smoke injection into the lower stratosphere by a large forest fire (part i): reference simulation. *Atmospheric Chemistry and Physics*, 6(12):5247–5260, 2006.
- A. Tsekeri, V. Amiridis, A. Lopatin, E. Marinou, E. Giannakaki, M. Pikridas, J. Sciare, E. Liakakou, E. Gerasopoulos, S. Duesing, et al. Aerosol absorption profiling from the synergy of lidar and sun-photometry: the actris-2 campaigns in germany, greece and cyprus. In *EPJ Web of Conferences*, volume 176, page 08005. EDP Sciences, 2018.
- C. H. Twohy, S. M. Kreidenweis, T. Eidhammer, E. V. Browell, A. J. Heymsfield, A. R. Bansemer, B. E. Anderson, G. Chen, S. Ismail, P. J. DeMott, et al. Saharan dust particles nucleate droplets in eastern atlantic clouds. *Geophysical Research Letters*, 36(1), 2009.
- F. Unga, M. Choël, Y. Derimian, K. Deboudt, O. Dubovik, and P. Goloub. Microscopic observations of core-shell particle structure and implications for atmospheric aerosol remote sensing. *Journal of Geophysical Research: Atmospheres*, 123(24):13–944, 2018.
- H. van de Hulst. *Light scattering by small particles*. Courier Corporation, 1981.
- I. Veselovskii, A. Kolgotin, V. Griaznov, D. Müller, U. Wandinger, and D. N. Whiteman. Inversion with regularization for the retrieval of tropospheric aerosol parameters from multiwavelength lidar sounding. *Applied optics*, 41(18):3685–3699, 2002.

- I. Veselovskii, O. Dubovik, A. Kolgotin, T. Lapyonok, P. Di Girolamo, D. Summa, D. N. Whiteman, M. Mishchenko, and D. Tanré. Application of randomly oriented spheroids for retrieval of dust particle parameters from multiwavelength lidar measurements. *Journal of Geophysical Research: Atmospheres*, 115(D21203), 2010. doi: 10.1029/2010JD014139.
- I. Veselovskii, D. Whiteman, M. Korenskiy, A. Suvorina, and D. Pérez-Ramírez. Use of rotational raman measurements in multiwavelength aerosol lidar for evaluation of particle backscattering and extinction. *Atmospheric Measurement Techniques*, 8(10): 4111–4122, 2015.
- I. Veselovskii, P. Goloub, T. Podvin, V. Bovchaliuk, Y. Derimian, P. Augustin, M. Fourmentin, D. Tanre, M. Korenskiy, D. Whiteman, et al. Retrieval of optical and physical properties of african dust from multiwavelength raman lidar measurements during the shadow campaign in senegal. *Atmos. Chem. Phys*, 16:7013–7028, 2016.
- I. Veselovskii, P. Goloub, T. Podvin, D. Tanre, A. Ansmann, M. Korenskiy, A. Borovoi, Q. Hu, and D. Whiteman. Spectral dependence of backscattering coefficient of mixed phase clouds over west africa measured with two-wavelength raman polarization lidar: Features attributed to ice-crystals corner reflection. *Journal of Quantitative Spectroscopy and Radiative Transfer*, 202:74–80, 2017.
- I. Veselovskii, P. Goloub, Q. Hu, T. Podvin, D. N. Whiteman, M. Korenskiy, and E. Landulfo. Profiling of  $\text{ch}_4$  background mixing ratio in the lower troposphere with raman lidar: a feasibility experiment. *Atmospheric Measurement Techniques Discussions*, 2018:1–21, 2018a. doi: 10.5194/amt-2018-298. URL <https://www.atmos-meas-tech-discuss.net/amt-2018-298/>.
- I. Veselovskii, P. Goloub, T. Podvin, D. Tanre, A. da Silva, P. Colarco, P. Castellanos, M. Korenskiy, Q. Hu, D. N. Whiteman, et al. Characterization of smoke and dust episode over west africa: comparison of merra-2 modeling with multiwavelength mie-raman lidar observations. *Atmospheric Measurement Techniques*, 11(2), 2018b.
- H. Volten, O. Munoz, E. Rol, J. d. Haan, W. Vassen, J. Hovenier, K. Muinonen, and

- T. Nousiainen. Scattering matrices of mineral aerosol particles at 441.6 nm and 632.8 nm. *Journal of Geophysical Research: Atmospheres*, 106(D15):17375–17401, 2001.
- U. Wandinger. Introduction to lidar in lidar-range-resolved optical remote sensing of the atmosphere. *Springer, New York*, 2005.
- U. Wandinger, V. Freudenthaler, and F. Molero. Earlinet instrument intercomparison campaigns: overview on strategy and results. 2016. URL <https://www.atmos-meas-tech.net/9/1001/2016/amtd-8-10473-2015.pdf>.
- C. Weitkamp. *Lidar: range-resolved optical remote sensing of the atmosphere*, volume 102. Springer Science & Business, 2006.
- D. Whiteman, B. Demoz, and Z. Wang. Subtropical cirrus cloud extinction to backscatter ratios measured by raman lidar during camex-3. *Geophysical research letters*, 31(12), 2004.
- D. N. Whiteman. Examination of the traditional raman lidar technique. ii. evaluating the ratios for water vapor and aerosols. *Applied optics*, 42(15):2593–2608, 2003.
- D. M. Winker, J. R. Pelon, and M. P. McCormick. The calipso mission: Spaceborne lidar for observation of aerosols and clouds. In *Lidar Remote Sensing for Industry and Environment Monitoring III*, volume 4893, pages 1–12. International Society for Optics and Photonics, 2003.
- D. M. Winker, M. A. Vaughan, A. Omar, Y. Hu, K. A. Powell, Z. Liu, W. H. Hunt, and S. A. Young. Overview of the calipso mission and caliop data processing algorithms. *Journal of Atmospheric and Oceanic Technology*, 26(11):2310–2323, 2009.
- P. Yang, K. Liou, M. I. Mishchenko, and B.-C. Gao. Efficient finite-difference time-domain scheme for light scattering by dielectric particles: application to aerosols. *Applied Optics*, 39(21):3727–3737, 2000.
- A. T. Young. Rayleigh scattering. *Phys. Today*, 35(1):42–48, 1982.

- C. S. Zender, R. Miller, and I. Tegen. Quantifying mineral dust mass budgets: Terminology, constraints, and current estimates. *Eos, Transactions American Geophysical Union*, 85(48):509–512, 2004.



**Appendix A:**  
**Supplementary materials**



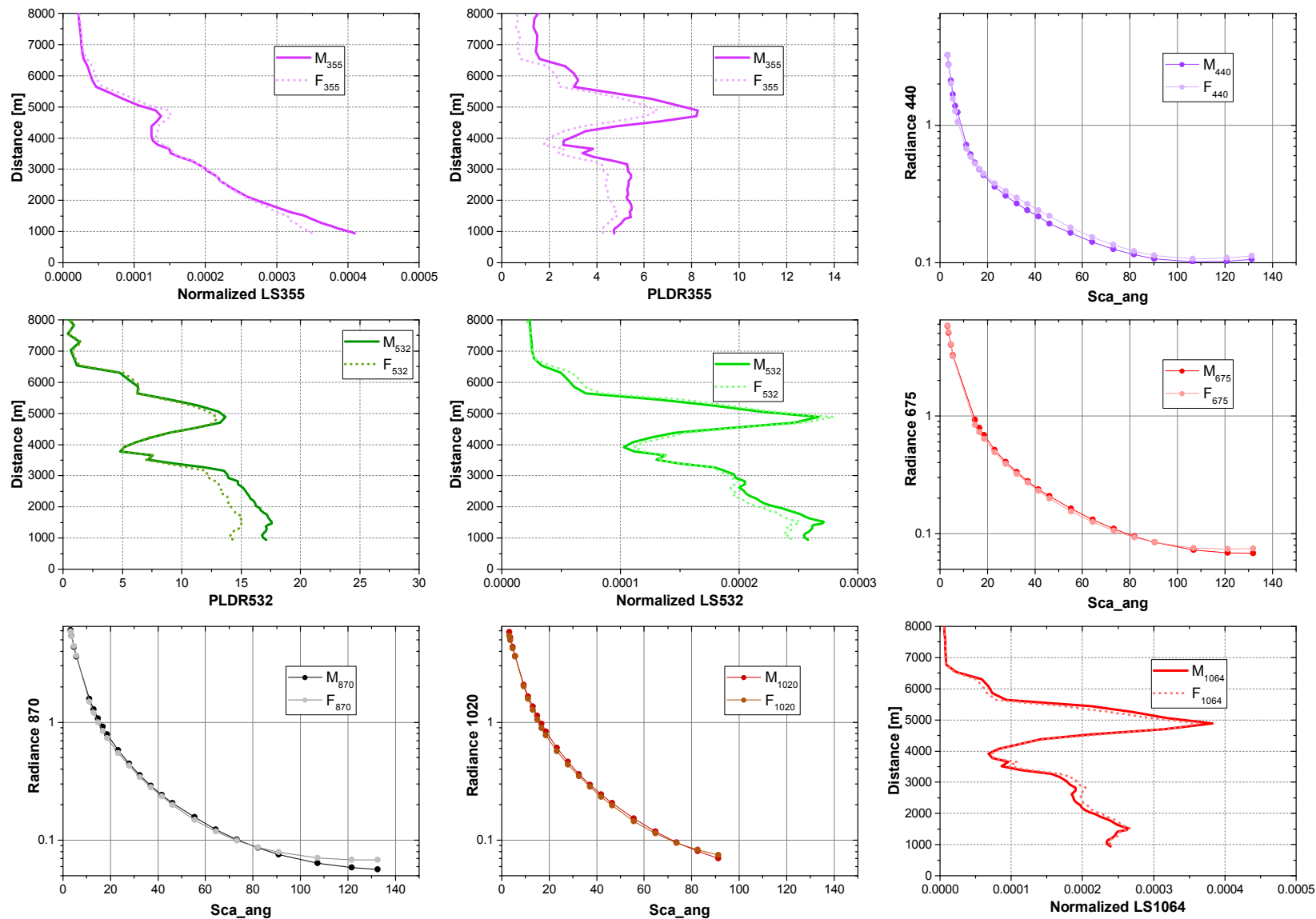
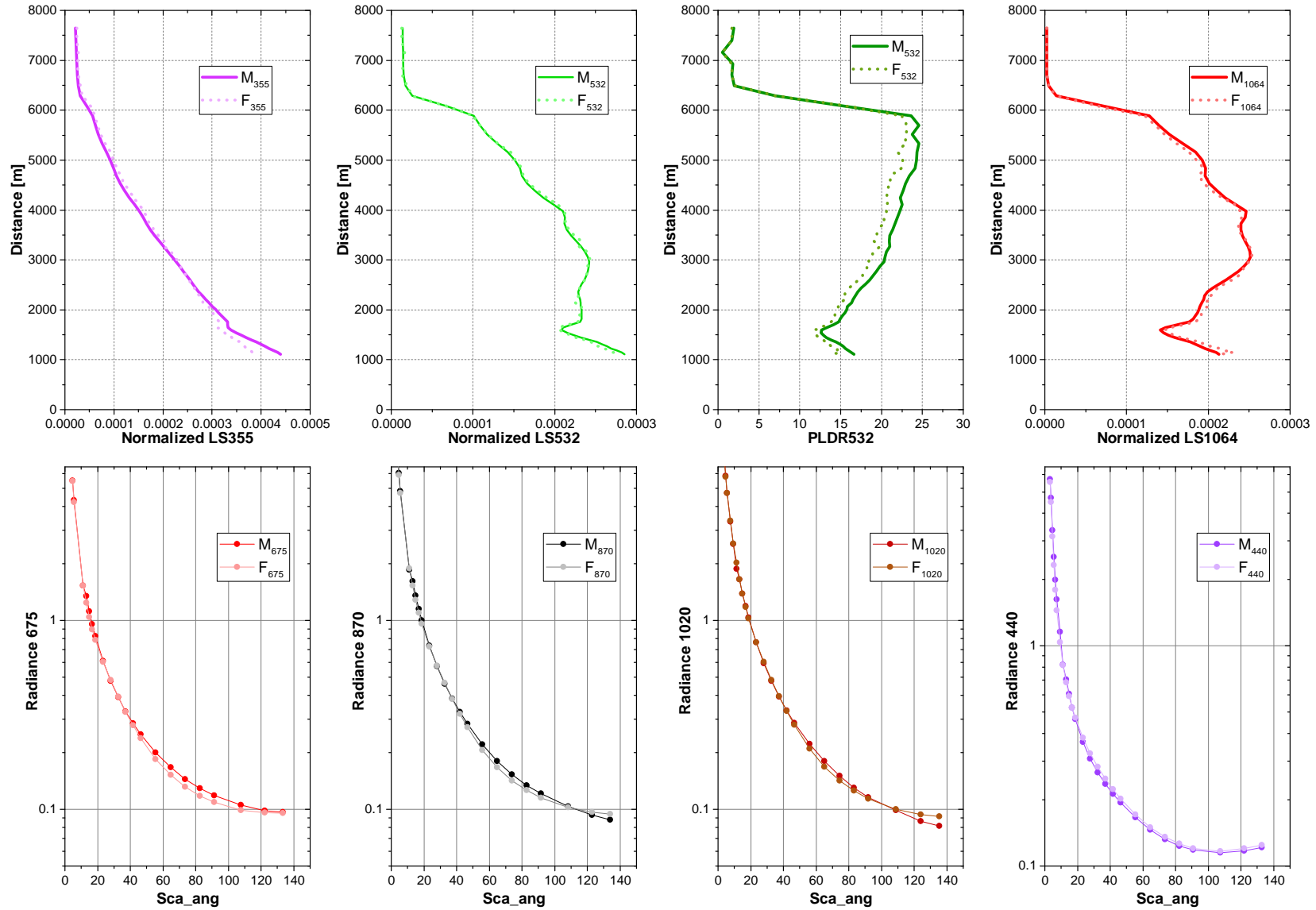
Figure A.1. Measurements and fittings from GARRLiC/GRASP on 20 January 2016. 'M' and 'F' denote *measurements* and *fittings*, respectively.

Figure A.2. Measurements and fittings from GARRLiC/GRASP on 11 April 2015. ‘M’ and ‘F’ denote *measurements* and *fittings*, respectively.



## **Appendix B:**

**Article published on ACPD**





# Long-range-transported Canadian smoke plumes in the lower stratosphere over northern France

Qiaoyun Hu<sup>1</sup>, Philippe Goloub<sup>1</sup>, Igor Veselovskii<sup>2</sup>, Juan-Antonio Bravo-Aranda<sup>3</sup>, Ioana Elisabeta Popovici<sup>1,4</sup>, Thierry Podvin<sup>1</sup>, Martial Haeffelin<sup>3</sup>, Anton Lopatin<sup>5</sup>, Oleg Dubovik<sup>1</sup>, Christophe Pietras<sup>3</sup>, Xin Huang<sup>5</sup>, Benjamin Torres<sup>1</sup>, and Cheng Chen<sup>1</sup>

<sup>1</sup>Univ. Lille, CNRS, UMR8518 – LOA – Laboratoire d'Optique Atmosphérique, 59000 Lille, France

<sup>2</sup>Physics Instrumentation Center of GPI, Troitsk, Moscow, 142190, Russia

<sup>3</sup>Institut Pierre Simon Laplace, École Polytechnique, CNRS, Université Paris-Saclay, 91128 Palaiseau, France

<sup>4</sup>CIMEL Electronique, 75011 Paris, France

<sup>5</sup>GRASP-SAS, Remote sensing developments, 59650 Villeneuve-d'Ascq, France

**Correspondence:** Qiaoyun Hu (qiaoyun.hu@univ-lille.fr)

Received: 29 June 2018 – Discussion started: 9 July 2018

Revised: 14 December 2018 – Accepted: 19 December 2018 – Published: 30 January 2019

**Abstract.** Long-range-transported Canadian smoke layers in the stratosphere over northern France were detected by three lidar systems in August 2017. The peaked optical depth of the stratospheric smoke layer exceeds 0.20 at 532 nm, which is comparable with the simultaneous tropospheric aerosol optical depth. The measurements of satellite sensors revealed that the observed stratospheric smoke plumes were transported from Canadian wildfires after being lofted by strong pyro-cumulonimbus. Case studies at two observation sites, Lille (lat 50.612, long 3.142, 60 m a.s.l.) and Palaiseau (lat 48.712, long 2.215, 156 m a.s.l.), are presented in detail. Smoke particle depolarization ratios are measured at three wavelengths: over 0.20 at 355 nm, 0.18–0.19 at 532 nm, and 0.04–0.05 at 1064 nm. The high depolarization ratios and their spectral dependence are possibly caused by the irregular-shaped aged smoke particles and/or the mixing with dust particles. Similar results are found by several European lidar stations and an explanation that can fully resolve this question has not yet been found. Aerosol inversion based on lidar  $2\alpha + 3\beta$  data derived a smoke effective radius of about 0.33  $\mu\text{m}$  for both cases. The retrieved single-scattering albedo is in the range of 0.8 to 0.9, indicating that the smoke plumes are absorbing. The absorption can cause perturbations to the temperature vertical profile, as observed by ground-based radiosonde, and it is also related to the ascent of the smoke plumes when exposed in sunlight. A direct radiative forc-

ing (DRF) calculation is performed using the obtained optical and microphysical properties. The calculation revealed that the smoke plumes in the stratosphere can significantly reduce the radiation arriving at the surface, and the heating rate of the plumes is about 3.5 K day<sup>-1</sup>. The study provides a valuable characterization for aged smoke in the stratosphere, but efforts are still needed in reducing and quantifying the errors in the retrieved microphysical properties as well as radiative forcing estimates.

## 1 Introduction

Stratospheric aerosols play an important role in the global radiative budget and chemistry–climate coupling (Deshler, 2008; Kremser et al., 2016; Shepherd, 2007). Volcanic eruption is a significant contributor of stratospheric aerosols because the explosive force could be sufficient enough to penetrate the tropopause, which is regarded as a barrier to the convection between the troposphere and stratosphere. In addition to volcanic eruption, biomass burning has been reported to be one important constituent of the increasing stratospheric aerosols (Hofmann et al., 2009; Khaykin et al., 2017; Zuev et al., 2017). The pyro-cumulonimbus clouds generated in intense fire activities have the potential to elevate fire emissions from the planetary boundary layer to the stratosphere

(Luderer et al., 2006; Trentmann et al., 2006). Stratospheric smoke plumes have been reported in many previous studies (Fromm et al., 2000, 2005; Fromm and Servranckx, 2003; Sugimoto et al., 2010).

In the summer of 2017, intense wildfires spread in the west and north of Canada. By mid-August, the burnt area had grown to almost 9000 km<sup>2</sup> in British Columbia, which broke the record set in 1958 (see <https://www.nceo.ac.uk/article/the-2017-canadian-wildfires-a-satellite-perspective/>, last access: 15 January 2019). The severe wildfires generated strong pyro-cumulonimbus clouds, which were recorded by the satellite imagery MODIS (Moderate Resolution Imaging Spectrometer). The GOES-15 (Geostationary Operational Environmental Satellite) detected five pyro-cumulonimbus clouds in British Columbia on 12 August 2017 (see <https://pyrocb.ssec.wisc.edu>, last access: 15 January 2019). Smoke plumes in the troposphere and lower stratosphere were observed by several European lidar stations in August and September 2017. Ansmann et al. (2018) and Haerig et al. (2018) observed stratospheric and tropospheric smoke layers originating from Canadian wildfires on 21–23 August 2017 in Leipzig, Germany. The maximum extinction coefficient of the smoke layers reached 0.5 km<sup>-1</sup>, about 20 times higher than the observation 10 months after the eruption of the Pinatubo volcano in 1991 (Ansmann et al., 1997). Khaykin et al. (2018) reported Canadian smoke layers in the stratosphere over southern France in August 2017 and they found that the smoke plumes can travel the whole globe (at middle latitudes) in about 3 weeks.

Reoccurring aerosol layers in the troposphere and lower stratosphere were detected by the lidar systems in northern France during 19 August and 12 September 2017. In this study, we present the stratospheric smoke observations from two French lidar stations: Lille (lat 50.612, long 3.142, 60 m a.s.l.) and Palaiseau (lat 48.712, long 2.215, 156 m a.s.l.), and a mobile lidar system. Satellite measurements from multiple sensors, including UVAI (ultraviolet aerosol index) from the OMPS NM (Ozone Mapping and Profiler Suite, Nadir Mapper), CO (carbon monoxide) concentration from AIRS (Atmospheric Infrared Sounder), and backscatter coefficient and depolarization ratio profiles from CALIPSO (Cloud-Aerosol Lidar and Infrared Pathfinder Satellite Observations) help identify the source and the transport pathway of the smoke layers. This study is focused on the retrieval of the aerosol optical and microphysical properties using lidar measurements. Further, the radiative effect of the smoke layer is presented.

## 2 Methodology

### 2.1 Lidar data processing

In this subsection, we present the method for processing lidar measurements and the error estimation is presented in

the Appendix. The Raman lidar technique (Ansmann et al., 1992) allows an independent calculation of extinction and backscatter coefficients. When the nitrogen Raman signal is not available, the Klett method (Klett, 1985) is used to calculate the extinction and backscatter coefficients, based on an assumption of the aerosol lidar ratio.

In this study, the stratospheric aerosol layers are at high altitudes at which the signal-to-noise ratio of Raman channels is not sufficient to obtain a high-quality extinction profile; therefore, we choose the Klett method.

To reduce the dependence of Klett inversion on the assumption of lidar ratio, we use a pre-calculated optical depth of the stratospheric aerosol layer as an additional constraint. We test a series of lidar ratios in the range of 10–120 sr and apply independent Klett inversion with each lidar ratio at a step of 0.5 sr. The integral of the extinction coefficient over the stratospheric layer, expressed below, is compared with the pre-calculated optical depth.

$$\tau^i(\lambda) = \int_{r_{\text{base}}}^{r_{\text{top}}} \alpha_a(\lambda, r) dr, \quad (1)$$

where  $\tau^i$  is the integral of extinction coefficient  $\alpha_a$ , derived from Klett inversion.  $r$  is the distance, the subscripts “top” and “base” represent the top and base of the stratospheric aerosol layer, and  $\lambda$  is the lidar wavelength.

The pre-calculated optical depth is derived from the elastic channel at 355 and 532 nm. The method is widely used in cirrus cloud studies (Platt, 1973; Young, 1995). By comparing the lidar signal with the molecular backscattered lidar signal, we found there is only molecular scattering below and above the smoke plumes. So we can calculate the optical depth of the smoke plumes as below:

$$\tau^u(\lambda) = \frac{1}{2} \ln \frac{\overline{P}_{\text{base}}(\lambda) r_{\text{base}}^2 \beta_m(\lambda, r_{\text{top}})}{\overline{P}_{\text{top}}(\lambda) r_{\text{top}}^2 \beta_m(\lambda, r_{\text{base}})} - \int_{r_{\text{base}}}^{r_{\text{top}}} \alpha_m(\lambda, r) dr, \quad (2)$$

where  $\tau^u$  is the optical depth of the stratospheric smoke layers.  $\overline{P}_{\text{top}}$  and  $\overline{P}_{\text{base}}$  represent the mean lidar signal at the top and the base of the stratospheric layer.  $\alpha_m$  and  $\beta_m$  are the molecular extinction and backscatter coefficients. We calculate the lidar signal mean within a window of 0.5 km at the top and the base of the aerosol layer to get  $\overline{P}(r_{\text{top}}, \lambda)$  and  $\overline{P}(r_{\text{base}}, \lambda)$ . We use this method to estimate the optical depth of the stratospheric layer for LILAS and IPRAL measurements. The lidar ratio leading to the best agreement of  $\tau^i$  and  $\tau^u$  is accepted as the retrieved lidar ratio of the stratospheric aerosol layer. We apply Klett inversion only to the stratospheric aerosol layer, from 1 km below the layer base to 1 km above the layer top. Therefore, the impact of tropospheric aerosols is excluded. Compared to the Raman method, the extinction and backscatter coefficients calculated from the Klett method are not independent because of the assumed

vertically constant aerosol lidar ratio. But in this study, the smoke particles are well mixed, so the vertical variation in lidar ratio is expected to be not significant. Additionally, using the Klett method avoids the effects of vertical smoothing that occur to the Raman derived extinction profile.

The particle linear depolarization ratio,  $\delta_p$ , is written as

$$\delta_p = \frac{R\delta_v(\delta_m + 1) - \delta_m(\delta_v + 1)}{R(\delta_m + 1) - (\delta_v + 1)}, \quad (3)$$

where  $R$  is the backscatter ratio,  $\delta_v$  is the volume linear depolarization ratio, and  $\delta_m$  is the molecular depolarization ratio.  $R$  is defined as the ratio of the total backscatter coefficient to the molecular backscatter coefficient.  $\delta_m = 0.004$  is used in the calculation of particle linear depolarization ratio.  $\delta_v$  is the ratio of the perpendicularly backscattered signal to the parallel backscattered signal, multiplied by a calibration coefficient. The depolarization calibration is designed to calibrate the electro-optical ratio between the perpendicular and parallel channels and is performed following the procedure proposed by Freudenthaler et al. (2009). The particle linear depolarization ratio is a parameter related to the shape of aerosol particles, and it is usually used in the lidar community for aerosol typing. The particle linear depolarization ratio of spherical particles is zero. For irregular-shaped particles, for example ice particles in cirrus clouds, the measured particle linear depolarization is about 0.40 (Sassen et al., 1985; Veselovskii et al., 2017).

## 2.2 Aerosol inversion and radiative forcing estimation

The  $3\beta + 2\alpha$  from lidar observations can be inverted to obtain particle microphysical parameters. The regularization algorithm is used to retrieve size distribution, wavelength-independent complex refractive indices, particle number, and surface and volume concentrations (Müller et al., 1999; Veselovskii et al., 2002). We apply GRASP (Generalized Retrieval of Aerosol and Surface Properties) to calculate the DRF (direct radiative forcing) effect of the stratospheric aerosol layer. GRASP is the first unified algorithm developed for characterizing atmospheric properties gathered from a variety of remote-sensing observations. Depending on the input data, GRASP can retrieve columnar and vertically resolved aerosol properties and surface reflectance (Dubovik et al., 2014). As a branch of the GRASP algorithm, GARRLiC (Generalized Aerosol Retrieval from Radiometer and Lidar Combined data, called GARRLiC/GRASP hereafter) algorithm was developed for the inversion of coincident single- or multi-wavelength lidar and sun photometer measurements (Lopatin et al., 2013; Bovchaliuk et al., 2016). The two main modules of GARRLiC/GRASP are the forward model and numerical inversion module. The forward module simulates the atmospheric radiation by using radiative transfer and by accounting for the interaction between light and trace gases, aerosols, and underlying surfaces. The aerosol scattering properties in the atmosphere are represented by one

or two aerosol components, whose optical properties can be described using a mixture of spheres and spheroids and are vertically independent. The vertically resolved optical properties, such as the extinction and backscatter coefficients etc., measured by lidar, are described by varying the aerosol vertical concentration. The forward model includes a radiative transfer model in order to simulate multiple types of observations. The radiative transfer equation in GARRLiC/GRASP is solved using this parallel plane approximation. The atmosphere is divided into a series of parallel planes and the optical properties of each parallel plane can be represented by the input parameters. The radiative transfer model is based on the study of Lenoble et al. (2007). The numerical inversion module follows the multi-term least-squares method strategy and derives a group of unknown parameters that fits the observations.

In this study, we apply the forward model of GARRLiC/GRASP to estimate the forcing effect of the observed stratospheric plume in contrast to a standard Rayleigh atmosphere. The input parameters for DRF are the retrieved aerosol microphysical properties from the regularization algorithm, including the size distribution, the complex refractive indices, and the assumed sphere fraction; the aerosol vertical distribution of the stratospheric plume; and surface BRDF (bidirectional reflectance distribution function) parameters. The forward model of GARRLiC/GRASP can produce downward and upward broadband flux, covering the 0.2–4.0  $\mu\text{m}$  spectrum, at vertical levels specified by the users. Hence, we can calculate the DRF and the heating rate specific to smoke plume.

## 3 Ground-based and satellite observations

### 3.1 Simultaneous lidar and sun photometer observations

LILAS (Lille Lidar Atmospheric Study) is a multi-wavelength Raman lidar (Bovchaliuk et al., 2016; Veselovskii et al., 2016) operated at LOA (Laboratoire d'Optique Atmosphérique, Lille, France). The LILAS system is transportable and has three elastic channels (355, 532, and 1064 nm), with the capability of measuring the depolarization ratios at these wavelengths. Further, it has three Raman channels at 387, 408, and 530 nm. The IPRAL system (IPSL Hi-Performance multi-wavelength Raman Lidar; Bravo-Aranda et al., 2016; Haeffelin et al., 2005) is a multi-wavelength Raman lidar operated at SIRTA (Site Instrumental de Recherche par Télédétection Atmosphérique, Palaiseau, France). The distance between the two systems is around 300 km. Lidar IPRAL has the same elastic channels as LILAS, but the three Raman channels are 387, 408, and 607 nm. In the IPRAL system, the depolarization ratio is only measured at 355 nm. The two lidar systems were operated independently and both observed reoccur-

ring smoke layers in the lower stratosphere during the period from 19 August to 12 September 2017. In addition, sun photometer measurements are available at Lille and Palaiseau, which are both affiliated stations of AERONET (AEROSol RObotic NETwork). The LILAS and IPRAL lidar systems are affiliated with EARLINET (European Aerosol Research Lidar Network) (Bösenberg et al., 2003; Böckmann et al., 2004; Matthais et al., 2004; Papayannis et al., 2008; Pappalardo et al., 2014). Both systems perform regular measurements and follow the standard EARLINET data quality check and calibration procedures (Freudenthaler et al., 2018).

On 29 August, three lidar systems in northern France simultaneously observed a stratospheric aerosol layer. The three lidar systems are LILAS, IPRAL, and a single wavelength (532 nm) CIMEL micro-pulse lidar, which is set up in a light mobile system, MAMS (Mobile Aerosol Monitoring System; Popovici et al., 2018), to explore aerosol spatial variability. MAMS was traveling between Palaiseau and Lille on 28 and 29 August. MAMS is equipped with a mobile sun photometer, PLASMA (Photomètre Léger Aéroporté pour la Surveillance des Masses d' Air, Karol et al., 2013), capable of measuring columnar aerosol optical depth (AOD) along the route. The configuration of the three lidar systems is summarized in Table 1.

Figure 1 shows the normalized lidar range-corrected signals and columnar AOD at 532 nm derived from sun photometer measurements on 29 August 2017. The aerosol layers in the lower stratosphere, stretching from 16 to 20 km, were detected by the three lidars. The IPRAL lidar system in Palaiseau detected the aerosol layer in the range of 16–20 km on 29 August. The columnar AOD showed no significant variations, staying between 0.30 and 0.40, from 10:00 to 16:00 UTC and started decreasing from 17:00 UTC. Along the route from Palaiseau to Lille, MAMS lidar observed a layer between 16 and 20 km consisting of two well-separated layers. The columnar AOD was very stable, around 0.40, all along the route from Palaiseau to Lille. Lidar LILAS in Lille observed a shallow layer between 18 and 20 km at about 08:00 UTC on 29 August. The thickness of the layer increased to 4 km until 16:00 UTC. The columnar AOD increased from 0.20 to 0.40 from 08:00 to 14:00 UTC. The lidar quick look indicated that the aerosol content in the lower troposphere did not show significant variations during 08:00 and 12:00 UTC, so the increased optical depth, 0.2, came mainly from the contribution of the stratospheric aerosol layer.

Figure 2 shows the lidar range-corrected signal at 1064 nm on 24–25 August 2017. The plume between 17 and 18.5 km is the smoke layer. Due to cirrus clouds and low clouds in the troposphere, the lidar signals in the plume are interrupted. In the nighttime, the plume base is stable at about 17 km. Just starting from the sunrise time at 04:51 UTC, a gradual and obvious ascent is observed. In 3–4 h, the plume base ascended by about 0.6 km. Between 10:00 and 16:00 UTC, the

plume base stayed stable. The ascent of smoke plume was also presented in Ansmann et al. (2018) and Khaykin et al. (2018). Khaykin et al. (2018) mentioned that the plume ascended very fast during the first few days after being injected into the troposphere. Based on the observation in Fig. 2, we derived the ascent rate of approximately 2.1–2.8 km per day, considering that the sunshine duration is 14 h (according to the latitude of Lille site) and that the vertical speed of the plume is constant. Ansmann et al. (2018) explained that the ascent of the plume may be related to the absorption of soot-containing aerosols and the wind velocity in the stratosphere. Figure 2 shows that the plume does not continuously ascend in the daytime. One possible explanation we infer is that the self-heating and the wind shear reached an equilibrium point in the plume, so it moved neither upward nor downward.

### 3.2 Radiosonde measurements

We take the radiosonde measurements from two stations closest to the lidar sites: Trappes (48.77° N, 1.99° E, France) and Beauvechain (50.78° N, 4.76° E, Belgium). Trappes is about 20 km from Palaiseau and Beauvechain is 120 km from Lille. Considering the large spatial distribution of the stratospheric aerosols, it is obvious that the radiosonde passed through this stratospheric smoke layer. Figure 3 shows the temperature at 00:00 and 12:00 UTC on 29 August for Trappes and 21:00 UTC on 29 August for Beauvechain. To compare, we plot the temperature profile of Trappes at 12:00 UTC on 21 August, when no stratospheric aerosol layers presented. The temperature profiles clearly show an enhancement between 16 and 20 km, which coincides with the altitude at which the stratospheric plumes appear. The spatial–temporal occurrence of this temperature enhancement and the stratosphere plume at two independent stations indicate that they are directly correlated. Fromm et al. (2005, 2008) also presented temperature increase in the stratospheric smoke layers.

### 3.3 MODIS measurements

MODIS is a key instrument onboard the Terra and Aqua satellites. Terra MODIS and Aqua MODIS view the entire Earth's surface every 1 to 2 days. Several episodes of Canadian wildfires have been observed by MODIS since early July 2017. On 12 August, MODIS observed a thick grey plume arising from British Columbia in the west of Canada (not shown; please see the web page of WorldView: <https://worldview.earthdata.nasa.gov>, last access: 15 January 2019). Figure 4 shows the Earth's true color image overlaid with the fires and thermal anomalies on 15 August 2017 when the plumes had spread over a large area. The region marked with the green dashed line is a huge visible smoke plume and in its southwest MODIS detected a belt of fire spots. Additionally, during the week of 13–19 August, MODIS (see <https://worldview.earthdata.nasa.gov>, last

**Table 1.** Three involved lidar systems and their configuration and locations.

Name	Configuration	Location
LILAS	Elastic + depolarization: 355, 532, 1064 nm Raman: 387, 408 (water vapor), 530 nm	LOA, Lille
IPRAL	Elastic: 355 (depolarization), 532, 1064 nm Raman: 387, 408 (water vapor), 608 nm	SIRTA, Palaiseau
MAMS lidar	Elastic: 532 nm	from Palaiseau to Lille (29 August)

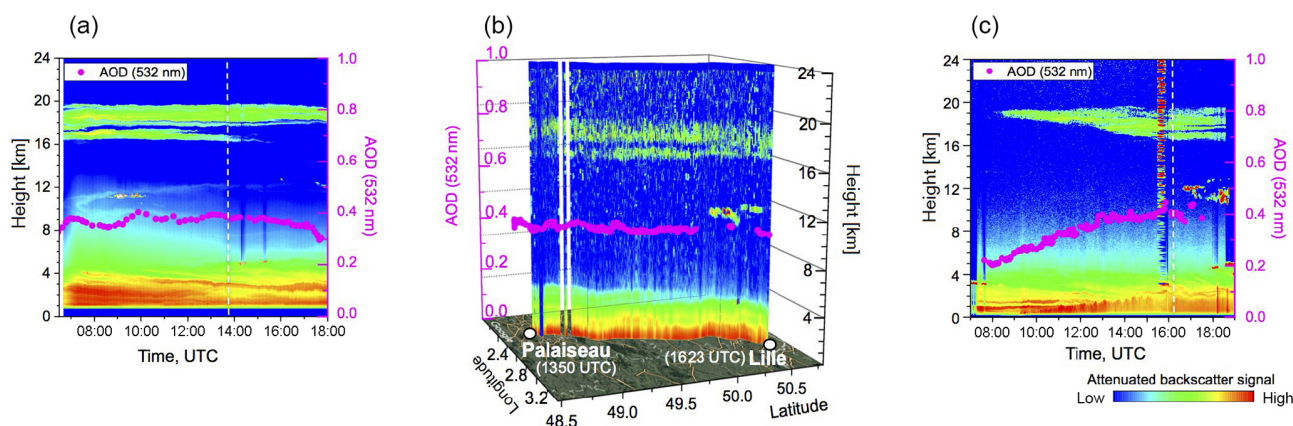


**Figure 1.** Lidar range-corrected signal and columnar AOD from the sun photometer at 532 nm on 29 August 2017. (a) IPRAL system in Palaiseau. (b) MAMS lidar en route from Palaiseau to Lille. (c) LILAS in Lille. Columnar AOD measurements are interpolated from AERONET (Lille and Palaiseau) and PLASMA (mobile system) measurements. MAMS started from Palaiseau at 13:53 UTC and arrived in Lille at 16:23 UTC. The departure and arriving times are indicated in (a) and (c) with the dashed white lines.

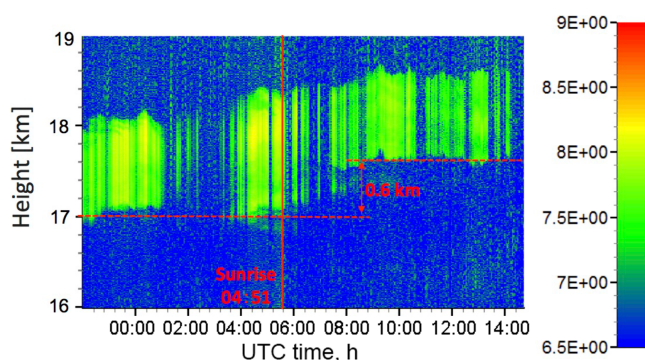


**Figure 2.** Lidar range-corrected signal at 1064 nm on 24–25 August 2017 measured by LILAS. The solid red line indicates the sunrise time. The two dashed red lines point out the approximate layer base before and after the sunrise. The sunrise and sunset times are 04:51 and 20:47 UTC, respectively. The corresponding daytime duration is about 14 h.

access: 15 January 2019) observed a widespread cloud coverage over Canada and showed that cloud layers were overshadowed by the smoke plumes, meaning that the plumes were lofted above the cloud layers, as shown in Fig. 4.

### 3.4 OMPS NM UVAI maps

UVAI is a widely used parameter in characterizing UV-absorbing aerosols, such as desert dust, carbonaceous aerosols coming from anthropogenic biomass burning, wildfires, and volcanic ash. The UVAI is determined using the 340 and 380 nm wavelength channels and is defined as

$$\text{UVAI} = -100 \times \left\{ \log_{10} \left[ \frac{I_{340}}{I_{380}} \right]_{\text{meas}} - \log_{10} \left[ \frac{I_{340}}{I_{380}} \right]_{\text{calc}} \right\}, \quad (4)$$

where  $I_{340}$  and  $I_{380}$  are the backscattered radiance at 340 and 380 nm. The subscript “meas” represents the measurements and “calc” represents the calculation using a radiative transfer model for pure Rayleigh atmosphere. The UVAI is defined so that positive values correspond to UV-absorbing aerosols and negative values correspond to non-absorbing aerosols (Hsu et al., 1999). The OMPS NM on board the Suomi NPP (National Polar-orbiting Partnership) is designed to measure the total column ozone using backscattered UV

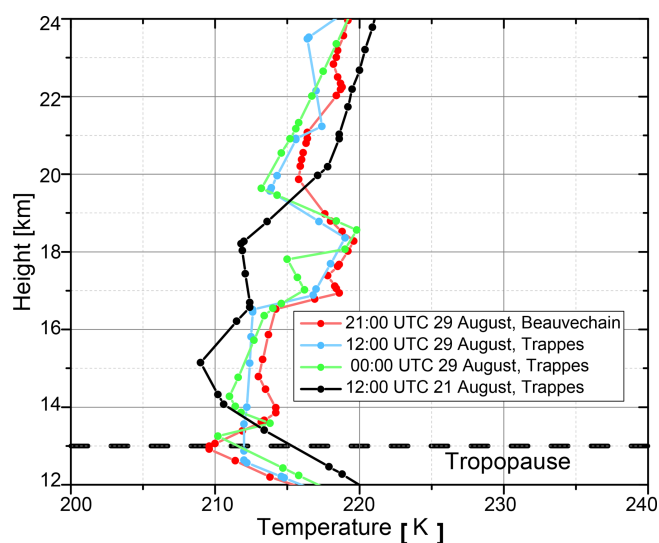


**Figure 3.** Temperature profiles from the radiosonde measurements. The green and cerulean lines are the temperature profiles of Trappes at 00:00 and 12:00 UTC on 29 August 2017. The red line shows the Beauvechain data at 21:00 UTC on 29 August 2017. The black line is for 12:00 UTC on 21 August in Trappes. The horizontal dashed black line at 13 km represents the approximate position of the tropopause.

radiation between 300 and 380 nm. A  $110^\circ$  FOV (field-of-view) telescope enables full daily global coverage (McPeters et al., 2000; Seftor et al., 2014). Figure 5 shows the evolution of UVAI from OMPS NM (Jaross, 2017) every 2 days from 11 to 29 August 2017. The evolution of the UVAI during this event has also been shown in the study of Khaykin et al. (2018). A plume with relatively high UVAI first occurred over British Columbia on 11 August, and the intensity of the plume was moderate. An obvious increase in UVAI from 11 to 13 August was observed over the northwest of Canada. It is a clear indication that the events on 12 August were responsible for the increase in UVAI. From 13 to 17 August, the plume spread in the northwest–southeast direction and the UVAI in the center of the plume reached 10. On 19 August, the plume center reached the Labrador Sea and the forefront of the plume reached Europe. From 21 to 29 August, the UVAI in the map was much lower than the previous week. During this period, we can still distinguish a plume propagating eastward from the Atlantic to Europe, with the UVAI damping during the transport. Figure 5e–j show that Europe was overshadowed by the high-UVAI plume during 19 and 29 August.

### 3.5 AIRS CO maps

AIRS is a continuously operating cross-track scanning sounder on board NASA's Aqua satellite launched in May 2002. AIRS covers the 3.7 to  $16\ \mu\text{m}$  spectral range with 2378 channels and a 13.5 km nadir FOV (Susskind et al., 2014;

Kahn et al., 2014). The daily coverage of AIRS is about 70 % of the globe. AIRS is designed to measure the water vapor and temperature profiles. It includes the spectral features of the key carbon trace gases,  $\text{CO}_2$ ,  $\text{CH}_4$ , and  $\text{CO}$  (Haskins and Kaplan, 1992). The current  $\text{CO}$  product from AIRS is very mature because the spectral signature is strong and the interference of water vapor is relatively low (McMillan et al., 2005).  $\text{CO}$ , as a product of the burning process, can be taken as a tracer of biomass burning aerosols (Andreae et al., 1988) due to its relatively long lifetime of 0.5 to 3 months.  $\text{CO}$  can also originate from anthropogenic sources, for example engines of vehicles (Vallero, 2014). In August 2017, the wild-fire activities were so intense that the  $\text{CO}$  plumes rising from the fire region were much more significant than the background. This strong contrast makes  $\text{CO}$  a good tracer for the transport of the smoke plumes.

Figure 6 shows the evolution of the total column  $\text{CO}$  concentration (Texeira, 2013) every 2 days during the period of 11 to 29 August 2017.  $\text{CO}$  concentration strongly increased in the west and north of Canada from 11 to 13 August, similar to the UVAI shown in Fig. 5. The forefront of the  $\text{CO}$  plume reached the west and north of Europe since 19 August. We find that the spatial distribution and temporal evolution of  $\text{CO}$  are strongly co-related with the UVAI. This correlation is very evident before 21 August. After 21 August, the correlation became weaker, for the UVAI in North America was decreasing fast while the  $\text{CO}$  concentration remained almost unchanged or decreased much more slowly. This is possibly due to the longer lifetime of  $\text{CO}$  compared to UVAI. Combining the MODIS image and the UVAI and  $\text{CO}$  spatial-temporal evolution, we conclude that the aerosol plumes observed in Europe were smoke transported from Canada.

### 3.6 CALIPSO measurements

CALIPSO measurements provide a good opportunity to investigate the vertical structure of the plumes and trace back the transport of the plumes. CALIPSO measures the backscattered signal at 532 and 1064 nm. One parallel channel and one perpendicular channel are coupled to derive the particle linear depolarization ratio at 532 nm. Figure 7a–f present the profiles of the backscatter coefficient and particle linear depolarization ratio at 532 nm, corresponding to the six locations a–f in Fig. 4. These data were obtained from the NASA Langley Research Center Atmospheric Science Data Center. The six locations are intentionally selected, falling in the region with elevated UVAI and  $\text{CO}$  concentration and following the transport pathway of the plume (in Figs. 5 and 6) from Canada to Europe. Figure 7 shows the enhancements of backscatter in the upper troposphere and lower stratosphere. Aerosol and cloud are both possible causes of the backscatter enhancements and can be distinguished by using the particle depolarization ratio. We have examined the temperature profiles over several sites in North America in August 2017 and found that, above 10 km, the temperature drops below

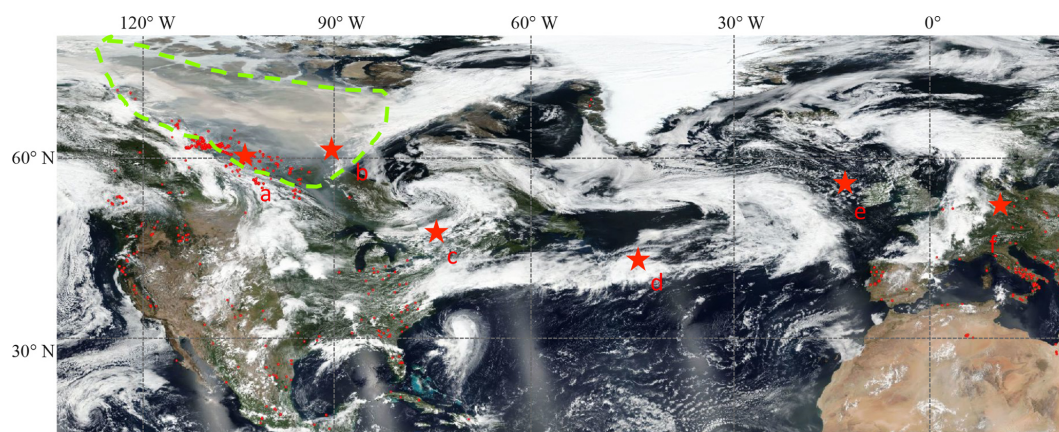


**Figure 4.** The corrected surface reflectance overlaid with fire and thermal anomalies from MODIS (15 August 2017). The region marked with the dashed green line in the northwest indicated a plume generated by fire activities. Six locations (labeled as red stars) on the tracks of CALIPSO are selected: (a) (61.47° N, 106.44° W), (b) (62.79° N, 91.54° W), (c) (46.97° N, 72.22° W), (d) (42.27° N, 42.08° W), (e) (55.97° N, 12.54° W), and (f) (52.37° N, 13.47° E). The corresponding overpass date is 14, 15, 17, 19, 21, and 23 August 2017.

−38 °C; at this temperature clouds consist mainly of ice crystals. The particle depolarization ratio is usually no less than 0.40 for ice cloud and from a few percent to about 0.40 for mixed-phase cloud.

Figure 7a and b show the aerosol layers observed on 14 and 15 August over the north of Canada; both locations lay in the area where MODIS observed a smoke plume on 15 August (Fig. 4) and the area with high UVAI and CO concentration. The particle linear depolarization ratio is about 0.05 in Fig. 7a and 0.10 in Fig. 7b, meaning that it is an aerosol layer instead of ice or mixed-phase cloud. Figure 7c and f show stratospheric layers detected at 10–20 km in height, with the depolarization varying from 0.10 to 0.18. The lower layer at about 9 km in Fig. 7d has a depolarization ratio between 0.20 and 0.45 (median 0.32), which falls into the category of ice or mixed-phase clouds. Profiles in Fig. 7f were captured over Berlin at 01:29 UTC on 23 August. About 150 km to the southwest, a lidar in Leipzig measured stratospheric smoke layers (Haarig et al., 2018). The particle depolarization ratio of CALIPSO at 532 nm on 23 August is consistent with ground-based lidar measurements in Lille and Leipzig, which will be presented in Sect. 4. It should be noted that aerosol types of the plumes in Fig. 7 are quite uncertain in the CALIPSO product. These layers are classified into scattered aerosol types, such as polluted dust, elevated smoke, and volcanic ash. This misclassification could introduce some extent of errors to the backscatter profile and particle depolarization profiles.

## 4 Results and analysis

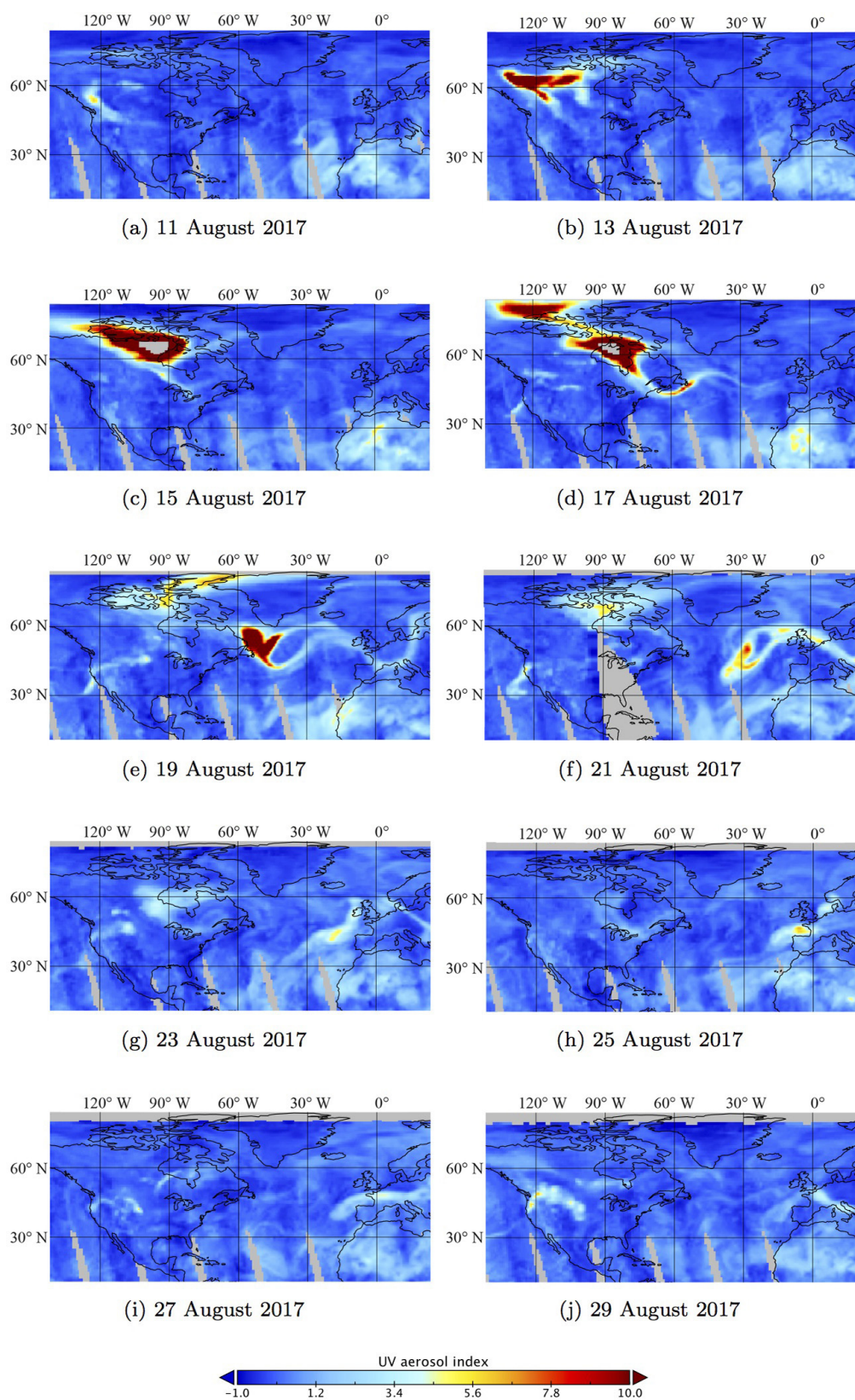
### 4.1 Overview of retrieved optical parameters

We selected and averaged the lidar measurements in 10 time intervals, among which five periods are from the LILAS sys-

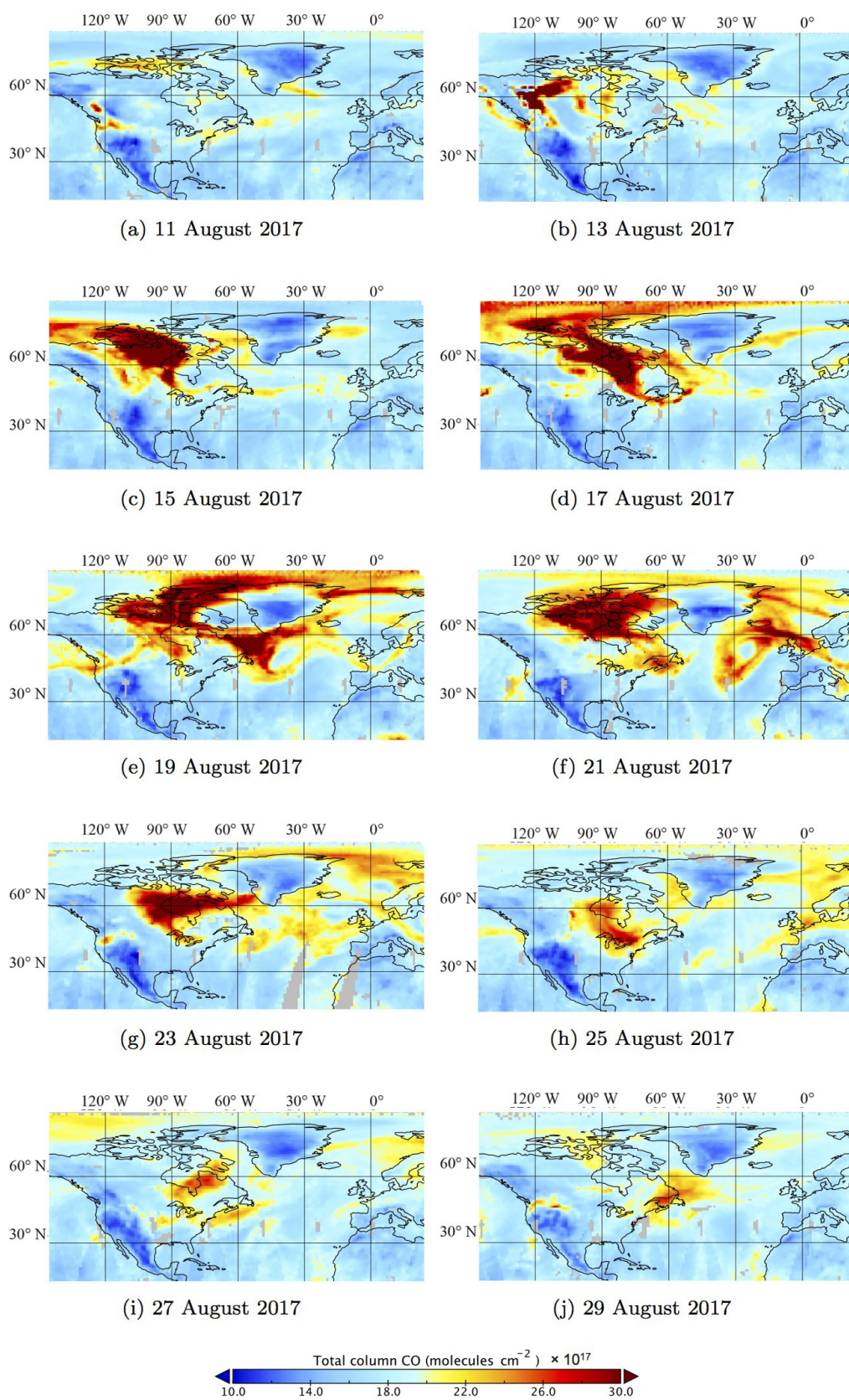
tem in Lille: 22:00 (24 August)–00:30 UTC (25 August); 13:00–16:00 UTC, 16:00–18:00 UTC (29 August); 20:00–23:00 UTC (31 August); and 23:00 (31 August)–02:00 UTC (1 September); two intervals are from the IPRAL system in Palaiseau: 16:00–18:00 and 19:20–21:20 UTC (28 August). Three intervals are from the mobile lidar in the MAMS system (29 August): 14:00–15:00 UTC (corresponding spatially to a 100 km distance from Palaiseau to Compiègne), 15:00–15:45 UTC (100 km on the route from Compiègne to Arras), and 16:15–16:30 UTC at Lille.

Figure 8 shows the optical depth of the stratospheric layer varying from 0.05 to 0.23 (at 532 nm). The spectral dependence of the optical depth of 355 and 532 nm is very weak. The maximal optical depth of the stratospheric layer was observed in the afternoon of 29 August, between 16:00 and 18:00 UTC. The LILAS system observed AOD of  $0.20 \pm 0.04$  at 355 nm and  $0.21 \pm 0.04$  at 532 nm. As discussed in Sect. 3.1, the columnar AOD at 532 nm from AERONET increased by about 0.20 after the presence of the stratospheric layer, which agrees well with the derived optical depth of the stratospheric layer. The minimum of the optical depth appeared in the night of 31 August 2017, giving  $0.04 \pm 0.02$  at 355 nm and  $0.05 \pm 0.02$  at 532 nm. The optical depth of the stratospheric layer along the route, observed by MAMS, is as follows: 0.19 over a distance of 100 km north from Palaiseau, 0.23 along 100 km of the middle of the transect from Compiègne to Arras, and 0.22 when arriving at Lille.

Due to the insufficient signal-to-noise ratio above the stratospheric plume, the MAMS lidar measurements are processed using the Klett method and constrained by the columnar AOD measured by the PLASMA sun photometer. Klett inversion is performed on the lidar profile from the surface to the top of the stratospheric layer, assuming a vertically independent lidar ratio. The optical depth of the stratospheric smoke layer is then calculated from the integral of the ex-



**Figure 5.** OMPS NM daily UVAI products from 11 to 29 August 2017. The results are plotted every 2 days. Grey indicates areas with no retrievals.



**Figure 6.** Total CO concentration (molecules cm<sup>-2</sup>) retrieved from AIRS. The maps are plotted every 2 days from 11 to 29 August 2017.

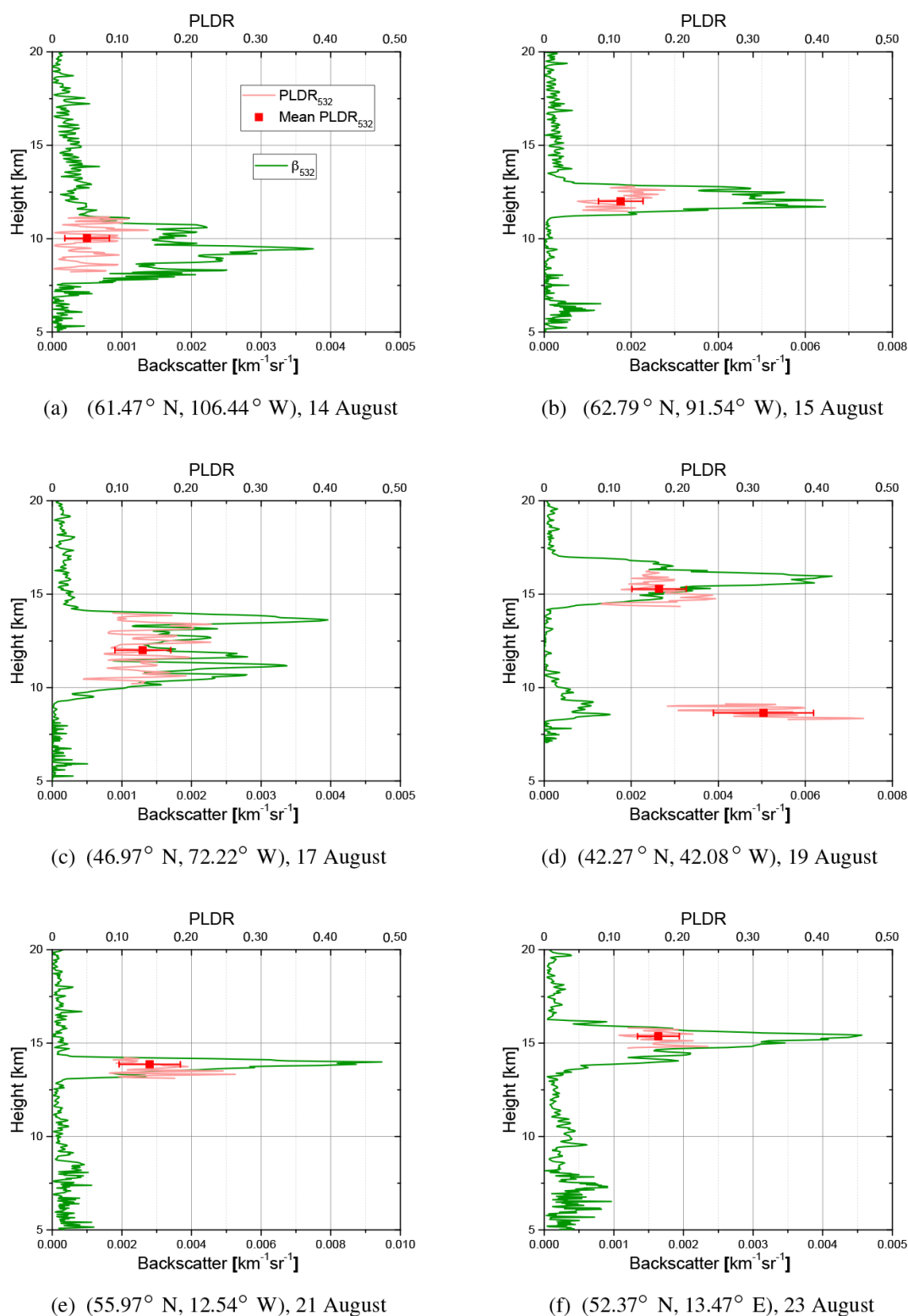


**Figure 7.** The profiles of backscatter coefficient and particle linear depolarization ratio (PLDR) at 532 nm from CALIPSO. Panels (a)–(f) correspond to the six locations (a)–(f) in Fig. 4. The corresponding CALIPSO tracks are (a) 09:50:19, 14 August 2017; (b) 08:54:37, 15 August 2017; (c) 07:03:13, 17 August 2017; (d) 06:50:44, 19 August 2017; (e) 03:20:25, 21 August 2017; and (f) 01:29:01, 23 August 2017. A total of 20 profiles are averaged over these six locations. The solid green and pink lines represent backscatter coefficient and particle linear depolarization ratio, respectively. The red squares with error bars represent the mean particle linear depolarization ratio and the standard deviation within each layer.

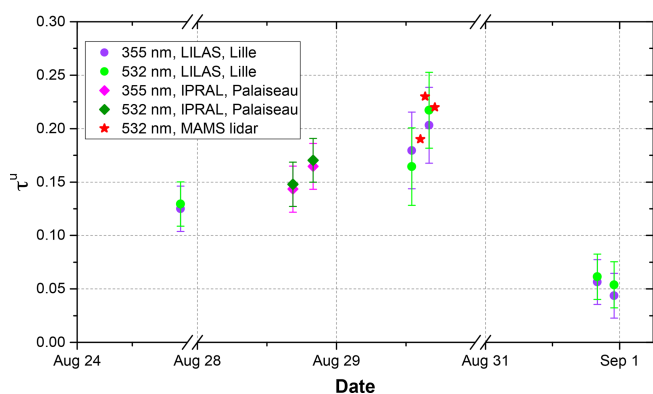


**Figure 8.** Optical depth of the stratospheric smoke layer at 355 and 532 nm estimated from lidar signals in August 2017. The optical depth estimated from LILAS (in Lille) is plotted with solid green (532 nm) and violet circles (355 nm). Optical depth calculated from IPRAL (in Palaiseau) is plotted with solid dark green (532 nm) and magenta (355 nm) diamonds. The red stars represent the optical depth calculated from the MAMS lidar.

tion profile. As a result, the error of the estimated smoke optical depth from MAMS measurements is difficult to quantify. Here we present the optical depth from MAMS lidar for a comparison.

Table 2 summarizes the lidar ratio and particle depolarization ratio in the stratospheric aerosol layer. Lidar ratios vary between  $54 \pm 9$  and  $58 \pm 23$  sr at 532 nm and between  $31 \pm 15$  and  $45 \pm 9$  sr at 355 nm. The results from two different lidar systems and with different observation times agree well, indicating that the properties of the stratospheric layer are spatially and temporally stable. We derived a higher lidar ratio at 532 than at 355 nm, which is a characteristic feature of aged smoke and has been observed in previous studies (Wandinger et al., 2002; Murayama et al., 2004; Müller et al., 2005; Sugimoto et al., 2010). In the night of 31 August, the error of lidar ratio is about 30%–35%, relatively higher than the other days because of the low optical depth. Although the error varies, the mean values of derived lidar ratios are relatively stable. The particle depolarization ratio decreases as wavelength increases. At 1064 nm, the particle linear depolarization ratio is very stable, varying from  $0.04 \pm 0.01$  to  $0.05 \pm 0.01$ . At 532 nm, the particle linear depolarization ratio is also stable, varying from  $0.18 \pm 0.03$  to  $0.20 \pm 0.03$ . The particle linear depolarization ratio at 355 nm increased from  $0.23 \pm 0.03$  on 24 August to  $0.28 \pm 0.08$  on 31 August. However, the increase is within the range of the uncertainties. The particle depolarization ratio at 532 nm is in good agreement with CALIPSO observations shown in Fig. 7c–f. The particle depolarization ratio at 355 nm measured by LILAS is consistent with the IPRAL system. Haarig et al. (2018) measured 0.23 at 355 nm, 0.18 at 532 nm, and 0.04 at 1064 nm in the stratospheric smoke layers on 22 August 2017, showing excellent agreements with our study.

The errors of particle depolarization ratio are calculated with the method in the Appendix. The estimated errors of the particle depolarization ratio are generally below 15%, except the 355 nm channel in the night of 31 August when the optical depth was the lowest in all the investigated observations in this study. On 31 August, the backscatter ratio, volume depolarization ratio, and molecular depolarization ratio at 355 nm are approximately: 3.5 (50%), 0.15 (10%), and 0.004 (200%). The values in the parentheses are the relative errors of the quantity on their left. The resulting error of particle depolarization is about 28%. At 532 nm, we derive 12% of error for the particle depolarization ratio when the backscatter ratio, volume depolarization ratio, and molecular depolarization ratio are 10 (50%), 0.15 (10%), and 0.004 (200%). In the same way, we derive less than 11% of error for the particle depolarization ratio at 1064 nm. The error at 355 nm is estimated to be higher than 532 and 1064 nm as the interferences of molecular scattering are stronger at this channel. When the layer is optically thicker, for example, on 24 August, the error of 355 nm is estimated to be less than 13%. Conservatively, we use 30% for the error of the particle linear depolarization ratio at 355 nm on 31 August and 15% for the error of the rest.

## 4.2 Case study

### 4.2.1 Optical properties

We select the night measurements of 24 August in Lille and 28 August in Palaiseau as two examples. The two systems were operating independently, so that the results from two different systems that measured at different times can be regarded as verifications for each other.

#### 24 August 2017, Lille

Figure 9 shows the retrieved optical properties of the stratospheric smoke layer observed by the LILAS system in the night of 24 August in Lille. The stratospheric aerosol layer is between 17 and 18 km, and we retrieved the extinction and backscatter profiles by assuming that the lidar ratios are 36 sr at 355 nm and 54 sr at 532 nm. The lidar ratio at 1064 nm is assumed to be 60 sr. The extinction coefficient within the layer is about  $0.12$ – $0.22$  km<sup>-1</sup> at 355 and 532 nm. It should be noted that the profile of the extinction coefficient is similar to the backscatter coefficient profile because we assume the aerosol lidar ratio is vertically constant within the smoke layer. A comparison of backscatter coefficient profile has been made (not shown) between Klett and Raman methods. We found that the difference of the backscatter coefficient profiles from the two methods is very minor, indicating that our results are reliable. Assuming a vertically constant aerosol lidar ratio in the smoke layer is not unrealistic, as one can see that the particle linear depolarization ratios in the smoke layer have no noticeable vertical varia-

**Table 2.** Retrieved lidar ratios (LRs), particle linear depolarization ratios (PLDRs), layer thickness, and mean extinction coefficients from multi-wavelength lidar systems LILAS in Lille and IPRAL in Palaiseau.  $\bar{\alpha}$  is the mean extinction coefficient in the stratospheric smoke layer.  $\Delta L$  is the thickness of the stratospheric smoke layer. The values after “ $\pm$ ” represent the errors. Error estimation is presented in the Appendix.

Lidar system	LILAS, Lille					IPRAL, Palaiseau
Date	24 August	29 August		31 August		28 August
Time (UTC)	22:00–00:30	13:00–16:00	16:00–18:00	20:00–23:00	23:00–02:00	19:20–21:20
$\Delta L$ (km)	1.0	3.0	3.4	1.4	1.3	2.3
$\bar{\alpha}_{355}$ ( $\text{km}^{-1}$ )	0.12	0.06	0.06	0.04	0.03	0.08
$\bar{\alpha}_{532}$ ( $\text{km}^{-1}$ )	0.14	0.06	0.06	0.04	0.03	0.08
LR <sub>355</sub> (sr)	35 $\pm$ 6	45 $\pm$ 9	41 $\pm$ 7	34 $\pm$ 12	31 $\pm$ 15	36 $\pm$ 6
LR <sub>532</sub> (sr)	54 $\pm$ 9	56 $\pm$ 12	54 $\pm$ 9	58 $\pm$ 20	58 $\pm$ 23	58 $\pm$ 7
PLDR <sub>355</sub>	0.23 $\pm$ 0.03	0.24 $\pm$ 0.04	0.24 $\pm$ 0.04	0.28 $\pm$ 0.08	0.28 $\pm$ 0.08	0.27 $\pm$ 0.05
PLDR <sub>532</sub>	0.20 $\pm$ 0.03	0.18 $\pm$ 0.03	0.19 $\pm$ 0.03	0.18 $\pm$ 0.03	0.18 $\pm$ 0.03	–
PLDR <sub>1064</sub>	0.05 $\pm$ 0.01	0.04 $\pm$ 0.01	0.05 $\pm$ 0.01	0.05 $\pm$ 0.01	0.05 $\pm$ 0.01	–

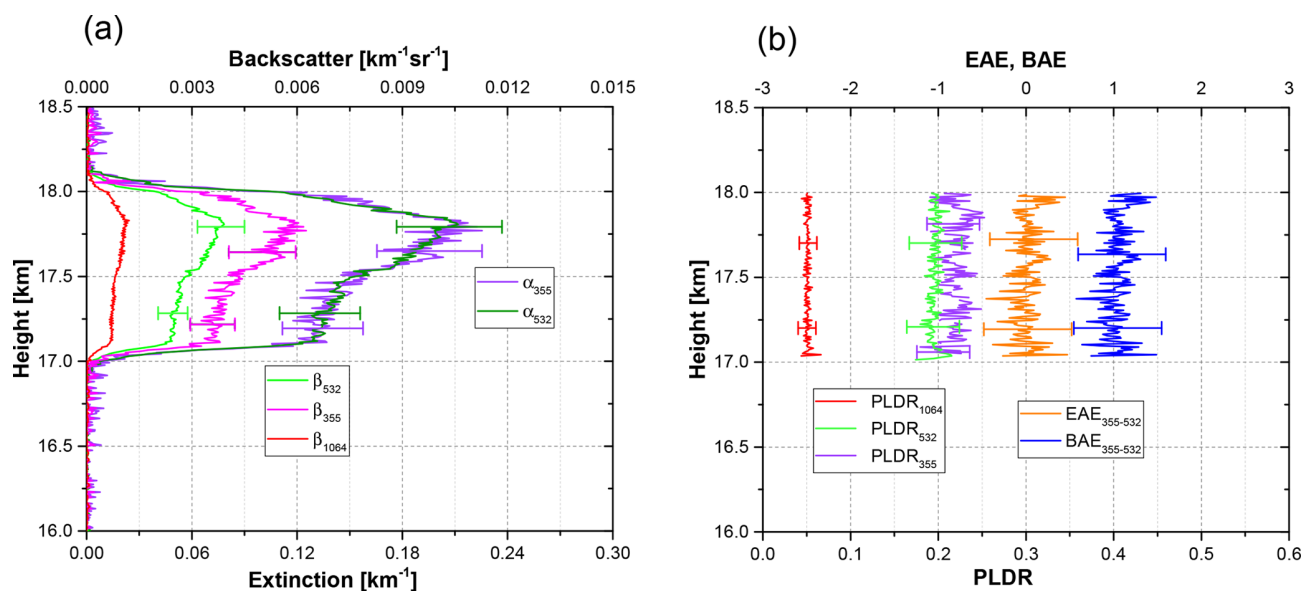


**Figure 9.** (a) Extinction and backscatter coefficients, (b) particle linear depolarization ratio (PLDR), and the extinction-related Ångström exponent (EAE) and backscatter-related Ångström exponent (BAE) retrieved from LILAS observations between 22:00 UTC on 24 August 2017 and 00:30 UTC on 25 August 2017 at Lille. The errors of extinction, backscatter coefficient, and corresponding Ångström exponent at 355 and 532 nm are attributed to the error of the optical depth.

tion, indicating that the smoke particles are well mixed. The extinction-related Ångström exponent for 355 and 532 nm is around  $0.0 \pm 0.5$ ; the backscatter-related Ångström exponent at corresponding wavelengths is about  $1.0 \pm 0.5$ . The particle depolarization ratios decrease as wavelength increases:  $0.23 \pm 0.03$  at 355 nm,  $0.20 \pm 0.03$  at 532 nm, and  $0.05 \pm 0.01$  at 1064 nm. No parameters in Fig. 9b exhibit noticeable vertical variations.

### 28 August 2017, Palaiseau

Figure 10 shows the retrieved optical parameters from IPRAL observations at 19:20–21:20 UTC on 28 August 2017 in Palaiseau. The thickness of the stratospheric layer is about 2.3 km, spreading from 17.2 to 19.5 km. Klett inversion was applied with an estimated lidar ratio of 36 sr at 355 nm and 58 sr at 532 nm. At 1064 nm the lidar ratio was assumed to be 60 sr. The maximum extinction coefficient in the layer reached  $0.12 \text{ km}^{-1}$  at 532 nm. The extinction-related Ångström exponent between 355 and 532 nm is about

$-0.06 \pm 0.5$ . The corresponding backscatter Ångström exponent is about  $1.2 \pm 0.5$ . The particle linear depolarization ratio at 355 nm is about  $0.27 \pm 0.05$ . The particle linear depolarization ratio at 355 nm and extinction and backscatter-related Ångström exponents between 355 and 532 nm do not show evident vertical variations.

#### 4.2.2 Microphysical properties

A regularization algorithm is applied to the vertically averaged extinction coefficients (at 355 and 532 nm) and backscatter coefficients (at 355, 532, and 1064 nm) in Figs. 9 and 10. Treating nonspherical particles is a challenging task. Many studies have been performed to model the light scattering of nonspherical particles. The spheroid model was used to retrieve dust properties (Dubovik et al., 2006; Mishchenko et al., 1997; Veselovskii et al., 2010). Both sphere and spheroid models are used to retrieve particle microphysical properties in our study. The retrievals using sphere and spheroid models are rather consistent except the imaginary part of the refractive index. The spheroid model tends to underestimate the imaginary part of the complex refractive indices, if the measured particle depolarization ratios are used. This demonstrates the deficiency of the spheroid mode in retrieving highly-absorbent and irregular-shaped smoke particles. The size of smoke particles is expected to be not very big so that a sphere model should be able to provide reasonable results. The particle linear depolarization ratio is not used in the retrieval, and the spectral dependence of complex refractive indices is also ignored. The derived effective radius ( $R_{\text{eff}}$ ), volume concentration ( $V_c$ ), and real ( $m_R$ ) and imaginary ( $m_I$ ) parts of the refractive indices are summarized in Table 3.

The retrieved particle size distributes in the range of 0.1 to 1.0  $\mu\text{m}$ , with an effective radius (volume-weighted sphere radius) of  $0.33 \pm 0.10$  for both Palaiseau data and Lille data. The volume concentration is  $15 \pm 5 \mu\text{m}^3 \text{cm}^{-3}$  for Palaiseau data and  $22 \pm 8 \mu\text{m}^3 \text{cm}^{-3}$  for Lille data. The complex refractive indices retrieved from Lille and Palaiseau data are also in good agreement, giving  $1.55 \pm 0.05$  and  $1.52 \pm 0.05$  for the real part and  $0.028 \pm 0.014$  and  $0.021 \pm 0.010$  for the imaginary part. The single-scattering albedos are estimated to be 0.82–0.89 for Lille data and 0.86–0.90 for Palaiseau data. The derived aerosol microphysical properties from Palaiseau and Lille data are consistent.

The errors of the retrieved parameters have been discussed in the relevant papers (Müller et al., 1999; Veselovskii et al., 2002; Pérez-Ramírez et al., 2013). About 30 % of relative error is derived for the effective radius and volume concentration,  $\pm 0.05$  (absolute value) is expected for the real part of refractive indices, and 50 % is derived for the imaginary part of refractive radius. In our case, one significant limitation is that using a sphere model does not allow us to reproduce the particle depolarization ratios. We input the retrieved size distribution (not shown) and complex refractive indices

in Table 3 into the spheroid model, and we found that the spheroid model (85 % spheroid and 15 % sphere) can reproduce the spectral depolarization ratios with satisfactory accuracy: 0.21, 0.19, and 0.07 at 355, 532, and 1064 nm, respectively. However, the argument is not enough to justify that the aforementioned uncertainty estimation from previous researchers is also applicable to our retrievals. We provide this estimate as a reference, but at the current stage, we are not able to provide more quantitative and accurate error estimation for the retrieved microphysical properties.

#### 4.2.3 Direct radiative forcing effect

The stratospheric plumes observed on 24 and 28 August in Lille and Palaiseau are optically thick, with an extinction coefficient about 10 times higher than in the volcanic ash observed by Ansmann et al. (1997) in April 1992, 10 months after the eruption of Mount Pinatubo. The radiative forcing imposed by the observed layers poses a curious question. We input the retrieved microphysical properties into GAR-RLiC/GRASP to estimate the DRF effect of the stratospheric plumes in Lille and Palaiseau. We assume the vertical volume concentration of aerosols follows the extinction profile in Figs. 9 and 10. The surface BRDF parameters for Lille and Palaiseau are taken from AERONET. The upward and downward flux and efficiencies as well as the net DRF ( $\Delta F$ , with respect to a pure Rayleigh atmosphere) of the stratospheric aerosol layers are calculated and Table 4 shows the daily averaged net DRF ( $\text{W m}^{-2}$ ) at four levels: at the bottom of the atmosphere (BOA), below the stratospheric layer, above the stratospheric layer, and at the top of the atmosphere (TOA). For the layer observed in Lille on 24 August, the top and base of the stratosphere are selected as 18.4 and 16.7 km and for Palaiseau observations they are 20 and 17.0 km.

At the TOA, the net DRF flux is estimated to be  $-1.2$  and  $-3.5 \text{ W m}^{-2}$  for Lille and Palaiseau data, respectively. The corresponding forcing efficiencies are  $-7.9$  and  $-21.5 \text{ W m}^{-2} \tau^{-1}$ . At the BOA, the net DRF flux is estimated to be  $-12.3 \text{ W m}^{-2}$  for Lille data and  $-14.5 \text{ W m}^{-2}$  for Palaiseau data. The corresponding forcing efficiencies are  $-79.6$  and  $-89.6 \text{ W m}^{-2} \tau^{-1}$ . We noticed that the difference in net DRF flux between the layer top and layer base is significant. For Lille data, we obtained  $9.9 \text{ W m}^{-2}$  of difference between the top and the base of the stratospheric layer and for Palaiseau, we obtained  $11.1 \text{ W m}^{-2}$ . Because of the high imaginary part of the refractive indices, the stratospheric aerosols have the capacity of absorbing the incoming radiation, thus reducing the upward radiation at the top of the stratospheric layer and the downward radiation at the base of the stratospheric aerosol layer. The heating rate of the stratospheric layer is estimated to be  $3.3 \text{ K day}^{-1}$  for Palaiseau data and  $3.7 \text{ K day}^{-1}$  for Lille data. This qualitatively explains the increase in temperature within the stratospheric layer, as observed by the radiosonde measurements shown in Fig. 3. Due to high uncertainty in the retrieved particle mi-

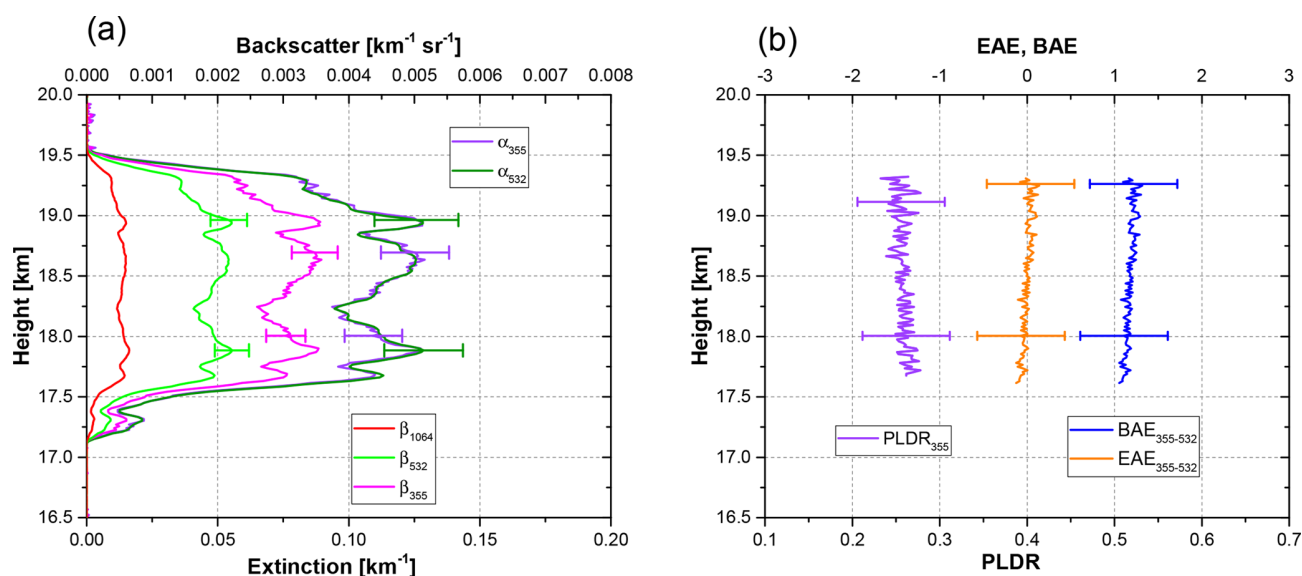


**Figure 10.** (a) Extinction and backscatter coefficients, (b) the particle linear depolarization ratio (PLDR) at 355 nm, and the extinction-related Ångström exponent (EAE) and backscatter-related Ångström exponent (BAE) (between 355 and 532 nm) retrieved from IPRAL observations between 19:20 and 21:20 UTC on 28 August 2017 in Palaiseau.

**Table 3.** Retrieved microphysical properties using the lidar data in Lille and Palaiseau. Extinction and backscatter coefficients shown in Figs. 9a and 10a are averaged in the range of 17–18.0 and 17.5–19.5 km, respectively. The averaged extinction and backscatter coefficients are used as the input of the regularization algorithm to retrieve particle microphysical properties.

	$R_{\text{eff}}$ ( $\mu\text{m}$ )	$V_c$ ( $\mu\text{m}^3 \text{cm}^{-3}$ )	$m_R$	$m_I$
Lille, 24 August	$0.33 \pm 0.10$	$22 \pm 8$	$1.55 \pm 0.05$	$0.028 \pm 0.014$
Palaiseau, 28 August	$0.33 \pm 0.10$	$15 \pm 5$	$1.52 \pm 0.05$	$0.021 \pm 0.011$

**Table 4.** Daily averaged net DRF flux calculated by GAR-RLiC/GRASP. Aerosol microphysical properties in Table 3 and aerosol vertical distributions in Figs. 9a and 10a are used to calculate the DRF effect at the following four vertical levels.

$\Delta F$ ( $\text{W m}^{-2}$ )	TOA	BOA	Layer top	Layer base
Lille, 24 August	−1.2	−12.3	−2.1	−12.0
Palaiseau, 28 August	−3.5	−14.5	−2.5	−13.6

crophysical properties, the uncertainty of the calculated DRF could be large.

## 5 Discussion

The measurements revealed high particle depolarization ratios in the stratospheric smoke at 355 and 532 nm. In particular, the particle depolarization ratio at 355 nm ranges from  $0.23 \pm 0.03$  to  $0.28 \pm 0.08$ , while at 532 nm it is about  $0.19 \pm 0.03$ . The depolarization ratio at 1064 nm is significantly lower, about  $0.05 \pm 0.01$ . Similar spectral dependences of depolarization ratios, 0.20, 0.09, and 0.02 at 355, 532,

and 1064 nm, respectively, were observed by Burton et al. (2015) in a smoke plume at 7–8 km in altitude (on 17 July 2014) in North American wildfires. Particle depolarization ratios of 0.07 and 0.02 at 532 and 1064 nm, respectively, were observed in a Canadian smoke plume at 6 km (on 2 August 2007) over the US (Burton et al., 2012). In Burton et al. (2012) and Burton et al. (2015), the smoke traveled approximately 3 days and 6 days, respectively. The travel times in both cases are shorter than in our study. The light-scattering process leading to high particle depolarization ratios of smoke particles has not been revealed yet. In previous studies, smoke mixed with soil particles was suggested to be the explanation (Fiebig et al., 2002; Murayama et al., 2004; Müller et al., 2007a; Sugimoto et al., 2010; Burton et al., 2012, 2015; Haarig et al., 2018). Strong convections occurring in fire activities in principle are capable of lifting soil particles into the smoke plume (Sugimoto et al., 2010).

A high depolarization ratio with similar spectral dependence has been observed in fine dust particles. Miffre et al. (2016) measured the particle depolarization ratio of two Arizona Test Dust samples at backscattering angle. The radii of the dust samples are mainly below  $1 \mu\text{m}$ . They obtained a higher depolarization ratio at 355 nm than at 532 nm, and the

depolarization ratios at both wavelengths are over 0.30. The sharp edges and corners in the artificial dust samples are a possible reason for the measured high particle depolarization ratio. In the study of Järvinen et al. (2016), over 200 dust samples were used to measure the near-backscattering ( $178^\circ$ ) properties and it is found that, for fine-mode dust, the particle depolarization ratio has a strong size dependence. Järvinen et al. (2016) obtained about 0.12–0.20 and 0.25–0.30 for the depolarization ratio for equivalent particle size parameters at 355 and 532 nm. Sakai et al. (2010) measured the depolarization of Asian and Saharan dust in the backscattering direction and obtained 0.14–0.17 at 532 nm for the samples with only sub-micrometer particles and 0.39 for the samples with high concentrations of super-micrometer particles. Mamouri and Ansmann (2017) concluded that the depolarization spectrum of fine dust is  $0.21 \pm 0.02$  at 355 nm,  $0.16 \pm 0.02$  at 532 nm, and  $0.09 \pm 0.02$  at 1064 nm. This spectrum is very similar to the Canadian stratospheric smoke aerosol presented in this study and Haarig et al. (2018).

However, Murayama et al. (2004) suggested that the coagulation of smoke particles to the clusters with complicated morphology is a more reasonable explanation because they found no signature of mineral dust after analyzing the chemical compositions of the smoke sample. Mishchenko et al. (2016) modeled the spectral depolarization ratios observed by Burton et al. (2015) and found that such behavior results from complicated morphology of smoke particles. Kahnert et al. (2012) modeled the optical properties of light-absorbing carbon aggregates (LACs) embedded in a sulfate shell. It was found that the particle depolarization ratio increases with the aggregate radius (volume-equivalent sphere radius). For the case of  $0.4 \mu\text{m}$  aggregate radius and 20% LAC volume fraction, the computed depolarization ratios are 0.12–0.20 at 304.0 nm, 0.08–0.18 at 533.1 nm, and about 0.015 at 1010.1 nm, which are comparable with the results in this study and Haarig et al. (2018). In this study, we are not able to assess which is the dominant factor leading to the high depolarization ratios, possibly both the soil particles and smoke aging process are partially responsible.

The derived lidar ratios are from  $31 \pm 15$  to  $45 \pm 9$  sr for 355 nm and from  $54 \pm 12$  to  $58 \pm 23$  sr for 532 nm. Considering the uncertainties of the lidar ratio, the derived values and the spectral dependence agree well with previous publications (Müller et al., 2005; Sugimoto et al., 2010; Haarig et al., 2018) about aged smoke observations. Haarig et al. (2018) obtained about 40 sr at 355 nm and 66 sr at 532 nm, using the Raman method. The retrieved effective radius is about  $0.33 \pm 0.10 \mu\text{m}$ , consistent with the particle size obtained by Haarig et al. (2018). The particle size is larger than the values of fresh smoke observed near the fire source (O'Neill et al., 2002; Nicolae et al., 2013). In particular, the retrieved particle size agrees well with the observed smoke transported from Canada to Europe (Wandinger et al., 2002; Müller et al., 2005). Müller et al. (2007b) found that the effective radius increased from 0.15–0.25  $\mu\text{m}$  (2–4 days after the emission)

to 0.3–0.4  $\mu\text{m}$  after 10–20 days of transport time, which is consistent with our results. But it is worth noting that Müller et al. (2007b) investigated only tropospheric smoke and it is not clear if this effect of the aging process is applicable to stratospheric smoke.

The real part of the refractive indices obtained in this study is  $1.52 \pm 0.05$  for Palaiseau data and  $1.55 \pm 0.05$  for Lille data, without considering the spectral dependence. The values are consistent with the results for tropospheric smoke (Dubovik et al., 2002; Wandinger et al., 2002; Taubman et al., 2004; Müller et al., 2005). As for the imaginary part, we derived  $0.021 \pm 0.010$  from Palaiseau data and  $0.028 \pm 0.014$  from Lille data. The imaginary part of refractive indices of smoke in previous studies is diverse. Müller et al. (2005) reported the imaginary part varying around 0.003 for non-absorbing tropospheric smoke originating from aged Siberian and Canadian forest fires. Wandinger et al. (2002) obtained 0.05–0.07 for the imaginary part of Canadian smoke in the troposphere over Europe. Dubovik et al. (2002) derived about 0.01 to 0.03 for the imaginary part of biomass burning using photometer observations. The retrieved imaginary part in our study falls into the range of previously reported values. Using a sphere model in the inversion is potentially an important error source, as spheres cannot fully represent the scattering of irregular aged smoke particles. The application on dust particles (Veselovskii et al., 2010) demonstrated that retrieved volume concentration and effective radius are still reliable and the main error is attributed to the imaginary part of the refractive index. Errors in the optical data are also a potential error source of the retrieved microphysical parameters.

The relative humidity in the smoke layer is one factor that impacts the refractive indices, the particle depolarization ratio, and lidar ratio of smoke particles. However, in some studies, the relative humidity is not mentioned, thus making the comparison difficult. Special attention should be paid to the relative humidity when comparing the complex refractive indices. Mixing with other aerosol types during transport is also a potential cause of the modification of aerosol properties, and its impact is not limited to the refractive indices. In this study, the smoke layers we observed were lofted to the lower stratosphere in the source region and then transported to the observation sites. They were isolated from other tropospheric aerosol sources and not likely to mix with them during the transport. The relative humidity in the stratospheric layer was below 10%, according to the radiosonde measurements. Our study provides a reference for aged smoke aerosols in a dry condition.

The retrieved particle parameters allow an estimation of direct aerosol radiative forcing. We derived  $-79.6 \text{ W m}^{-2} \tau^{-1}$  for the DRF efficiency at the BOA for Lille data. And for Palaiseau data, we derived  $-89.6 \text{ W m}^{-2} \tau^{-1}$ . This indicates that the observed stratospheric aerosol layers strongly reduce the radiation reaching the terrestrial surface mainly by absorbing solar radiation.

Derimian et al. (2016) evaluated the radiative effect of several aerosol models, among which the daily net DRF efficiency of biomass burning aerosols is estimated to be  $-74$  to  $-54 \text{ W m}^{-2} \tau^{-1}$  at the BOA. Mallet et al. (2008) studied the radiative forcing of smoke and dust mixtures over Djougou and derived  $-68$  to  $-50 \text{ W m}^{-2} \tau^{-1}$  for the DRF efficiency at the BOA. Our results are comparable with the values in the publications. Additionally, the mean heating rate of the stratospheric smoke layer is estimated to be about  $3.5 \text{ K day}^{-1}$  for Lille and for Palaiseau data, which qualitatively supports the temperature increase within the stratospheric smoke layer. The warming effect in the layer is potentially responsible for the upward movements of soot-containing aerosol plumes (Laat et al., 2012; Ansmann et al., 2018). The high uncertainty in the retrieved microphysical properties, especially the imaginary part of the refractive indices, will propagate into the DRF estimation. At the current stage, we are not able to accurately estimate the uncertainty in the microphysical properties and in the DRF calculation. Varying the imaginary part by  $\pm 50\%$ , we calculated the variability in the DRF efficiency at the BOA and the heating rate, and we derived about  $20\%$  variation in the DRF efficiency at the BOA and  $40\%$  variation in the heating rate.

## 6 Conclusion

In the summer of 2017, large-scale wildfires spread in the west and north of Canada. The severe fire activities generated strong convections that lofted smoke plumes up to the high altitudes. After long-range transport, the smoke plumes spread over large areas. Three lidar systems in northern France observed aged smoke plumes in the stratosphere, about 10–17 days after the intense fire emissions in mid-August. Unlike fresh smoke particles, the aged smoke particles showed surprisingly high particle depolarization ratios, indicating the presence of irregular smoke particles. Lidar data inversion revealed that the smoke particles are relatively bigger compared to fresh smoke particles and very absorbent. The strong absorption of the observed smoke plumes is related to the perturbation of the temperature profile and the ascent of the plume when exposed to sunlight. In addition, the DRF estimation indicated that the stratospheric smoke can strongly reduce the radiation reaching the bottom of the atmosphere.

This study shows the capability of multi-wavelength Raman lidar in aerosol profiling and characterization. We reported important optical and microphysical properties derived from lidar observations; these results help to improve our knowledge about smoke particles and aerosol classification, which is an important topic in the lidar community. Future improvements in better quantifying the uncertainty in the optical and microphysical properties are highly anticipated. Moreover, this event is also a good opportunity for the study of the atmospheric model. The injection of smoke into

the upper troposphere and lower stratosphere by strong convection needs to be considered in atmospheric models. The self-lifting of absorbing smoke is not yet considered in any aerosol transport model. Additionally, this event provides a favorable chance for studying smoke aging processes, the smoke plumes stayed in the stratosphere more than 1 month and were observed by ground-based lidars and CALIPSO. Much more effort is needed in investigating these measurements.

*Data availability.* The satellite data from OMPS and AIRS can be found in NASA's GES DIS service center. CALIPSO data are obtained from the Langley Atmospheric Science Data Center. The radiosonde data are taken from the website of the University of Wyoming (<http://weather.uwyo.edu/upperair/sounding.html>, last access: 15 January 2019). All the lidar data used in this paper and data processing code or softwares are available upon request to the corresponding author.

## Appendix A: Error estimation

### A1 Errors of optical depth

The errors in the lidar signal at the top and the base of the stratospheric layers are considered to be the major error sources in the error estimation of the optical depth. We estimate the error of the lidar signal  $\overline{P}(\lambda, r_{\text{top}})$  and  $\overline{P}(\lambda, r_{\text{base}})$  to be 3 %–5 %, based on the statistical error of photon distributions. According to Eq. (2), the error of the optical depth,  $\frac{\Delta\tau^u}{\tau^u}$ , is written as

$$\left(\frac{\Delta\tau^u}{\tau^u}\right)^2 = F_{\overline{P}_{\text{top}}} \left(\frac{\Delta\overline{P}(\lambda, r_{\text{top}})}{\overline{P}(\lambda, r_{\text{top}})}\right)^2 + F_{\overline{P}_{\text{base}}} \left(\frac{\Delta\overline{P}(\lambda, r_{\text{base}})}{\overline{P}(\lambda, r_{\text{base}})}\right)^2, \quad (\text{A1})$$

$$F_{\overline{P}_{\text{top,base}}} = \left(\frac{\overline{P}(\lambda, r_{\text{top,base}})}{\tau^u} \frac{\partial\tau^u}{\partial\overline{P}(\lambda, r_{\text{top,base}})}\right)^2, \quad (\text{A2})$$

where  $\Delta\tau^u$  represents the absolute error of  $\tau^u$ . The calculation of molecular extinction and backscattering coefficient is based on the study of Bucholtz (1995). The temperature and pressure profiles are taken from the closest radiosonde stations, Trappes and Beauvechain, and the errors of molecular scattering are neglected.

The error of optical depth propagates into the lidar ratio and vertically integrated backscatter coefficient. Additionally, the error of the lidar ratio also relies on the step width of lidar ratio between two consecutive iterations and the fitting error of the optical depth of the stratospheric aerosol layer, which can be limited by narrowing the step of the iteration. In our calculation, we use a step of 0.5 sr and achieve the fitting error of optical depth of less than 1 % which is negligible compared to the contribution of the error of optical depth to the error of lidar ratio. However, we can basically estimate the error of the integral of the backscatter coefficient within the stratospheric aerosol layer, not the error of the backscatter coefficient profile.

### A2 Errors of Ångström exponent

Ångström exponent  $\mathring{A}$  is defined as follows:

$$\frac{x_{\lambda_1}}{x_{\lambda_2}} = \left(\frac{\lambda_1}{\lambda_2}\right)^{-\mathring{A}}, \quad (\text{A3})$$

where  $x$  is usually the optical quantities such as optical depth  $\tau$ , extinction coefficient  $\alpha$ , and backscatter coefficient  $\beta$ . The error of the Ångström exponent results from the error of the optical quantities at two involved wavelengths:

$$(\Delta\mathring{A})^2 = \left(\log\left(\frac{\lambda_1}{\lambda_2}\right)\right)^{-2} \left[ \left(\frac{\Delta x_{\lambda_1}}{x_{\lambda_1}}\right)^2 + \left(\frac{\Delta x_{\lambda_2}}{x_{\lambda_2}}\right)^2 \right], \quad (\text{A4})$$

where  $\Delta x$  is the error of the quantity  $x$  in absolute values. When the error of the optical depth at 355 and 532 nm is approximately 15 %, the resulting error in the Ångström exponent is about 0.5.

### A3 Errors of particle depolarization ratio

According to Eq. (3), the error of the particle depolarization ratio lies in three terms: the backscatter ratio  $R$ , volume depolarization ratio  $\delta_v$ , and molecular depolarization ratio  $\delta_m$ .

$$\left(\frac{\Delta\delta_p}{\delta_p}\right)^2 = F_R \left(\frac{\Delta R}{R}\right)^2 + F_{\delta_v} \left(\frac{\Delta\delta_v}{\delta_v}\right)^2 + F_{\delta_m} \left(\frac{\Delta\delta_m}{\delta_m}\right)^2, \quad (\text{A5})$$

$$F_X = \left(\frac{X}{\delta_p} \frac{\partial\delta_p}{\partial X}\right)^2, \quad X = R, \delta_v, \delta_m. \quad (\text{A6})$$

As the backscatter ratio and the volume depolarization increase, the dependence of particle depolarization ratio on the backscatter ratio decreases. In the stratospheric smoke layer, the measured volume depolarization ratio is higher in the shorter wavelength and the backscatter ratio is higher in the longer wavelength; the increased volume depolarization ratio or the backscatter ratio allows us to conservatively assume a preliminary error level for the backscatter ratio  $R$ . The potential error sources of the volume depolarization come from the optics and the polarization calibration. The optics have been carefully maintained and adjusted to minimize the errors originating from misalignments. After long-term lidar operation and monitoring of the depolarization calibration, we conservatively expect 10 % relative errors in the volume depolarization ratio. The theoretical molecular depolarization ratio is calculated to be 0.0036 with negligible wavelength dependence (Miles et al., 2001). In the historical record since 2013, LILAS measured molecular depolarization ratios of approximately 0.005–0.013 at 532 nm, 0.012–0.018 at 355 nm, and 0.007–0.010 at 1064 nm. IPRAL measured a molecular depolarization ratio of about 0.020 at 355 nm in this study. Molecular depolarization ratios measured by both the LILAS and IPRAL systems exceed the theoretical value. In addition to the error in the polarization calibration, the error of molecular depolarization ratio arises mainly from the optics, more precisely, the cross-talks between the two polarization channels. The imperfections of the optics cannot be avoided, but a careful characterization is helpful to eliminate the cross-talks as much as possible (Freudenthaler, 2016). In our study, we simply assume 200 % and 300 % for the error of molecular depolarization ratio measured by the LILAS and IPRAL systems, respectively. The total error of the particle depolarization ratio is calculated according to Eq. (A5).

*Author contributions.* QH carried out the experiments at the Lille station, processed the data, and wrote the paper. PG and OD supervised the project and helped with paper correction. IV helped in the data analysis and paper correction. JBA contributed in providing IPRAL measurements and paper correction. IEP performed experiments using the MAMS system, analyzed the data, and helped with paper corrections. TP contributed in LILAS measurements and calibration (with QH). MH and CP helped in paper correction and IPRAL operation. AL and XH contributed in developing and implementing the GARRLiC/GRASP algorithm and radiative transfer code, respectively. CC helped in obtaining and interpreting satellite products. BT helped in paper correction.

*Special issue statement.* This article is part of the special issue “EARLINET aerosol profiling: contributions to atmospheric and climate research”. It is not associated with a conference.

*Competing interests.* The authors declare that they have no conflict of interest.

*Acknowledgements.* We wish to thank the ESA/IDEAS program (ESRIN/VEGA 4000111304/14/I-AM), who supported this work. FEDER/Region Hauts-de-France and CaPPA Labex are acknowledged for their support for the LILAS multi-wavelength Raman lidar and MAMS systems. H2020-ACRIS-2/LiCAL calibration center, EARLINET, ACTRIS-France, ANRT France, CIMEL Electronique, and Service National Observation PHOTONS/AERONET from CNRS-INSU are acknowledged for their support. The development of lidar retrieval algorithms was supported by the Russian Science Foundation (project 16-17-10241). The authors would like to acknowledge the use of the GRASP inversion algorithm (<http://www.grasp-open.com>, 16 January 2019) in this work. NASA and the Langley Atmospheric Science Data Center are acknowledged for providing satellite products. The SIRTa observatory and supporting institutes are acknowledged for providing IPRAL data. Finally we thank all the co-authors for their kind cooperation and professional help.

Edited by: Vassilis Amiridis

Reviewed by: three anonymous referees

## References

- Andreae, M. O., Browell, E. V., Garstang, M., Gregory, G., Harri-  
riss, R., Hill, G., Jacob, D. J., Pereira, M., Sachse, G., Setzer,  
A., Silva Dias, P. L., Talbot, R. W., Torres, A. L., and Wofsy, S.  
C.: Biomass-burning emissions and associated haze layers over  
Amazonia, *J. Geophys. Res.-Atmos.*, 93, 1509–1527, 1988.
- Ansmann, A., Riebesell, M., Wandinger, U., Weitkamp, C., Voss,  
E., Lahmann, W., and Michaelis, W.: Combined Raman elastic-  
backscatter lidar for vertical profiling of moisture, aerosol ex-  
tinction, backscatter, and lidar ratio, *Appl. Phys. B*, 55, 18–28,  
1992.
- Ansmann, A., Mattis, I., Wandinger, U., Wagner, F., Reichardt, J.,  
and Dethler, T.: Evolution of the Pinatubo aerosol: Raman lidar  
observations of particle optical depth, effective radius, mass, and  
surface area over Central Europe at 53.4 N, *J. Atmos. Sci.*, 54,  
2630–2641, 1997.
- Ansmann, A., Baars, H., Chudnovsky, A., Mattis, I., Veselovskii,  
I., Haarig, M., Seifert, P., Engelmann, R., and Wandinger, U.:  
Extreme levels of Canadian wildfire smoke in the stratosphere  
over central Europe on 21–22 August 2017, *Atmos. Chem.  
Phys.*, 18, 11831–11845, <https://doi.org/10.5194/acp-18-11831-2018>, 2018.
- Böckmann, C., Wandinger, U., Ansmann, A., Bösenberg, J.,  
Amiridis, V., Boselli, A., Delaval, A., De Tomasi, F., Frioud, M.,  
Grigoriev, I. V., Hågård, A., Horvat, M., Iarlori, M., Komguem,  
L., Kreipl, S., Larchevêque, G., Matthias, V., Papayannis, A.,  
Pappalardo, G., Rocadenbosch, F., Rodrigues, J. A., Schneider,  
J., Shcherbakov, V., and Wiegner, M.: Aerosol lidar intercom-  
parison in the framework of the EARLINET project. 2. Aerosol  
backscatter algorithms, *Appl. Optics*, 43, 977–989, 2004.
- Bösenberg, J., Matthias, V., Linné, H., Comerón Tejero, A., Ro-  
cadenbosch Burillo, F., Pérez López, C., and Baldasano Recio,  
J. M.: EARLINET: A European Aerosol Research Lidar Network  
to establish an aerosol climatology, Report, Max-Planck-Institut  
für Meteorologie, 1–191, 2003.
- Bovchaliuk, V., Goloub, P., Podvin, T., Veselovskii, I., Tanre, D.,  
Chaikovskiy, A., Dubovik, O., Mortier, A., Lopatin, A., Koren-  
skiy, M., and Vignati, S.: Comparison of aerosol properties re-  
trieved using GARRLiC, LIRIC, and Raman algorithms applied  
to multi-wavelength lidar and sun/sky-photometer data, *Atmos.  
Meas. Tech.*, 9, 3391–3405, <https://doi.org/10.5194/amt-9-3391-2016>, 2016.
- Bravo-Aranda, J. A., Belegante, L., Freudenthaler, V., Alados-  
Arboledas, L., Nicolae, D., Granados-Muñoz, M. J., Guerrero-  
Rascado, J. L., Amodeo, A., D’Amico, G., Engelmann, R., Pap-  
palardo, G., Kokkalis, P., Mamouri, R., Papayannis, A., Navas-  
Guzmán, F., Olmo, F. J., Wandinger, U., Amato, F., and Haeffel-  
lin, M.: Assessment of lidar depolarization uncertainty by means  
of a polarimetric lidar simulator, *Atmos. Meas. Tech.*, 9, 4935–  
4953, <https://doi.org/10.5194/amt-9-4935-2016>, 2016.
- Bucholtz, A.: Rayleigh-scattering calculations for the terrestrial at-  
mosphere, *Appl. Optics*, 34, 2765–2773, 1995.
- Burton, S. P., Ferrare, R. A., Hostetler, C. A., Hair, J. W., Rogers, R.  
R., Obland, M. D., Butler, C. F., Cook, A. L., Harper, D. B., and  
Froyd, K. D.: Aerosol classification using airborne High Spectral  
Resolution Lidar measurements – methodology and examples,  
*Atmos. Meas. Tech.*, 5, 73–98, <https://doi.org/10.5194/amt-5-73-2012>, 2012.
- Burton, S. P., Hair, J. W., Kahnert, M., Ferrare, R. A., Hostetler,  
C. A., Cook, A. L., Harper, D. B., Berkoff, T. A., Seaman, S.  
T., Collins, J. E., Fenn, M. A., and Rogers, R. R.: Observa-  
tions of the spectral dependence of linear particle depolariza-  
tion ratio of aerosols using NASA Langley airborne High Spec-  
tral Resolution Lidar, *Atmos. Chem. Phys.*, 15, 13453–13473,  
<https://doi.org/10.5194/acp-15-13453-2015>, 2015.
- Derimian, Y., Dubovik, O., Huang, X., Lapyonok, T., Litvinov,  
P., Kostinski, A. B., Dubuisson, P., and Ducos, F.: Comprehen-  
sive tool for calculation of radiative fluxes: illustration of short-  
wave aerosol radiative effect sensitivities to the details in aerosol  
and underlying surface characteristics, *Atmos. Chem. Phys.*, 16,  
5763–5780, <https://doi.org/10.5194/acp-16-5763-2016>, 2016.

- Deshler, T.: A review of global stratospheric aerosol: Measurements, importance, life cycle, and local stratospheric aerosol, *Atmos. Res.*, 90, 223–232, 2008.
- Dubovik, O., Holben, B., Eck, T. F., Smirnov, A., Kaufman, Y. J., King, M. D., Tanré, D., and Slutsker, I.: Variability of absorption and optical properties of key aerosol types observed in worldwide locations, *J. Atmos. Sci.*, 59, 590–608, 2002.
- Dubovik, O., Sinyuk, A., Lapyonok, T., Holben, B. N., Mishchenko, M., Yang, P., Eck, T. F., Volten, H., Muñoz, O., Veihelmann, B., Veihelmann, B., van der Zande, W. J., Leon, J.-F., Sorokin, M., and Slutsker, I.: Application of spheroid models to account for aerosol particle nonsphericity in remote sensing of desert dust, *J. Geophys. Res.-Atmos.*, 111, D11208, <https://doi.org/10.1029/2005JD006619>, 2006.
- Dubovik, O., Lapyonok, T., Litvinov, P., Herman, M., Fuertes, D., Ducos, F., Lopatin, A., Chaikovsky, A., Torres, B., Derimian, Y., Huang, X., Aspetsberger, M., and Federspiel, C.: GRASP: a versatile algorithm for characterizing the atmosphere, *SPIE Newsroom*, 25, <https://doi.org/10.1117/2.1201408.005558>, 2014.
- Fiebig, M., Petzold, A., Wandinger, U., Wendisch, M., Kiemle, C., Stifter, A., Ebert, M., Rother, T., and Leiterer, U.: Optical closure for an aerosol column: Method, accuracy, and inferable properties applied to a biomass-burning aerosol and its radiative forcing, *J. Geophys. Res.-Atmos.*, 107, LAC 12-1–LAC 12-15, <https://doi.org/10.1029/2000JD000192>, 2002.
- Freudenthaler, V.: About the effects of polarising optics on lidar signals and the  $\Delta 90$  calibration, *Atmos. Meas. Tech.*, 9, 4181–4255, <https://doi.org/10.5194/amt-9-4181-2016>, 2016.
- Freudenthaler, V., Esselborn, M., Wiegner, M., Heese, B., Tesche, M., Ansmann, A., Müller, D., Althausen, D., Wirth, M., Fix, A., Ehret, G., Knippertz, P., Toledano, C., Gasteiger, J., Garhammer, M., and Seefeldner, M.: Depolarization ratio profiling at several wavelengths in pure Saharan dust during SAMUM 2006, *Tellus B*, 61, 165–179, 2009.
- Freudenthaler, V., Linné, H., Chaikovsky, A., Rabus, D., and Groß, S.: EARLINET lidar quality assurance tools, *Atmos. Meas. Tech. Discuss.*, <https://doi.org/10.5194/amt-2017-395>, in review, 2018.
- Fromm, M., Alfred, J., Hoppel, K., Hornstein, J., Bevilacqua, R., Shettle, E., Servranckx, R., Li, Z., and Stocks, B.: Observations of boreal forest fire smoke in the stratosphere by POAM III, SAGE II, and lidar in 1998, *Geophys. Res. Lett.*, 27, 1407–1410, 2000.
- Fromm, M., Bevilacqua, R., Servranckx, R., Rosen, J., Thayer, J. P., Herman, J., and Larko, D.: Pyro-cumulonimbus injection of smoke to the stratosphere: Observations and impact of a super blowup in northwestern Canada on 3–4 August 1998, *J. Geophys. Res.-Atmos.*, 110, D08205, <https://doi.org/10.1029/2004JD005350>, 2005.
- Fromm, M., Shettle, E., Fricke, K., Ritter, C., Trickl, T., Giehl, H., Gerding, M., Barnes, J., O'Neill, M., Massie, S., Blum, U., McDermid, I. S., Leblanc, T., and Deshler, T.: Stratospheric impact of the Chisholm pyrocumulonimbus eruption: 2. Vertical profile perspective, *J. Geophys. Res.-Atmos.*, 113, D08203, <https://doi.org/10.1029/2007jd009147>, 2008.
- Fromm, M. D. and Servranckx, R.: Transport of forest fire smoke above the tropopause by supercell convection, *Geophys. Res. Lett.*, 30, <https://doi.org/10.1029/2002gl016820>, 2003.
- Haarig, M., Ansmann, A., Baars, H., Jimenez, C., Veselovskii, I., Engelmann, R., and Althausen, D.: Depolarization and lidar ratios at 355, 532, and 1064 nm and microphysical properties of aged tropospheric and stratospheric Canadian wildfire smoke, *Atmos. Chem. Phys.*, 18, 11847–11861, <https://doi.org/10.5194/acp-18-11847-2018>, 2018.
- Haefelin, M., Barthès, L., Bock, O., Boitel, C., Bony, S., Bouniol, D., Chepfer, H., Chiriaco, M., Cuesta, J., Delanoë, J., Drobninski, P., Dufresne, J.-L., Flamant, C., Grall, M., Hodzic, A., Hourdin, F., Lapouge, F., Lemaître, Y., Mathieu, A., Morille, Y., Naud, C., Noël, V., O'Hirok, W., Pelon, J., Pietras, C., Protat, A., Romand, B., Scialom, G., and Vautard, R.: SIRTa, a ground-based atmospheric observatory for cloud and aerosol research, *Ann. Geophys.*, 23, 253–275, <https://doi.org/10.5194/angeo-23-253-2005>, 2005.
- Haskins, R. and Kaplan, L.: Remote sensing of trace gases using the Atmospheric InfraRed Sounder, in: *IRS*, 92, 278–281, 1992.
- Hofmann, D., Barnes, J., O'Neill, M., Trudeau, M., and Neely, R.: Increase in background stratospheric aerosol observed with lidar at Mauna Loa Observatory and Boulder, Colorado, *Geophys. Res. Lett.*, 36, L15808, <https://doi.org/10.1029/2009GL039008>, 2009.
- Hsu, N. C., Herman, J., Torres, O., Holben, B., Tanre, D., Eck, T., Smirnov, A., Chatenet, B., and Lavenu, F.: Comparisons of the TOMS aerosol index with Sun-photometer aerosol optical thickness: Results and applications, *J. Geophys. Res.-Atmos.*, 104, 6269–6279, 1999.
- Jaross, G.: OMPS-NPP L3 NM Ozone ( $O_3$ ) Total Column 1.0 deg grid daily V2, Greenbelt, MD, USA, Goddard Earth Sciences Data and Information Services Center (GES DISC), <https://doi.org/10.5067/7Y7KSA1QNQP8>, 2017.
- Järvinen, E., Kemppinen, O., Nousiainen, T., Kociok, T., Möhler, O., Leisner, T., and Schnaiter, M.: Laboratory investigations of mineral dust near-backscattering depolarization ratios, *J. Quant. Spectrosc. Ra.*, 178, 192–208, 2016.
- Kahn, B. H., Irion, F. W., Dang, V. T., Manning, E. M., Nasiri, S. L., Naud, C. M., Blaisdell, J. M., Schreier, M. M., Yue, Q., Bowman, K. W., Fetzer, E. J., Hulley, G. C., Liou, K. N., Lubin, D., Ou, S. C., Susskind, J., Takano, Y., Tian, B., and Worden, J. R.: The Atmospheric Infrared Sounder version 6 cloud products, *Atmos. Chem. Phys.*, 14, 399–426, <https://doi.org/10.5194/acp-14-399-2014>, 2014.
- Kahnert, M., Nousiainen, T., Lindqvist, H., and Ebert, M.: Optical properties of light absorbing carbon aggregates mixed with sulfate: assessment of different model geometries for climate forcing calculations, *Optics Exp.*, 20, 10042–10058, 2012.
- Karol, Y., Tanré, D., Goloub, P., Ververde, C., Balois, J. Y., Blarel, L., Podvin, T., Mortier, A., and Chaikovsky, A.: Airborne sun photometer PLASMA: concept, measurements, comparison of aerosol extinction vertical profile with lidar, *Atmos. Meas. Tech.*, 6, 2383–2389, <https://doi.org/10.5194/amt-6-2383-2013>, 2013.
- Khaykin, S., Godin-Beekmann, S., Hauchecorne, A., Pelon, J., Ravetta, F., and Keckhut, P.: Stratospheric smoke with unprecedentedly high backscatter observed by lidars above southern France, *Geophys. Res. Lett.*, 45, 1639–1646, 2018.
- Khaykin, S. M., Godin-Beekmann, S., Keckhut, P., Hauchecorne, A., Jumelet, J., Vernier, J.-P., Bourassa, A., Degenstein, D. A., Rieger, L. A., Bingen, C., Vanhellefont, F., Robert, C., DeLand, M., and Bhartia, P. K.: Variability and evolution of the midlatitude stratospheric aerosol budget from 22 years of ground-based

- lidar and satellite observations, *Atmos. Chem. Phys.*, 17, 1829–1845, <https://doi.org/10.5194/acp-17-1829-2017>, 2017.
- Klett, J. D.: Lidar inversion with variable backscatter/extinction ratios, *Appl. Optics*, 24, 1638–1643, 1985.
- Kremser, S., Thomason, L. W., Hobe, M., Hermann, M., Deshler, T., Timmreck, C., Toohey, M., Stenke, A., Schwarz, J. P., Weigel, R., Fueglistaler, S., Prata, F. J., Vernier, J.-P., Schlager, H., Barnes, E. J., Antuna-Marrero, J.-C., Fairlie, D., Palm, M., Mahieu, E., Notholt, J., Rex, M., Bingen, C., Vanhellemont, F., Bourassa, A., Plane, J. M. C., Klocke, D., Carn, S. A., Clarisse, L., Trickl, T., Neely, R. D., James, A., Rieger, L., Wilson, C. J., and Meland, B.: Stratospheric aerosol – Observations, processes, and impact on climate, *Rev. Geophys.*, 54, 278–335, 2016.
- Laat, A., Stein Zweers, D. C., and Boers, R.: A solar escalator: Observational evidence of the self-lifting of smoke and aerosols by absorption of solar radiation in the February 2009 Australian Black Saturday plume, *J. Geophys. Res.-Atmos.*, 117, D04204, <https://doi.org/10.1029/2011JD017016>, 2012.
- Lenoble, J., Herman, M., Deuzé, J., Lafrance, B., Santer, R., and Tanré, D.: A successive order of scattering code for solving the vector equation of transfer in the earth's atmosphere with aerosols, *J. Quant. Spectrosc. Ra.*, 107, 479–507, 2007.
- Lopatin, A., Dubovik, O., Chaikovsky, A., Goloub, P., Lapyonok, T., Tanré, D., and Litvinov, P.: Enhancement of aerosol characterization using synergy of lidar and sun-photometer coincident observations: the GARRLiC algorithm, *Atmos. Meas. Tech.*, 6, 2065–2088, <https://doi.org/10.5194/amt-6-2065-2013>, 2013.
- Luderer, G., Trentmann, J., Winterrath, T., Textor, C., Herzog, M., Graf, H. F., and Andreae, M. O.: Modeling of biomass smoke injection into the lower stratosphere by a large forest fire (Part II): sensitivity studies, *Atmos. Chem. Phys.*, 6, 5261–5277, <https://doi.org/10.5194/acp-6-5261-2006>, 2006.
- Mallet, M., Pont, V., Lioussé, C., Gomes, L., Pelon, J., Osborne, S., Haywood, J., Roger, J.-C., Dubuisson, P., Mariscal, A., Thouret, V., and Goloub, P.: Aerosol direct radiative forcing over Djougou (northern Benin) during the African Monsoon Multidisciplinary Analysis dry season experiment (Special Observation Period-0), *J. Geophys. Res.-Atmos.*, 113, D00C01, <https://doi.org/10.1029/2007JD009419>, 2008.
- Mamouri, R.-E. and Ansmann, A.: Potential of polarization/Raman lidar to separate fine dust, coarse dust, maritime, and anthropogenic aerosol profiles, *Atmos. Meas. Tech.*, 10, 3403–3427, <https://doi.org/10.5194/amt-10-3403-2017>, 2017.
- Matthais, V., Freudenthaler, V., Amodeo, A., Balin, I., Balis, D., Bösenberg, J., Chaikovsky, A., Chourdakis, G., Comeron, A., Delaval, A., De Tomasi, F., Eixmann, R., Hågård, A., Komguem, L., Kreipl, S., Matthey, R., Rizi, V., Rodrigues, J. A., Wandinger, U., and Wang, X.: Aerosol lidar intercomparison in the framework of the EARLINET project. 1. Instruments, *Appl. Optics*, 43, 961–976, 2004.
- McMillan, W., Barnet, C., Strow, L., Chahine, M., McCourt, M., Warner, J., Novelli, P., Korontzi, S., Maddy, E., and Datta, S.: Daily global maps of carbon monoxide from NASA's Atmospheric Infrared Sounder, *Geophys. Res. Lett.*, 32, <https://doi.org/10.1029/2004GL021821>, 2005.
- McPeters, R. D., Bhartia, P., Krueger, A. J., Herman, J. R., Wellemeyer, C. G., Sefior, C. J., Byerly, W., and Celarier, E. A.: Total Ozone Mapping Spectrometer (TOMS) Level-3 data products user's guide, available at: <https://ntrs.nasa.gov/archive/nasa/casi>.
- ntrs.nasa.gov/20010044085.pdf (last access: 15 January 2019), 2000.
- Miffre, A., Mehri, T., Francis, M., and Rairoux, P.: UV–VIS depolarization from Arizona Test Dust particles at exact backscattering angle, *J. Quant. Spectrosc. Ra.*, 169, 79–90, 2016.
- Miles, R. B., Lempert, W. R., and Forkey, J. N.: Laser rayleigh scattering, *Meas. Sci. Technol.*, 12, R33–R51, 2001.
- Mishchenko, M. I., Travis, L. D., Kahn, R. A., and West, R. A.: Modeling phase functions for dustlike tropospheric aerosols using a shape mixture of randomly oriented polydisperse spheroids, *J. Geophys. Res.-Atmos.*, 102, 16831–16847, 1997.
- Mishchenko, M. I., Dlugach, J. M., and Liu, L.: Linear depolarization of lidar returns by aged smoke particles, *Appl. Optics*, 55, 9968–9973, 2016.
- Müller, D., Wandinger, U., and Ansmann, A.: Microphysical particle parameters from extinction and backscatter lidar data by inversion with regularization: theory, *Appl. Optics*, 38, 2346–2357, 1999.
- Müller, D., Mattis, I., Wandinger, U., Ansmann, A., Althausen, D., and Stohl, A.: Raman lidar observations of aged Siberian and Canadian forest fire smoke in the free troposphere over Germany in 2003: Microphysical particle characterization, *J. Geophys. Res.-Atmos.*, 110, D17201, <https://doi.org/10.1029/2004JD005756>, 2005.
- Müller, D., Ansmann, A., Mattis, I., Tesche, M., Wandinger, U., Althausen, D., and Pisani, G.: Aerosol-type-dependent lidar ratios observed with Raman lidar, *J. Geophys. Res.-Atmos.*, 112, D16202, <https://doi.org/10.1029/2006JD008292>, 2007a.
- Müller, D., Mattis, I., Ansmann, A., Wandinger, U., Ritter, C., and Kaiser, D.: Multiwavelength Raman lidar observations of particle growth during long-range transport of forest-fire smoke in the free troposphere, *Geophys. Res. Lett.*, 34, L05803, <https://doi.org/10.1029/2006GL027936>, 2007b.
- Murayama, T., Müller, D., Wada, K., Shimizu, A., Sekiguchi, M., and Tsukamoto, T.: Characterization of Asian dust and Siberian smoke with multi-wavelength Raman lidar over Tokyo, Japan in spring 2003, *Geophys. Res. Lett.*, 31, L23103, <https://doi.org/10.1029/2004GL021105>, 2004.
- Nicolae, D., Nemuc, A., Müller, D., Talianu, C., Vasilescu, J., Bellegante, L., and Kolgotin, A.: Characterization of fresh and aged biomass burning events using multiwavelength Raman lidar and mass spectrometry, *J. Geophys. Res.-Atmos.*, 118, 2956–2965, 2013.
- O'Neill, N., Eck, T., Holben, B., Smirnov, A., Royer, A., and Li, Z.: Optical properties of boreal forest fire smoke derived from Sun photometry, *J. Geophys. Res.-Atmos.*, 107, AAC 6-1–AAC 6-14, 2002.
- Papayannis, A., Amiridis, V., Mona, L., Tsaknakis, G., Balis, D., Bösenberg, J., Chaikovski, A., De Tomasi, F., Grigorov, I., Mattis, I., Mitev, V and Mueller, Detlef and Nickovic, S and Perez, C and Pietruczuk, A and Pisani, G., Ravetta, F., Rizi, V., Sicard, M., Trickl, T., Wiegner, M., Gerding, M., and Mamouri, R. E.: Systematic lidar observations of Saharan dust over Europe in the frame of EARLINET (2000–2002), *J. Geophys. Res.-Atmos.*, 113, D10204, <https://doi.org/10.1029/2007JD009028>, 2008.
- Pappalardo, G., Amodeo, A., Apituley, A., Comeron, A., Freudenthaler, V., Linné, H., Ansmann, A., Bösenberg, J., D'Amico, G., Mattis, I., Mona, L., Wandinger, U., Amiridis, V., Alados-Arboledas, L., Nicolae, D., and Wiegner, M.: EARLINET: to-

- wards an advanced sustainable European aerosol lidar network, *Atmos. Meas. Tech.*, 7, 2389–2409, <https://doi.org/10.5194/amt-7-2389-2014>, 2014.
- Pérez-Ramírez, D., Whiteman, D. N., Veselovskii, I., Kolgotin, A., Korenskiy, M., and Alados-Arboledas, L.: Effects of systematic and random errors on the retrieval of particle microphysical properties from multiwavelength lidar measurements using inversion with regularization, *Atmos. Meas. Tech.*, 6, 3039–3054, <https://doi.org/10.5194/amt-6-3039-2013>, 2013.
- Platt, C.: Lidar and radiometric observations of cirrus clouds, *J. Atmos. Sci.*, 30, 1191–1204, 1973.
- Popovici, I. E., Goloub, P., Podvin, T., Blarel, L., Loisil, R., Unga, F., Mortier, A., Deroo, C., Victori, S., Ducos, F., Torres, B., Delegove, C., Choël, M., Pujol-Söhne, N., and Pietras, C.: Description and applications of a mobile system performing on-road aerosol remote sensing and in situ measurements, *Atmos. Meas. Tech.*, 11, 4671–4691, <https://doi.org/10.5194/amt-11-4671-2018>, 2018.
- Sakai, T., Nagai, T., Zaizen, Y., and Mano, Y.: Backscattering linear depolarization ratio measurements of mineral, sea-salt, and ammonium sulfate particles simulated in a laboratory chamber, *Appl. Optics*, 49, 4441–4449, 2010.
- Sassen, K., Liou, K. N., Kinne, S., and Griffin, M.: Highly supercooled cirrus cloud water: Confirmation and climatic implications, *Science*, 227, 411–413, 1985.
- Seftor, C., Jaross, G., Kowitz, M., Haken, M., Li, J., and Flynn, L.: Postlaunch performance of the Suomi National Polar-orbiting Partnership Ozone Mapping and Profiler Suite (OMPS) nadir sensors, *J. Geophys. Res.-Atmos.*, 119, 4413–4428, 2014.
- Shepherd, T. G.: Transport in the middle atmosphere, *J. Meteorol. Soc. Jpn.*, 85, 165–191, 2007.
- Sugimoto, N., Tatarov, B., Shimizu, A., Matsui, I., and Nishizawa, T.: Optical characteristics of forest-fire smoke observed with two-wavelength Mie-scattering lidars and a high-spectral-resolution lidar over Japan, *SOLA*, 6, 93–96, 2010.
- Susskind, J., Blaisdell, J. M., and Iredell, L.: Improved methodology for surface and atmospheric soundings, error estimates, and quality control procedures: the atmospheric infrared sounder science team version-6 retrieval algorithm, *J. Appl. Remote Sens.*, 8, 084994, <https://doi.org/10.1117/1.JRS.8.084994>, 2014.
- Taubman, B. F., Marufu, L. T., Vant-Hull, B. L., Piety, C. A., Doddridge, B. G., Dickerson, R. R., and Li, Z.: Smoke over haze: Aircraft observations of chemical and optical properties and the effects on heating rates and stability, *J. Geophys. Res.-Atmos.*, 109, 084994-1–084994-33, <https://doi.org/10.1117/1.JRS.8.084994>, 2004.
- Teixeira, A. S. T.: AIRS/Aqua L3 Daily Standard Physical Retrieval (AIRS-only) 1 degree × 1 degree V006, Greenbelt, MD, USA, Goddard Earth Sciences Data and Information Services Center (GES DISC), <https://doi.org/10.5067/Aqua/AIRS/DATA303>, 2013.
- Trentmann, J., Luderer, G., Winterrath, T., Fromm, M. D., Servranckx, R., Textor, C., Herzog, M., Graf, H.-F., and Andreae, M. O.: Modeling of biomass smoke injection into the lower stratosphere by a large forest fire (Part I): reference simulation, *Atmos. Chem. Phys.*, 6, 5247–5260, <https://doi.org/10.5194/acp-6-5247-2006>, 2006.
- Vallero, D.: Fundamentals of air pollution, Academic Press, 814 pp., available at: <https://books.google.fr/books?hl=en&lr=&id=iFcXAAwAAQBAJ&oi=fnd&pg=PP1&dq=Fundamentals+of+air+pollution+vallero&ots=rfJer-585s&sig=6N7KMdclAy3x6qPn3YbPA-eoXtg#v=onepage&q=Fundamentals%20of%20air%20pollution%20vallero&f=false> (last access: 16 January 2019), 2014.
- Veselovskii, I., Kolgotin, A., Griaznov, V., Müller, D., Wandinger, U., and Whiteman, D. N.: Inversion with regularization for the retrieval of tropospheric aerosol parameters from multiwavelength lidar sounding, *Appl. Optics*, 41, 3685–3699, 2002.
- Veselovskii, I., Dubovik, O., Kolgotin, A., Lapyonok, T., Di Girolamo, P., Summa, D., Whiteman, D. N., Mishchenko, M., and Tanré, D.: Application of randomly oriented spheroids for retrieval of dust particle parameters from multiwavelength lidar measurements, *J. Geophys. Res.-Atmos.*, 115, D21203, <https://doi.org/10.1029/2010JD014139>, 2010.
- Veselovskii, I., Goloub, P., Podvin, T., Bovchaliuk, V., Derimian, Y., Augustin, P., Fourmentin, M., Tanre, D., Korenskiy, M., Whiteman, D. N., Diallo, A., Ndiaye, T., Kolgotin, A., and Dubovik, O.: Retrieval of optical and physical properties of African dust from multiwavelength Raman lidar measurements during the SHADOW campaign in Senegal, *Atmos. Chem. Phys.*, 16, 7013–7028, <https://doi.org/10.5194/acp-16-7013-2016>, 2016.
- Veselovskii, I., Goloub, P., Podvin, T., Tanre, D., Ansmann, A., Korenskiy, M., Borovoi, A., Hu, Q., and Whiteman, D.: Spectral dependence of backscattering coefficient of mixed phase clouds over West Africa measured with two-wavelength Raman polarization lidar: Features attributed to ice-crystals corner reflection, *J. Quant. Spectrosc. Ra.*, 202, 74–80, 2017.
- Wandinger, U., Müller, D., Böckmann, C., Althausen, D., Matthias, V., Bösenberg, J., Weiß, V., Fiebig, M., Wendisch, M., Stohl, A., et al.: Optical and microphysical characterization of biomass-burning and industrial-pollution aerosols from-multiwavelength lidar and aircraft measurements, *J. Geophys. Res.-Atmos.*, 107, LAC 7-1–LAC 7-20, <https://doi.org/10.1029/2000JD000202>, 2002.
- Young, S. A.: Analysis of lidar backscatter profiles in optically thin clouds, *Appl. Optics*, 34, 7019–7031, 1995.
- Zuev, V. V., Burlakov, V. D., Nevzorov, A. V., Pravdin, V. L., Savelieva, E. S., and Gerasimov, V. V.: 30-year lidar observations of the stratospheric aerosol layer state over Tomsk (Western Siberia, Russia), *Atmos. Chem. Phys.*, 17, 3067–3081, <https://doi.org/10.5194/acp-17-3067-2017>, 2017.

